CZECH TECHNICAL UNIVERSITY IN PRAGUE
FACULTY OF CIVIL ENGINEERING

IMPACTS OF SOIL PROPERTIES ON WATER RETENTION AND RUNOFF DYNAMICS IN THE LANDSCAPE

Habilitation thesis

Praha 2022 **Ing. David Zumr, Ph.D.**

Title:

Impacts of soil properties on water retention and runoff dynamics in the landscape – collection of published scientific articles

Název:

Význam půdních vlastností pro dynamiku odtoku a retenci vody v krajině – soubor publikovaných odborných prací

Program:

Water management and water structures (Vodní hospodářství a vodní stavby)

Affiliation:

Department of Landscape Water Conservation, Faculty of Civil Engineering, Czech Technical University in Prague

Author:

Ing. David Zumr, Ph.D.

Autorské prohlášení a poděkování za finanční podporu

Prohlašuji, že jsem tuto práci napsal samostatně, s využitím řádně ocitovaných vlastních prací. Další publikace, zdroje informací a použité materiály jsou citovány a uvedeny v seznamu literatury. Práce odkazuje rovněž na řadu výstupů pořízených v rámci grantů a výzkumných projektů:

- Grantová agentura České republiky: Dynamika odtoku vody a eroze půdy na obdělávaném povodí v závislosti na časově proměnlivé struktuře a vlastnostech půdy, GP13-20388P
- Ministerstvo školství, mládeže a tělovýchovy : Fire effects on soils, LTC20001
- Evropská komise: Transforming Unsustainable management of soils in key agricultural systems in EU and China. Developing an integrated platform of alternatives to reverse soil degradation, 101000224
- Ministerstvo školství, mládeže a tělovýchovy : Výzkum a modelování přímých a nepřímých dopadů erozních a transportních procesů, 7AMB16AT002
- Ministerstvo školství, mládeže a tělovýchovy : Standardizace metod výzkumu a měření eroze půdy, 7AMB16AT002
- Ministerstvo školství, mládeže a tělovýchovy : Výzkum a modelování přímých a nepřímých dopadů erozních a transportních procesů, 7AMB 78p17
- Ministerstvo zemědělství: Stanovení aktuálních hodnot ochranného účinku vegetace za účelem kvantifikace a zefektivnění protierozní ochrany zemědělské půdy v České republice, QJ1530181
- Evropská komise: Macro and Microplastic in Agricultural Soil Systems, 955334 — SOPLAS
- Ministerstvo zemědělství: Ochrana vodních toků před vstupem erozních splavenin a vázaných chemických látek ze zemědělské půdy, QK1810311
- Ministerstvo vnitra: Erozní smyv - zvýšené riziko ohrožení obyvatel a jakosti vody v souvislosti s očekávanou změnou klimatu, VG20122015092
- Grantová agentura České republiky : Kinetic energy of rainfall as driving force of soil detachment and transport, GF17-33751L
- Evropská komise: Cooperating towards Advanced MAnagement ROutines for land use impacts on the water regime in the Danube river basin, CAMARO-D
- Ministerstvo školství, mládeže a tělovýchovy : Vliv změny využití území na erozní ohroženost, transport splavenin, kvalitu vody a odtokový režim, LTC18030
- Evropská komise: Soil Hydrology research platform underpinning innovation to manage water scarcity in European and Chinese cropping systems, 773903
- Ministerstvo školství, mládeže a tělovýchovy: Konektivita transportu sedimentu v povodích s intenzivním zemědělským využitím, LTAUSA19019

V Praze dne :

Acknowledgements

Many thanks to all of you! Obviously the fieldwork and the excessive data analyses cannot be done by one individual, the work presented here is a team effort and I am grateful for the great help of all my colleagues. I apologize for not mentioning you all by name. You are numerous, I thank you for your support and I am pleased to have been fortunate enough to work with you. I am especially grateful to Milena Císlerová, who has been a great teacher, mentor and friend to me.
Many thanks to Vanda, Ruda and Eda. Without you I would have handed in the thesis much earlier, but life would have been terribly boring.

Abstract

The habilitation thesis presents the results of research in the field of the water balance of intensively managed agricultural landscapes. The text analyses current approaches and methods for determining the water balance of the catchment, for monitoring the relationship between precipitation and runoff, for determining the runoff pathways and residence time of water in the soil and aquifers, for noninvasive monitoring of the stratification of a shallow soil profile using electrical resistivity tomography, to monitor the temporal and spatial variability of soil properties, to monitor soil moisture, to describe erosion processes and the transport of mobilised sediment in the landscape, and to numerically model the hydrological regime at the scale from soil profile to watershed. The thesis is divided into two blocks. The first part includes a review of the literature summarising the current status and causes of soil degradation in the Czech Republic, a theoretical introduction to the main processes affecting the retention and runoff characteristics of the landscape, and an introduction to modern tools for monitoring and modelling hydrological processes in the landscape. In the second part, nine previously published scientific articles are appended, in which specific problems and tasks are solved.

Keywords:

soil water regime, rainfall-runoff processes, soil moisture, cosmic rays neutron sensing, electrical resistivity tomography, stable isotopes

Abstrakt (česky)

V předkládané habilitační práci jsou prezentovány výsledky výzkumu v oblasti hydrologického režimu kulturní, zejména zemědělsky obdělávané, krajiny. V textu jsou analyzovány aktuální přístupy a metody pro stanovení vodní bilance povodí, sledování vztahu mezi příčinnou srážkou a odtokem vody z území, určení odtokových drah a doby zdržení vody v půdním prostředí, neinvazivní monitorování zvrstvení mělkého půdního profilu s využitím elektrické odporové tomografie, sledování časové a prostorové variability půdních charakteristik, monitorování vlhkosti půdy, popis erozních procesů a transportu mobilizovaného sedimentu v krajině, a numerické modelování hydrologického režimu v měřítkách půdního profilu až po povodí. Práce je strukturována do dvou bloků. První část zahrnuje literární rešerši shrnující stav a příčiny degadace půd v České republice, teoretický úvod do klíčových procesů, které ovlivňují retenci a odtokové charakteristiky krajiny, a představení moderních nástrojů pro sledování a modelování hydrologických procesů v krajině. V druhé části je přiloženo devět dříve publikovaných vědeckých článků, ve kterých jsou řešeny specifické problémy a úlohy.

Klíčová slova:

vodní režim půd, srážko-odtokové procesy, vlhkost půdy, CRNS, elektrická rezistivní tomografie, stabilní isotopy

CONTENTS

PART I

1. Introduction 9
2. State of the art 12
   2.1 Soils degradation in Czechia 12
      2.1.1 Soil erosion 13
      2.1.2 Soil compaction and soil structure changes 15
      2.1.3 Soils contamination 19
   2.2 Components driving the water runoff dynamics in the landscape 21
      2.2.1 Soil water 22
      2.2.2 Topsoil properties variability 23
      2.2.3 Soil surface changes due to soil erosion 25
      2.2.4 Vegetation and root zone patterns 26
3. Overview of the selected experimental methods 27
   3.1 Catchment scale monitoring of rainfall-runoff processes 27
   3.2 Spatially distributed topsoil moisture monitoring 29
   3.3 Geophysical surveying – electric resistivity tomography 31
   3.4 Water residence time and water mixing 32
4. Future prospects 33
5. References 35

PART II

1. Soil water dynamics, small scale experiments 47
2. Hydrological processes on a catchment scale 94
3. Interaction of water with earth structures 125

PART I

1. INTRODUCTION

Soils provide a variety of ecosystem services such as primary production (food, wood, etc.), nutrient cycling, climate regulation, or water purification. Together with the landscape, soils are a cultural heritage that reflects centuries of human activity. Soils form the basis of all terrestrial ecosystems and agricultural provisioning services and are the structural medium for the terrestrial biosphere and human infrastructure. Nevertheless, the importance of soils for sustainable living is currently not properly recognised by the public. Soils are exploited with the aim of maximising short-term profits (Nolan et al., 2021). It is very likely that degradation processes will accelerate in the near future due to climate change, changing landscape patterns and land use, groundwater depletion, intensive agriculture, and global uniformity of food production (Kraamwinkel et al., 2021). The main factors leading to soil degradation in the Czech cultural landscape are soil erosion, soil compaction, organic matter degradation, loss of soil structure, and soil contamination (Dostál et al., 2006).

Soil properties, soil quality, spatial and temporal heterogeneity and stratification of the soil profile are among the crucial parameters that determine rainfall-runoff processes and water retention in the landscape. Understanding the distribution of precipitation water, its pathways into rivers or groundwater and the residence time in the stratified soil profile are important prerequisites for water management, flood and nutrient control.

While research on arable soils often focuses on crop yields, overland runoff or soil degradation, spatially distributed monitoring and modelling of soil water content dynamics is usually limited to more permanent landscape types such as forests or pastures. Identifying the predominant runoff mechanisms and pathways is not straightforward, even in seemingly uniform agriculture fields, due to soil heterogeneity, the complexity of micro- and macromorphology and the intermittently variable hydrological connectivity of the landscape. Standard monitoring techniques based on soil and water sampling and point sensors do not provide sufficient data for a good understanding of the hydrological behaviour of the system. Parameterisation and calibration of physically based distributed numerical models is complicated due to high uncertainties in inputs and lack of relevant calibration and validation data. Process-based understanding of hydrological processes on arable lands represents a challenge. To make a progress in this direction is needed.

Intensive agriculture is a source of diffuse pollution of water bodies. This pollution is transported to water bodies not only by overland flow, but also via groundwater recharge or runoff through the tile

drainage systems. Information on the average residence time of soil water in agricultural fields is therefore essential. The residence time can be estimated with the help of stable isotope analyses. The residence time of soil water (the so-called age of the water) in the catchment's storage pools has been shown to directly influence the chemical composition of runoff (Rinaldo et al., 2015). A considerable part of the runoff may consist of water that has been stored in the catchment for a long period of time, and only a part of the runoff consists of rainwater (event water), which makes the hydrochemical regime very complex (McDonnell et al., 2010). Knowledge of residence time also helps to understand how and where a catchment stores and releases water, as it is related to the diversity of flow pathways in the catchment (Zhou et al., 2021). Spatio-temporal water distribution is also influenced by vegetation development. Tracking stable water isotopes in combination with detailed monitoring of the water balance in the soil profile are tools to study this not yet fully understood problem (Kleine et al., 2020).

The effects of soil properties and stratification on water and sediment transport are very complex and can be studied at different spatial and temporal scales with different methods and objectives. Among others, ponded and tension infiltration experiments are used to observe the spatial and temporal variability of topsoil hydraulic conductivity (Zumr et al., 2019), plot-scale rainfall experiments help to assess the large-scale soil infiltration capacity and surface runoff regime (Zumr et al., 2015, Jeřábek et al., 2020, 2022), geophysical surveys are applied to observe the heterogeneity of the deep and shallow subsurface (Zumr et al., 2012, Jeřábek et al., 2017, 2021), monitoring of runoff processes at the catchment scale provides information on the overall hydrological dynamics of the landscape (Zumr et al., 2015, Li et al., 2021), numerical modelling helps to understand the main morphological, soil and climatic variables and their sensitivities that influence the hydrological regime (Zumr et al., 2015, Noreika et al., 2021).

There are a variety of small and specific research problems, such as preferential flow, the effects of temporal instability of hydraulic properties related to soil structure and soil compaction, or splash erosion leading to changes in surface microtopography. It is one of the tasks of modern hydrology to deal with these processes and to clarify how water behaves in the soil under different conditions. How long does water remain in the soil profile and in the groundwater? Which part of water (precipitation water, soil water, groundwater) is in the streams during floods? In what pathways does the water flow through the soil? Does the precipitation water displace older water from the soil, or does it flow directly into the recipient? Similar questions can be addressed also to the mobilised eroded sediments, fertilisers or pesticides. Traditionally, empirical black-box models have often been

used to describe runoff and soil erosion processes in agricultural catchments. However, it has been found that the oversimplified models do not adequately predict water and sediment fluxes. Therefore, they can hardly be used to simulate, for example, the spread of pollution in a catchment or to model extreme events for which the models have often not been empirically parameterised.

Meanwhile, the understanding of hydrological processes has made considerable progress. Modern tools such as spatially distributed soil sensor networks (soil moisture, matric potential or temperature sensors, electrical conductivity and permittivity probes), shallow subsurface runoff monitoring, advanced numerical models, remote sensing (leaf area index mapping, vegetation indicies imagery or surface temperature mapping), geophysical surveys, isotope hydrology and many others help to increase knowledge.

This thesis summarises the main research activities and results on water balance in the landscape carried out or supervised by the author[1]. The thesis is conceived as a collection of published manuscripts. The collection is introduced by a presentation of the state of the art and selected methods that have been used to study the processes under investigation (PART I). This is followed by the manuscripts, which are divided thematically into three sections (PART II). Each section is introduced with a brief summary of the articles listed and is supplemented by additional references to the work in which the author has been involved.

[1] It needs to be noted that all activities and results were achieved within the framework of the work of an entire research team. In the field of hydrology, especially experimental hydrology, collaboration is essential. I am therefore grateful to all my colleagues and students for their important contribution.

2. STATE OF THE ART

2.1 SOILS DEGRADATION IN CZECHIA

In general, soil degradation is usually the result of more than one degradation process. Currently, the most prominent problem with agricultural soils in the Czech Republic is irreversible soil sealing, associated with uncontrolled expansion of settlements and related infrastructure. Soil loss, mostly on high-quality lands, has accelerated significantly in the last 25 years. Other serious degradation processes are water and wind erosion, soil compaction and soil organic matter depletion (Janků et al., 2016; Kozák et al., 2010). It is often not possible to assess what degradation factor is the primary cause and what is the consequence, e.g., in the case of soil erosion and low organic matter content. The impacts of unhealthy soils are vast, ranging from biodiversity problems to the quantity and quality of groundwater.

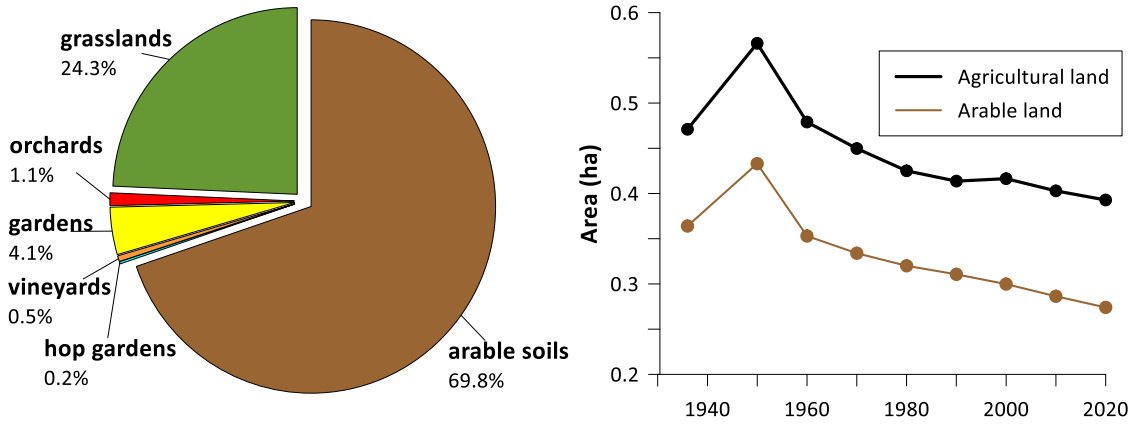

Figure 1: Ratios of Agricultural land use (left), and the temporal evolution of the Arable area per capita (right) (based on data from Czech Statistical Office).

The Czech agricultural landscape is characterized by large fields, which are a heritage of land collectivization in the 20th century. Intensive industrial farming speeds up the soil degradation processes. On top of that the area of arable land keeps decreasing (Figure 1). More than 55 % of the agricultural land in the Czech Republic is potentially threatened by surface runoff and subsequent soil erosion, and about 10 % is threatened by wind erosion (Dostál et al., 2006) . Transported soil

particles and substances bound to them pollute water sources, clog reservoir storage areas, reduce the flow capacity of streams, and cause turbidity and eutrophication of surface waters. Over 45% of arable soils are threatened by soil compaction (Lhotský, 2000). As a consequence, infiltration of rainwater into the soil is reduced, resulting in increased runoff during rainfall events, and increasing again the risk of soil erosion and soil structure degradation.

2.1.1 Soil erosion

In comparison with the rest of the world, the Czech Republic has relatively low soil erosion potential, as it lacks high mountains and heavy convective rainstorms, and a considerable part of the area is covered by forests (Kozák et al., 2010). Nevertheless, soil erosion (especially water erosion) is the most frequently highlighted soil degradation process. A total of 43% of the arable land is on slopes ranging from 3° to 7°, and 10 % of the land is on slopes exceeding 7°. Wind erosion occurs mainly, but not exclusively, in the south-eastern part of the Czech Republic, where the climate is warmer and the soils are lighter. The estimated annual soil loss from agricultural land for the whole country is estimated to be 21 million tons, which represents an economic loss of up to CZK 4.3 billion (Podhrázská et al., 2016). Soil translocation due to tillage operations has also been studied (Hrabalíková et al., 2018; Novák et al., 2006). Up to 16% of arable land is negatively affected by the tillage operations, especially in the most fertile regions of south and northeast Moravia (Žížala et al., 2021).

The Czech Republic contains densely populated areas where soil erosion is usually accompanied by the off-site negative impacts of considerable economic damage to water structures (e.g., ditches, rivers and reservoirs affected by siltation and consequently by eutrophication) or to the civil infrastructure (local flash floods, mud flows into villages and gardens) (Bauer et al., 2019; Jáchymová et al., 2020; Krása et al., 2019). Over 40 % of reported erosion cases end up with damage to roads, over 30% with damage to the civil infrastructure, and more than 17 % with damage to water bodies (Kapička et al., 2020). Eroded soils in the Czech Republic produce lower crop yields per hectare. The reported yields are lower by 15 – 20 % on moderately eroded soils and by as much as 75 % on heavily eroded soils (Kapička et al., 2020).

Agriculture is the main non-point pollution source of surface waters and groundwater. Surface runoff containing detached soil particles introduces considerable loads of adsorbed pollutants, mainly

phosphorus (Krása et al., 2019) and nitrogen (Rosendorf et al., 2016). The unsatisfactory present-day situation is connected with mass production in agriculture and with extreme changes in land use (the so-called collectivization process in the 1950s), when large units of arable land were consolidated and the soil degradation process accelerated dramatically in some areas (Figure 2) (Devátý et al., 2019). Dostál et al. (2006) identified the following dominant factors which have contributed to a dramatic increase in soil erosion:

- Establishment of very large fields (on an average 20 ha, but there are even parcels of 200 ha (Podhrázská & Karásek, 2014)
- Removal of the dense network of linear and spot elements in the landscape (such as dirt roads, paths, ridges, grass belts, groves, etc.) which could potentially prevent or terminate surface runoff
- Extensive soil amelioration with introduction of dense networks of tile drains, straightening and deepening of streams
- Transformation of grasslands and pastures into arable areas in morphologically unfavorable landscape areas (foothills, slope areas).
- Drainage of inundation areas, leading to more arable land but to lower water retention capacity of the landscape.
- Utilization of heavy machinery, which has resulted in soil compaction and reduced soil infiltration capacity
- Planting of wide row crops (e.g., corn, potatoes)
- A drastic reduction in organic matter inputs, due to reduced livestock production since the 1990s.
- Increased application of mineral fertilizers since the 1970s
- Insufficient use of modern technologies, lack of knowhow, and a lack of political support for soil protective cultivation of the land

Effective measures against soil erosion have been historically known, but for decades ignored. They should be increasingly applied on fields in the Czech countryside. So far, effective measures have usually been implemented at the local level, either on fields that have already been repeatedly affected by erosion or by a limited number of progressive farmers and landowners. Nevertheless, the ongoing process of land consolidation (aimed at reducing the high ownership fragmentation caused by the restitution of confiscated land in the 1990s) provides a great opportunity to reshape the rural landscape matrix, to introduce stabilizing elements e.g., pathways, grass strips, alleys, ditches, green

vegetation, among others (Jakšík et al., 2015), and to improve the resistance of the soil to degradation (Homoláč & Tomsik, 2016; Moravcová et al., 2017).

Figure 2: An example of the change in the landscape pattern between 1954 (left) and 2020 (right) due to the collectivization of agriculture (vicinity of the Nučice experimental catchment, (Li et al., 2021)). (Source of the historical orthophotograph CENIA 2010, current situation ČÚZK, available from: http://geoportal.gov.cz).

2.1.2 Soil compaction and soil structure changes

Soils on farmlands are losing their structure, mostly due to intensive tillage and soil compaction. Soil compaction, caused by overuse of heavy machinery, intensive cropping and inappropriate soil management, has been recognized as one of the major problems of modern agriculture (Hamza & Anderson, 2005). Compaction results not only in soil deformation, but also in changes in the conductivity and connectivity of the pores. One can commonly observe the formation of dense soil layers with very low macroporosity and hydraulic conductivity in the shallow soil profile (Jeřábek et al., 2017). Consequently, water infiltration is reduced, and in addition this situation causes reduced gas and heat fluxes within the soil profile. In a global perspective, this can influence the global carbon and nitrogen cycles (Beare et al., 2009; Novara et al., 2012).

Soil structure

The soil structure of arable land has a significant impact on water and soil air availability, nutrient uptake and leaching (Sněhota et al., 2008). Thereby, the soil structure indirectly affects the ground and surface water supply and water quality. The aggregation of soil particles and interconnected large pores increase the bypass flow in the soil. Healthy structured soils exhibit increased infiltration rates,

reduced surface runoff, water percolating deeper into the soil profile, and usually, but not necessarily, also higher yields.

Agricultural management practices (the tillage system, crop rotation, fertilizers, etc.) can significantly impact the stability of the topsoil aggregates and soil hydraulic properties (Kodešová et al., 2011). Growing crops, tillage and subsequent reconsolidation due to natural wetting and drying cycles causes changes in the soil bulk density and porosity, the ratio of macropores, the soil hydraulic properties, the surface roughness or the depression storage of rainwater. The stability of soil aggregates is maintained mainly by the organic matter content, the clay content, iron oxides and biological activity (Kodešová et al., 2009).

A decline in the soil organic matter (SOM) and the microbial biomass in the topsoil has been considered a major agronomic and environmental problem, mainly due to its negative impact on soil properties (Hofman et al., 2004; Kozák et al., 2010, Or et al., 2021). Several studies based on long-term monitoring of SOM on various soil types in the Czech Republic indicate a lower current SOM content with worse qualitative parameters than decades ago (Horáček et al., 2008; Menšík et al., 2019; Usowicz & Lipiec, 2020). The SOM decline is attributed mainly to tillage, to the intensification of farming and to reduced application of manure due to the reduced numbers of livestock. Bednář & Šarapatka (2018) showed high SOM losses on drained fields and on parcels affected by water erosion. Soil type and the farmer's attitude are also significant factors for loss of SOM, as shown by Walmsley et al. (2020). Farmers often do not treat soil in a sustainable manner, because they usually do not own the parcels nor have a long tenure contract. As was noted earlier, farming of leased farmland is widespread in the Czech Republic, and a lack of a sense of responsibility for the soil is therefore often a problem.

There have been several research activities related to the soil physical properties of farmed soils in the Czech Republic. The effects of different soil and agricultural management on soil structure and soil hydraulic properties were analyzed by means of long-term monitoring and numerical modelling on Luvisol at the Hněvčeves experimental station (maintained by the Crop Research Institute in Prague) (e.g. Kočárek et al., 2016; Kodešová et al., 2009; Kodesova et al., 2011). These studies showed that land use significantly influences the soil hydraulic properties in the upper part of the soil profile (A and Bt1 horizons, down to a depth of approximately 60 cm). Soil water retention and near-saturation hydraulic conductivity were higher in a soil profile with grassland compared to a soil with periodic tillage. Seasonal variability of soil bulk density, saturated water content and unsaturated hydraulic conductivity were analyzed by Zumr et al. (2019) on the Nučice experimental site (Li et al.,

2021). The soil water holding capacity generally decreased during the vegetation season as a result of the rainfall kinetic energy, poor soil structure stability and a compacted shallow plough pan which caused frequent topsoil saturation.

A poor soil structure accelerates other soil degradation processes. Agricultural uplands are very susceptible to soil water erosion when they are tilled repeatedly and are left without a protective cover. Erosion tends to preferentially remove low density or light particles, including both clay and soil organic carbon, which are two of the primary bonding agents in the aggregation process (Weissmannová et al., 2019).

Soil compaction

Approximately 38% - 45% of the Czech farmlands are negatively affected by topsoil and subsoil compaction (Lhotský, 2000). This makes the soil compaction, together with soil erosion, loss of organic matter and soil sealing, one of the most prominent soil degradation processes. The consequences of excessive soil compaction are very serious, as the most-affected soils are very fertile (Javůrek & Vach, 2008).

Less than 30% of the threatened soils are vulnerable to so-called pedogenetic compaction, and more than 70% are vulnerable to the so-called technogenic compaction (VÚMOP, 2021). Pedogenetic compaction arises during the formation of whitish illuvial or gley layers, and is therefore typical for soil profiles with a comparatively high clay content. Technogenic soil compaction, resulting from mechanical pressure caused by field trafficking by agricultural machines, is dangerous mainly due to the possibility that it can occur in soils of any textural composition (Pražan et al., 2014). Current overcompaction has been caused mainly by excessively intensive farming in recent decades, mainly disproportionate doses and an incorrect assortment of mineral fertilizers, an insufficient supply of organic matter, and the use of heavy machinery. Conservation and minimum tillage technologies are the main practices in the Czech Republic, while direct seeding is marginal. Livestock trampling causes problems only locally on pastures. Kroulík et al. (2009) showed that the ground area percentage that is trafficked at least once in a year is almost 90% for conventional tillage and 72% for conservation tillage. Direct seeding technology requires approximately one half of the trafficked area. Controlled traffic farming with a fixed track system, which has been introduced on many farms, reduces the trafficked area to nearly 30% (Kroulík et al., 2011).

In general, soil compaction tends to be a more serious problem for soils with a high clay content (Bednář & Šarapatka, 2018). At present, the situation is more complicated, as the long-term

degradation has resulted in compaction in subsoil horizons which is very persistent and cannot be removed easily. So far, only minimal attention has been paid to finding an effective solution to this serious issue in agricultural enterprises. Compacted soils exhibit low infiltration capacity and water retention, reduced biological activity due to worse aeration and thermal regimes, higher bulk density, limited effective depth of the soil profile, fast soil drying, fast runoff, and often waterlogging. The direct consequences are increased power consumption during tillage, impaired nutrient utilization by plants, lower quality and a lower amount of yields (Javůrek & Vach, 2008).

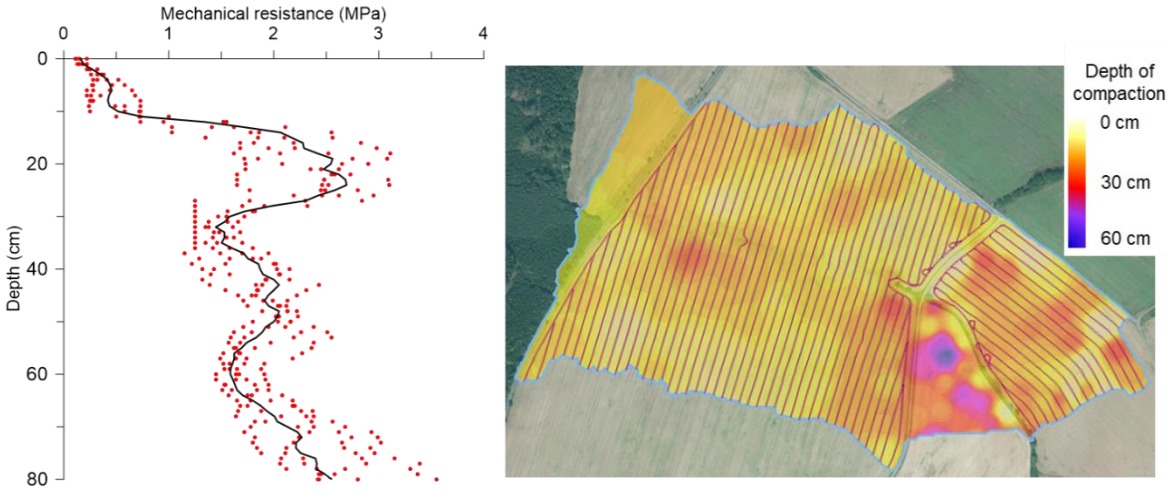

Figure 3 Mechanical resistance against penetration at one of the observation points in the Nučice catchment. The red dots represent single measured values, and the black line shows the average resistance depth profile (left). The map of the plough pan position was reconstructed on the basis of over 100 measured soil profiles. The lines represent the wheel tracks which are mostly followed during trafficking (right), based on (Jeřábek et al. 2017).

A comprehensive study of the compacted subsoil layer and its spatial homogeneity was carried out by (Jeřábek et al., 2017) at the Nučice experimental catchment. The research was based on a combination of direct soil sampling, mechanical penetration resistance monitoring, geophysical methods (shallow electrical resistivity tomography) and remote sensing (delineation of wheel tracks). The measurements showed that the plough pan was homogeneous in a large part of the catchment, and its mean depth was between 11 and 14 cm (Figure 3). Zumr et al. (2015) showed by means of rainfall runoff monitoring and numerical modelling that the shallow plough pan can explain immediate response to intense rainfall and the low soil water retention capacity of the Nučice catchment (Noreika et al., 2020).

2.1.3 Soils contamination

Pollution by various contaminants may cause disturbances in the functioning of the soil ecosystem and presents a risk to humans and to the environment. The main contaminants in the Czech soils are Potentially Toxic Elements (PTASs) and man-made organic chemicals (xenobiotics), such as synthetic pesticides, dissolving agents, hydrocarbons and drugs. The chemical elements of greatest concern are arsenic, cadmium, nickel, lead and chromium. In most cases, soil contamination does not cause diffuse pollution, and the contaminated sites are usually small and disconnected. The most affected areas are those with heavy industry and mining activities (West Bohemia, North Moravia) (Kozák et al., 2010), and areas with high transportation (Prague and its surroundings) (Skála et al., 2017; Vácha et al., 2016). Soils are locally also contaminated in the alluvial plains, due to occasional inundations containing wastewater (Vaverková et al., 2017). Sewage sludge has only rarely been deposited or added to arable soils, as there are strict limits on its chemical composition. Contamination of the surrounding soils from modern landfills has also not been a serious problem (Ministry of the Environment of the Czech Republic, 2019).

The maximum tolerable values of risk elements and persistent organic pollutants are set in the Czech legislation (Kozák et al., 2010; Poláková et al., 2010). Since 1992, arable soils have been regularly tested for agrochemicals and hazardous substances within the Basal Soil Monitoring System organized by the Central Institute for Supervising and Testing in Agriculture (UKZUZ). The results of the monitoring, which has taken place within the area of the whole Czech Republic, show that the limiting values are only rarely (in approximately 1% of the samples) exceeded for cadmium and for arsenic (Dušek et al., 2006), while the remaining tested elements exceed the limits even less often. The limits for the tested organic pollutants (mono and polyaromatic hydrocarbons, PCB, HCB, DDT, styrene, PCDD and PCDF) were also exceeded only in exceptional cases (Podlešáková & Nemecek, 2000; Poláková et al., 2010). Long-term monitoring has not proven any significant temporal trends in soil contamination (Holubová et al., 2011; Kozák et al., 1995; Weissmannová et al., 2019). Nevertheless, a small number of hotspots remain where soils are strongly contaminated, mainly due to mining activities, industry or historical landfills (Sáňka, 2018).

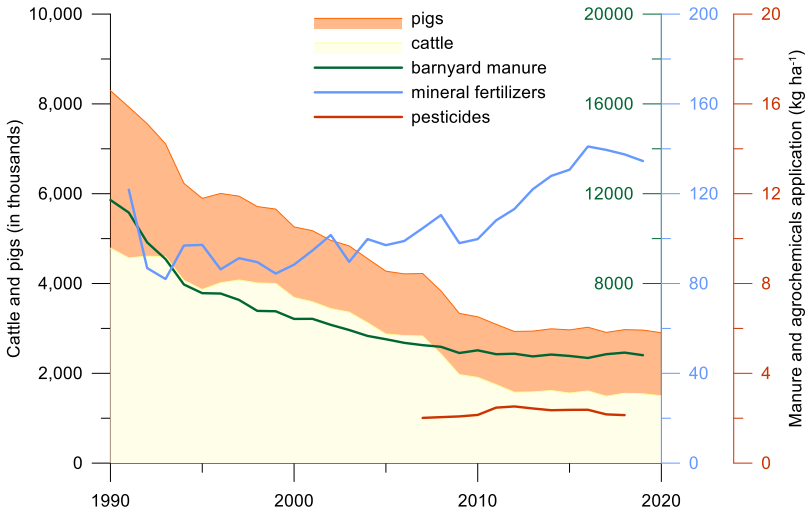

Figure 4: A decline in numbers of livestock and available barnyard manure has resulted in increased application rates of mineral fertilizers (mainly N, P, K). Data for pesticides is not available for the period before 2006. The consumption of pesticides has decreased slightly in recent years. (source of data, Czech Statistical Office, UKZUZ).

A present-day problem of Czech arable soils is insufficient manuring and unsustainable overdosing of agrochemicals, namely pesticides, herbicides and mineral fertilizers. The main reason of the manure deficit is a dramatic decrease in livestock production, especially of cattle (Figure 4). UKZUZ (2020) estimates that due to the lack of organic matter in arable soils, which is being recompensed with fertilizers, the soils will require at least 30 years to recover their function in the ecosystem. In recent years, the average annual fertilizers consumption has been around 130 – 140 kg ha^{-1} of mineral fertilizers (approximately 75% of which is nitrogen, 15% is phosphorus, and 10% is potassium) and 2 kg ha^{-1} of pesticides (Czech Statistical Office). The statistical data show that the consumption of plant protection products has been declining in recent years, mainly due to lower application of glyphosates (Vašíčková et al., 2019). Nevertheless, pesticide residues in arable soils continue to pose an environmental threat, especially in the case of triazine and conazole fungicides (Shegunova et al., 2007). In addition, residues of organochlorinated pesticides, which have not been applied since the 1990s, still persisted in the topsoil layers (Kodešová et al., 2008). Pesticides can be transported by infiltrating water into deeper horizons, especially in soils with a heterogeneous structure with the presence of preferential flow (Kosubová et al., 2020).

A comprehensive analysis of the current situation and spatial and temporal trends of pesticides in the topsoil has been presented by (Kodeš, 2020). The study is based on the monitoring period of 2014 – 2017. Samples from 34 different localities with various soil types were analyzed for 64 currently-used

fungicides and insecticides, including conazole and triazines, and recently banned pesticides (e.g. atrazine, acetochlor, and linuron). The intensive use of protecting agents has resulted in their frequent and widespread occurrence in soils, both for currently-used products and for recently-banned products (and their transformation products). The highest numbers of pesticides have been observed on fields where rapeseed and wheat were cultivated (these are the most widely-grown crops in the Czech Republic). Kodeš (2020) point out that glyphosate, which is of environmental concern and is applied in large doses, has not been not evaluated within this study. In 2014-2019, monitoring performed by the Czech Hydrometeorological Institute detected above-limit concentrations, mostly of metabolites of herbicides, in approximately 30% of groundwater samples. Most of the affected samples were collected in the vicinity of fields with rapeseed planted for biofuels (Fer et al., 2018; Hiller & Šebesta, 2017; Klement et al., 2018; Kočárek et al., 2016; Kodešová et al., 2015, 2016, 2019).

2.2 Components driving the water runoff dynamics in the landscape

The runoff response of a catchment is determined by climate, size, topography, land use, and soil parameters. Infiltration regime and runoff routing depend on many factors at various spatial and temporal scales. Runoff can make its way to watercourses via several pathways including overland flow, subsurface stormflow, pipeflow or groundwater flow (Saffarpour et al., 2016).

The small water cycle is a complex process of water movement within a landscape that consists of several water flow components ranging from evapotranspiration to rainfall, water infiltration, percolation, and runoff. The general theory is well known and described elsewhere, incl. textbooks. In this chapter, only selected components of the water cycle are summarized which are relevant for the research topics covered in the attached collection of the published manuscripts (later in PART II).

2.2.1 Soil water

Water flows in the soil through an intricate network of pores and fissures. In principle, the movement of water within the porous domain can be viewed at the microscopic level of individual pores, where one observes what is happening at each point in space. For saturated flow, the Navier-Stokes equations can be theoretically utilized and solved with knowledge of the boundary conditions at the fluid-solid interface. However, this approach is impractical as it is impossible to determine the complex geometry of the soil medium in detail. Even if it were possible, we cannot monitor state variables such as pressure at a given scale, and thus cannot verify our models.

In general, the flow of water through heterogeneous soil environments is very complex. Water flows mostly continuously, the dynamics of the water regime is influenced by processes such as time-varying infiltration, evaporation from the surface, transpiration, drainage to the water table. In the actual environment, it is not pure water that flows, but a soil solution with often complicated chemical properties. The soil temperature changes in time and space, changes in connectivity, and pore distribution occur due to physical processes (soil compaction, freezing cycles, swelling or shrinking of clays, agrotechnical operations, transport of small particles, etc.) and biological processes bring another complication (due to e.g. growth of roots, moulds and fungi, movement of soil edaphon). Therefore, we utilize the so-called macroscopic approach, where the physical variables of the porous medium are defined on a larger, representative, volume (described e.g. by Hillel, 2003). In large-scale studies, where the key objectives focus, e.g., on an annual water balance or sediment fluxes from the landscape, most of the unstable soil characteristics can be neglected. But in many situations, such as infiltration during heavy rainstorms, splash erosion, surface runoff, or evapotranspiration of rapidly growing crops, one needs to be cautious not to oversimplify the conceptual model which is supposed to describe the real processes in the environment.

The rainfall-runoff processes taking place on intensively cultivated fields and catchments have certain specifics. On one hand the land use and cover crops are spatially rather homogeneous, but the hydraulic conditions differ considerably in time due to periodical cultivation of the soils (Zumr et al., 2019). The topsoil conditions and its physical parameters are temporarily very unstable also due to agrotechnical operations (ploughing, tillage, seeding, harvesting), fast crop growth and natural climatic conditions (such as freezing, thawing, raindrops impact) (Jabro et al., 2010). On arable lands the soil is exposed to rapid structural changes within each growing season resulting in changes in

shape, size and spatial distribution of the soil aggregates, changes in surface microtopography and mechanical resistance towards soil erosion. Soil compaction affect the pores arrangement and thus govern the water infiltration and soil moisture regime (Hamza & Anderson, 2005).

Each change in pore network structure or soil surface conditions govern the hydraulic and sediment connectivity (or disconnectivity) (Jeřábek et al., 2022). The gradual deformation of the soil structure within a growing season causes a reduction in the volume and in the connectivity of inter-aggregate voids. Eroded fine particles clog the macropores and preferential pathways, and infiltration capacity and soil water storage decrease. Originally, connected large pores normally serve as a quick bypass for infiltrating water. Therefore, based on the state of the topsoil structure and subsoil permeability, one can expect different water runoff mechanisms; ranging from deep percolation and shallow subsurface lateral flow to surface runoff to play a greater or lesser role in runoff generation (Zumr et al., 2015).

Theory related to soil hydraulic characteristics, soil physical properties, soil water potential, or governing equation describing water and solutes flow through porous media will not be described in this thesis, as the general theory can be easily found in the textbooks. The relationships such as Darcy's law, Richards equation, advection dispersion equation, kinematic and diffusive waves to simulate free water runoff, or Penman-Monteith equation for evapotranspiration estimation, which are based on the macroscopic description of water and solute fluxes, were utilized in the presented studies.

2.2.2 Topsoil properties variability

As already mentioned, the physical properties of the soil in arable fields change in time and space for several reasons. The presence of a shallow compacted layer (Jeřábek et al., 2017) affects the subsoil structure and thus influences soil water regime and accelerates shallow subsurface runoff (Figure 5). The subsequent irregular transpiration of the crop influences the soil water regime and soil moisture distribution. Temporary bare soil surface is exposed to the rainfall, which causes topsoil compaction, crusting and dramatic decrease of near-saturated hydraulic conductivity (Zumr et al., 2019). Rapidly growing crops and agricultural operations alter soil macroporosity (Hudek et al., 2022). Once surface runoff begins after a heavy rainfall event, flowing water changes the surface microtopography and

usually increases the surface and connectivity (Jeřábek et al., 2022; Schönenberger & Stamm, 2021; Tenreiro et al., 2022).

The soil structure of arable land has a significant impact on water availability, nutrient uptake, and leaching. Agricultural management practices can significantly influence soil hydraulic properties and processes in space and time (Schwen et al., 2011). Tillage and subsequent reconsolidation due to wetting and drying can change the bulk density and porosity of the soil, the hydraulic properties of the soil, the surface roughness, and the storage of surface depressions. Aggregation and interconnected pores increase bypass flow in soil (Ohrstrom et al., 2002). This can result in increased infiltration, reduced runoff, and the movement of water deeper into the soil profile.

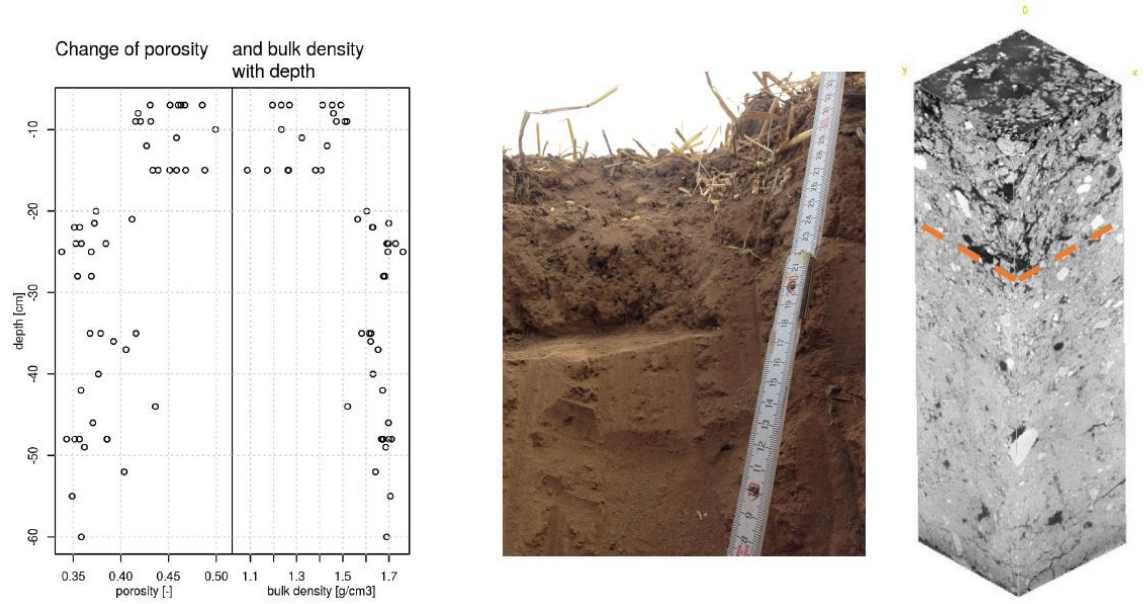

Figure 5: Sharp divide between a topsoil and subsoil on an intensively cultivated agricultural field (Jerabek et al, 2017)

Soils on farmlands are losing its structure mostly due to tillage and soil compaction (Green,et al., 2003). Soil compaction, caused by overuse of machinery, intensive cropping and inappropriate soil management, is one of the major problems of modern agriculture (Hamza and Anderson 2005). The compaction results not only in soil deformation, but also in changes of the pores conductivity and connectivity. Consequently, not only water infiltration is reduced, but it also causes reduced gas and heat fluxes within the soil profile (Lipiec et al., 2009), which in global perspective can influence global nitrogen cycle (Perera & Maharjan, 2021). Shallow lateral subsurface runoff, which often forms on

the low permeable plough pan, may be a dominant component of the overall runoff into the streams (Tenreiro et al., 2022).

Precision agriculture usually implements GPS-navigated trafficking within the same pathways during the vegetation season. Compacted wheel tracks, which are typically submerged below the surrounding surface, serve as a preferential pathway for surface runoff when oriented down the slope. Jerabek et al. (2022) showed that wheel tracks drain also surrounding topsoil and significantly increase the connectivity of the catchment.

Figure 6: Concentrated surface runoff accelerated due to the high catchment connectivity (photographs by D. Zumr)

2.2.3 Soil surface changes due to soil erosion

Agricultural uplands are very susceptible to soil water erosion when repeatedly tilled and left without a protective cover. Erosion tends to preferentially remove low-density or light particles, including both clay and soil organic carbon, which are two of the primary bonding agents in aggregation.

The surface of the soil is constantly exposed to variable weather conditions that affect the properties of the topsoil. Intensive rainfall over a bare soil causes soil aggregates destruction, particles detachment and translocation (Zambon et al., 2020, 2021). Slacking during fast infiltration into dry soil also leads to the breakdown of aggregates. The kinetic energy of the raindrops and drying can result in soil compaction, and if clays are present, swelling can occur. All these processes result in changes in soil volumetric changes and soil surface microtopography.

Comparably high inter-aggregate porosity, which is formed after a tillage, is being during the vegetation season gradually decreased (Zumr et al., 2019). Therefore, the pore size distribution

changes with time. Consequently, associated soil hydraulic and transport properties also vary with time . Several authors (Alvaro-Fuentes et al. 2008, Daraghmeh,et al., 2009) reported temporal changes in aggregate stability and hydraulic conductivity during the growing season as a result of the interacting processes of rain drop impact, microclimatic, plant growth, and soil microorganisms activity. As a consequence, both vertical and horizontal runoff connectivity vary in space and time, which makes the interpretation of the driving runoff processes extremely complicated.

2.2.4 Vegetation and root zone patterns

In addition to crop yield, agricultural land provides other ecosystem services, such as protection against soil erosion and an increase in water infiltration. These functions are mainly influenced by the root system. The root systems of many plants and crops support the formation of large noncapillary pores and, once the roots decay, promotes the infiltration of rainfall due to preferential flow (Figure 7). The root system also generally develops in a horizontal direction, which has a positive effect on the stability of the soil structure.

Figure 7. Dyed preferential pathways as a result of decayed crop's roots, textural heterogeneities and clay cracks (photograph by M.. Císlerová)

Some crops have very dense roots, which are concentrated mainly in the topsoil. Such crops are beneficial for the soils as the roots, once fully developed, prevent excessive water erosion. On top of the crops, the weed and vegetation along the fields and riparian vegetation partly govern the connectivity of different landscape units (Young et al., 2021), stabilize the banks and hedges and

provide other important ecosystem services (Kiffney & Richardson, 2010; Sabater et al., 2015). Spatial composition of vegetation species, plants density or their health status (i.e. expressed by NDVI) help to identify the surface and subsurface flow pathways both within the fields and in the boundaries (Mayor et al., 2008; Wang et al., 2021).

3. OVERVIEW OF THE SELECTED EXPERIMENTAL METHODS

3.1 CATCHMENT SCALE MONITORING OF RAINFALL-RUNOFF PROCESSES: NUČICE EXPERIMENTAL CATCHMENT

A catchment, as a hydrologically quasi-closed system, is a commonly used spatial unit for observations of water fluxes in the landscape. With the objectives of studying the long-term water balance of the agricultural landscape, dynamic behavior during rainfall runoff events, and soil erosion processes, the Nučice experimental catchment was established in 2011 (Zumr et al., 2015, 2017). Since then the monitoring and sampling network has been upgraded and has been involved in several research projects. Published results include research on temporal variability of topsoil hydraulic conductivity (Zumr et al., 2019), crop adoption scenarios (Noreika et al., 2020), or shallow soil electrical properties (Jeřábek et al., 2017; Jeřábek & Zumr, 2021). Recently, the Nučice dataset (WALNUD) was made publicly available (Li et al.,2021). The catchment is one of the pilot sites in three EU HORIZON 2020 projects related to sustainable crop yields (SHui), soil health (Tudi) (Gómez et al., 2019), advanced soil moisture monitoring (SoMMet) and the SOPLAS ITN project of the EU on the transport of microplastics in agriculture systems.

The catchment is located approximately 30 km eastwards from Prague, its area is 0.5 km^2. 96.4 % of the area is arable land. The catchment is drained with a central tile drain and an ephemeral stream. The average altitude of the catchment is 401 m a.s.l. and the slopes range from 1 to 12 %. The climate at the catchment is humid continental with average annual precipitation of 630 mm and average annual evapotranspiration between 500 – 550 mm. The soil is classified as Haplic Luvisols and Cambisols with sandy loam soil texture (9 % clay, 58 % silt, and 33 % sand). The catchment is divided

into three fields, the two largest fields have developed a homogeneous compacted layer in the depth of ca 12 – 15 cm due to the agricultural operations (Figure 8) (Jeřábek et al., 2017; Jerabek & Zumr, 2021; Li et al., 2020, 2021; Noreika et al., 2020; Zumr et al., 2015, 2019).

The catchment is instrumented with two meteorological stations, two additional ET towers, and four rain gauges. The stream discharge and basic water quality indicators (turbidity, EC, pH, T, dissolved oxygen) are monitored at four profiles along the stream (complete water quality only at the catchment outlet). Groundwater level is monitored in several piezometers. Soil water regime (soil water content, matric potential, temperature) is monitored at 19 locations, typically at the edges of the fields (SWC nests consist of nine SMT100 SWC probes – Truebner GmbH – and a logger with IoT data transmission). Two permanent CRNS systems (StyX Neutronica) monitor topsoil water content over an area of approximately 5 ha.

Regular sampling on soil cores to study the temporal and spatial variability of the soil properties has been done. Water samples from different water pools (rain, stream water, drainage, groundwater) are collected for stable isotopes analysis. The facility was used for several experiments to study e.g. shallow subsurface lateral runoff, splash erosion or sediment resuspention in headwater streams during flood events (Zumr et al., 2017).

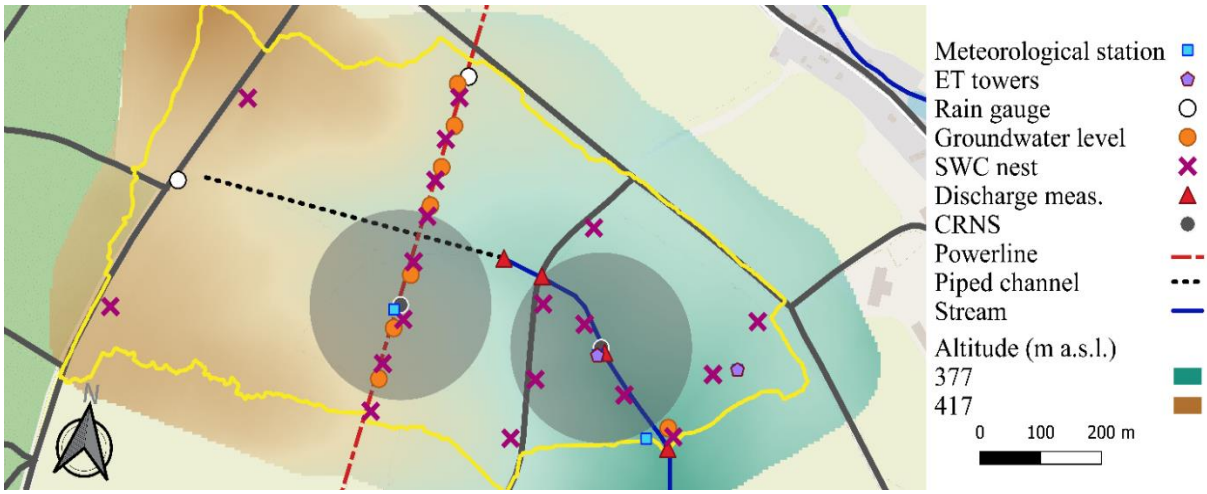

Figure 8. Experimental catchment Nučice

3.2 Spatially distributed topsoil moisture monitoring

The soil water content is one of the key drivers of runoff generation. Antecedent catchment saturation decides which pathways will the rainfall water follow when routing towards a stream, which water will be displaced into the stream, what runoff mechanism will take place, and last but not least how much water will be released into the stream. Although cultivated fields appear to be homogeneous, in reality, the soil moisture distribution is spatially variable. The actual soil saturation pattern of the catchment influences the hydrological connectivity of the landscape.

Point sensors

At Nučice catchment several methods are implemented to monitor the topsoil moisture and estimate its effect on the water runoff dynamics, as briefly described in previous section. On top of the permanent sensors also recurrent monitoring with handheld TDR probes (Hydrosense II, Campbell Sci., UK) are done. The measurements are done in a dense grid during a single day to obtain the topsoil moisture snapshots. An example of the soil moisture map is shown on figure 9.

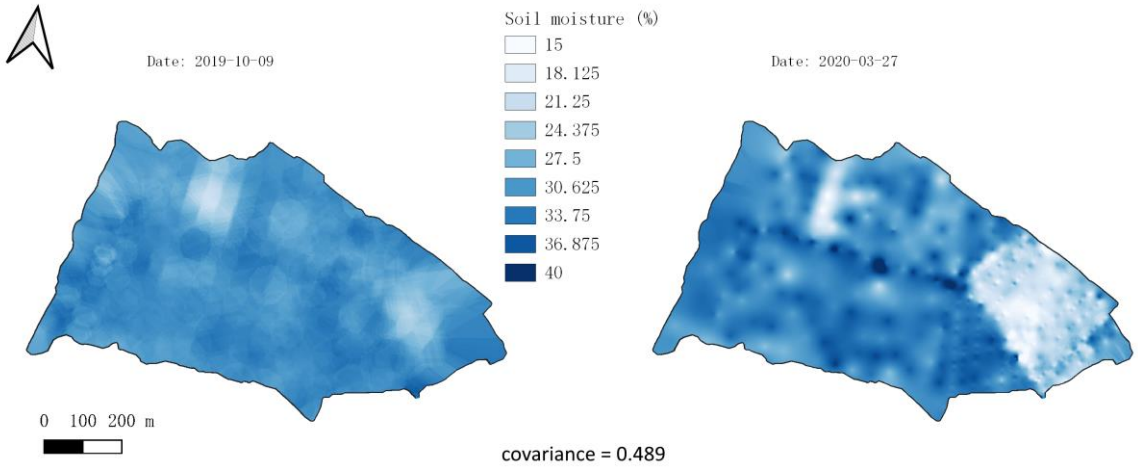

Figure 9. Two snapshots of the soil moisture distribution on the Nučice catchment. Event though taken during different times of the vegetation season. The drier and wetter areas remain the same. (Li et al., 2021b)

Nowadays, the soil water content (SWC) nest networks are used to analyse the spatio-temporal variability of SWC. For instance, a wireless soil moisture monitoring sensor network was used to capture the soil moisture dynamics with a high temporal resolution in a forested catchment in

Germany (Bogena et al., 2010). Similar system is installed in the Nučice catchment. Traditional SWC probes however only provide information from a single location, even if used in a dense network. Moreover, permanent sensors are difficult to be installed in arable fields. The approaching techniques which partially overcome the point sensors shortcomings are e.g. remote sensing or a cosmic rays neutron sensing (Bogena et al., 2022; Franz et al., 2020).

Figure 10. Cosmic rays neutron sensor (Styx Neutronica, Germany) and the meteorological station on the Nučice catchment (photograph by T. Li)

Cosmic-ray neutron sensing

. The CRNS sensors have recently been deployed to obtain the intermediate-scale and spatially integrating information about the shallow soil water content (Schrön et al., 2018). The CRNS method combined with a network of soil moisture sensors can be used to better understand the spatial variations of soil moisture on the field scale (Heistermann et al., 2021; Schrön et al., 2017). In farmland, the combination of CRNS and wireless sensor network (SoilNET) was used to study the SWC heterogeneity (Fersch et al., 2020). They found that the CNRS can represent the hourly soil moisture dynamics in the heterogeneous cropland. However, CRNS only provides the neutron count which needs to be further calibrated to get SWC (Schrön et al., 2017). In addition, a mobile detector (e.g. Soil moisture rover, suitcase probe) uses the same detection principle as the stationary probes,

but covers a larger area in a shorter recording time, which can be used for the calibration and validation of the stationary probe (Schrön et al., 2018; Franz et al., 2015).

Cosmic ray neutron sensing has been introduced as a new method to monitor the topsoil moisture on a medium scale, which represent individual fields on the Nučice catchment (Figure 10).

3.3 Geophysical surveying – electric resistivity tomography

The modern geophysical surveys, especially combination of different methods, have been becoming fast and cheap option for the subsurface inspection (Beneš et al., 2011; Busato et al., 2016; Perri et al., 2014). Common techniques are electrical resistivity tomography (ERT) (Jerabek & Zumr, 2021; Loke et al., 2013; Michot et al., 2003; Zumr et al., 2018), ground penetrating radar (GPR) (Kim et al., 2020; Minet et al., 2012; Wu et al., 2019), electromagnetic methods (Sungkono et al., 2014) or rarely also seismic surveys (Karl et al., 2011). Most methods were originally designed for prospecting of deep soil horizons or even geological formations. GPR is an appropriate device for the shallow soil profile monitoring, the ERT can be also used for the shallow surveys if the electrodes spacing is relatively fine (Jeřábek et al., 2017).

Figure 11. Electric resistivity tomography monitoring system (ARES, GF Instruments, Brno)

Electrical resistivity tomography (electrical resistivity profiling) was originally developed for the detection of soil and rock stratification, it is frequently used in hydrogeological, mining, hydrotechnical and environmental surveys. In the fields of soil physics and mechanics, ERT is used to identify the physicochemical properties of soils and to determine the spatial variability of these

properties. ERT is the most commonly used geophysical method for monitoring the internal structure of earth dams or embankments, although the application of the technique is still matter of research (Al-Fares, 2011; Zumr et al., 2020).

The method is based on detecting the resistivity of the environment from the measured values of voltage and current of the DC electric field injected into the ground (Figure 11). Both the advantage and disadvantage of the method is the measurement over a relatively large spatial scale, where local environmental variabilities affecting the electrical resistivity are integrated over the whole measured area. This makes it possible to determine effective environmental parameters; on the other hand, processes that occur only in a very small part of the soil profile, such as the detail of preferential flow during infiltration, cannot usually be observed (Zumr et al., 2012). If the distance between adjacent electrodes is small, ERT can be used to detect relatively small environmental inhomogeneities (Jeřábek et al., 2017).

3.4 Water residence time and water mixing investigated with use of stable isotopes and numerical modelling

The water residence time and water travel time distribution (RTD and TTD) are useful metrics to investigate the hydrology of the catchment (Asadollahi et al., 2020; McDonnell et al., 2010). A single domain model combined with the advection-dispersion equation was used studies to investigate the TTD at the soil profile scale (e.g. Stumpp et al., 2012). Sprenger et al. (2016) showed with a 1D model that the water travel time in the vadose zone can be driven by subsequent rainfall events and by the seasonality of evapotranspiration (ET). The dual permeability model was used to investigate the travel time distribution in several hillslope compartments by Dusek & Vogel (2018); macropore flow was identified as the driver of the fast hillslope response and the importance of transpiration was emphasized in the TTD calculation. The StorAge Selection (SAS) function, which represents the TTD and RTD ratio, infers whether older or younger water is more prone to be released into the discharge (Rinaldo et al., 2015). The SAS function helps to identify the age of the water in soils (Asadollahi et al., 2020) or in runoff (Benettin et al., 2017), and has also been applied with a 3D distributed model in a small agricultural catchment (Björn Rodriguez et al., 2021).

The mixing of pre-event and event water during a runoff episode depends on the soil structure, e.g. on the activation of preferential flow and matrix flow. Water mixing is strongly related to the mobilization of pre-event water in fast runoff and to the translatory flow theory (Hewlett and Hilbert, 1967). These phenomena were vastly studied in forested areas (e.g. Dušek & Vogel, 2018, von Freyberg et al., 2022), but also on arable land. Zajíček et al. (2016) found that the pre-event and event water mixing regime at a tile-drained arable field differs depending on the season: event water contributed to the discharge with up to 58 %, and the peak in the amount of event water did not coincide with the total discharge peak. A similar study (Stone & Wilson, 2006) showed that there was 11 – 51 % of event water in the discharge, but also that the event water peak did coincide with the total discharge peak. The authors highlighted the importance of shallow groundwater level (GWL) on activation of transport in the tile-drain system. In contrast, Klaus et al. (2013) indicated that a small portion of event water (20 %) reached the tile drains through macropores, suggesting that already mixed water is predominantly transported via the macropores.

Isotope hydrology has become a standard monitoring technique for the detailed observation of the water flow pathways on the hillslope and in small catchment scales. Tracing the water from various pools of the catchment helps to understand the processes of water retention and water runoff. And consequently, combining the stable isotope hydrology and physical based numerical modelling are successfully used to estimate the solutes fluxes in the system.

4. FUTURE PROSPECTS

Thanks to modern monitoring and numerical modelling techniques, significant progress can be expected in the process-based understanding of water dynamics in catchments. We will further concentrate on:

- Using cosmic neutron sensing for topsoil water content at a medium scale.
- Monitoring soil moisture at different scales (point sensors, CRNS, UAV-based surveys, satellite remote sensing) to understand the spatial heterogeneity of water content on seemingly homogeneous agricultural land.
- Using stable isotopes to track runoff pathways to understand the hydrological connectivity of the catchment and its temporal variability.

- To implement distributed, physically based numerical models to explain the dynamics of rainfall-runoff.
- To use geophysical methods to analyze the near-surface stratification of the subsurface. The compacted plough pan has been shown to cause shallow, lateral subsurface flow, and water ponding due to saturation excess conditions.

Although the specific research topics are of a basic research nature, we will also continue to investigate processes and variables that are important to water managers, farmers, policy makers, and other stakeholders. We have already contributed to applied research in the areas of water retention in the landscape, soil properties, soil quality and health, soil erosion, or water scarcity scenarios due to climate change through many national and international applied projects. We will continue in this direction.

5. REFERENCES

Al-Fares, W. (2011). Contribution of the geophysical methods in characterizing the water leakage in Afamia B dam, Syria. Journal of Applied Geophysics, 75(3). https://doi.org/10.1016/j.jappgeo.2011.07.014

Álvaro-Fuentes, J., Arrúe, J. L., Cantero-Martínez, C., López, M. v. (2008). Aggregate breakdown during tillage in a Mediterranean loamy soil. *Soil and Tillage Research*, 101(1–2), 62–68. https://doi.org/10.1016/J.STILL.2008.06.004

Asadollahi, M., Stumpp, C., Rinaldo, A., & Benettin, P. (2020). Transport and Water Age Dynamics in Soils: A Comparative Study of Spatially Integrated and Spatially Explicit Models. *Water Resources Research*, *56*(3), no-no. https://doi.org/10.1029/2019WR025539

Bauer, M., Dostal, T., Krasa, J., Jachymova, B., David, V., Devaty, J., Strouhal, L., & Rosendorf, P. (2019). Risk to residents, infrastructure, and water bodies from flash floods and sediment transport. *Environmental Monitoring and Assessment*, *191*(2). https://doi.org/10.1007/s10661-019-7216-7

Beare, M. H., Gregorich, E. G., & St-Georges, P. (2009). Compaction effects on CO2 and N2O production during drying and rewetting of soil. *Soil Biology and Biochemistry*, *41*(3), 611–621. https://doi.org/10.1016/J.SOILBIO.2008.12.024

Bednář, M., & Šarapatka, B. (2018). Relationships between physical–geographical factors and soil degradation on agricultural land. *Environmental Research*, *164*, 660–668. https://doi.org/10.1016/j.envres.2018.03.042

Beneš, V., Tesař, M., & Boukalová, Z. (2011). Repeated geophysical measurement: The basic principle of the GMS methodology used to inspect the condition of flood control dikes. *WIT Transactions on Ecology and the Environment*, *146*. https://doi.org/10.2495/RM110101

Benettin, P., Soulsby, C., Birkel, C., Tetzlaff, D., Botter, G., & Rinaldo, A. (2017). Using SAS functions and high-resolution isotope data to unravel travel time distributions in headwater catchments. *Water Resources Research*, *53*(3), 1864–1878. https://doi.org/10.1002/2016WR020117

Björn Rodriguez, N., Pfister, L., Zehe, E., & Klaus, J. (2021). A comparison of catchment travel times and storage deduced from deuterium and tritium tracers using StorAge Selection functions. *Hydrology and Earth System Sciences*, *25*(1). https://doi.org/10.5194/hess-25-401-2021

Bogena, H. R., Herbst, M., Huisman, J. A., Rosenbaum, U., Weuthen, A., & Vereecken, H. (2010). Potential of Wireless Sensor Networks for Measuring Soil Water Content Variability. *Vadose Zone Journal*, *9*(4), 1002–1013. https://doi.org/10.2136/VZJ2009.0173

Bogena, H. R., Schrön, M., Jakobi, J., Ney, P., Zacharias, S., Andreasen, M., Baatz, R., Boorman, D., Duygu, M. B., Eguibar-Galán, M. A., Fersch, B., Franke, T., Geris, J., González Sanchis, M., Kerr, Y., Korf, T., Mengistu, Z., Mialon, A., Nasta, P., … Vereecken, H. (2022). COSMOS-Europe: a European network of cosmic-ray neutron soil moisture sensors. *Earth System Science Data*, *14*(3). https://doi.org/10.5194/essd-14-1125-2022

Busato, L., Boaga, J., Peruzzo, L., Himi, M., Cola, S., Bersan, S., & Cassiani, G. (2016). Combined geophysical surveys for the characterization of a reconstructed river embankment. *Engineering Geology*, *211*. https://doi.org/10.1016/j.enggeo.2016.06.023

Daraghmeh, O.A., Jensen, J.R., Petersen, C.T. (2008). Near-Saturated Hydraulic Properties in the Surface Layer of a Sandy Loam Soil under Conventional and Reduced Tillage. *Soil Sci. Soc. Am. J.* 72, 1728. https://doi.org/10.2136/sssaj2007.0292

Devátý, J., Dostál T., & Krása, J. (2019). Effects of historical land use and land pattern changes on soil erosion – Case studies from Lower Austria and Central Bohemia. *Land Use Policy*, *82*. https://doi.org/10.1016/j.landusepol.2018.11.058

Dostál, T., Janecek, M., Kliment, Z., Krása, J., Langhammer, J., Váška, J., & Vrana, K. (2006). Czech Republic. In J. Boardman & J. Poesen (Eds.), *Soil Erosion in Europe* (pp. 107–116). John Wiley & Sons, Ltd. https://doi.org/10.1002/0470859202.ch10

Dušek, J., & Vogel, T. (2018). Hillslope hydrograph separation: The effects of variable isotopic signatures and hydrodynamic mixing in macroporous soil. *Journal of Hydrology*, *563*. https://doi.org/10.1016/j.jhydrol.2018.05.054

Dušek, J., Vogel, T., Dohnal, M., Lichner, L., & Čipáková, A. (2006). Simulated cadmium transport in macroporous soil during heavy rainstorm using dual-permeability approach. *Biologia (Poland)*, *61*(19), S251–S254. https://doi.org/10.2478/s11756-006-0167-9

Fer, M., Kodešová, R., Golovko, O., Schmidtová, Z., Klement, A., Nikodem, A., Kočárek, M., & Grabic, R. (2018). Sorption of atenolol, sulfamethoxazole and carbamazepine onto soil aggregates from the illuvial horizon of the haplic luvisol on loess. *Soil and Water Research*, *13*(3), 177–183. https://doi.org/10.17221/82/2018-SWR

Fersch, B., Francke, T., Heistermann, M., Schrön, M., Döpper, V., Jakobi, J., Baroni, G., Blume, T., Bogena, H., Budach, C., Gränzig, T., Förster, M., Güntner, A., Franssen, H. J. H., Kasner, M., Köhli, M., Kleinschmit, B., Kunstmann, H., Patil, A., … Oswald, S. (2020). A dense network of cosmic-ray neutron sensors for soil moisture observation in a highly instrumented pre-Alpine headwater catchment in Germany. *Earth System Science Data*, *12*(3). https://doi.org/10.5194/essd-12-2289-2020

Franz, T. E., Wahbi, A., Zhang, J., Vreugdenhil, M., Heng, L., Dercon, G., Strauss, P., Brocca, L., & Wagner, W. (2020). Practical Data Products From Cosmic-Ray Neutron Sensing for Hydrological Applications. *Frontiers in Water*, *2*. https://doi.org/10.3389/frwa.2020.00009

Gomiero, T. (2016). Soil degradation, land scarcity and food security: Reviewing a complex challenge. *Sustainability (Switzerland)*, *8*(3). https://doi.org/10.3390/SU8030281

Green, T. R., Ahuja, L. R., Benjamin, J. G. (2003). Advances and challenges in predicting agricultural management effects on soil hydraulic properties. *Geoderma*, 116(1–2), 3–27. https://doi.org/10.1016/S0016-7061(03)00091-0

Hamza, M. A., & Anderson, W. K. (2005). Soil compaction in cropping systems: A review of the nature, causes and possible solutions. In *Soil and Tillage Research* (Vol. 82, Issue 2, pp. 121–145). Elsevier. https://doi.org/10.1016/j.still.2004.08.009

Heistermann, M., Francke, T., Schrön, M., & Oswald, S. E. (2021). Spatiooral soil moisture retrieval at the catchment scale using a dense network of cosmic-ray neutron sensors. *Hydrology and Earth System Sciences*, *25*(9). https://doi.org/10.5194/hess-25-4807-2021

Hewlett, J.D., and A.R. Hibbert. (1967). Factors affecting the response of small watersheds to precipitation in humid areas. *For. Hydrol.* 1: 275--290.

Hillel, D. (2003). Introduction to Environmental Soil Physics. In *Introduction to Environmental Soil Physics*. https://doi.org/10.1016/B978-0-12-348655-4.X5000-X

Hiller, E., & Šebesta, M. (2017). Effect of temperature and Soil pH on the sorption of ibuprofen in agricultural soil. *Soil and Water Research*, *12*(2), 78–85. https://doi.org/10.17221/6/2016-SWR

Hofman, J., Dušek, L., Klánová, J., Bezchlebová, J., & Holoubek, I. (2004). Monitoring microbial biomass and respiration in different soils from the Czech Republic - A summary of results. *Environment International*, *30*(1), 19–30. https://doi.org/10.1016/S0160-4120(03)00142-9

Holubová, K., Zumr, D., & Císlerová, M. (2011). Numerical Simulation of Water Dynamics and Contaminant Transport at Quarry Dump Hájek. *Waste Forum*, *2*, 82–91.

Homoláč, L., & Tomsik, K. (2016). Historical development of land ownership in the Czech Republic since the foundation of the Czechoslovakia until present. *Agricultural Economics (Czech Republic)*, *62*(11), 528–536. https://doi.org/10.17221/250/2015-AGRICECON

Horáček, J., Kolář, L., Čechová, V., & Hřebečková, J. (2008). Phosphorus and carbon fraction concentrations in a cambisol soil as affected by tillage. *Communications in Soil Science and Plant Analysis*, *39*(13–14), 2032–2045. https://doi.org/10.1080/00103620802134867

Hrabalíková, M., Huisová, P., Holubík, O., Žížala, D., Ureš, J., & Kumhalová, J. (2018). Assessment of changes in topsoil depth redistribution by different tillage technologies. In M. Zlatic & S. Kostadinov (Eds.), *SOIL AND WATER RESOURCES PROTECTION IN THE CHANGING ENVIRONMENT* (Vol. 45, pp. 200–210).

Hudek, C., Putinica, C., Otten, W., & de Baets, S. (2022). Functional root trait-based classification of cover crops to improve soil physical properties. *European Journal of Soil Science*, *73*(1). https://doi.org/10.1111/ejss.13147

Jabro, J. D., Stevens, W. B., Iversen, W. M., & Evans, R. G. (2010). Tillage effects on bulk density and hydraulic properties of a sandy loam soil in the Mon-Dak Region , USA. *Soil Solutions for a Changing World*, *August*.

Jáchymová, B., Krása, J., Dostál, T., & Bauer, M. (2020). Can lumped characteristics of a contributing area provide risk definition of sediment flux? *Water (Switzerland)*, *12*(6). https://doi.org/10.3390/w12061787

Jakšík, O., Kodešová, R., Kubiš, A., Stehlíková, I., Drábek, O., & Kapička, A. (2015). Soil aggregate stability within morphologically diverse areas. *Catena*, *127*, 287–299. https://doi.org/10.1016/j.catena.2015.01.010

Javůrek, M., & Vach, M. (2008). *The negative impacts of soil overcompaction and set of measures for their remedy*. Výzkumný ústav rostlinné výroby, v.v.i.

Jeřábek, J., & Zumr, D. (2021). Geophysical survey as a tool to reveal subsurface stratification at a small agricultural headwater catchment: a case study. *Stavební Obzor - Civil Engineering Journal*, *30*(3), 766–778. https://doi.org/10.14311/CEJ.2021.03.0059

Jeřábek, J., Zumr D., & Dostál, T. (2017). Identifying the plough pan position on cultivated soils by measurements of electrical resistivity and penetration resistance. *Soil & Tillage Research*, *174*. https://doi.org/10.1016/j.still.2017.07.008

Jeřábek, J., Zumr, D., Laburda, T., Krása, J., & Dostál, T. (2022). Soil surface connectivity of tilled soil with wheel tracks and its development under simulated rainfall. *Journal of Hydrology*, 128322. https://doi.org/10.1016/J.JHYDROL.2022.128322

Kapička, J., Žížala, D., & Novotný, I. (2020). *Monitoring eroze zemědělské půdy -Závěrečná zpráva*. Research Institute for Soil and Water Conservation.

Karl, L., Fechner, T., Schevenels, M., François, S., & Degrande, G. (2011). Geotechnical characterization of a river dyke by surface waves. *Near Surface Geophysics*, *9*(6). https://doi.org/10.3997/1873-0604.2011030

Kiffney, P. M., & Richardson, J. S. (2010). Organic matter inputs into headwater streams of southwestern British Columbia as a function of riparian reserves and time since harvesting. *Forest Ecology and Management*, *260*(11), 1931–1942. https://doi.org/10.1016/J.FORECO.2010.08.016

Kim, J. H., Yi, M.-J., Song, Y., Seol, S. J., Chung, S.-H., & Kim, K.-S. (2020). *Application of Geophysical Methods to the Safety Analysis of an Earth Dam*. https://doi.org/10.3997/2214-4609-pdb.15.m-04

Klaus, J., Zehe, E., Elsner, M., Külls, C., & McDonnell, J. J. (2013). Macropore flow of old water revisited: Experimental insights from a tile-drained hillslope. *Hydrology and Earth System Sciences*, *17*(1). https://doi.org/10.5194/hess-17-103-2013

Kleine, L., Tetzlaff, D., Smith, A., Wang, H., & Soulsby, C. (2020). Using water stable isotopes to understand evaporation, moisture stress, and re-wetting in catchment forest and grassland soils of the summer drought of 2018. *Hydrology and Earth System Sciences*, *24*(7), 3737–3752. https://doi.org/10.5194/HESS-24-3737-2020

Klement, A., Kodešová, R., Bauerová, M., Golovko, O., Kočárek, M., Fér, M., Koba, O., Nikodem, A., & Grabic, R. (2018). Sorption of citalopram, irbesartan and fexofenadine in soils: Estimation of sorption coefficients from soil properties. *Chemosphere*, *195*, 615–623. https://doi.org/10.1016/j.chemosphere.2017.12.098

Kočárek, M., Kodešová, R., Vondráčková, L., Golovko, O., Fér, M., Klement, A., Nikodem, A., Jakšík, O., & Grabic, R. (2016). Simultaneous sorption of four ionizable pharmaceuticals in different horizons of three soil types. *Environmental Pollution*, *218*, 563–573. https://doi.org/10.1016/j.envpol.2016.07.039

Kodeš, V. (2020). Směsi cizorodých látek v podzemních vodách. *TZB-Info*.

Kodešová, R., Grabic, R., Kočárek, M., Klement, A., Golovko, O., Fér, M., Nikodem, A., & Jakšík, O. (2015). Pharmaceuticals' sorptions relative to properties of thirteen different soils. *Science of the Total Environment*, *511*, 435–443. https://doi.org/10.1016/j.scitotenv.2014.12.088

Kodesova, R., Jirku, V., Kodes, V., Muhlhanselova, M., Nikodem, A., & Žigová, A. (2011). Soil structure and soil hydraulic properties of Haplic Luvisol used as arable land and grassland. *Soil and Tillage Research*, *111*(2), 154–161. https://doi.org/10.1016/j.still.2010.09.007

Kodešová, R., Klement, A., Golovko, O., Fér, M., Kočárek, M., Nikodem, A., & Grabic, R. (2019). Soil influences on uptake and transfer of pharmaceuticals from sewage sludge amended soils to spinach. *Journal of Environmental Management*, *250*. https://doi.org/10.1016/j.jenvman.2019.109407

Kodešová, R., Kočárek, M., Klement, A., Golovko, O., Koba, O., Fér, M., Nikodem, A., Vondráčková, L., Jakšík, O., & Grabic, R. (2016). An analysis of the dissipation of pharmaceuticals under thirteen different soil conditions. *Science of the Total Environment*, *544*, 369–381. https://doi.org/10.1016/j.scitotenv.2015.11.085

Kodešová, R., Kočárek, M., Kodeš, V., Šimůnek, J., & Kozák, J. (2008). Impact of Soil Micromorphological Features on Water Flow and Herbicide Transport in Soils. *Vadose Zone Journal*, *7*(2), 798–809. https://doi.org/10.2136/vzj2007.0079

Kodešová, R., Rohošková, M., & Žigová, A. (2009). Comparison of aggregate stability within six soil profiles under conventional tillage using various laboratory tests. *Biologia*, *64*(3), 550–554. https://doi.org/10.2478/s11756-009-0095-6

Kosubová, P., Škulcová, L., Poláková, Hofman, J., & Bielská, L. (2020). Spatial and temporal distribution of the currently-used and recently-banned pesticides in arable soils of the Czech Republic. *Chemosphere*, *254*, 126902. https://doi.org/10.1016/j.chemosphere.2020.126902

Kozák, J., Borůvka, L., Kodešová, R., Jacko, K., & Hladík, J. (2010). *Soil atlas of the Czech Republic*. CULS Prague.

Kozák, J., Janku, J., & Jehlicka, J. (1995). The Problems of Heavily Polluted Soils in the Czech Republic: A Case Study. In *Heavy Metals* (pp. 287–300). Springer Berlin Heidelberg. https://doi.org/10.1007/978-3-642-79316-5_17

Kraamwinkel, C. T., Beaulieu, A., Dias, T., & Howison, R. A. (2021). Planetary limits to soil degradation. *Communications Earth & Environment*, *2*(1). https://doi.org/10.1038/S43247-021-00323-3

Krása, J., Dostál, T., Jáchymová, B., Bauer M., & Devátý, J. (2019). Soil erosion as a source of sediment and phosphorus in rivers and reservoirs – Watershed analyses using WaTEM/SEDEM. *Environmental Research*, *171*(0). https://doi.org/10.1016/j.envres.2019.01.044

Kroulík, M., Kumhála, F., Hůla, J., & Honzík, I. (2009). The evaluation of agricultural machines field trafficking intensity for different soil tillage technologies. *Soil and Tillage Research*, *105*(1), 171–175. https://doi.org/10.1016/j.still.2009.07.004

Kroulík, M., Kvíz, Z., Kumhála, F., Hůla, J., & Loch, T. (2011). Procedures of soil farming allowing reduction of compaction. *Precision Agriculture*, *12*(3), 317–333. https://doi.org/10.1007/s11119-010-9206-1

Lhotský, J. (2000). *Soil compaction and measures against it*. Ústav zemědělských a potravinářských informací. https://katalog.mendelu.cz/records/d0f8bd4e-7e7f-47cc-9eeb-ddcdb22aa904

Li, T., Jeřábek, J., Noreika, N., Dostál T., & Zumr, D. (2021). An overview of hydrometeorological datasets from a small agricultural catchment (Nučice) in the Czech Republic. *Hydrological Processes*, *35*(2). https://doi.org/10.1002/hyp.14042

Li, T., Jeřábek, J., Zumr, D., Noreika N., & Dostál, T. (2021). Assessing spatial soil moisture patterns at a small agricultural catchment. *2021 IEEE International Workshop on Metrology for Agriculture and Forestry*, *175226*. https://doi.org/10.1109/MetroAgriFor52389.2021.9628588

Li, T., Noreika, N., Jeřábek J., & Zumr, D. (2020). An overview of hydrometeorological datasets from a small agricultural catchment (Nučice) in the Czech Republic. *Sborník Hydrologie, GIS a Životní Prostředí 2020*. http://storm.fsv.cvut.cz/data/files/Konference/GISZP/Sborn%C3%ADk_HyGIS_2020_final.pdf

Lipiec, J., Wójciga, A., & Horn, R. (2009). Hydraulic properties of soil aggregates as influenced by compaction. *Soil and Tillage Research*, *103*(1). https://doi.org/10.1016/j.still.2008.10.021

Loke, M. H., Chambers, J. E., Rucker, D. F., Kuras, O., & Wilkinson, P. B. (2013). Recent developments in the direct-current geoelectrical imaging method. *Journal of Applied Geophysics*, *95*. https://doi.org/10.1016/j.jappgeo.2013.02.017

Mayor, Á. G., Bautista, S., Small, E. E., Dixon, M., & Bellot, J. (2008). Measurement of the connectivity of runoff source areas as determined by vegetation pattern and topography: A tool for assessing potential water and soil losses in drylands. *Water Resources Research*, *44*(10). https://doi.org/10.1029/2007WR006367

McDonnell, J. J., McGuire, K., Aggarwal, P., Beven, K. J., Biondi, D., Destouni, G., Dunn, S., James, A., Kirchner, J., Kraft, P., Lyon, S., Maloszewski, P., Newman, B., Pfister, L., Rinaldo, A., Rodhe, A., Sayama, T., Seibert, J., Solomon, K., … Wrede, S. (2010). How old is streamwater? Open questions in catchment transit time conceptualization, modelling and analysis. *Hydrological Processes*, *24*(12), 1745–1754. https://doi.org/10.1002/HYP.7796

Menšík, L., Hlisnikovský, L., & Kunzová, E. (2019). The State of the Soil Organic Matter and Nutrients in the Long-Term Field Experiments with Application of Organic and Mineral Fertilizers in Different Soil-Climate Conditions in the View of Expecting Climate Change. In *Organic Fertilizers - History, Production and Applications*. IntechOpen. https://doi.org/10.5772/intechopen.86716

Michot, D., Benderitter, Y., Dorigny, A., Nicoullaud, B., King, D., & Tabbagh, A. (2003). Spatial and temporal monitoring of soil water content with an irrigated corn crop cover using surface electrical resistivity tomography. *Water Resources Research*, *39*(5). https://doi.org/10.1029/2002WR001581

Minet, J., Bogaert, P., Vanclooster, M., & Lambot, S. (2012). Validation of ground penetrating radar full-waveform inversion for field scale soil moisture mapping. *Journal of Hydrology*, *424–425*. https://doi.org/10.1016/j.jhydrol.2011.12.034

Ministry of the Environment of the Czech Republic. (2019). Decree no. 271/2019 on the procedures for ensuring the protection of agricultural land. *Collection of Laws*.

Moravcová, J., Koupilová, M., Pavlíček, T., Zemek, F., Kvítek, T., & Pečenka, J. (2017). Analysis of land consolidation projects and their impact on land use change, landscape structure, and agricultural land resource protection: case studies of Pilsen-South and Pilsen-North (Czech Republic). *Landscape and Ecological Engineering*, *13*(1), 1–13. https://doi.org/10.1007/s11355-015-0286-y

Nolan, M., Stanton, K. J., Evans, K., Pym, L., Kaufman, B., & Duley, E. (2021). From the ground up: prioritizing soil at the forefront of ecological restoration. *Restoration Ecology*, *29*(8). https://doi.org/10.1111/REC.13453

Noreika, N., Li, T., Zumr, D., Krasa, J., Dostal, T., & Srinivasan, R. (2020). Farm-Scale Biofuel Crop Adoption and Its Effects on In-Basin Water Balance. *Sustainability 2020, Vol. 12, Page 10596*, *12*(24), 10596. https://doi.org/10.3390/SU122410596

Novák, P., Hůla, J., & Kumhálová, J. (2006). Translocation of soil praticles ad different speed of tillers. *In: Proceedings of 6th International Conference on Trends in Agricultural Engineering*, 433–437.

Novara, A., Armstrong, A., Gristina, L., Semple, K. T., & Quinton, J. N. (2012). Effects of soil compaction, rain exposure and their interaction on soil carbon dioxide emission. *Earth Surface Processes and Landforms*, *37*(9), 994–999. https://doi.org/10.1002/ESP.3224

Or, D., Keller, T., Schlesinger, W.H. (2021). Natural and managed soil structure: On the fragile scaffolding for soil functioning. *Soil Tillage Res.* 208, 104912. https://doi.org/10.1016/j.still.2020.104912

Perera, R. N. N., & Maharjan, B. (2021). Ecological boundaries and interference with the global nitrogen cycle: A review on soil nitrogen management strategies. *Journal of Agricultural Sciences - Sri Lanka*, *16*(1). https://doi.org/10.4038/jas.v16i1.9193

Perri, M. T., Boaga, J., Bersan, S., Cassiani, G., Cola, S., Deiana, R., Simonini, P., & Patti, S. (2014). River embankment characterization: The joint use of geophysical and geotechnical techniques. *Journal of Applied Geophysics*, *110*. https://doi.org/10.1016/j.jappgeo.2014.08.012

Podhrázská, J., & Karásek, P. (2014). *Systém analýzy území a návrhu opatření k ochraně půdy a vody v krajině* (1st ed.). VUMOP.

Podhrázská, J., Kučera, J., Karásek, P., & Konečná, J. (2016). Land degradation by erosion and its economic consequences for the region of South Moravia (Czech Republic). *Soil and Water Research*, *10*(No. 2), 105–113. https://doi.org/10.17221/143/2014-swr

Podlešáková, E., & Nemecek, J. (2000). Contamination and Degradation of Soils in the Czech Republic - Contemporary and Future State. In *Soil Quality, Sustainable Agriculture and Environmental Security in Central and Eastern Europe* (pp. 79–86). Springer Netherlands. https://doi.org/10.1007/978-94-011-4181-9_6

Poláková, Š., Kubík, L., Malý, S., & Němec, P. (2010). *Monitoring of agricultural soils in the Czech Republic, 1992-2007* (1st ed.). Central Institute for Supervising and Testing in Agriculture.

Pražan, R., Kubín, K., & Gerndtová, I. (2014). Key factors of technogenic soil compaction. *Mechanizace Zemědělství*, *64*(1), 11–13. http://www.vuzt.cz/svt/vuzt/publ/AnotaHTM/2014-006.htm

Rinaldo, A., Benettin, P., Harman, C. J., Hrachowitz, M., McGuire, K. J., van der Velde, Y., Bertuzzo, E., & Botter, G. (2015). Storage selection functions: A coherent framework for

quantifying how catchments store and release water and solutes. *Water Resources Research*, *51*(6), 4840–4847. https://doi.org/10.1002/2015WR017273

Rosendorf, P., Vyskoč, P., Prchalová, H., & Fiala, D. (2016). Estimated contribution of selected non-point pollution sources to the phosphorus and nitrogen loads in water bodies of the Vltava river basin. *Soil and Water Research*, *11*(3), 196–204. https://doi.org/10.17221/15/2015-SWR

Sabater, F., Butturini, A., Martí, E., Muñoz, I., Romaní, A., Wray, J., & Sabater, S. (2015). Effects of riparian vegetation removal on nutrient retention in a Mediterranean stream. *Https://Doi.Org/10.2307/1468120*, *19*(4), 609–620. https://doi.org/10.2307/1468120

Saffarpour, S., Western, A. W., Adams, R., & McDonnell, J. J. (2016). Multiple runoff processes and multiple thresholds control agricultural runoff generation. *Hydrology and Earth System Sciences*, *20*(11). https://doi.org/10.5194/hess-20-4525-2016

Sáňka, M. (2018). Je hospodaření s půdou udržitelné? *Veronica*, *1*, 2–5.

Schönenberger, U., & Stamm, C. (2021). Hydraulic shortcuts increase the connectivity of arable land areas to surface waters. *Hydrology and Earth System Sciences*, *25*(4). https://doi.org/10.5194/hess-25-1727-2021

Schrön, M., Köhli, M., Scheiffele, L., Iwema, J., Bogena, H. R., Lv, L., Martini, E., Baroni, G., Rosolem, R., Weimar, J., Mai, J., Cuntz, M., Rebmann, C., Oswald, S. E., Dietrich, P., Schmidt, U., & Zacharias, S. (2017). Improving calibration and validation of cosmic-ray neutron sensors in the light of spatial sensitivity. *Hydrology and Earth System Sciences*, *21*(10). https://doi.org/10.5194/hess-21-5009-2017

Schrön, M., Rosolem, R., Köhli, M., Piussi, L., Schröter, I., Iwema, J., Kögler, S., Oswald, S. E., Wollschläger, U., Samaniego, L., Dietrich, P., & Zacharias, S. (2018). Cosmic-ray Neutron Rover Surveys of Field Soil Moisture and the Influence of Roads. *Water Resources Research*, *54*(9), 6441–6459. https://doi.org/10.1029/2017WR021719

Schwen, A., G. Bodner, P. Scholl, G.D. Buchan, and W. Loiskandl (2011). Temporal dynamics of soil hydraulic properties and the water-conducting porosity under different tillage. *Soil Tillage Res.* 113(2): 89–98. doi: 10.1016/j.still.2011.02.005.

Shegunova, P., Klánová, J., & Holoubek, I. (2007). Residues of organochlorinated pesticides in soils from the Czech Republic. *Environmental Pollution*, *146*(1), 257–261. https://doi.org/10.1016/j.envpol.2006.03.057

Skála, J., Vácha, R., Hofman, J., Horváthová, V., Sáňka, M., & Čechmánková, J. (2017). Spatial differentiation of ecosystem risks of soil pollution in floodplain areas of the Czech Republic. *Soil and Water Research*, *12*(1), 1–9. https://doi.org/10.17221/53/2016-SWR

Sněhota, M., Sobotková, M., & Císlerová, M. (2008). Impact of the entrapped air on water flow and solute transport in heterogeneous soil: experimental set-up. *Journal of Hydrology and Hydrodynamics*, *56*(4), 247–256.

Sprenger, M., Seeger, S., Blume, T., & Weiler, M. (2016). Predicting shifts in rainfall-runoff partitioning duringmultiyear drought: Roles of dry period and catchment characteristics. *Water Resources Research*, *52*.

Stone, W. W., & Wilson, J. T. (2006). Preferential Flow Estimates to an Agricultural Tile Drain with Implications for Glyphosate Transport. *Journal of Environmental Quality*, *35*(5). https://doi.org/10.2134/jeq2006.0068

Stumpp, C., Stichler, W., Kandolf, M., & Šimůnek, J. (2012). Effects of Land Cover and Fertilization Method on Water Flow and Solute Transport in Five Lysimeters: A Long-Term Study Using Stable Water Isotopes. *Vadose Zone Journal*, *11*(1). https://doi.org/10.2136/VZJ2011.0075

Sungkono, Husein, A., Prasetyo, H., Bahri, A. S., Monteiro Santos, F. A., & Santosa, B. J. (2014). The VLF-EM imaging of potential collapse on the LUSI embankment. *Journal of Applied Geophysics*, *109*. https://doi.org/10.1016/j.jappgeo.2014.08.004

Tenreiro, T. R., Jeřábek, J., Gómez, J. A., Zumr, D., Martínez, G., García-Vila, M., & Fereres, E. (2022). Simulating water lateral inflow and its contribution to spatial variations of rainfed wheat yields. *European Journal of Agronomy*, *137*, 126515. https://doi.org/10.1016/J.EJA.2022.126515

UKZUZ. (2020). *Data on the consumption of active substances contained in Plant Protection Products*.

Usowicz, B., & Lipiec, J. (2020). The effect of exogenous organic matter on the thermal properties of tilled soils in Poland and the Czech Republic. *Journal of Soils and Sediments*, *20*(1), 365–379. https://doi.org/10.1007/s11368-019-02388-2

Vácha, R., Sánka, M., Skála, J., Čechmánková, J., & Horváthová, V. (2016). Soil Contamination Health Risks in Czech Proposal of Soil Protection Legislation. In *Environmental Health Risk - Hazardous Factors to Living Species*. InTech. https://doi.org/10.5772/62456

Vašíčková, J., Hvězdová, M., Kosubová, P., & Hofman, J. (2019). Ecological risk assessment of pesticide residues in arable soils of the Czech Republic. *Chemosphere*, *216*, 479–487. https://doi.org/10.1016/j.chemosphere.2018.10.158

Vaverková, M. D., Zloch, J., Radziemska, M., & Adamcová, D. (2017). Environmental impact of landfill on soils – The example of the Czech Republic. *Polish Journal of Soil Science*, *50*(1), 93–105. https://doi.org/10.17951/pjss.2017.50.1.93

von Freyberg, J., Rücker, A., Zappa, M., Schlumpf, A., Studer, B., & Kirchner, J. W. (2022). Four years of daily stable water isotope data in stream water and precipitation from three Swiss catchments. *Scientific Data*, *9*(1). https://doi.org/10.1038/s41597-022-01148-1

VÚMOP. (2021). *Soils in numbers*. Https://Statistiky.Vumop.Cz/.

Walmsley, A., Azadi, H., Tomeckova, K., & Sklenicka, P. (2020). Contrasting effects of land tenure on degradation of Cambisols and Luvisols: The case of Central Bohemia Region in the Czech Republic. *Land Use Policy*, *99*, 104956. https://doi.org/10.1016/j.landusepol.2020.104956

Wang, L., Zhang, Y., Jia, J., Zhen, Q., & Zhang, X. (2021). Effect of vegetation on the flow pathways of steep hillslopes: Overland flow plot-scale experiments and their implications. *Catena*, *204*. https://doi.org/10.1016/J.CATENA.2021.105438

Weissmannová, H. D., Mihočová, S., Chovanec, P., & Pavlovský, J. (2019). Potential ecological risk and human health risk assessment of heavy metal pollution in industrial affected soils by coal mining and metallurgy in Ostrava, Czech Republic. *International Journal of Environmental Research and Public Health*, *16*(22). https://doi.org/10.3390/ijerph16224495

Wu, K., Rodriguez, G. A., Zajc, M., Jacquemin, E., Clément, M., de Coster, A., & Lambot, S. (2019). A new drone-borne GPR for soil moisture mapping. *Remote Sensing of Environment*, *235*. https://doi.org/10.1016/j.rse.2019.111456

Young, E. O., Ross, D. S., Jaisi, D. P., & Vidon, P. G. (2021). Phosphorus Transport along the Cropland–Riparian–Stream Continuum in Cold Climate Agroecosystems: A Review. *Soil Systems 2021, Vol. 5, Page 15*, *5*(1), 15. https://doi.org/10.3390/SOILSYSTEMS5010015

Zajíček, A., Pomije, T., & Kvítek, T. (2016). Event water detection in tile drainage runoff using stable isotopes and a water temperature in small agricultural catchment in Bohemian-Moravian Highlands, Czech Republic. *Environmental Earth Sciences*, *75*(9). https://doi.org/10.1007/s12665-016-5561-1

Zambon, N., Johannsen, L. L., Strauss, P., Dostal, T., Zumr, D., Cochrane, T. A., & Klik, A. (2021). Splash erosion affected by initial soil moisture and surface conditions under simulated rainfall. *Catena*, *196*. https://doi.org/10.1016/j.catena.2020.104827

Zambon, N., Johannsen, L. L., Strauss, P., Dostal, T., Zumr, D., Neumann, M., Cochrane, T. A., & Klik, A. (2020). Rainfall Parameters Affecting Splash Erosion under Natural Conditions. *Applied Sciences*, *10*(12), 4103. https://doi.org/10.3390/app10124103

Zhou, J., Liu, G., Meng, Y., Xia, C. C., Chen, K., & Chen, Y. (2021). Using stable isotopes as tracer to investigate hydrological condition and estimate water residence time in a plain region, Chengdu, China. *Scientific Reports 2021 11:1*, *11*(1), 1–12. https://doi.org/10.1038/s41598-021-82349-3

Žížala, D., Juřicová, A., Kapička, J., & Novotný, I. (2021). The potential risk of combined effects of water and tillage erosion on the agricultural landscape in Czechia. https://doi.org/10.1080/17445647.2021.1942251

Zumr, D., Snehota, M., & Cislerova, M. (2012). Numerical simulation of tension infiltration experiment monitored by 3D ERT. *5th Asia-Pacific Conference on Unsaturated Soils 2012*, *2*.

Zumr, D., Dostál, T., & Devátý, J. (2015). Identification of prevailing storm runoff generation mechanisms in an intensively cultivated catchment. *Journal of Hydrology and Hydromechanics*, *63*(3). https://doi.org/10.1515/johh-2015-0022

Zumr, D., Dostál, T., Devátý, J., Valenta, P., Rosendorf, P., Eder A., & Strauss, P. (2017). Experimental determination of the flood wave transformation and the sediment resuspension in a small regulated stream in an agricultural catchment. *Hydrology and Earth System Sciences*, *21*(11). https://doi.org/10.5194/hess-21-5681-2017

Zumr, D., David, V., Krása, J., & Nedvěd, J. (2018). *Geophysical Evaluation of the Inner Structure of a Historical Earth-Filled Dam*. Proceedings, https://doi.org/10.3390/proceedings2110664

Zumr, D., Jeřábek, J., Klípa, V., Dohnal, M., & Sněhota, M. (2019). Estimates of tillage and rainfall effects on unsaturated hydraulic conductivity in a small central European agricultural catchment. *Water (Switzerland)*, *11*(4). https://doi.org/10.3390/w11040740

Zumr, D., David, V., Jeřábek, J., Noreika N., & Krása, J. (2020). Monitoring of the soil moisture regime of an earth-filled dam by means of electrical resistance tomography, close range photogrammetry, and thermal imaging. *Environmental Earth Sciences*, *79*(12). https://doi.org/10.1007/s12665-020-09052-w

PART II

Collection of selected manuscript

This section presents nine peer-reviewed manuscripts indexed in the Web of Science™ database, where David Zumr is the leading author, or which were written by doctoral candidates Jakub Jeřábek and Tailin Li, who have been supervised by David Zumr (and DZ is a co-author).

The manuscripts are organized into subsections according to their main scope. Each subsection is introduced with a brief summary of the attached manuscripts. A list of additional relevant publications in which David Zumr participated is attached.

List of the attached manuscripts:

1) SOIL WATER DYNAMICS, SMALL SCALE EXPERIMENTS

a) ***Zumr, D.**, Jeřábek, J., Klípa, V., Dohnal, M., & Sněhota, M. (2019). Estimates of tillage and rainfall effects on unsaturated hydraulic conductivity in a small central European agricultural catchment.*

b) ***Zumr, D.**, Mützenberg, D., Neumann, M., Jeřábek, J., Laburda, T., Kavka, P., Johannsen, L. L., Zambon, N., Klik, A., Strauss P., & Dostál, T. (2020). Experimental Setup for Splash Erosion Monitoring—Study of Silty Loam Splash Characteristics. Sustainability, 12(1).*

c) *Jeřábek, J., **Zumr, D.**, Laburda, T., Krása, J., & Dostál, T. (2022). Soil surface connectivity of tilled soil with wheel tracks and its development under simulated rainfall. Journal of Hydrology, 128322. https://doi.org/10.1016/J.JHYDROL.2022.128322*

2) HYDROLOGICAL PROCESSES ON A CATCHMENT SCALE

a) ***Zumr, D.**, Dostál, T., & Devátý, J. (2015). Identification of prevailing storm runoff generation mechanisms in an intensively cultivated catchment. Journal of Hydrology and Hydromechanics, 63(3).*

b) *Jeřábek, J., **Zumr D.**, & Dostál, T. (2017). Identifying the plough pan position on cultivated soils by measurements of electrical resistivity and penetration resistance. Soil & Tillage Research, 174.*

c) *Li, T., Jeřábek, J., Noreika, N., Dostál, T., & **Zumr, D.** (2021). An overview of hydrometeorological datasets from a small agricultural catchment (Nučice) in the Czech Republic. Hydrological Processes, 35(2), e14042.*

3) INTERACTION OF WATER WITH EARTH STRUCTURES

a) ***Zumr, D.**, Dostál, T., Devátý, J., Valenta, P., Rosendorf, P., Eder A., & Strauss, P. (2017). Experimental determination of the flood wave transformation and the sediment resuspension in a small regulated stream in an agricultural catchment. Hydrology and Earth System Sciences, 21(11).*

b) ***Zumr, D.**, & Císlerová, M. (2010). Soil moisture dynamics in levees during flood events variably saturated approach. Journal of Hydrology and Hydromechanics, 58(1).*

c) ***Zumr, D.**, David, V., Jeřábek, J., Noreika, N., & Krása, J. (2020). Monitoring of the soil moisture regime of an earth-filled dam by means of electrical resistance tomography, close range photogrammetry, and thermal imaging. Environmental Earth Sciences, 79(12).*

1. SOIL WATER DYNAMICS, SMALL SCALE EXPERIMENTS

Attached research articles:

- ***Zumr, D.**, Jeřábek, J., Klípa, V., Dohnal, M., & Sněhota, M. (2019). Estimates of tillage and rainfall effects on unsaturated hydraulic conductivity in a small central European agricultural catchment. Water, 11(4). https://doi.org/10.3390/w11040740*

  The size, shape and spatial distributions of the soil aggregates are considerably altered during a growing season and therefore affect the water infiltration and the soil moisture regime. We studied the temporal variability of the physical characteristics of the topsoil (bulk density, saturated water content) and measured the quasi-saturated hydraulic conductivity (at h_c = -3 cm) for three consecutive years. The main aim was to observe how properties change during natural topsoil consolidation between seeding and harvest of crops.

- ***Zumr, D.**, Mützenberg, D., Neumann, M., Jeřábek, J., Laburda, T., Kavka, P., Johannsen, L. L., Zambon, N., Klik, A., Strauss P., & Dostál, T. (2020). Experimental Setup for Splash Erosion Monitoring—Study of Silty Loam Splash Characteristics. Sustainability, 12(1). https://doi.org/10.3390/su12010157*

  Small-scale experiments were performed to study the initial stage of the soil erosion process. The aim was to investigate how the kinetic energy of the rainfall activates the splash erosion and how the rainfall destroys the soil aggregates and influences the roughness of the soil surface. We identified a linear relationship between the kinetic energy of the rain and the amount of splashed material. Minimal threshold rainfall kinetic energy must be exceeded to initiate the erosion process.

- *Jeřábek, J., **Zumr, D.**, Laburda, T., Krása, J., & Dostál, T. (2022). Soil surface connectivity of tilled soil with wheel tracks and its development under simulated rainfall. Journal of Hydrology, 128322. https://doi.org/10.1016/J.JHYDROL.2022.128322*

  Wheel tracks on the soil surface significantly influence the surface runoff routing during heavy rainfall events. Based on their orientation, they may serve as preferential pathways, or as obstacles trapping the flowing water. This study presents a quantitative evaluation of surface roughness and runoff connectivity, including the effects of wheel tracks, during rainfall.

Additional relevant publications:

- ***Zumr, D.**, Dohnal, M., Hrnčíř, M., Císlerová, M., Vogel, T., & Doležal, F. (2006). Simulation of soil water dynamics in structured heavy soils with respect to root water uptake. Biologia, 61(19). https://doi.org/10.2478/s11756-006-0181-y*

  Evapotranspiration is one of the dominant components of the water cycle. In this study, we quantitively evaluated the effect of rapidly growing root system (in this case potatoes) on the soil water regime. The growing root zone was implemented in a dual-permeability unsaturated soil water flow model S1D (Vogel et al., 2000). The dual permeability model (Gerke & van Genuchten, 1993) was implemented due to the preferential flow character, which was observed earlier. The model was inversely optimized to fit the measured soil water potential at several depths of a soil profile. The results show that the distribution of the root zone is a sensitive parameter in the case of seasonal crops. The duel permeability model was capable of fitting fast water front propagation through preferential pathways.

- *Doležal, F., **Zumr, D.**, Vacek, J., Zavadil, J., Battilani, A., Plauborg, F. L., Hansen, S., Abrahamsen, P., Bízik, J., Takáč, J., Mazurczyk, W., Coutinho, J., & Štekauerová, V. (2007). Dual permeability soil water dynamics and water uptake by roots in irrigated potato fields. Biologia, 62(5). https://doi.org/10.2478/s11756-007-0109-1*

  The follow-up of the article of Zumr et al. (2006) where also soil water regime of irrigated potato fields, which did not experience significant water stress, were analyzed.

- *Jeřábek, J., **Zumr, D.**, Dostál, T., Tenreiro, T. R., Vaverková M.D., & Strauss, P. (2021). The effects of management practices and fires on soil water dynamics at three locations across Europe. 2021 IEEE International Workshop on Metrology for Agriculture and Forestry. https://doi.org/10.1109/MetroAgriFor52389.2021.9628785*

  Numerical modelling exercise to quantify the impact of various soil management practices (namely conventional tillage, conservation tillage, no-till, mulching, and prescribed fires) on soil hydraulic characteristics. The aim was to analyze the effects of management practices on water infiltration and surface runoff dynamics.

- *Laburda, T., Krása, J., **Zumr, D.**, Devátý, J., Vrána, M., Zambon, N., Johannsen, L. L., Klik, A., Strauss P., & Dostál, T. (2021). SfM-MVS Photogrammetry for Splash Erosion Monitoring under Natural Rainfall. Earth Surface Processes and Landforms, 46(5).*

  The follow-up of the manuscript of Zumr et al. (2020) which concentrates on the surface changes caused by a rainfall. The surface was analyzed with the use of close-range photogrammetry. We were able to measure the degree of soil compaction during the events and show that soil properties decide on the consolidation regime.

- *Li, T., Jeřábek, J., Winkler, J., Vaverková, M.D. & **Zumr, D.** (2022). Effects of prescribed fire on topsoil properties: a small-scale straw burning experiment. Journal of hydrology and hydromechanics, 70(4), 450-461. , 46(5). doi: 10.2478/johh-2022-0032*

  Hydrological analysis of the impact of a small-scale wildfire on a seasonal soil profile water regime. The analysis is based on a field experiment and monitoring of the temporal changes of the physical and hydrological properties of the topsoil. The monitoring was complemented by the vegetation recovery survey. The results show that the fire plot infiltration capacity was increased and the soil water content was higher than the control plot throughout the year, providing suitable habitat for colonizing vegetation. The results suggest that small-scale controlled biomass burning can be risk-free for the soil ecosystem and may even temporarily improve the hydraulic properties of the upper soil layer.

water

MDPI

Article

Estimates of Tillage and Rainfall Effects on Unsaturated Hydraulic Conductivity in a Small Central European Agricultural Catchment

David Zumr *, Jakub Jeřábek, Vladimír Klípa, Michal Dohnal and Michal Sněhota

Faculty of Civil Engineering, Czech Technical University in Prague, Thákurova 7, 166 29 Prague 6, Czech Republic; jakub.jerabek@fsv.cvut.cz (J.J.); vladimir.klipa@fsv.cvut.cz (V.K.); michal.dohnal@cvut.cz (M.D.); michal.snehota@fsv.cvut.cz (M.S.)

* Correspondence: david.zumr@fsv.cvut.cz

Received: 29 December 2018; Accepted: 29 March 2019; Published: 10 April 2019

Abstract: In arable land, topsoil is exposed to structural changes during each growing season due to agricultural management, climate, the kinetic energy of rainfall, crop and root growth. The shape, size, and spatial distributions of soil aggregates are considerably altered during the season and thus affect water infiltration and the soil moisture regime. Agricultural topsoils are prone to soil compaction and surface sealing which result in soil structure degradation and disconnection of preferential pathways. To study topsoil infiltration properties over time, near-saturated hydraulic conductivity of topsoil was repeatedly assessed in a catchment in central Bohemia (Czech Republic) during three consecutive growing seasons, using a recently developed automated tension minidisk infiltrometer (MultiDisk). Seasonal variability of soil bulk density and saturated water content was observed as topsoil consolidated between seedbed preparations. Topsoil unsaturated hydraulic conductivity was lower in spring and increased in the summer months during two seasons, and the opposite trend was observed during one season. Temporal unsaturated hydraulic conductivity variability was higher than spatial variability. Cumulative kinetic energy of rainfall, causing a seasonal decrease in soil macroporosity and unsaturated hydraulic conductivity, was not a statistically significant predictor.

Keywords: soil structure; soil aggregates; topsoil; rainfall kinetic energy; soil water retention curve; unsaturated hydraulic conductivity; tension infiltration experiment

1. Introduction

The spatial arrangement of soil aggregates significantly affects the process of water infiltration and the subsequent moisture regime of the soil profile. In arable land, the soil is exposed to rapid structural changes, both abrupt and continuous, within each growing season due to agrotechnical practices [1], quick crop and root growth [2], soil biota and climatic conditions [3,4]. Agricultural soils are prone to soil compaction and soil structure degradation, depending strongly on the intensity of agricultural production, fertilization, cover crops, tillage, and harvesting technologies [5].

Soil cultivation causes specific topsoil conditions. Soil aggregates on the surface after tillage are rather large, the topsoil is loose, the soil surface is rough and free of vegetation (see, for example, the review by Strudley et al. [4]) and the soil has a lower bulk density, higher macroporosity, high pore connectivity and high saturated hydraulic conductivity [6]. However, this state is mechanically unstable. Intense rainfall can initiate splash erosion [7] wherein fine soil particles are detached and translocated from aggregates and clog the large elongated voids connecting the surface to the soil profile. Rainfall with high kinetic energy over a recently tilled soil, therefore, often results in topsoil compaction and soil crusting [8,9], and the topsoil quickly consolidates. This consolidation caused by

rainfall propagates a soil profile. Rousseva et al. [10] measured the soil macroporosity of a loamy soil profile during rainfall events and detected a decrease in macroporosity down to a depth of 6 cm below the soil surface. Moreover, soil exposure to rainfall and the subsequent destruction of soil aggregates lead to further soil degradation, resulting in higher emissions of soil carbon dioxide [11] and increased soil erosion [12,13].

The splash erosion and structural changes in topsoil are, among other factors, influenced by the kinetic energy of rainfall [14]. Rainfall kinetic energy (KE) is a quantity dependent on the raindrop's mass (drop size distribution) and velocity. This kinetic energy is usually estimated with empirical relationships which express kinetic energy as a function of rainfall intensity (KE-I) [15]. It has been shown that the KE-I relationship is tied to the specific climatic conditions of a given location [16,17].

Compacted soils with poor structure (lacking macropores) are usually considered unfavorable for crop growth due to low water infiltration into the root zone [18]. However, under unsaturated conditions, the size of the contact area between the neighboring aggregates is important for vertical water movement. Therefore soil consolidation often results in the increase of its infiltration capacity [19,20]. Soil with well-developed aggregates can be assessed by a dual-continuum system of two mutually communicating porous media: (a) preferential flow domain and (b) matrix flow domain [21]. The preferential flow domain is represented by large inter-aggregate voids, which create a well-connected network of hydraulically conductive pores and the matrix domain consists of much finer intra-aggregate micropores.

The structure of the micropore matrix is quite stable; on the contrary, macropores can easily be created or destroyed by tillage and soil compaction processes [22,23]. Preferential flow dominates during saturated and nearly saturated flow conditions, in which water percolates through the network of the preferential pathways bypassing the aggregates to the deep soil profile. Most natural rainfall in Central Europe is not sufficiently intense to create area-wide ponding on a tilled surface [24], leaving the large pores and voids between the aggregates drained. Water under unsaturated conditions flows only through the aggregates and via capillary bridges that are formed at the aggregates' contacts and in the close vicinity. Wetting front propagation is, therefore, slower than one would assume based on the value of the soil matrix hydraulic conductivity alone.

Unsaturated hydraulic conductivity is routinely measured in the field with tension infiltrometers. There are many different types of apparatus available for conducting tension infiltration experiments. Infiltrometers differ in measurement methods, levels of automation and infiltration disk diameters. Simple versions of disk infiltrometers require manual read-outs of the cumulative infiltration, which can be inefficient, especially in cases where experiments take a long time due to low hydraulic conductivity or when a large number of datasets is needed. Therefore, Ankeny et al. [25], Moret et al. [26] and Madsen and Chandler [27] among others, have suggested several automation techniques. Recently, Klipa et al. [28] developed an automatic mini-disk tension infiltrometer which can be used as a multi-point version of six coupled infiltrometers (MultiDisk).

The effect of soil consolidation on water flow has been studied at the scales of individual aggregates [19,20] to those in the vicinity of a root tip [29]. On the other hand, according to our knowledge, there are no field data on the seasonal variability of the unsaturated hydraulic conductivity that would show increased values with increasing soil compaction. An increasing trend of unsaturated hydraulic conductivity (pressure head of -3 cm) during vegetation season was observed by Logsdon et al. [30], but the increase was attributed to the soil swelling, not to topsoil consolidation. Hu et al. [31] did not observe any significant temporal changes in hydraulic conductivity (K) from near saturation up to pressure heads of -15 cm across sites with different land-use. Decreasing unsaturated hydraulic conductivity measured during a growing season, specifically with the pressure head set between -4 and -6 cm, were presented by [32,33], for example. Statistically non-significant temporal variability of unsaturated hydraulic conductivity overshadowed by spatial variation was also reported [34,35].

Somaratne and Smettem [36] reported that the unsaturated hydraulic conductivity for a pressure head of -4 cm was constant at the beginning of the growing season, decreased in July and remained

constant until the time of harvest. It was concluded that fine soil particles, detached due to the impact of raindrops, blocked pores from conducting water under a pressure head of −4 cm. Decreases in topsoil hydraulic conductivity after an artificial rainfall experiment, compared to conditions before the experiment, observed a pressure head of −2 cm. No significant decrease of unsaturated hydraulic conductivity for a pressure head of −4 cm was observed after the experiment, suggesting that only the pores larger than 0.75 mm consolidated [36].

The purposes of this study were threefold. Firstly, it aimed to introduce the automatic multi-point tension infiltrometer (MultiDisk) based on the automation technique of Klipa et al. [28] and to use the MultiDisk for the measurement of near-saturated hydraulic conductivity across a period of three years. Secondly, it aimed to observe the temporal variability of unsaturated topsoil hydraulic conductivity during the vegetation season and test whether the changes could be attributed to the rainfall kinetic energy. Thirdly, it aimed to study the impact of soil cultivation on soil hydraulic properties.

2. Materials and Methods

2.1. Study Area

The infiltration experiments were carried out on plots located in the Nučice experimental catchment (Figure 1). This catchment is situated in a moderately hilly area of central Bohemia (Czech Republic), 30 km east of Prague (approximate closing profile position 49°57′49.230″ N, 14°52′13.242″ E). The catchment area is 0.531 km^2. More than 95% of the area is arable land, while the remainder includes watercourse, riparian trees and shrubs and paved roads. There are no forests, grasslands or urbanized areas. The Nučice catchment is drained by a narrow stream, which has been piped in the uppermost part [37]. The average altitude is 401 m a.s.l., the mean land slope is 3.9%, and the climate is humid continental. Based on the records from 1975 to 2015, the average annual precipitation is 630 mm, potential evapotranspiration ranges from 500 to 550 mm [38], and mean annual air temperature is 7.9 °C [24]. Precipitation and temperature data were recorded in 5 min intervals and the distance between the tipping-bucket rain gauge and the infiltration plots was approximately 300 m (Figure 1).

The arable land is cultivated down to the stream banks, and conservation tillage has been practiced since 2000. Compact disk harrows and cultivators are employed, and the maximum disturbance of the soil profile due to tillage operations reaches 16 cm. The constant parallel traffic lines with a span of 8 m are maintained using a GPS guidance system. The standard crop rotation includes winter wheat (*Triticum aestivum* L.), rapeseed (*Brassica napus*), summer oats (*Avena sativa)* and mustard (*Sinapis alba* L.) (Table 1).

Since the establishment of the experimental catchment in 2011, we have been collecting undisturbed soil samples (100 cm^3) on a regular basis to study the temporal variability in topsoil physical properties. Soil cores are taken from the top 7 cm between the plants and analyzed by standard gravimetric methods to measure the bulk density, porosity, and hydraulic characteristics.

The soils are developed on conglomerates, which consist of sandstone and siltstone, and are classified according to the World Reference Base for Soil Resources as Haplic Luvisols and Cambisols, which are a USDA Soil Taxonomy quasi-equivalent to Alfisols and Inceptisols. Based on geophysical monitoring conducted in a close-by location, the bedrock emerges at depths of 15–20 m and the groundwater level is more than 2 m below the surface. On the basis of the standard laboratory particle size distribution analysis (a combination of the sieving and sedimentation hydrometer methods), the proportions of the textural classes were determined to be 9% clay, 58% silt, and 33% sand; the soil was classified as silty loam. The loamy Ap horizon (10–15 cm deep, C_{ox} of 1.1%) with well-developed soil aggregation is underlined by a silty and silty-clay Bt horizon with a compact structure. There is a clear divide between tilled topsoil and compacted subsoil, which was found at a depth of 14 ± 2 cm below the soil surface [39]. A single topsoil water retention curve was determined in the laboratory with use of a sand-box for the wet end and a pressure plate apparatus for the dry end. The soil hydraulic model of van Genuchten [40] was fit to the measured retention curve. These parameters were considered the

reference for further retention curve scaling in the region close to saturation. The van Genuchten's empirical parameters of the reference soil water retention curve of the topsoil were: $\alpha = 0.05$ cm^{-1} and $n = 1.25$.

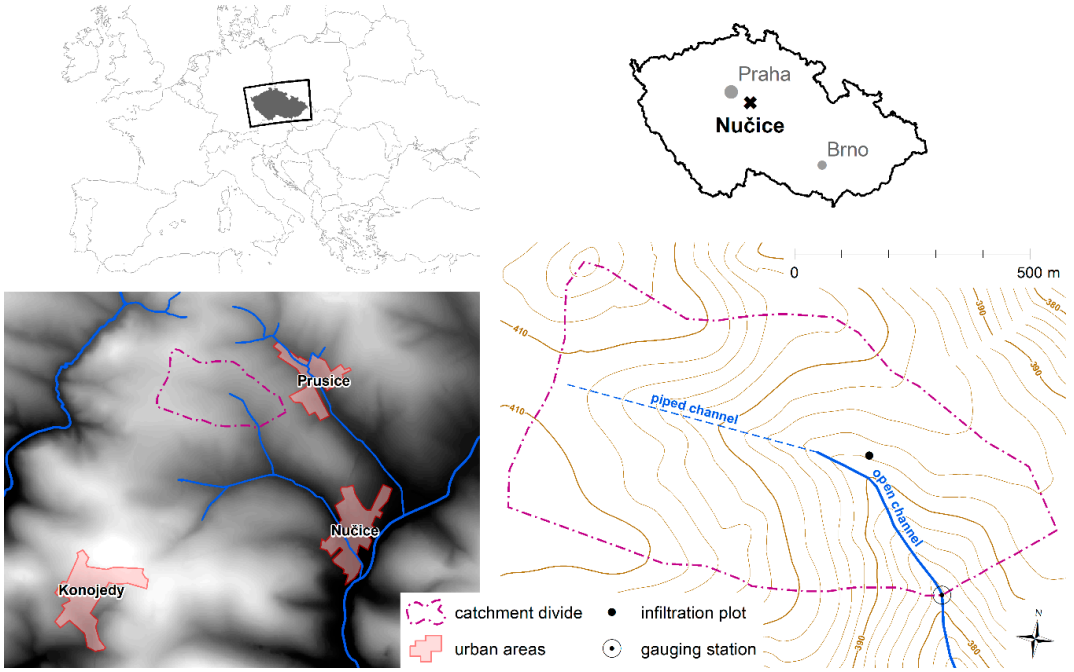

Figure 1. Geographic position and a map of the Nučice catchment.

Table 1. General overview of the agricultural activities and infiltration experiments (lines highlighted in grey), seedbed cultivation (s.c.) is marked in the Notes column.

Date	Crop	Agricultural Activity	Notes
October 2012		stubble breaking	depth 10–12 cm (s.c.)
6 April 2013		fertilization	nitrogen fertilizer
22 April 2013		Tension infiltration experiments—IE1	
27 April 2013	naked oat	sowing	chisel plowing, depth 14 cm (s.c.)
17 May 2013	naked oat	crop-spraying	herbicide
1 July 2013	naked oat	crop-spraying	fungicide and herbicide
25 July 2013	naked oat	Tension infiltration experiments—IE2	
17 August 2013	naked oat	harvest	
19 August 2013		stubble breaking	depth 10–12 cm (s.c.)
10 September 2013		crop-spraying	herbicide and insecticide
25 September 2013	winter wheat	sowing, fertilization	chisel plowing—depth 14 cm, combined fertilizer
4 October 2013	winter wheat	Tension infiltration experiments—IE3	
10 October 2013	winter wheat	crop-spraying	herbicide and insecticide
20 February 2014	winter wheat	fertilization	nitrogen fertilizer
3 March 2014	winter wheat	fertilization	fertilizer containing sulfur
13 March 2014	winter wheat	Tension infiltration experiments—IE4	
17 March 2014	winter wheat	fertilization	nitrogen fertilizer
9 April 2014	winter wheat	fertilization	morphoregulators, fertilizers containing B, Cu, Mn, Mg
10 April 2014	winter wheat	Tension infiltration experiments—IE5	
22 April 2014	winter wheat	crop-spraying, fertilization	herbicide, fungicide, wetting agent, nitrogen fertilizer
15 May 2014	winter wheat	Tension infiltration experiments—IE6	
9 June 2014	winter wheat	crop-spraying	fungicide, insecticide, wetting agent
19 June 2014	winter wheat	Tension infiltration experiments—IE7	
17 July 2014	winter wheat	crop-spraying	herbicide

Table 1. *Cont.*

Date	Crop	Agricultural Activity	Notes
6 August 2014	winter wheat	Tension infiltration experiments—IE8	
9 August 2014	winter wheat	harvest	
10 August 2014		stubble breaking	depth 10–12 cm (s.c.)
24 September 2014		fertilization and plowing	manure, depth of plowing 22 cm
October 1 2014		Tension infiltration experiments—IE9	
3 November 2014		plowing	deepening to 25–28 cm (s.c.)
22 March 2015	white mustard	sowing, fertilization	chisel plowing—depth 14 cm, fertilizer (s.c.)
26 March 2015	white mustard	Tension infiltration experiments—IE10	
8 April 2015	white mustard	fertilization	fertilizer containing sulfur
25 April 2015	white mustard	crop-spraying, fertilization	herbicide, nitrogen fertilizer
12 May 2015	white mustard	crop-spaying, fertilization	fungicide, morphoregulator, fertilizer containing boron
12 May 2015	white mustard	Tension infiltration experiments—IE11	
6 June 2015	white mustard	crop-spaying, fertilization	fungicide, fertilizer containing boron and copper
2 July 2015	white mustard	Tension infiltration experiments—IE12	
30 July 2015	white mustard	Tension infiltration experiments—IE13	
3 August 2015	white mustard	harvest	

2.2. Infiltration Experiments

The infiltration experiments were carried out at the experimental site with the use of automatic minidisk infiltrometers (MultiDisk). All measurements were performed with a pressure head h_0 of -3 cm. The chosen pressure head represents the equivalent pore diameter of 1 mm, which ensures reliable elimination of preferential pathways for the soil in this study [41]. Thus, data collected during the infiltration experiments characterized flow in the soil matrix only. The reason for setting of h_0 to -3 cm was mainly practical. Lower values prolong the experiments considerably and a pressure head closer to saturation (e.g., -1 cm) would not avoid the large pores (as also mentioned by Bodner et al. [23]).

Thirteen regular infiltration campaigns (72 individual tension infiltration experiments, as six infiltrations were terminated due to technical problems) were conducted during the growing seasons from March 2013 until July 2015. Agricultural activities and associated crop life cycles are summarized in Table 1. In general, the agricultural practices envelop the complete life cycle from sowing, through harvest, to postharvest stubble breaking.

A single experimental plot with an approximate size of 5×5 m was selected in the experimental catchment (Figure 1) and repeatedly used for all measurement campaigns. The plot was situated on a gentle slope (incline below 1%) in the middle part of the hillslope and at least 2 m from the tractor wheel tracks. The infiltration rate was measured on barren surfaces and in the rows between the sown crops. The soil crust was removed, if present, to ensure a flat soil surface which is essential for the correct course of infiltration run. No more than three centimeters of soil were removed (depending on the actual soil roughness) to guarantee that the infiltration rate measurements were representative of the topsoil and not influenced by the different hydraulic properties of the thin soil surface crust, or by the compacted subsoil. The soil was manually leveled, and a very thin layer (ca. 1 mm) of dry fine quartz sand (grain composition 0.10–0.63 mm) was added to ensure hydraulic contact between the disk and the soil. The sand was moistened with a fine sprinkler immediately before infiltration.

Moreover, three undisturbed soil samples (volume of 100 cm^3) were taken before the infiltration experiment to determine the bulk density and the actual and saturated water content of the topsoil. Six smaller soil samples (volume of 26.5 cm^3) were taken directly below each infiltrometer of the MultiDisk immediately after the experiments. Samples were analyzed for soil bulk density, water content and saturated water content with standard gravimetric methods. The specific volume of the smaller soil samples was selected on the basis of extensive numerical modeling of infiltration from the MultiDisk to ensure homogeneity and representativeness of excavated soil volume for a wide variety of soil types.

Infiltrations started when the preparation of each location was finished and when infiltrometers were applied on contact sand layers. Termination criteria for individual experiments were as follows: (i) infiltration time exceeded two hours, (ii) water reservoir storage became empty, or (iii), an unavoidable circumstance occurred (rainfall event, sensor failure, operator error, etc.).

The experiments were performed with the use of a newly developed infiltration device. The automated multipoint minidisk infiltrometer, "MultiDisk", consists of six infiltrometer modules (see Figure 2) with stainless steel porous disks with a diameter of 4.45 cm and 3 mm thickness. The proposed device is automated using a high precision load cell with a mounted vertical bar which is immersed in water in the reservoir tube (with a maximum storage volume of 175 cm^3). The volume of infiltrated water is measured via changes of buoyant force acting on the vertical bar [28]. The output signal of the load cell is recalculated to the actual cumulative infiltration; cumulative infiltration data are directly fitted using the Philip equation [42], and unsaturated hydraulic conductivity is evaluated using the modified Zhang method [43,44].

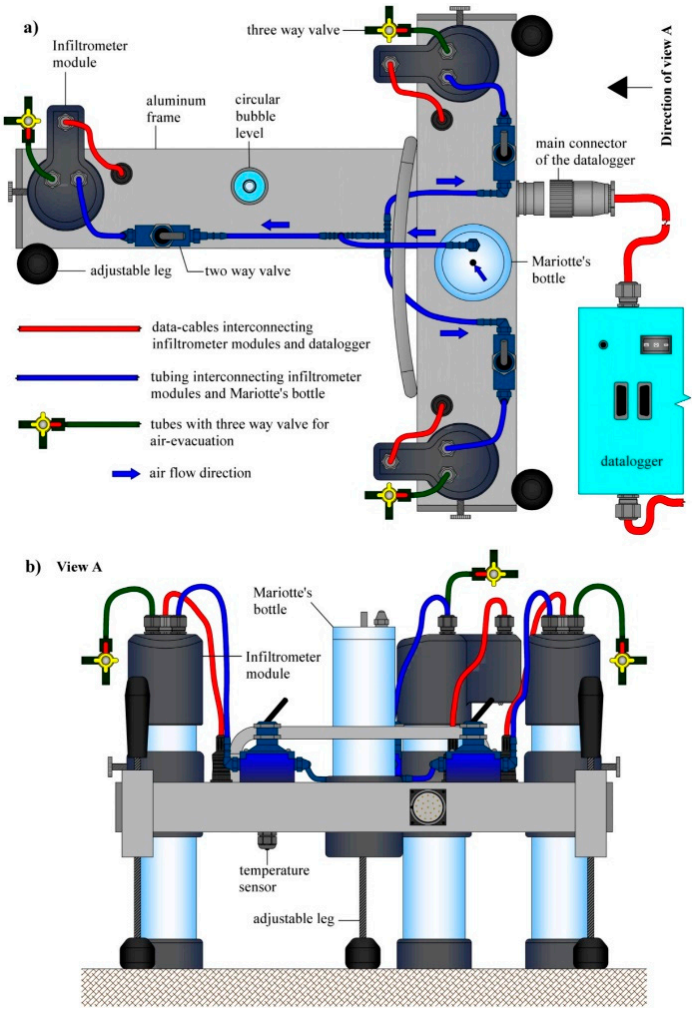

Figure 2. Scheme of one triplet of the MultiDisk infiltrometer modules held by an aluminum frame viewed, (**a**) from the top and (**b**) from the side (View A). Note that one apparatus-MultiDisk-consists of two identical triplets.

The automated multipoint minidisk tension infiltrometer (MultiDisk) consists of two separable identical aluminous frames and an enclosure containing the datalogger and battery. Each of the two frames is equipped with three infiltrometer modules and a single Mariotte bottle that allows for the application of a constant pressure head during the infiltration experiments. Figure 2 presents the

single frame with three infiltration modules in an operational configuration. Bisection of the MultiDisk allows the preparation of each part independently (see Figure 3) at different locations, while another advantage is the possibility of setting different degrees of pressure head for both triplets of infiltrometer modules, ranging from −0.5 cm to −6.0 cm. All MultiDisk's modules must have perfect hydraulic contact between the porous disc and soil surface. This can be achieved by leveling the frame into a ground plane using three leveling screws. The datalogger is placed in the transport box during the measurement.

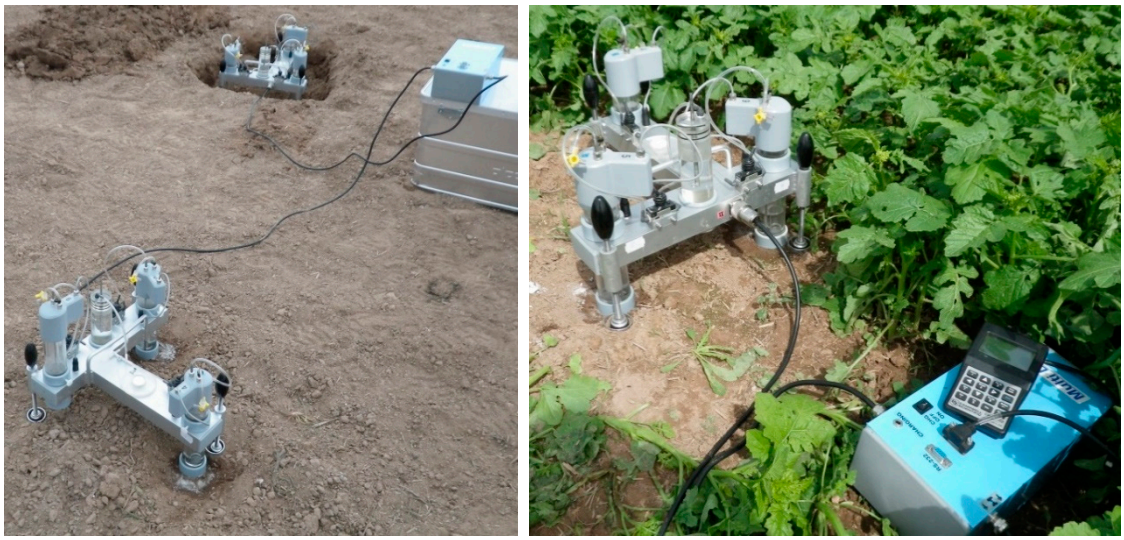

Figure 3. The MultiDisk infiltrometer performing an infiltration in the Nučice catchment.

2.3. Estimation of K in Soils with Changing Structure

In the present study, we assume that gradual topsoil consolidation (change of bulk density) induced by mechanical compression, stubble breaking, raindrop impacts etc. can be characterized by measured saturated water content. To prove the correlation between the bulk density and the saturated water content, we analyzed 217 undisturbed soil samples from the topsoil. The sampling was conducted during the growing seasons of 2013 and 2014. The samples, each with a volume of 100 cm^3, were collected from fields within the Nučice experimental catchment, no further than 400 m from the infiltration experiments.

We adopted the suggestion of Nimmo [45] who hypothesized that the pore size distribution and therefore the soil water retention curve varies due to agricultural practice predominantly in the region of large pores, i.e., low-pressure heads. This key hypothesis is also supported by the results of Ahuja et al. [46] who showed that tillage influences mainly larger pore-sizes and that the topsoil saturated water content increases after tillage. As the volume of the large pores in the topsoil varied for each infiltration experiment, we modified the retention curves accordingly. The modification was done based on the measured actual saturated water content.

Soil samples were taken after each infiltration experiment. Experiment-specific retention curves resulted from the fitting of resampled points to the reference retention curve across the range of pressure heads (−100 cm to −10,000 cm) and the measured saturated water content. The only optimized retention parameter was van Genuchten's empirical parameter α (cm^{-1}). Residual water content and empirical van Genuchten's parameter n, often associated with the pore size distribution (e.g., [47]) rather than changes in macroporosity, exhibited very low sensitivity to the θ_s variability and therefore remained fixed. Thus, experiment-specific retention curves were obtained for each infiltration experiment. For presentation, in Figure 4 the soil matrix parameters are scaled using scaling factors of pressure head and water content [48]. Scaling factors allow each of the experiment-specific retention

curves to be characterized by a unique set of scaling factors representing a single measurement campaign (IE1 to IE13, see Table 1).

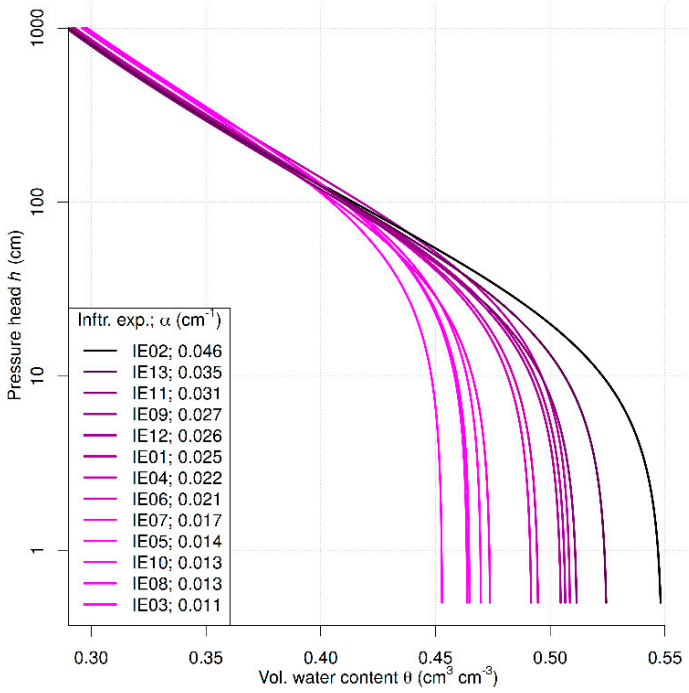

Figure 4. Scaled retention curves of fitted experiment-specific retention curves from individual infiltration campaigns.

Subsequently, we utilized the two parameter infiltration equation by Philip [42], which was originally derived for one-dimensional flow. The same equation with a different interpretation of coefficients was used for three-dimensional flow:

$$IC = C_1 t^{1/2} + C_2 t \tag{1}$$

where IC is the cumulative infiltration rate (m), t is time (s), and C_1 (m s$^{-1/2}$) and C_2 (m s^{-1}) are coefficients which can be determined by fitting Equation (1) to the measured infiltration data. Zhang suggested that hydraulic conductivity is dependent on the value of C_2, the van Genuchten's retention parameters n (-) and α (cm^{-1}), the disk pressure h_0 (m) and the radius of the infiltration disk r_0 (m) [43]. For near-saturated hydraulic conductivity and $n < 1.35$ [44] Equation (2) holds:

$$K_{h_0} = \frac{C_2(\alpha r_0)^{0.6}}{11.65(n^{0.82} - 1)\ \exp\left[34.65(n - 1.19)\alpha h_0\right]} \tag{2}$$

where K_{h0} (cm s^{-1}) is the unsaturated hydraulic conductivity corresponding to the pressure h_0. The set of experiment-specific retention curves allows for determination of experiment-specific near-saturated hydraulic conductivity, which reflects changing soil structure over time.

2.4. Rainfall Kinetic Energy Calculation

Measured rainfall intensity was used for the calculation of cumulative rainfall kinetic energy. Rainfall kinetic energy was calculated based on the empirical exponential expression [15]:

$$ke = 28.3(1 - 0.52\exp(-0.042i)) \tag{3}$$

where *ke* stands for kinetic energy per unit rainfall depth (J mm^{-1} m^{-2}) and *i* stands for rainfall intensity (mm h^{-1}). The cumulative kinetic energy, to which the surface was exposed, is based on the accumulated kinetic energy between two seedbed cultivations. It is assumed that after each seedbed cultivation, the topsoil pore size distribution recovers to its initial state. The cumulative kinetic energy is the sum of kinetic energies per unit rainfall height (Equation (3)) and corresponding rainfall intensities:

$$KE_n = \sum_{i=1}^{n} I_i ke_i \quad (4)$$

where KE_n (J m^{-2}) stands for kinetic energy the soil surface exposed to between 1st and *n*th rainfall record of a given period delineated by subsequent seedbed cultivations, I_i stands for the *i*th rainfall amount (mm) and ke_i stands for kinetic energy per unit of rainfall height of the *i*th rainfall record based on Equation (3). The seedbed cultivation dates are shown in the Table 1. The second infiltration measurement (IE2 in Table 1) was performed in the period when rainfall data was missing due to a power failure at the meteorological station. The last rainfall data were recorded seven days prior to the measurement.

3. Results

3.1. Temporal Variability of Bulk Density and Saturated Water Content

The dataset from the long-term topsoil physical characteristics monitoring shows large variability (Figure 5) with statistically significant dependence of bulk density on saturated water content, as the zero-slope hypothesis was rejected at the $\alpha = 0.05$ level of significance ($p < 0.0001$). In general, the saturated water content of the topsoil decreased with the increasing bulk density (as a result of the topsoil consolidation).

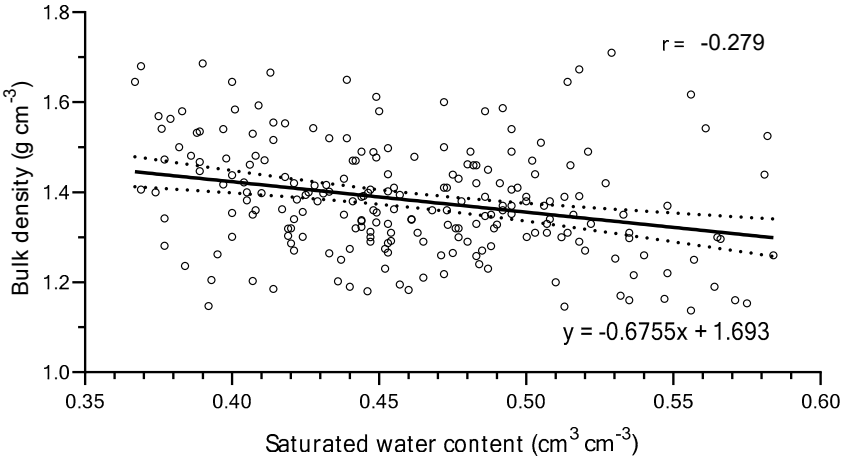

Figure 5. Saturated water content and bulk density as measured on 217 undisturbed topsoil samples during two growing seasons. The gray area represents the 95% confidence interval of the fitted line; *r* stands for correlation coefficient.

3.2. Tension Infiltration Experiments

The infiltration experiments were carried out during the vegetation season across various states of topsoil, various initial soil moisture conditions and different climatic conditions. The timing of the experiments is depicted in Figure 6 by symbols representing soil water content before and after each experiment. Initial soil water content ranged from 0.04 cm^3 cm^{-3} to 0.37 cm^3 cm^{-3}, with dry topsoil typically in June and July and wet topsoil in the spring and autumn. Measured saturated water content ranged from 0.46 cm^3 cm^{-3} to 0.55 cm^3 cm^{-3} with an average of 0.50 cm^3 cm^{-3}. The unsaturated water content temporal variability ranged between the saturated and initial water content variability,

with an average of 0.33 cm^3 cm^{-3}, minimum of 0.24 cm^3 cm^{-3} and maximum of 0.39 cm^3 cm^{-3}. The meteorological, hydropedological and infiltration data are published together with the manuscript as the Supplementary Materials.

Note the low water content and high air temperatures in July 2015, when the last infiltration experiments were performed. The summer of 2015 was characterized by exceptionally high temperatures and below average precipitation in Central Europe [49].

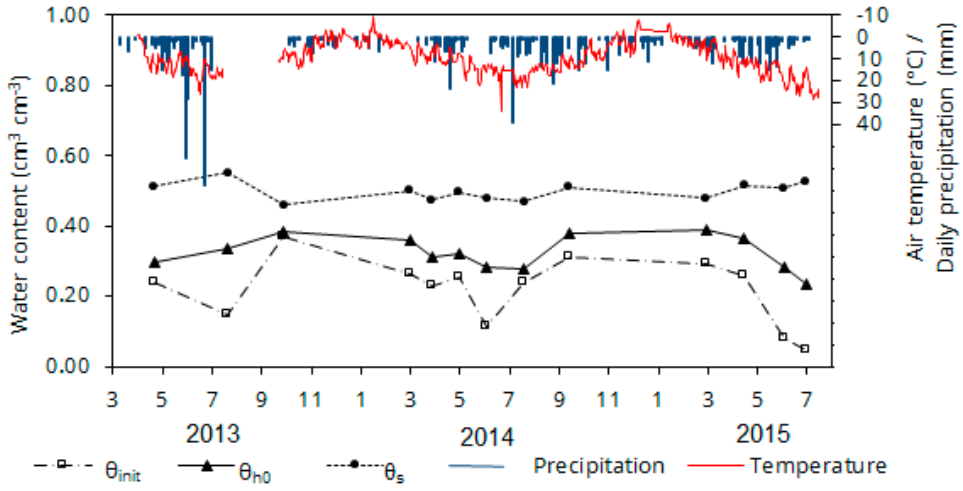

Figure 6. Meteorological and pedological conditions during experiments. Air temperature was measured at a height of 200 cm.

Observed unsaturated hydraulic conductivity (K_{h0}) during three growing seasons shows high temporal variability (Figure 7). The difference between the blue (K_{h0} calculated without retention curve scaling) and the green box-plots (K_{h0} calculated with retention curve scaling) varies for each infiltration experiment.

Unsaturated hydraulic conductivity was lowest in early spring and increased at the beginning of summer in the years 2013–2014. During the summer and autumn (2013–2014), the unsaturated hydraulic conductivity remained relatively unchanged. In contrast, results in the year 2015 showed the opposite trend—the highest hydraulic conductivity was observed in early spring and gradually decreased until the end of July. In 2015 the measured hydraulic conductivity was twice as high as previous seasons.

Differences in trends of unsaturated hydraulic conductivities in the years 2013–2014 and year 2015 were probably caused by different precipitation regimes (2013 and 2014 were average, 2015 was very dry), agricultural management and the timing of the first spring measurement. The first two infiltration experiments (IE1, IE2) in the year 2013 took place before the spring seedbed cultivation. In 2013 and 2015, plowing was conducted in the previous year, but the first measurement was performed a few days after seedbed preparation. In 2014, plowing and sowing were carried out in the previous year and the first infiltration experiment (IE4) was conducted after winter, into the sown soil. However, the exact impact of individual agricultural procedures was not fully apparent in the dataset.

Proportionality between the soil bulk density and hydraulic conductivity for three seasons (13 experiments) was not detected at the $\alpha = 0.05$ level of significance (Figure 7 and Table 2). The *t*-test did not show a significant non-zero slope for individual years either (Table 2). Measured unsaturated hydraulic conductivity was not dependent on initial soil water content, or on the saturated and quasi-saturated water content, with the exception of the year 2015 for the latter.

Table 2. *t*-test of the linear regressions assessing the relationship between unsaturated hydraulic conductivity at the −3 cm pressure head (K_{h0}) and bulk density (ρ_b), initial water content (θ_{init}), saturated water content (θ_s) and water content under the pressure head of −3 cm (θ_{h0}). *N* stands for number of data points, a for the slope and b for the interception.

Model	Time Period	N	Slope (a)	Slope *p*-Value
$K_{h0} = a\rho_b + b$	All	13	0.0021	0.69
	2013	3	0.0140	0.44
	2014	6	0.0008	0.81
	2015	4	0.0009	0.51
$K_{h0} = a\theta_{init} + b$	All	13	−0.0016	0.65
	2013	3	−0.0058	0.56
	2014	6	−0.0001	0.97
	2015	4	−0.0068	0.07
$K_{h0} = a\theta_s + b$	All	13	−0.0018	0.85
	2013	3	−0.025	0.50
	2014	6	−0.0051	0.38
	2015	4	−0.050	0.23
$K_{h0} = a\theta_{h0} + b$	All	13	0.007	0.32
	2013	3	0.004	0.86
	2014	6	0.0027	0.69
	2015	4	0.012	0.03

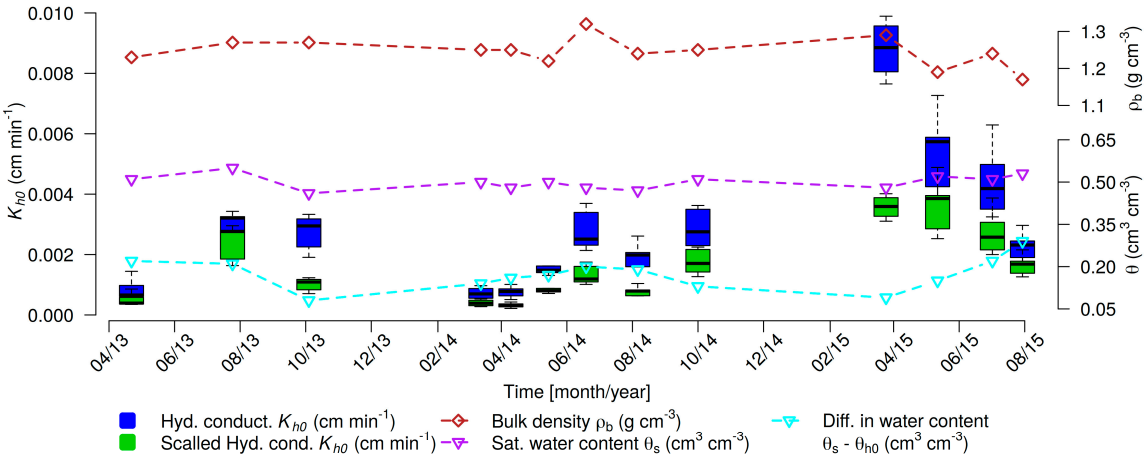

Figure 7. Seasonal variation of unsaturated hydraulic conductivity at the pressure head of −3 cm (blue boxes before retention curve scaling, green boxes after scaling). The bottom and top of the box are the first and third quartiles and the band inside the box represents the weighted average of K_{h0} weighted by inverse values of the RMSE. Ends of whiskers represent minimal and maximal values of K_{h0}. Dashed lines stand for bulk density, saturated water content and fraction of empty pores at the pressure head of −3 cm.

3.3. Effect of Rainfall on Unsaturated Hydraulic Conductivity

Development of the cumulative rainfall's kinetic energy during three monitored seasons is shown in Figures 8–10. It is assumed that each seedbed cultivation interrupts the topsoil consolidation effect of the previous rainfall period. In the years 2013 and 2015, seedbed cultivation was performed twice, once in spring (before sowing) and once in late summer (after the harvest). For the 2014 season, the winter wheat was previously sown at the end of 2013. During the winter of 2013–2014 the rainfall impact could have been reduced due to snow precipitation and snow cover, and this winter period was not taken into account.

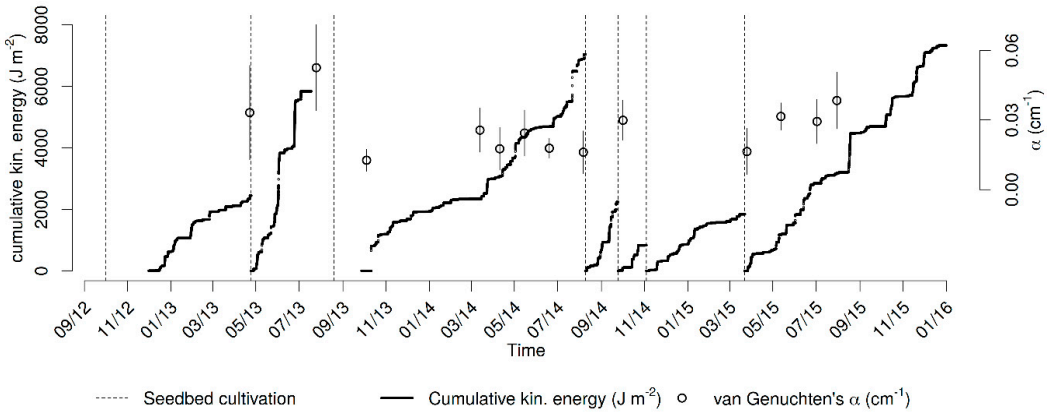

Figure 8. Seasonal variability of the van Genuchten's parameter α related to cumulative rainfall kinetic energy. Seedbed cultivation (dashed line) is assumed to interrupt the effect of the previous rainfall.

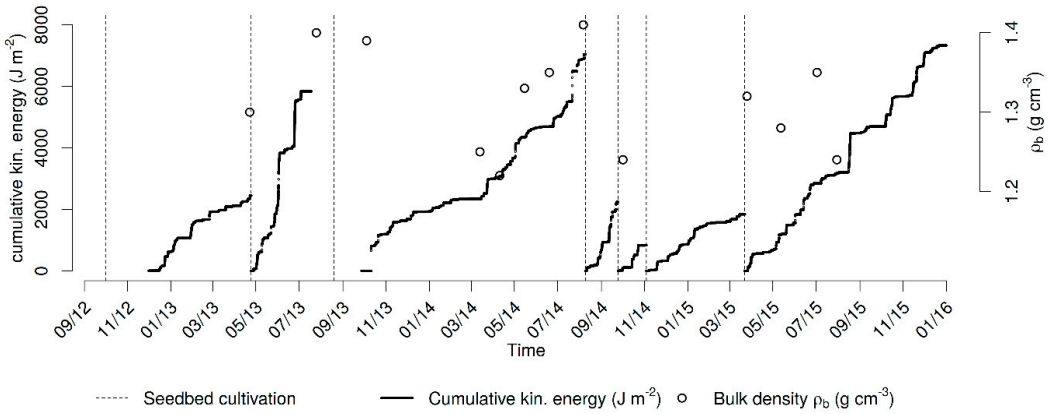

Figure 9. Seasonal variability of the bulk density (ρ_d) related to cumulative rainfall kinetic energy. Seedbed cultivation (dashed line) is assumed to interrupt the effect of the previous rainfall.

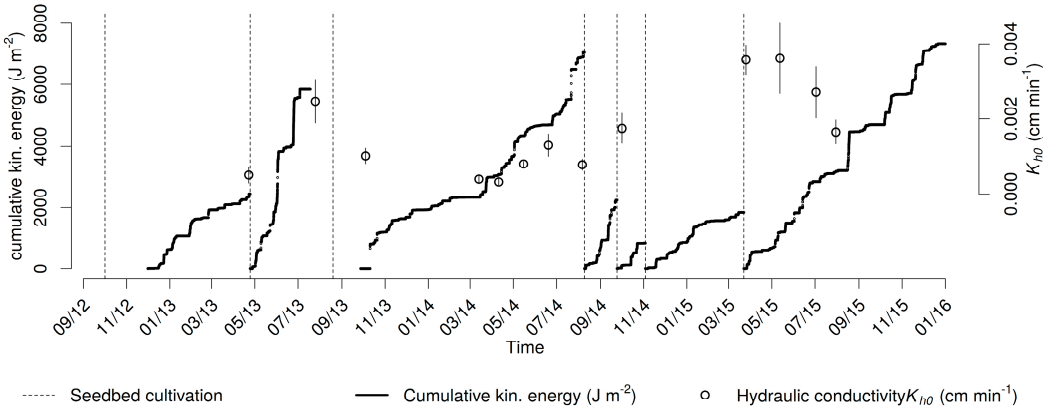

Figure 10. Seasonal variability of the scaled unsaturated hydraulic conductivity related to cumulative rainfall kinetic energy. Seedbed cultivation (dashed line) is assumed to interrupt the effect of the previous rainfall.

Linear regressions between cumulative kinetic energy KE, unsaturated hydraulic conductivity K_{h0}, van Genuchten's parameter α and bulk density ρ_b are shown in Figure 11. Hydraulic conductivity exhibited a negative correlation with the corresponding cumulative KE as shown in Figure 11A. In 2015, the negative trend was stronger compared to the overall trend as depicted by the trend line and the value of the correlation coefficient. In Figure 11B, the relationship between parameter α and the corresponding cumulative KE is shown, and the trend line exhibited a weak positive correlation. The trend, however, differs among the years. Although the data show an increase of α with cumulative

KE in 2013 and 2015, the trend in 2014 is the opposite. It has to be noted that α and hydraulic conductivity K_{h0} are not independent variables, as α is used to derive K_{h0}.

Bulk density was positively correlated with the cumulative KE (Figure 11C), with the only exception in 2013 where the data points corresponding to the lowest cumulative kinetic energy exhibited larger values. An increasing trend corresponds with the idea of gradual compaction between consecutive seedbed cultivations due to a complex set of factors including the impact of the rainfall. In Figure 11D, the trend between saturated water content and the corresponding cumulative KE is negative. A gradual increase of the topsoil saturated water content during the growing season is visible in all the years up to the cumulative kinetic energy of 3000 J m^{-2}, then the θ_s decreases. For our interpretation of the results, the changes in the saturated water content serve as a proxy for macroporosity.

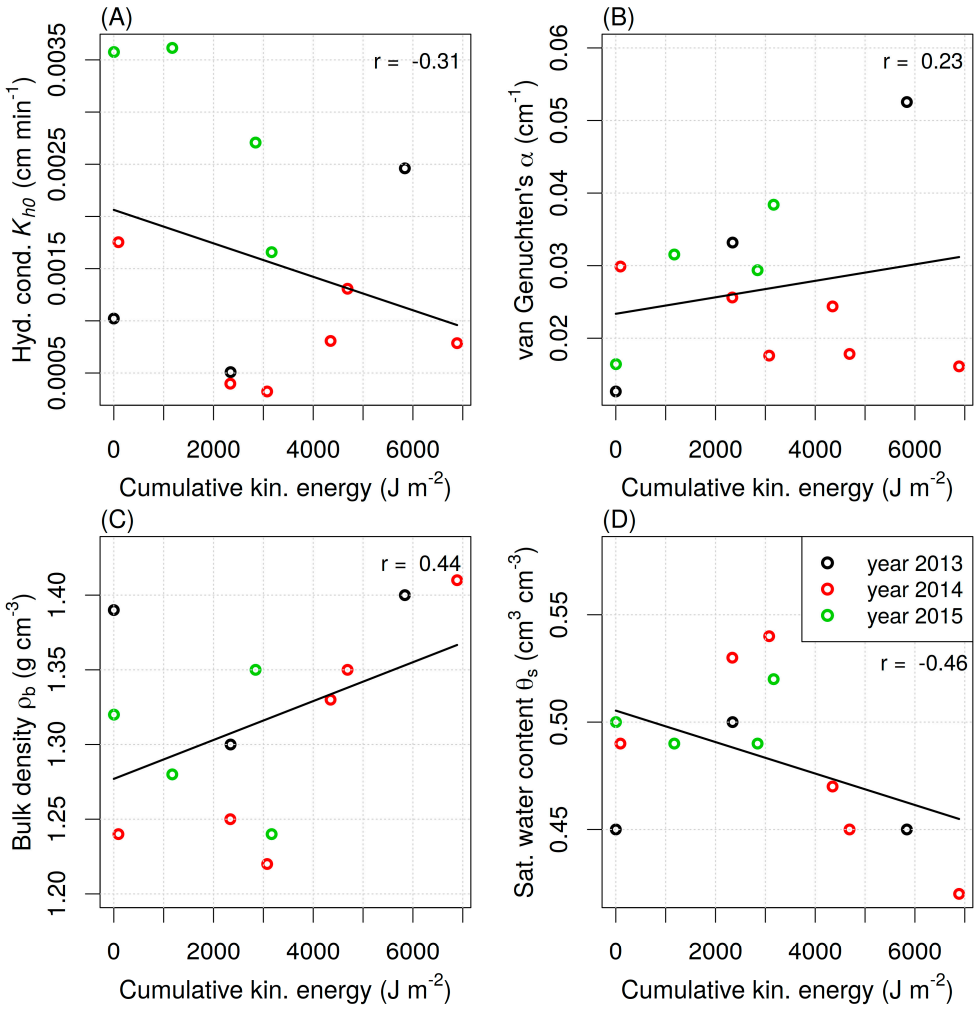

Figure 11. Correlation between cumulative rainfall kinetic energy and unsaturated hydraulic conductivity K_{h0} (**A**), van Genuchten's parameter α (**B**), bulk density ρ_b (**C**) and saturated water content θ_s (**D**). The correlation coefficient r is calculated based on all data points in each graph. The color, which distinguishes data from different years, only serves for visual interpretation of the data.

The dataset shown in Figure 11 was further tested to determine whether there was a significant linear relationship between the variables. Where the slope of the regression line is significantly different from zero, with the use of Student's t-test it is possible to conclude that there is a significant relationship. The results of the test are shown in the Table 3. Based on the test, the slope of all trend lines is not significantly different from zero. Only bulk density and saturated water content showed smaller p-values, however none reached the level of significance, 0.05.

Table 3. Results of statistical hypothesis testing using Student's *t*-test of the non-zero slope of the regression line between cumulative kinetic energy KE and soil physical properties: unsaturated hydraulic conductivity K_{h0}, van Genuchten's α, bulk density ρ_b and saturated water content θ_s. 13 data points were used for every test. The a stands for the slope and b for the interception.

Model	Slope (a)	Slope *p*-Value
K_{h0} = aKE + b	-1.602×10^{-7}	0.31
α = akE + b	1.135×10^{-6}	0.46
ρ_b = aKE + b	1.302×10^{-5}	0.13
θ_s = aKE + b	-7.329×10^{-6}	0.11

4. Discussion

4.1. Tension Infiltration Experiments

The key problems relating to the tension infiltration experiments are the long duration of a single infiltration and the high spatial variability of unsaturated hydraulic conductivity, as it is strongly dependent on actual pore geometry. The selection of an appropriate method for the given conditions and soils is important to obtain representative values of hydraulic conductivity [50]. We have shown that the use of the MultiDisk, consisting of two triplets with automated infiltration modules, is a very effective way to perform a large number of infiltration experiments. The obtained values of the unsaturated hydraulic conductivity were within the range of previously published results measured in agricultural tilled soils, e.g., [51–54].

The temporal variability of K_{h0} was approximately ten times higher than the spatial variability observed during each infiltration campaign (Figure 7). A similar conclusion was presented by Moret and Arrue [54] who observed a significant impact of tillage on soil hydrophysical properties in both short-term and seasonal scales, which outweighed the effects of spatial variability. The main driver of K_{h0} temporal variability on the tilled soil studied is attributed to the actual state of the topsoil structure; namely the macropores, mesopores and large inter-aggregate void proportion and connectivity changes, as also suggested by, for example, [10,41,55,56]. Additional explanations for the increase of the hydraulically active pores during the season are biological activity, carbon content, root growth, and wetting/drying cycles [57].

In 2013 and 2014, the K_{h0} was increasing as topsoil was consolidating after tillage, which is in agreement with other studies [57,58]. This trend suggests that the loose soil after tillage has a high proportion of larger inter-aggregate voids that decrease water flux during unsaturated conditions [20]. Also, high precipitation resulted in a higher soil water content throughout the seasons (compared to 2015) which was the driver for the slightly increasing K_{h0}. We can exclude the effect of the surface soil crusting; the crust, if present, was always removed before the experiments. The K_{h0} trend was different in 2015 when compared to the previous years. Surprisingly, in 2015 the K_{h0} increased throughout the season, and the measured K_{h0} values were significantly higher than in previous years. Similar trends were observed in previous studies, but usually due to the surface clogging or because lower suction pressure was applied during the infiltration [59]. Decreasing unsaturated hydraulic conductivity through the growing season has been reported as well due to clogging of pores by fine soil particles detached from aggregates by rainfall impact [36] or rainfall induced soil surface sealing [60]. The reason for the different outcome in our case is not clear; however, a possible explanation could lie in the specific weather conditions in 2015, which resulted in exceptionally dry topsoil conditions before the spring tillage and throughout the season. Soil moisture conditions and soil aeration affect the amount and properties of macropores [61]. Tillage of very dry soil could also lead to lower stability and differing sizes and arrangement of soil aggregates. The unstable soil aggregates could break down and regroup, even during tension infiltration, so that the fine particles fill the inter-aggregate voids. A high water pressure gradient due to very low initial soil moisture, caused rapid water fluxes and

probably resulted in a slightly overestimated K_{h0} for the experiments performed in July. Different year-on-year trends in hydraulic conductivity that cannot be easily explained were also observed by Jirku et al. [62].

Unfortunately, neither the soil aggregate stability nor imaging techniques to measure the macroporosity and pore connectivity were implemented. Therefore, the proposed explanation remains a hypothesis that cannot be proven with the available data. CT imaging, especially, would be a great asset, as similar studies have proved [59,63–65].

4.2. Temporal Variability of Physical Properties of the Soil

It is a known fact that tillage changes the topsoil characteristics, generally leading to a decrease in bulk soil density and an increase in the soil aggregate size and macroporosity. The soil aggregate arrangement is unstable, so the topsoil eventually reverts to its former state [3,46,66].

We observed an anticipated gradual increase in the topsoil bulk density and decrease in saturated water content after each seedbed preparation. Similar results with a comparable scale of temporal changes have already been published by, for example, [62,67,68].

None of the monitored soil physical characteristics were recognized as being the significant cause of the measured unsaturated hydraulic conductivity variability. As suggested by Sandin et al. [59], the reasons for K_{h0} temporal variability are complex and the pore connectivity and macroporosity also need to be evaluated. As Leij et al. [69] noted, the data on soil structural dynamics needed to propose a reliable model that would explain its effect on the water dynamics are still lacking.

4.3. Effect of Rainfall on Soil Water Regime

The impact of rainfall on topsoil consolidation and soil structure has been already studied, but rainfall kinetic energy is often missing from the rainfall properties tested. Detailed rainfall properties, including kinetic energy, are commonly analyzed in soil erosion studies, especially when evaluating splash erosion [70–72]. It has been shown that rainfall intensity and duration affect the degree of topsoil compaction (increase of bulk density and decrease of macroporosity) and surface seal formation [8,73]. The inverse relationship between rainfall event kinetic energy and saturated hydraulic conductivity has also been observed [74].

The analysis of our dataset did not show a significant relationship between the cumulative rainfall kinetic energy and monitored soil physical properties, but it needs to be emphasized that we did not evaluate the changes in the upper 1–3 cm, where the consolidation effects are stronger [10], and we did not evaluate the changes after every significant rainfall. Only during the 2014 season did we observe the expected relationship for bulk density (p-value of 0.0072) and saturated water content (p-value of 0.0068). Trends for the soil moisture retention curve and unsaturated hydraulic conductivity were not detected. The significant relationship can be partly explained by the high number and well-distributed timing of the infiltration experiments during 2014, so we were able to detect gradual changes between the seedbed preparations.

The measured data do not clearly show the variable seasonal gradient of alterations in the topsoil properties, which is mainly due to the limited number of infiltration experiments. In addition, the analysis considers kinetic energy of rainfall, but the kinetic energy of the raindrops hitting the soil surface is attenuated due to growing crops (oat, wheat, mustard) during the season, especially between May and July. Also, during this period, other factors such as roots and soil fauna strongly influence the soil water regime. One would expect that the largest changes would be detected after heavy rainfall events, especially when the soil surface is bare (spring and early summer). Bryk et al. [75] observed the largest soil structure alterations during spring under similar climate and soil conditions to ours, and they also did not find a statistically valid correlation with precipitation.

5. Conclusions

The newly developed, automated, multi-point infiltrometer (MultiDisk) was successfully used for long-term unsaturated hydraulic conductivity monitoring of intensively cultivated topsoil. The device proved to be reliable, with 72 out of 78 (over 90%) infiltration experiments recorded and analyzed successfully.

The topsoil K_{h0} varied during the growing season. K_{h0} had an increasing trend between the seedbed preparation and harvest in 2013 and 2014, but a decreasing trend was observed in 2015. We attribute this different outcome to the distinct climatic conditions in 2015, which resulted in very dry topsoil during most of the season. The temporal K_{h0} variability, within the single seasons and across the years, was higher than the spatial variability under the studied conditions. The topsoil bulk density and saturated soil water content changed as expected with the gradual topsoil consolidation during the growing season.

Based on the seasonal dataset we could not observe a statistically significant trend between topsoil physical characteristic changes and cumulative rainfall kinetic energy, nor between KE and K_{h0}. We assume that analysis performed on a single rainfall events basis could provide better results. Such a study requires K_{h0} monitoring after every significant rainfall event, which is very labor intensive in the field conditions but would be feasible to perform with the use of the multi-point automated MultiDisk. More detailed data could better explain how changes in topsoil hydraulic characteristics over time are the main drivers of the topsoil temporal variability. This information would be beneficial for detailed hydrological models that need to include topsoil temporal variability.

Supplementary Materials: The following are available online at http://www.mdpi.com/2073-4441/11/4/740/s1, Supplementary: the data on temporary variable soil physical properties measured within the infiltration experiments (bulk density, initial soil water content, saturated water content, K_{h0} and meteorological data (rainfall, rainfall kinetic energy).

Author Contributions: Conceptualization, D.Z. and M.D.; Formal analysis, J.J. and V.K.; Methodology, M.D. and M.S.; Project administration, D.Z.; Supervision, D.Z. and M.S.; Visualization, J.J.; Writing—original draft, D.Z.; Writing—review & editing, J.J., M.D. and M.S.

Funding: This research was performed within the project "Kinetic energy of rainfall as driving force of soil detachment and transport", jointly funded by The Czech Science Foundation (GACR), grant number GF17-33751L, and by the Austrian Science Fund (FWF), grant number I 3049. The automated multi-point mini-disk infiltrometer was developed in the framework of project no. TA01021844 funded by the Technology Agency of the Czech Republic. Additional funding was provided by the Grant Agency of the Czech Technical University in Prague, grant no. SGS18/122/OHK1/2T/11.

Acknowledgments: We thank our dear colleague Milena Cislerova who provided insight and expertise that greatly assisted the research.

Conflicts of Interest: The authors declare no conflicts of interest. The funders had no role in the design of the study; in the collection, analyses, or interpretation of data; in the writing of the manuscript, or in the decision to publish the results.

References

1. Pagliai, M.; Vignozzi, N.; Pellegrini, S. Soil structure and the effect of management practices. *Soil Tillage Res.* **2004**, *79*, 131–143. [CrossRef]
2. Angers, D.A.; Caron, J. Plant-induced changes in soil structure: Processes and feedbacks. *Biogeochemistry* **1998**, *42*, 55–72. [CrossRef]
3. Bronick, C.J.; Lal, R. Soil structure and management: A review. *Geoderma* **2005**, *124*, 3–22. [CrossRef]
4. Strudley, M.; Green, T.; Ascoughii, J. Tillage effects on soil hydraulic properties in space and time: State of the science. *Soil Tillage Res.* **2008**, *99*, 4–48. [CrossRef]
5. Horn, R.; Domżżał, H.; Słowińska-Jurkiewicz, A.; van Ouwerkerk, C. Soil compaction processes and their effects on the structure of arable soils and the environment. *Soil Tillage Res.* **1995**, *35*, 23–36. [CrossRef]
6. Schlüter, S.; Großmann, C.; Diel, J.; Wu, G.-M.; Tischer, S.; Deubel, A.; Rücknagel, J. Long-term effects of conventional and reduced tillage on soil structure, soil ecological and soil hydraulic properties. *Geoderma* **2018**, *332*, 10–19. [CrossRef]

7. Fernández-Raga, M.; Palencia, C.; Keesstra, S.; Jordán, A.; Fraile, R.; Angulo-Martínez, M.; Cerdà, A. Splash erosion: A review with unanswered questions. *Earth-Sci. Rev.* **2017**, *171*, 463–477. [CrossRef]
8. Augeard, B.; Bresson, L.M.; Assouline, S.; Kao, C.; Vauclin, M. Dynamics of soil surface bulk density: Role of water table elevation and rainfall duration. *Soil Sci. Soc. Am. J.* **2008**, *72*, 412–423. [CrossRef]
9. Bresson, L.M.; Moran, C.J. Role of compaction versus aggregate disruption on slumping and shrinking of repacked hardsetting seedbeds. *Soil Sci.* **2003**, *168*, 585–594. [CrossRef]
10. Rousseva, S.; Torri, D.; Pagliai, M. Effect of rain on the macroporosity at the soil surface. *Eur. J. Soil Sci.* **2002**, *53*, 83–93. [CrossRef]
11. Novara, A.; Armstrong, A.; Gristina, L.; Semple, K.T.; Quinton, J.N. Effects of soil compaction, rain exposure and their interaction on soil carbon dioxide emission. *Earth Surf. Process. Landf.* **2012**, *37*, 994–999. [CrossRef]
12. Baartman, J.E.M.; Jetten, V.G.; Ritsema, C.J.; Vente, J. Exploring effects of rainfall intensity and duration on soil erosion at the catchment scale using openLISEM: Prado catchment, SE Spain. *Hydrol. Process.* **2012**, *26*, 1034–1049. [CrossRef]
13. Sharma, P.P.; Gupta, S.C.; Foster, G.R. Raindrop-induced soil detachment and sediment transport from interrill areas. *Soil Sci. Soc. Am. J.* **1995**, *59*, 727–734. [CrossRef]
14. Wilken, F.; Baur, M.; Sommer, M.; Deumlich, D.; Bens, O.; Fiener, P. Uncertainties in rainfall kinetic energy-intensity relations for soil erosion modelling. *Catena* **2018**, *171*, 234–244. [CrossRef]
15. Van Dijk, A.I.J.; Bruijnzeel, L.; Rosewell, C. Rainfall intensity–kinetic energy relationships: A critical literature appraisal. *J. Hydrol.* **2002**, *261*, 1–23. [CrossRef]
16. Angulo-Martínez, M.; Beguería, S.; Kyselý, J. Use of disdrometer data to evaluate the relationship of rainfall kinetic energy and intensity (KE-I). *Sci. Total Environ.* **2016**, *568*, 83–94. [CrossRef]
17. Lobo, G.P.; Bonilla, C.A. Effect of temporal resolution on rainfall erosivity estimates in zones of precipitation caused by frontal systems. *Catena* **2015**, *135*, 202–207. [CrossRef]
18. Hamza, M.A.; Anderson, W.K. Soil compaction in cropping systems. *Soil Tillage Res.* **2005**, *82*, 121–145. [CrossRef]
19. Carminati, A.; Kaestner, A.; Hassanein, R.; Ippisch, O.; Vontobel, P.; Flühler, H. Infiltration through series of soil aggregates: Neutron radiography and modeling. *Adv. Water Resour.* **2007**, *30*, 1168–1178. [CrossRef]
20. Berli, M.; Carminati, A.; Ghezzehei, T.A.; Or, D. Evolution of unsaturated hydraulic conductivity of aggregated soils due to compressive forces. *Water Resour. Res.* **2008**, *44*. [CrossRef]
21. Gerke, H.H. Preferential flow descriptions for structured soils. *J. Plant Nutr. Soil Sci.* **2006**, *169*, 382–400. [CrossRef]
22. Kribaa, M.; Hallaire, V.; Curmi, P.; Lahmar, R. Effect of various cultivation methods on the structure and hydraulic properties of a soil in a semi-arid climate. *Soil Tillage Res.* **2001**, *60*, 43–53. [CrossRef]
23. Bodner, G.; Scholl, P.; Loiskandl, W.; Kaul, H.-P. Environmental and management influences on temporal variability of near saturated soil hydraulic properties. *Geoderma* **2013**, *204–205*, 120–129. [CrossRef]
24. Zumr, D.; Dostál, T.; Devátý, J. Identification of prevailing storm runoff generation mechanisms in an intensively cultivated catchment. *J. Hydrol. Hydromech.* **2015**, *63*, 246–254. [CrossRef]
25. Ankeny, M.D.; Kaspar, T.C.; Horton, R. Design for an automated tension infiltrometer. *Soil Sci. Soc. Am. J.* **1988**, *52*, 893–896. [CrossRef]
26. Moret, D.; López, M.V.; Arrúe, J.L. TDR application for automated water level measurement from Mariotte reservoirs in tension disc infiltrometers. *J. Hydrol.* **2004**, *297*, 229–235. [CrossRef]
27. Madsen, M.D.; Chandler, D.G. Automation and use of mini disk infiltrometers. *Soil Sci. Soc. Am. J.* **2007**, *71*, 1469–1472. [CrossRef]
28. Klípa, V.; Sněhota, M.; Dohnal, M. New automatic minidisk infiltrometer: Design and testing. *J. Hydrol. Hydromech.* **2015**, *63*, 110–116. [CrossRef]
29. Aravena, J.E.; Berli, M.; Ghezzehei, T.A.; Tyler, S.W. Effects of root-induced compaction on rhizosphere hydraulic properties—X-ray microtomography imaging and numerical simulations. *Environ. Sci. Technol.* **2011**, *45*, 425–431. [CrossRef]
30. Logsdon, S.D.; Jordahl, J.L.; Karlen, D.L. Tillage and crop effects on ponded and tension infiltration rates. *Soil Tillage Res.* **1993**, *28*, 179–189. [CrossRef]
31. Hu, W.; Shao, M.; Wang, Q.; Fan, J.; Horton, R. Temporal changes of soil hydraulic properties under different land uses. *Geoderma* **2009**, *149*, 355–366. [CrossRef]

32. Messing, I.; Jarvis, N.J. Temporal variation in the hydraulic conductivity of a tilled clay soil as measured by tension infiltrometers. *J. Soil Sci.* **1993**, *44*, 11–24. [CrossRef]
33. Farkas, C.; Gyuricza, C.; Birkás, M. Seasonal changes of hydraulic properties of a Chromic Luvisol under different soil management. *Biologia* **2006**, *61*, S344–S348. [CrossRef]
34. Bormann, H.; Klaassen, K. Seasonal and land use dependent variability of soil hydraulic and soil hydrological properties of two Northern German soils. *Geoderma* **2008**, *145*, 295–302. [CrossRef]
35. Alletto, L.; Coquet, Y. Temporal and spatial variability of soil bulk density and near-saturated hydraulic conductivity under two contrasted tillage management systems. *Geoderma* **2009**, *152*, 85–94. [CrossRef]
36. Somaratne, N.M.; Smettem, K.R.J. Effect of cultivation and raindrop impact on the surface hydraulic properties of an Alfisol under wheat. *Soil Tillage Res.* **1993**, *26*, 115–125. [CrossRef]
37. Zumr, D.; Dostál, T.; Devátý, J.; Valenta, P.; Rosendorf, P.; Eder, A.; Strauss, P. Experimental determination of the flood wave transformation and the sediment resuspension in a small regulated stream in an agricultural catchment. *Hydrol. Earth Syst. Sci.* **2017**, *21*. [CrossRef]
38. Hanel, M.; Mrkvičková, M.; Máca, P.; Vizina, A.; Pech, P. Evaluation of simple statistical downscaling methods for monthly regional climate model simulations with respect to the estimated changes in runoff in the Czech Republic. *Water Resour. Manag.* **2013**, *27*, 5261–5279. [CrossRef]
39. Jeřábek, J.; Zumr, D.; Dostál, T. Identifying the plough pan position on cultivated soils by measurements of electrical resistivity and penetration resistance. *Soil Tillage Res.* **2017**, *174*, 231–240. [CrossRef]
40. Van Genuchten, M.T. A closed-form equation for predicting the hydraulic conductivity of unsaturated soils. *Soil Sci. Soc. Am. J.* **1980**, *44*, 892–898. [CrossRef]
41. Kodešová, R.; Jirků, V.; Kodeš, V.; Mühlhanselová, M.; Nikodem, A.; Žigová, A. Soil structure and soil hydraulic properties of Haplic Luvisol used as arable land and grassland. *Soil Tillage Res.* **2011**, *111*, 154–161. [CrossRef]
42. Philip, J.R. The theory of infiltration, 1. The infiltration equation and its solution. *Soil Sci.* **1957**, *83*, 345–357. [CrossRef]
43. Zhang, R. Determination of soil sorptivity and hydraulic conductivity from the disk infiltrometer. *Soil Sci. Soc. Am. J.* **1997**, *61*, 1024–1030. [CrossRef]
44. Dohnal, M.; Dusek, J.; Vogel, T. Improving hydraulic conductivity estimates from minidisk infiltrometer measurements for soils with wide pore-size distributions. *Soil Sci. Soc. Am. J.* **2010**, *74*, 804–811. [CrossRef]
45. Nimmo, J.R. Modeling structural influences on soil water retention. *Soil Sci. Soc. Am. J.* **1997**, *61*, 712–719. [CrossRef]
46. Ahuja, L.R.; Fiedler, F.; Dunn, G.H.; Benjamin, J.G.; Garrison, A. Changes in soil water retention curves due to tillage and natural reconsolidation. *Soil Sci. Soc. Am. J.* **1998**, *62*, 1228–1233. [CrossRef]
47. Ghezzehei, T.A.; Kneafsey, T.J.; Su, G.W. Correspondence of the Gardner and van Genuchten-Mualem relative permeability function parameters. *Water Resour. Res.* **2007**, *43*. [CrossRef]
48. Vogel, T.; Cislerova, M.; Hopmans, J.W. Porous media with linearly variable hydraulic properties. *Water Resour. Res.* **1991**, *27*, 2735–2741. [CrossRef]
49. Ionita, M.; Tallaksen, L.M.; Kingston, D.G.; Stagge, J.H.; Laaha, G.; Van Lanen, H.A.J.; Scholz, P.; Chelcea, S.M.; Haslinger, K. The European 2015 drought from a climatological perspective. *Hydrol. Earth Syst. Sci.* **2017**, *21*, 1397–1419. [CrossRef]
50. Bagarello, V.; Iovino, M.; Tusa, G. Factors affecting measurement of the near-saturated soil hydraulic conductivity. *Soil Sci. Soc. Am. J.* **2000**, *64*, 1203–1210. [CrossRef]
51. Das Gupta, S.; Mohanty, B.P.; Köhne, J.M. Soil hydraulic conductivities and their spatial and temporal variations in a vertisol. *Soil Sci. Soc. Am. J.* **2006**, *70*, 1872–1881. [CrossRef]
52. Mohanty, B.P.; Ankeny, M.D.; Horton, R.; Kanwar, R.S. Spatial analysis of hydraulic conductivity measured using disc infiltrometers. *Water Resour. Res.* **1994**, *30*, 2489–2498. [CrossRef]
53. Lin, H.S.; McInnes, K.J.; Wilding, L.P.; Hallmark, C.T. Low tension water flow in structured soils. *Can. J. Soil Sci.* **1997**, *77*, 649–654. [CrossRef]
54. Moret, D.; Arrúe, J.L. Dynamics of soil hydraulic properties during fallow as affected by tillage. *Soil Tillage Res.* **2007**, *96*, 103–113. [CrossRef]
55. Chandrasekhar, P.; Kreiselmeier, J.; Schwen, A.; Weninger, T.; Julich, S.; Feger, K.-H.; Schwärzel, K.; Chandrasekhar, P.; Kreiselmeier, J.; Schwen, A.; et al. Why we should include soil structural dynamics of agricultural soils in hydrological models. *Water* **2018**, *10*, 1862. [CrossRef]

56. Logsdon, S.D.; Jaynes, D.B. Methodology for determining hydraulic conductivity with tension infiltrometers. *Soil Sci. Soc. Am. J.* **1993**, *57*, 1426–1431. [CrossRef]
57. Schwen, A.; Bodner, G.; Scholl, P.; Buchan, G.D.; Loiskandl, W. Temporal dynamics of soil hydraulic properties and the water-conducting porosity under different tillage. *Soil Tillage Res.* **2011**, *113*, 89–98. [CrossRef]
58. Zhang, Z.; Lin, L.; Wang, Y.; Peng, X. Temporal change in soil macropores measured using tension infiltrometer under different land uses and slope positions in subtropical China. *J. Soils Sediments* **2016**, *16*, 854–863. [CrossRef]
59. Sandin, M.; Koestel, J.; Jarvis, N.; Larsbo, M. Post-tillage evolution of structural pore space and saturated and near-saturated hydraulic conductivity in a clay loam soil. *Soil Tillage Res.* **2017**, *165*, 161–168. [CrossRef]
60. Armenise, E.; Simmons, R.W.; Ahn, S.; Garbout, A.; Doerr, S.H.; Mooney, S.J.; Sturrock, C.J.; Ritz, K. Soil seal development under simulated rainfall: Structural, physical and hydrological dynamics. *J. Hydrol.* **2018**, *556*, 211–219. [CrossRef]
61. Josa, R.; Gorchs, G.; Ginovart, M.; Solé-Benet, A. Influence of tillage on soil macropore size, shape of top layer and crop development in a sub-humid environment. *Biologia* **2013**, *68*, 1099–1103. [CrossRef]
62. Jirků, V.; Kodešová, R.; Nikodem, A.; Mühlhanselová, M.; Žigová, A. Temporal variability of structure and hydraulic properties of topsoil of three soil types. *Geoderma* **2013**, *204–205*, 43–58. [CrossRef]
63. Katuwal, S.; Norgaard, T.; Moldrup, P.; Lamandé, M.; Wildenschild, D.; de Jonge, L.W. Linking air and water transport in intact soils to macropore characteristics inferred from X-ray computed tomography. *Geoderma* **2015**, *237–238*, 9–20. [CrossRef]
64. Fohrer, N.; Berkenhagen, J.; Hecker, J.-M.; Rudolph, A. Changing soil and surface conditions during rainfall. *Catena* **1999**, *37*, 355–375. [CrossRef]
65. Rabot, E.; Wiesmeier, M.; Schlüter, S.; Vogel, H.-J. Soil structure as an indicator of soil functions: A review. *Geoderma* **2018**, *314*, 122–137. [CrossRef]
66. Sandin, M.; Jarvis, N.; Larsbo, M. Consolidation and surface sealing of nine harrowed Swedish soils. *Soil Tillage Res.* **2018**, *181*, 82–92. [CrossRef]
67. Angulo-Jaramillo, R.; Thony, J.L.; Vachaud, G.; Moreno, F.; Fernandez-Boy, E.; Cayuela, J.A.; Clothier, B.E. Seasonal variation of hydraulic properties of soils measured using a tension disk infiltrometer. *Soil Sci. Soc. Am. J.* **1997**, *61*, 27–32. [CrossRef]
68. Linh, T.B.; Ghyselinck, T.; Khanh, T.H.; Van Dung, T.; Guong, V.T.; Van Khoa, L.; Cornelis, W. Temporal variation of hydro-physical properties of paddy clay soil under different rice-based cropping systems. *L. Degrad. Dev.* **2017**, *28*, 1752–1762. [CrossRef]
69. Leij, F.J.; Ghezzehei, T.A.; Or, D. Modeling the dynamics of the soil pore-size distribution. *Soil Tillage Res.* **2002**, *64*, 61–78. [CrossRef]
70. Vaezi, A.R.; Ahmadi, M.; Cerdà, A. Contribution of raindrop impact to the change of soil physical properties and water erosion under semi-arid rainfalls. *Sci. Total Environ.* **2017**, *583*, 382–392. [CrossRef]
71. Angulo-Martínez, M.; Beguería, S.; Navas, A.; Machín, J. Splash erosion under natural rainfall on three soil types in NE Spain. *Geomorphology* **2012**, *175–176*, 38–44. [CrossRef]
72. Salles, C.; Poesen, J. Rain properties controlling soil splash detachment. *Hydrol. Process.* **2000**, *14*, 271–282. [CrossRef]
73. Assouline, S.; Mualem, Y. Modeling the dynamics of seal formation and its effect on infiltration as related to soil and rainfall characteristics. *Water Resour. Res.* **1997**, *33*, 1527–1536. [CrossRef]
74. Torri, D.; Regüés, D.; Pellegrini, S.; Bazzoffi, P. Within-storm soil surface dynamics and erosive effects of rainstorms. *Catena* **1999**, *38*, 131–150. [CrossRef]
75. Bryk, M.; Kołodziej, B.; Słowińska-Jurkiewicz, A.; Jaroszuk-Sierocińska, M. Evaluation of soil structure and physical properties influenced by weather conditions during autumn-winter-spring season. *Soil Tillage Res.* **2017**, *170*, 66–76. [CrossRef]

sustainability

MDPI

Article

Experimental Setup for Splash Erosion Monitoring—Study of Silty Loam Splash Characteristics

David Zumr [1,*], Danilo Vítor Mützenberg [1], Martin Neumann [1], Jakub Jeřábek [1], Tomáš Laburda [1], Petr Kavka [1], Lisbeth Lolk Johannsen [2], Nives Zambon [2], Andreas Klik [2], Peter Strauss [3] and Tomáš Dostál [1]

1 Faculty of Civil Engineering, Czech Technical University in Prague, Thákurova 7, 166 29 Prague 6, Czech Republic; danilo.mutz@gmail.com (D.V.M.); martin.neumann@fsv.cvut.cz (M.N.); jakub.jerabek@fsv.cvut.cz (J.J.); tomas.laburda@fsv.cvut.cz (T.L.); petr.kavka@fsv.cvut.cz (P.K.); dostal@fsv.cvut.cz (T.D.)

2 Institute for Soil Physics and Rural Water Management, University of Natural Resources and Life Sciences, 1190 Vienna, Austria; lisbeth.johannsen@boku.ac.at (L.L.J.); nives.zambon@boku.ac.at (N.Z.); andreas.klik@boku.ac.at (A.K.)

3 Federal Agency for Water Management, Institute for Land & Water Management Research, 3252 Petzenkirchen, Austria; peter.strauss@baw.at

* Correspondence: david.zumr@fsv.cvut.cz

Received: 21 November 2019; Accepted: 22 December 2019; Published: 24 December 2019

Abstract: An experimental laboratory setup was developed and evaluated in order to investigate detachment of soil particles by raindrop splash impact. The soil under investigation was a silty loam Cambisol, which is typical for agricultural fields in Central Europe. The setup consisted of a rainfall simulator and soil samples packed into splash cups (a plastic cylinder with a surface area of 78.5 cm^2) positioned in the center of sediment collectors with an outer diameter of 45 cm. A laboratory rainfall simulator was used to simulate rainfall with a prescribed intensity and kinetic energy. Photographs of the soil's surface before and after the experiments were taken to create digital models of relief and to calculate changes in surface roughness and the rate of soil compaction. The corresponding amount of splashed soil ranged between 10 and 1500 g m^{-2} h^{-1}. We observed a linear relationship between the rainfall kinetic energy and the amount of the detached soil particles. The threshold kinetic energy necessary to initiate the detachment process was 354 J m^{-2} h^{-1}. No significant relationship between rainfall kinetic energy and splashed sediment particle-size distribution was observed. The splash erosion process exhibited high variability within each repetition, suggesting a sensitivity of the process to the actual soil surface microtopography.

Keywords: splash erosion; rainfall simulator; splash cup; soil loss; soil detachment; disdrometer; rainfall kinetic energy

1. Introduction

The initial stage of the erosion process (splash erosion) occurs when raindrops with high kinetic energy hit bare soil, breaking down aggregates and detaching soil particles. Such particles are translocated a short distance from the raindrop's impact and they then settle on the soil's surface and block the interaggregate pores reducing the topsoil's infiltration capacity and accelerating the formation of surface runoff. Hence, understanding the relationships between various rainfall characteristics and splash erosion is important to be able to predict the dominant runoff mechanisms of unprotected soils and to determine the rainfall kinetic energy threshold for erosion initiation.

Various monitoring techniques have been developed over the years to measure the degree of soil detachment in relation to the kinetic energy of raindrops. Besides splash cups (which are used

in this study), splash boards or tracers have also been used in previous studies (as reviewed by Fernández-Raga et al. [1]). When monitoring splash erosion, there are several considerations to take into account when developing study design:

(A) collection mechanism:

- detached soil is splashed into a collector located around the soil sample (e.g., [2], Figure 1a)
- detached soil is splashed into a collector surrounded by the soil material (e.g., [3–5], Figure 1b)

(B) sample preparation:

- disturbed soil sample (e.g., [6,7])
- in situ undisturbed soil (e.g., [2–4]).

Each approach has its advantages and disadvantages. One needs to estimate the contributing area of the surrounding soil (Figure 1b), otherwise it is not possible to calculate the detached soil amount per specific area. This problem occurs (to some extent) in the Morgan setup [2] because some soil particles are transported within the sampling area (Figure 1a). Therefore, the optimum sampling area is a tradeoff between underestimating the splash, representativeness of the collected sample, as well as ease of sample handling [3].

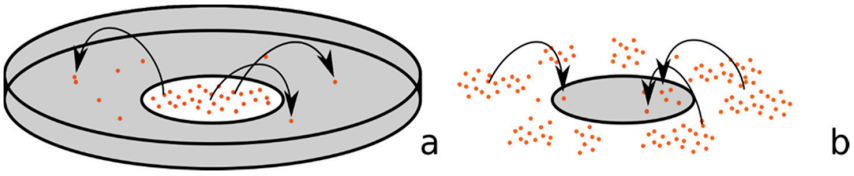

Figure 1. Two methods to collect detached soil particles: (**a**) collector is around the soil sample; (**b**) collector is surrounded by the sampled soil.

Wei et al. [8] showed that the splash erosion rate is dependent on soil sample water saturation and texture. Sandy soil was not sensitive to degree of saturation whereas samples with increasing clay content were, and similar results were reported by Khaledi Darvishan et al. [9]. To the contrary, Watung et al. [10] did not observe any significant difference in soil splash under variable saturated conditions for tropical soil (Oxisol). Utilizing disturbed soil samples allows for the control of soil sample conditions. In situ measurement on undisturbed samples does not allow for the control of soil conditions; on the other hand the measurement may be more representative for a given location since soil structure and soil surface characteristics are preserved. Therefore, there are a lot of factors to consider when designing an experimental setup.

The splash-collecting device needs to have sufficient dimensions to trap most of the detached particles. As Leogun et al. [11] and Marzen et al. [12] showed, the amount of detached soil decreases exponentially with increasing distance from the soil sample. The transport splash distance increases with decreasing soil particle size. Fu et al. [13] added that the splashed distance is not only related to particle or aggregate sizes, but also to rainfall kinetic energy.

Transport distances ranged between 10 cm and 20 cm for aggregates with diameters between 0.5 mm and 1 mm and up to 35 cm for soil aggregates with diameters from 0.05 mm to 0.5 mm in a study by Legout et al. [11]. Most of the splashed particles were observed within 20 cm from the soil sample in Fu et al. [14] and within 35 cm in [12].

The most common problem with splash erosion experiments is that it is difficult to compare results across studies due to each author's differing experimental setup [15]. Many different splash cup setups with various sizes and trapping principles have been used to measure splash erosion. Pioneering studies were performed using single soil fractions and cylindrically shaped cups [16–18]. Kinnell [6] added a thin external ring around the soil sample to exclude surface runoff which may

occur during ponding conditions. Scholten et al. [7] developed splash cups in which sample saturation was controlled, their setup maintained nearly constant water content of the sample, and allowed for the simultaneous draining of rainfall. Two types of splash cups (cups and funnels) were compared by Fernández-Raga et al. [4]. The funnels collected systematically more particles because they prevent particle transport back to the surrounding soil (backsplash). The most frequently used splash cup design is inspired by Morgan (1981) (for example, [9,19–22]). In all studies reported above, the sediment loss was determined by weighing the dry sample prior to and after the measurement period. The Morgan setup is also suitable for use in both indoor and outdoor conditions with disturbed or undisturbed soil samples.

In general, the splash erosion process is very complex and the reported results usually exhibit high variability. Angulo-Martinez et al. [23] evaluated the effects of rainfall characteristics, rainfall erosivity index and soil type with a linear mixed-effects model. The rainfall erosivity index explained 55% of the data variability but soil type did not have a statistically significant influence on erosion. Up to 74% of the variability within a single soil type was attributed to random effects. The role of slope (and upward/downward splash) and rainfall intensity were investigated. It was reported that slope altered the splashed particle-size distribution and the role of slope for total splashed material varied for various rainfall intensities [22]. The rainfall itself is also a very important factor, and authors emphasize the need of accurate drop-shape estimation in order to obtain adequate kinetic energy of the rainfall. Rainfall changes the surface microtopography [24] which may have further effects on water infiltration, surface water retention and surface runoff [25]. A common method for the analysis of surface relief changes is close-range photogrammetry [26]. It has been shown that especially loose soils are prone to a fast decrease in microrelief roughness, leading to accelerated soil erosion [27,28].

Rainfall kinetic energy (KE) is often estimated based on measured rainfall intensity (KE-I relationship) due to the lack of a direct rainfall kinetic energy measurement [29]. Lobo and Monilla [30] tested several KE-I relationships for various geographical locations and concluded that parameters of the KE-I relationships are site specific. Meshesa et al. [31] tested parametric relationships between rainfall intensity and rainfall kinetic energy using artificial rainfall, noting that artificial rainfall exhibits raindrops with different sizes than natural rainfall. Therefore, KE-I relationships derived under natural conditions should not be applied to rainfall simulators.

The relationship between the rainfall kinetic energy and the amount of splash erosion on a bare surface varies for different soil types and tillage practices. Most of the studies of splash erosion on real soils come from arid or semi-arid climates, such as the Mediterranean region, Loess Plateau of China or southern states of the USA [1]. In Central Europe, soil erosion processes have been studied extensively, but splash erosion has not usually been considered or evaluated. Rainfall in Central Europe often does not generate overland flow (due to low intensity and/or short duration), but soil detachment and resulting soil surface changes take place from the impact of first drops with sufficient kinetic energy [32]. The lack of knowledge of splash erosion rates on agriculturally cultivated Cambisols is the main motivation for the presented research.

In this study we present a splash erosion experimental setup which utilizes techniques from previously published works. We utilize the Morgan design and provide an open-source, easy to manufacture splash cup. The objective of these experiments is to determine the impact of rainfall kinetic energy on splash detachment for a typical agricultural soil in Central Europe. An associated aim is to evaluate the particle-size distribution of the eroded material and to analyze the effects of the rainfall kinetic energy on soil consolidation.

2. Materials and Methods

2.1. Splash Erosion Collection Device

The monitoring setup is designed for both indoor and outdoor measurements and is similar to the system proposed by Morgan [2].

The monitoring device includes (Figure 2): (1) the sediment collector, (2) the cylindric splash cup, (3) the photogrammetry reference targets, (4) the LED illumination ring, (5) the outlet for the sediment collection and (6) the splash cup holder. The sizes and proportions of the device components and the angle between the rim of the splash cup and the collector were adjusted to capture the maximum amount of splashed soil while allowing unchanged raindrop impact on the soil sample.

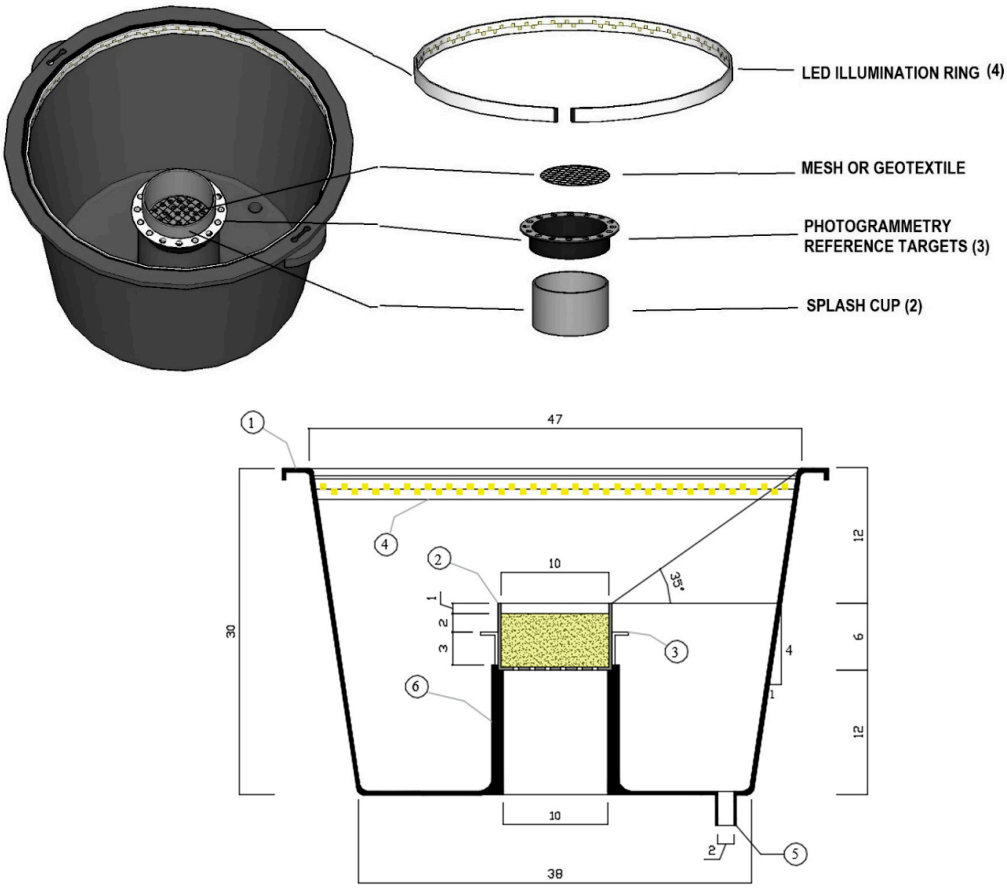

Figure 2. Splash erosion device and its parts and dimensions (units in centimeters).

The splash cup (2 in Figure 2) consists of a polypropylene cylinder with a height of 60 mm, inner diameter of 100 mm and a surface area of 7854 mm^2. The cylinder's wall is 2.7 mm thick and the upper rim of the splash cup is sharpened. The bottom of the cup is perforated in order to allow for draining of percolated water. A fine mesh is placed in the bottom of the cup to prevent soil loss during manipulation and water percolation. Each tested soil is filled to one centimeter below the rim of the splash cup to prevent runoff in case of ponding water on the sample's surface. The sediment collector's purpose is to capture eroded (splashed) soil particles. Its walls are angled in order to funnel the water with soil particles to the outlet (5 in Figure 2) which leads to a storage bucket under the sediment collector. In the center, there is a holder (6 in Figure 2) which is used to support the splash cup above the sediment collector's base so that the soil sample is protected from the backsplash of soil particles that accumulate inside the collector. The holder does not have a bottom, therefore, water percolating through the soil sample can freely drip out. This water is not usually collected. The collector is made from a commercially available polypropylene bucket, and all the firmly attached components (the holder and the outlet) are butt welded to the collector. The CAD drawings of the splash cup's components as well as mounting procedure are freely available here: rain.fsv.cvut.cz/splashcup.

After every experiment, the detached particles still attached to the collector's walls or settled on the collector's bottom were washed into the outlet and added to the remaining eroded particles. The suspension of the collected sediment and rainfall water was then filtered, oven dried and weighed.

The splash erosion device was then prepared for photogrammetrical analysis of soil sample surface changes due to rainfall impact. Typically, 10 to 15 referenced photographs from different angles were taken for the successful reconstruction of a digital surface model. Therefore, around the splash cup there is a white ring with the photogrammetry reference targets (3 in Figure 2). An LED illumination ring (4 in Figure 3) was attached to the sediment collector to provide adequate illumination to ensure that there were no shadows on the surface. The specification of the LED light strip was: chromaticity 4250 K, power 12 W/m, 60 LEDs/m, luminous flux 1050 lm/m.

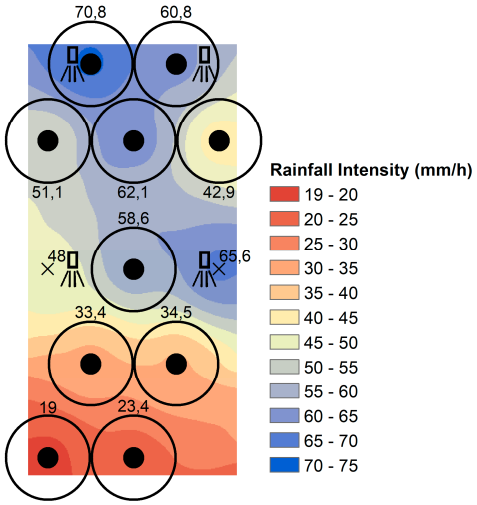

Figure 3. Sketch of the 10 fixed positions and the rainfall intensity distribution below the nozzles. The positions of four nozzles used in the experiment are depicted with a spray symbol, and the X marks denote additional positions where the rainfall intensity was also measured.

2.2. Soil Sample Preparation and Analysis

The soil used for testing of the splash collection system was taken from a topsoil horizon (upper 10 cm) of a cultivated field at the experimental site of Bykovice in Central Bohemia, Czech Republic. The soil type is classified as a Cambisol, and the texture corresponds to silty loam according to the World Reference Base (WRB) classification [33] (12.7% sand, 76.6% silt, 10.7% clay), $CaCO_3$ content is <0.92%, pH 6.9, and total organic carbon 1.7%.

Soil was collected in April 2017 during seedbed conditions. The soil was transported to the laboratory, stripped of large organic residues (stems, roots), large clods and stones, and then air dried.

Collected soil was sieved to remove particles and aggregates larger than 10 mm before filling the splash cup. A piece of permeable geotextile was placed inside the cup to prevent the soil from passing through the splash cup's perforations. The splash cup was then loosely packed with the same amount of prepared soil to reach a similar bulk density to that of seedbed conditions (0.83 g cm^{-3}). The soil sample was not compacted; we only distributed soil aggregates equally along the sample surface and removed any remaining organic residues. Then, the filled splash cups were placed inside the sediment collectors so that the splash cup's surface was level.

After each rainfall simulation the eroded soil particles were carefully washed out from the sediment collector, and the suspension of rain water and eroded sediment was transferred to the laboratory. The obtained sample was filtered on a paper filter with a mesh size of 5 mm, oven dried (at 40 °C) and weighed.

The dried soil was further analyzed using a laser diffraction particle-size analyzer (Mastersizer 3000, Malvern Panalytical Ltd., UK) to determine soil texture. We mixed the splashed material from all

the repetitions to obtain enough soil for this analysis. Each soil sample was dispersed in distilled water and placed into an ultrasonic bath for 320 s to disaggregate the soil. Then the sample was analyzed by the laser diffractometer. Measurements were repeated 25 times for every sample. The procedure is described in detail by Kubínová [34].

2.3. Rainfall Simulation

A laboratory Norton Ladder type rainfall simulator was used to generate rainfall. The simulator had an experimental area of 0.9 × 4 m. The rainfall was produced by eight oscillating nozzles, type Veejet 80100, which were mounted in two parallel sections at 2.6 m above the soil samples. Tap water was used, water pressure was set to 32 kPa and rainfall intensity was controlled by the nozzle oscillating frequency. The average raindrop diameter generated by the simulator was 2.3 mm according to monitoring with disdrometers [35].

In this experiment we took advantage of the fact that rainfall intensity spatially varies over the experimental plot. Eleven positions with the rainfall intensity between 20 and 70 mm h^{-1} were chosen for further testing. Figure 3 shows the spatial distribution of rainfall intensity. The pattern is based on the intensity measurements of the splash cup positions and inverse distance weighted interpolation. The rainfall kinetic energy was measured with the Laser Precipitation Monitor (LPM) by Thies Clima® and the KE-I relationship for the given rainfall simulator was established in advance of the splash erosion simulations. The rainfall simulation lasted 15 min, then the soil samples were collected and the splashed amount was analyzed. The whole procedure was repeated five times (totaling 55 samples analyzed).

3. Results and Discussion

The measured relationship between rainfall intensity and rainfall kinetic energy is shown in Figure 4. The observed trend of the KE-I is linear with the slope of 18.69. Compared to the published relationships for natural rainfall (e.g., [36–39]) the KE of the simulated rainfall is lower by approximately 35%. Similar results show that underestimation of the simulated rainfall kinetic energy were also obtained by Petrů and Kalibová [40]. The KE-I relationship is strongly dependent on the rainfall simulator design, nozzle types and water pressure (e.g., simulators generating larger raindrops than the natural rainfall overestimate KE) [31].

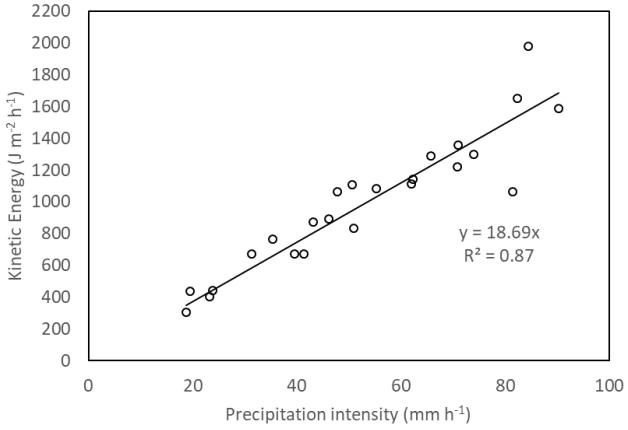

Figure 4. Measured relationship between simulated rainfall intensity and kinetic energy.

The measured soil splash rate ranged between 10 and 2012 g m^{-2} h^{-1} for rainfall kinetic energy between 380 and 1450 J m^2 h^{-1}. The threshold kinetic energy needed to initiate the detachment process was identified by extrapolation to be 354 J m^{-2} h^{-1}. The recorded mass of the detached particles exhibits large variability across the five replicates at each position (Figure 5). The variability

was higher for the positions where higher soil erosion was recorded (positions with higher rainfall intensity and kinetic energy). Similar variability during comparable experiments was reported in literature [23]. The variability could be explained by very complex soil erosion behavior which is influenced by size distribution and arrangement of the soil particles and aggregates on the sample's surface (random roughness).

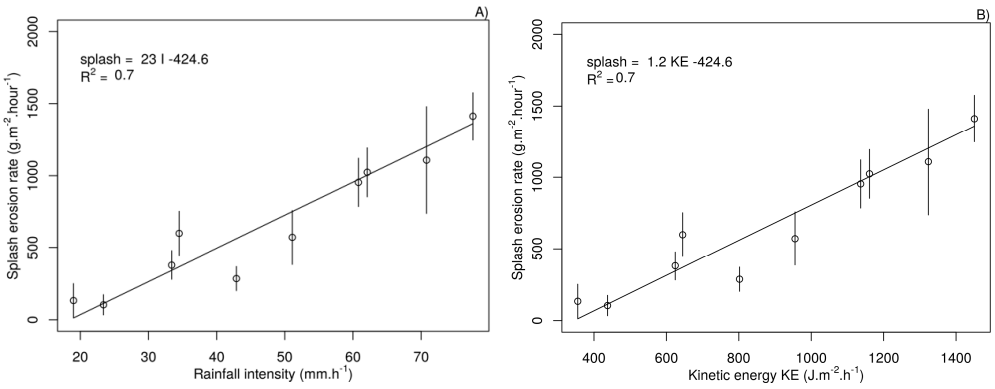

Figure 5. Relationships between rainfall intensity (**A**) and rainfall kinetic energy (**B**) and splash erosion rate. The bars stand for standard deviation, the marker denotes the mean value.

The overall relationship between the mass of the eroded particles and the rainfall kinetic energy has a linear trend (Figure 5). The coefficient of determination is 0.7 which is higher than or in a similar range as presented in comparable studies (e.g., [6,15,41]). Table 1 summarizes selected splash erosion experiments from the literature to show how the experiments vary in setup. They show similar, most often linear, relationships between the amount of detached soil particles and various rainfall characteristics. The slope of the linear trendline differs in each study because of differing experimental setups (rainfall duration, sample preparation) and soil properties [6,15,42]. Bisal [17] and Mazurak and Mosher [18] already experimentally showed that the splashed amount is linearly dependent on drop size and velocity. Surprisingly, in contrast to the more recently published studies, Bisal [17] did not find a significant relationship between rainfall intensity and the amount of sand splashed as long as no ponding occurred on the sand's surface.

Table 1. Comparison of the results with the published splash erosion studies.

Reference	Soil	Sample Preparation, Experiment Specifications	Rainfall Intensity (mm h^{-1})	Rainfall Kinetic Energy (J m^{-2} mm^{-1})	Splash–Rainfall Relationship
Bisal 1960 [17,18]	Sand	Leveled with the rim	76–152	-	No significant relationship (R^2 = 0.31)
Angulo-Martinez et al. 2012 [23]	Silty soil	Leveled 25 mm below the rim, under natural rainfall	12–93	2–12	Linear function
Geissler et al., 2012 [41]	Fine sand	Leveled with the rim; measured under forest vegetation where the throughfall's KE is reported as 2.53 times higher	1–45	-	Linear function (R^2 = 0.74)
Boroghani et al., 2012 [43]	Silt-clay-loam	Not known, only three datapoints measured	69–120	-	Linear function (R^2 = 0.91)
Wu et al., 2019 [44]	Silty loam, seedbed conditions	Leveled with the rim	48–150	4–7	Polynomial function
Fernández-Raga et al., 2019 [15]	Fine sand	Leveled to the rim	38–160	26–29	Linear function (R^2 = 0.18)
This study	Silty loam, seed bed conditions (Cambisol)	Leveled 10 mm below the rim	19–78	11	Linear function (R^2 = 0.70)

The observed splash–KE trendline is strongly influenced by duration of the rainfall experiment. Splash erosion varies over time, especially in the case of structured soils with developed aggregates that are initially broken down into smaller fractions by raindrops. It has been observed that the splash increases with decreasing aggregate size [45,46] and increasing event duration [47,48]. The fact that splash erosion is strongly dependent on surface microtopography is another reason why it is difficult to compare results across studies. Artificial samples filled with smooth, fine-grained sand produce different erosion than natural soils with higher surface roughness and particle cohesion. This is, as noted above, due to the smaller size of individual particles, but is also due to microrelief variation. The effect of surface roughness on splash erosion is not a straightforward process [49]. Some authors found decreasing erosion with increasing roughness [50], and some the opposite trend [49]. The changes in surface microrelief in one sample (applied kinetic energy of 1150 J m^{-2} h^{-1}, recorded average soil surface consolidation of 0.75 mm) is shown in Figure 6. The soil surface consolidated due to rainfall and splash erosion. Figure 7 shows the linear relationship between rainfall kinetic energy and soil consolidation even though the measured soil settling is very heterogeneous and the coefficient of determination is low.

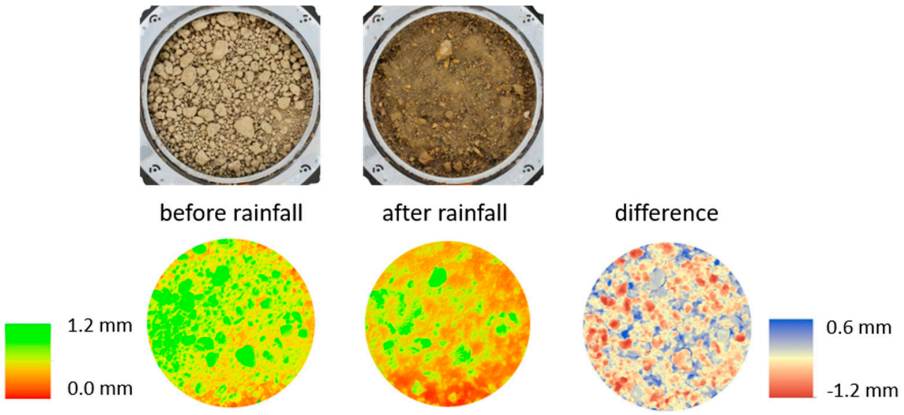

Figure 6. Soil sample surface before and after simulated rainfall. The lower photos represent digital surface models (DSM) in which green areas have higher elevation than the red areas. The soil surface consolidated in the average by 0.75 mm.

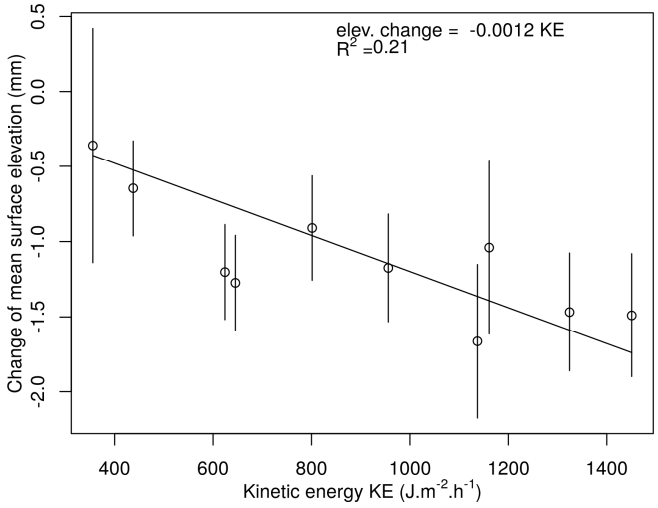

Figure 7. Relationship between rainfall kinetic energy and soil surface settling.

Analysis of the splashed material particle-size distribution (PSD) did not show a significant relationship between rainfall kinetic energy (KE) and detached sediment texture (Figure 8).

The Pearson's correlation coefficient of KE versus clay content was 0.36 (p-value 0.39, for a = 0.05), KE versus silt −0.22 (p-value 0.61) and KE versus sand −0.24 (p-value 0.56). The PSD of the detached sediment is not significantly different from the texture of the original soil sample (see the horizontal dashed lines on Figure 7). Therefore, all particle fractions are detached uniformly with no preference toward fine or coarse fractions, no matter the kinetic energy applied. It is important to note that the splashed sediment is usually detached in the form of aggregates and therefore the aggregate size distribution should be evaluated. We have not done this analysis as we were not able to collect the undisturbed splashed soil aggregates. For example, Fu et al. [13] show that especially the fine particle and aggregate (<0.053 mm) ratios change with variable rainfall KE. The KE per mm of rainfall is the same for all the measured points shown in Figure 8, which is due to the design of the rainfall simulator. The results may change if different types of the rainfall simulators (with various drop size distribution or drop velocities) are applied.

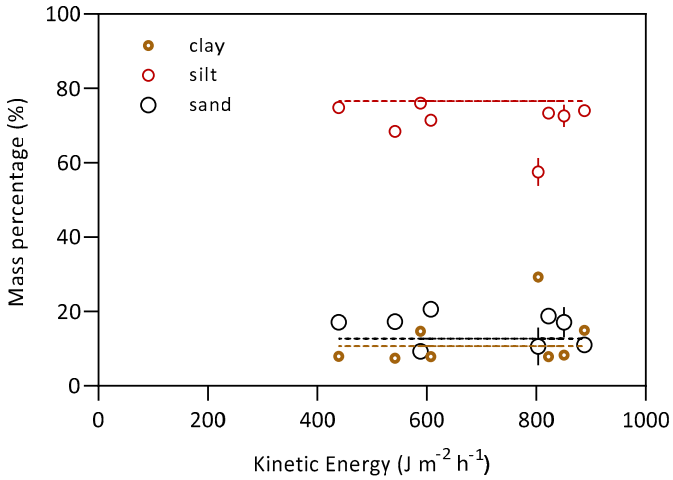

Figure 8. Relationship between rainfall kinetic energy and textural classes (clay, silt, sand) of detached sediment. The dashed lines represent the texture of the Bykovice soil. No significant difference between the soil sample and splashed sediment was observed.

Fernández-Raga et al. [15] demonstrated that splash erosion estimation is strongly dependent on the splash collection setup. Poesen and Torri [3] found that the area of the splash cup is the main influencer defining the amount splashed and therefore coefficients for different splash cup areas should be used. Even the trendline between the amount splashed and the rainfall kinetic energy differs based on the methodology of collection. The experimental design proposed in this study, a modified version of Morgan's splash cup, proved to be reliable, practical and easy to handle. As the splash cups are compact, light, and robust, they can be easily mounted to any support mechanism either in the laboratory and in the terrain. Due to the materials used, the device is durable and can be used for several seasons under field conditions. The soil sample can be packed separately from the collection tray and fixed to its position just before the rainfall experiment.

4. Conclusions

A splash cup methodology was presented and used to analyze splash erosion of a silty loam agricultural topsoil with simulated rainfall across various kinetic energies.

The splash cup, which consists of commercially available components, proved to be a versatile and practical tool for the monitoring of splash erosion. The design follows the dimensions proposed by Morgan, therefore, the splash cup can be used for comparison with other studies in which Morgan's device was employed. Even though the soil particle detachment process is very sensitive to factors other than experimental design, standardization or harmonization of splash cup designs would be a beneficial step forward in the complex research area of the splash erosion process. Therefore, we

provide a detailed description of the splash erosion setup, including technical drawings, assembly manual and description of sample preparation and collection on the website rain.fsv.cvut.cz/splashcup.

The results of the presented splash erosion experiment show similar results to previously published studies. The relationship between rainfall kinetic energy and splashed soil amount is linear and there is a kinetic energy threshold to initiate erosion. Even under controlled experimental conditions, when the soil samples were prepared the same way and rainfall characteristics remained constant during the experiment, the eroded soil amount varies across each replicate. This reinforces that splash erosion is a very complex process and the resulting erosion is sensitive to small changes in soil properties and soil surface relief which is problematic and remains an open question that needs to be studied further.

Author Contributions: Conceptualization, D.Z. and T.D.; Formal analysis, D.V.M., J.J., M.N., T.L., L.L.J. and N.Z.; Methodology, D.Z. and P.K.; Project administration, T.D. and A.K.; Supervision, A.K., P.S. and T.D.; Visualization, D.V.M., T.L. and J.J.; Writing—original draft, D.Z.; Writing—review & editing, All. All authors have read and agreed to the published version of the manuscript.

Funding: This research was performed within the project "Kinetic energy of rainfall as a driving force of soil detachment and transport". Financial support was provided through the Czech Science Foundation (GACR): GF17-33751L and the Austrian Science Fund (FWF): I 3049-N29.

Conflicts of Interest: The authors declare no conflict of interest.

References

1. Fernández-Raga, M.; Palencia, C.; Keesstra, S.; Jordán, A.; Fraile, R.; Angulo-Martínez, M.; Cerdà, A. Splash erosion: A review with unanswered questions. *Earth-Sci. Rev.* **2017**, *171*, 463–477. [CrossRef]
2. Morgan, R.P.C. Field measurement of splash erosion. *Int. Assoc. Sci. Hydrol. Publ.* **1981**, *133*, 373–382.
3. Poesen, J.; Torri, D. The effect of cup size on splash detachment and transport measurements. Part I. Field measurements. *Geomorphic Process. Environ. Strong Seas. Contrasts Vol. I Hillslope Process. Catena Suppl.* **1988**, *12*, 113–126.
4. Fernández-Raga, M.; Fraile, R.; Keizer, J.J.; Teijeiro, M.E.V.; Castro, A.; Palencia, C.; Calvo, A.I.; Koenders, J.; Marques, R.L.D.C. The kinetic energy of rain measured with an optical disdrometer: An application to splash erosion. *Atmos. Res.* **2010**, *96*, 225–240. [CrossRef]
5. Truman, C.C.; Bradford, J.M. Soil Science Society of America journal. *Soil Sci. Soc. Am. J.* **1976**, *59*, 519–526. [CrossRef]
6. Kinnell, P.I.A. Splash Erosion: Some Observations on the Splash-Cup Technique 1. *Soil Sci. Soc. Am. J.* **1974**, *38*, 657–660. [CrossRef]
7. Scholten, T.; Geißler, C.; Goc, J.; Kühn, P.; Wiegand, C. A new splash cup to measure the kinetic energy of rainfall. *J. Plant Nutr. Soil Sci.* **2011**, *174*, 596–601. [CrossRef]
8. Wei, Y.; Wu, X.; Cai, C. Splash erosion of clay–sand mixtures and its relationship with soil physical properties: The effects of particle size distribution on soil structure. *Catena* **2015**, *135*, 254–262. [CrossRef]
9. Khaledi Darvishan, A.; Sadeghi, S.H.; Homaee, M.; Arabkhedri, M. Measuring sheet erosion using synthetic color-contrast aggregates. *Hydrol. Process.* **2014**, *28*, 4463–4471. [CrossRef]
10. Watung, R.L.; Sutherland, R.A.; El-Swaify, S.A. Influence of rainfall energy flux density and antecedent soil moisture content on splash transport and aggregate enrichment ratios for a Hawaiian Oxisol. *Soil Technol.* **1996**, *9*, 251–272. [CrossRef]
11. Legout, C.; Leguedois, S.; Le Bissonnais, Y.; Issa, O.M. Splash distance and size distributions for various soils. *Geoderma* **2005**, *124*, 279–292. [CrossRef]
12. Marzen, M.; Iserloh, T.; Casper, M.C.; Ries, J.B. Quantification of particle detachment by rain splash and wind-driven rain splash. *CATENA* **2015**, *127*, 135–141. [CrossRef]
13. Fu, Y.; Li, G.; Wang, D.; Zheng, T.; Yang, M. Raindrop Energy Impact on the Distribution Characteristics of Splash Aggregates of Cultivated Dark Loessial Cores. *Water* **2019**, *11*, 1514. [CrossRef]
14. Fu, Y.; Li, G.; Zheng, T.; Li, B.; Zhang, T. Splash detachment and transport of loess aggregate fragments by raindrop action. *Catena* **2017**, *150*, 154–160. [CrossRef]
15. Fernández-Raga, M.; Campo, J.; Rodrigo-Comino, J.; Keesstra, S.D. Comparative Analysis of Splash Erosion Devices for Rainfall Simulation Experiments: A Laboratory Study. *Water* **2019**, *11*, 1228. [CrossRef]
16. Bisal, F. Calibration of splash cup for soil erosion studies. *Agric. Eng.* **1950**, *31*, 621–622.

17. Bisal, F. The effect of raindrop size and impact velocity on sand-splash. *Can. J. Soil Sci.* **1960**, *40*, 242–245. [CrossRef]
18. Mazurak, A.P.; Mosher, P.N. Detachment of Soil Particles in Simulated Rainfall 1. *Soil Sci. Soc. Am. J.* **1968**, *32*, 716–719. [CrossRef]
19. Vigiak, O.; Okoba, B.O.; Sterk, G.; Groenenberg, S. Modelling catchment-scale erosion patterns in the East African Highlands. *Earth Surf. Process. Landf.* **2005**, *30*, 183–196. [CrossRef]
20. Vigiak, O.; Sterk, G.; Romanowicz, R.J.; Beven, K.J. A semi-empirical model to assess uncertainty of spatial patterns of erosion. *Catena* **2006**, *66*, 198–210. [CrossRef]
21. Moghadam, B.K.; Jabarifar, M.; Bagheri, M.; Shahbazi, E. Effects of land use change on soil splash erosion in the semi-arid region of Iran. *Geoderma* **2015**, *241*, 210–220. [CrossRef]
22. Sadeghi, S.H.; Harchegani, M.K.; Asadi, H. Variability of particle size distributions of upward/downward splashed materials in different rainfall intensities and slopes. *Geoderma* **2017**, *290*, 100–106. [CrossRef]
23. Angulo-Martinez, M.; Beguería, S.; Navas, A.; Machin, J. Splash erosion under natural rainfall on three soil types in NE Spain. *Geomorphology* **2012**, *175*, 38–44. [CrossRef]
24. Dexter, A.R. Effect of rainfall on the surface micro-relief of tilled soil. *J. Terramechanics* **1977**, *14*, 11–22. [CrossRef]
25. Assouline, S.; Mualem, Y. Modeling the dynamics of seal formation and its effect on infiltration as related to soil and rainfall characteristics. *Water Resour. Res.* **1997**, *33*, 1527–1536. [CrossRef]
26. Bretar, F.; Arab-Sedze, M.; Champion, J.; Pierrot-Deseilligny, M.; Heggy, E.; Jacquemoud, S. An advanced photogrammetric method to measure surface roughness: Application to volcanic terrains in the Piton de la Fournaise, Reunion Island. *Remote Sens. Environ.* **2013**, *135*, 1–11. [CrossRef]
27. de Oro, L.A.; Buschiazzo, D.E. Degradation of the soil surface roughness by rainfall in two loess soils. *Geoderma* **2011**, *164*, 46–53. [CrossRef]
28. Luo, J.; Zheng, Z.; Li, T.; He, S. Spatial heterogeneity of microtopography and its influence on the flow convergence of slopes under different rainfall patterns. *J. Hydrol.* **2017**, *545*, 88–99. [CrossRef]
29. Angulo-Martínez, M.; Beguería, S.; Kyselý, J. Use of disdrometer data to evaluate the relationship of rainfall kinetic energy and intensity (KE-I). *Sci. Total Environ.* **2016**, *568*, 83–94. [CrossRef]
30. Lobo, G.P.; Bonilla, C.A. Sensitivity analysis of kinetic energy-intensity relationships and maximum rainfall intensities on rainfall erosivity using a long-term precipitation dataset. *J. Hydrol.* **2015**, *527*, 788–793. [CrossRef]
31. Meshesha, D.T.; Tsunekawa, A.; Tsubo, M.; Haregeweyn, N.; Tegegne, F. Evaluation of kinetic energy and erosivity potential of simulated rainfall using Laser Precipitation Monitor. *CATENA* **2016**, *137*, 237–243. [CrossRef]
32. Bauer, B. Soil splash as an important agent of erosion. *Geogr. Pol.* **1990**, *58*, 99–106.
33. Chesworth, W.; Camps Arbestain, M.; Macías, F.; Spaargaren, O.; Spaargaren, O.; Mualem, Y.; Morel-Seytoux, H.J.; Horwath, W.R.; Almendros, G.; Chesworth, W.; et al. *Classification of Soils: World Reference Base (WRB) for Soil Resources*; Springer: Dordrecht, The Netherlands, 2008; pp. 120–122.
34. Kubínová, R. Grain Size Distribution of Eroded Soil. Master's Thesis, Faculty of Civil Engineering, Czech Techical University in Prague, Prague, Czech Republic, 2019.
35. Kavka, P.; Neumann, M.; Laburda, T.; Zumr, D. Developing of the laboratory rainfall simulator for testing the technical soil surface protection measures and droplets impact. In Proceedings of the XVII ECSMGE-2019 European Conference on Soil Mechanics and Geotechnical Engineering, Reykjavik, Iceland, 1–6 September 2019.
36. Van Dijk, A.I.J.; Bruijnzeel, L.; Rosewell, C. Rainfall intensity–kinetic energy relationships: A critical literature appraisal. *J. Hydrol.* **2002**, *261*, 1–23. [CrossRef]
37. Steiner, M.; Smith, J.A.; Steiner, M.; Smith, J.A. Reflectivity, Rain Rate, and Kinetic Energy Flux Relationships Based on Raindrop Spectra. *J. Appl. Meteorol.* **2000**, *39*, 1923–1940. [CrossRef]
38. Wischmeier, W.H.; Smith, D.D. *Predicting Rainfall Erosion Losses—A Guide to Conservation Planning*; Science and Education Administration United States Department of Agriculture: Hyattsville, MD, USA, 1978; p. 58.
39. Brown, L.C.; Foster, G.R. Storm Erosivity Using Idealized Intensity Distributions. *Trans. ASABE* **1987**, *30*, 0379–0386. [CrossRef]
40. Petrů, J.; Kalibová, J. Measurement and computation of kinetic energy of simulated rainfall in comparison with natural rainfall. *Soil Water Res.* **2018**, *13*, 226–233.

41. Geißler, C.; Kühn, P.; Böhnke, M.; Bruelheide, H.; Shi, X.; Scholten, T. Splash erosion potential under tree canopies in subtropical SE China. *CATENA* **2012**, *91*, 85–93. [CrossRef]
42. Angulo-Martínez, M.; Beguería, S.; Latorre, B.; Fernández-Raga, M. Comparison of precipitation measurements by OTT Parsivel^2 and Thies LPM optical disdrometers. *Hydrol. Earth Syst. Sci.* **2018**, *22*, 2811–2837. [CrossRef]
43. Boroghani, M.; Hayavi, F.; Noor, H. Affectability of splash erosion by polyacrylamide application and rainfall intensity. *Soil Water Res.* **2012**, *7*, 159–165. [CrossRef]
44. Wu, B.; Wang, Z.; Zhang, Q.; Shen, N.; Liu, J. Evaluating and modelling splash detachment capacity based on laboratory experiments. *CATENA* **2019**, *176*, 189–196. [CrossRef]
45. Farres, P.J. The dynamics of rainsplash erosion and the role of soil aggregate stability. *CATENA* **1987**, *14*, 119–130. [CrossRef]
46. Ekwue, E.I. The effects of soil organic matter content, rainfall duration and aggregate size on soil detachment. *Soil Technol.* **1991**, *4*, 197–207. [CrossRef]
47. Ma, R.-M.; Li, Z.-X.; Cai, C.-F.; Wang, J.-G. The dynamic response of splash erosion to aggregate mechanical breakdown through rainfall simulation events in Ultisols (subtropical China). *CATENA* **2014**, *121*, 279–287. [CrossRef]
48. Rezaei Arshad, R.; Mahmoodabadi, M.; Farpoor, M.H.; Fekri, M. Experimental investigation of rain-induced splash and wash processes under wind-driven rain. *Geoderma* **2019**, *337*, 1164–1174. [CrossRef]
49. Luo, J.; Zheng, Z.; Li, T.; He, S. Assessing the impacts of microtopography on soil erosion under simulated rainfall, using a multifractal approach. *Hydrol. Process.* **2018**, *32*, 2543–2556. [CrossRef]
50. Helming, K.; Roth, C.H.; Wolf, R.; Diestel, H. Characterization of rainfall-microrelief interactions with runoff using parameters derived from digital elevation models (DEMs). *Soil Technol.* **1993**, *6*, 273–286. [CrossRef]

Journal of Hydrology 613 (2022) 128322

Contents lists available at ScienceDirect

Journal of Hydrology

journal homepage: www.elsevier.com/locate/jhydrol

Research papers

Soil surface connectivity of tilled soil with wheel tracks and its development under simulated rainfall

Jakub Jeřábek *, David Zumr, Tomáš Laburda, Josef Krása, Tomáš Dostál

Department of Landscape Water Conservation, Faculty of Civil Engineering, Czech Technical University in Prague, 16629 Prague, Czech Republic

ARTICLE INFO

This manuscript was handled by Marco Borga, Editor-in-Chief, with the assistance of Kelly Kibler, Associate Editor.

Keywords:
Surface runoff
Erosion
Microrelief
Connectivity
Structure from motion
Agricultural fields

ABSTRACT

Although wheel tracks cover only a small portion of the surface of agricultural fields, their effect on surface runoff and sediment transport is substantial. Wheel tracks change the microrelief of the soil surface, and influence how the surface is further altered by rainfall and runoff. This study presents a plot-scale microrelief analysis of a tilled surface with wheel tracks under simulated rainfall. Digital elevation models of the microrelief with 1 cm spatial resolution were obtained using the Structure from Motion method. The random roughness, the structural connectivity, and functional connectivity were calculated for before-rainfall and after-rainfall soil surface conditions. The experiments were carried out on inclined, freshly-tilled plots (8 m long, 2 m wide). The wheel tracks were created by four passages of machinery in the slope direction (SWT) and in the contour-line direction (CWT). The experiments were compared to reference plots without wheel tracks (NWT). The wheel tracks increase water and sediment connectivity if they are oriented in slope-wise direction. Microrelief analysis shows that SWT drains water from the surrounding soil. The soil surface adjacent to SWT can also become more connected with the wheel track, due to changes in microrelief introduced by rainfall and runoff. The calculated higher connectivity in the SWT plot corresponded to the measured increased sediment loads. This suggests faster overland flow and therefore shorter flow pathways on the soil surface microrelief. CWT leads to a decrease in the water and sediment connectivity compared to the NWT and SWT plots. Although the surface runoff can overflow the CWT, the network of flow paths results in decreased flow velocity and a slower sediment transport rate. However, the CWT effect is not permanent, and declines as the wheel tracks become silted with the deposited sediment. It is shown that detailed microrelief data provide relevant information for a study of the changes in flow routing in a tilled agricultural field with the presence of a wheel track. SWT accelerates the runoff and especially the sediment transport. During a rainfall event, the hydraulic connection between the wheel track and the surrounding soil increases dramatically. CWT reduces the surface runoff and also the sediment transport. In the long term, rainfall events and surface runoff alter the microrelief connectivity, causing the soil surface to be more hydraulically connected, irrespective of the wheel track orientation. This study demonstrates the effect of wheel tracks on water and sediment transport. The results draw attention to the importance of appropriate soil protection measures, as a bare unprotected surface microrelief exposed to rainfall leads to increased sediment connectivity.

1. Introduction

Surface runoff and sediment transport from arable land have a negative impact on soil quality (Boardman and Poesen, 2006), and this is nowadays the topic of international strategies such as the EU Soil Strategy for 2030 EC COM (2021) 699 (European Commission, 2021). Surface runoff and sediment transport also have negative off-site effects, such as damage to the infrastructure (Boardman et al., 2019), siltation of streams and water reservoirs (e.g. Krása et al., 2005), loss of nutrients from fields (e.g. Probst, 1985), and eutrophication of water bodies (e.g. Carpenter et al., 1998). Although water-driven nutrient transport can also occur in shallow groundwater flow (Outram et al., 2016) or sometimes via percolation through tile drainage systems (Deasy et al., 2009), surface runoff prevails in agricultural fields (e.g. Carpenter et al., 1998).

Direct wheel track compaction has been recognized as a cause of soil

* Corresponding author at: CTU in Prague, Faculty of Civil Engineering, The Department of Landscape Water Conservation, Thakurova 7, 166 29 Praha 6, Czech Republic.
E-mail address: jakub.jerabek@fsv.cvut.cz (J. Jeřábek).

https://doi.org/10.1016/j.jhydrol.2022.128322
Received 2 February 2022; Received in revised form 2 June 2022; Accepted 7 August 2022
Available online 24 August 2022

degradation, because compaction changes the physical and infiltration properties of soils (Lal, 1999; Lindstrom et al., 1981). Topsoil saturated hydraulic conductivity may decrease up to fourfold in the upper soil horizon, mainly due to the decrease in macroporosity under direct compaction (e.g. (Kim et al., 2010)). The effect of compaction was observed mainly in the top 10 cm of the soil profile, where the proportion of elongated pores decreased rapidly (Pagliai et al., 2003). Compacted soil in wheel tracks also exhibits reduced near-saturated hydraulic conductivity due to the reduction in water-conducting pores (e.g. Ankeny et al., 1990; Seehusen et al., 2019; Daraghmeh et al., 2008; Pagliai et al., 2004). The decrease in porosity (and the increase in bulk density) is in fact an effect of rearrangements of the soil particles, which lead to an increased risk of runoff and erosion events.

GPS tracking shows that most parts of agricultural fields are crossed by a tractor at least once in the course of a single season, and some of the wheel tracks remain undisrupted on the soil surface until the harvest (Kroulík et al., 2011; Augustin et al., 2020). Wheel tracks act as preferential pathways for surface runoff and sediment transport, if they are oriented in the direction of the slope (Heathwaite et al., 2005; Silgram et al., 2010; Ryken et al., 2018), and they act as an obstacle if they are oriented in the contour-line direction (Heathwaite et al., 2005). Moreover, the flow direction introduced by the tillage exceeded the flow direction based on topography on 50% to 100% of the catchment area (Souchere et al., 1998; Takken et al., 2001; Couturier et al., 2013). Thus wheeltrack-induced compaction may affect runoff, sediment transport and therefore soil quality on the scale of whole parcels or fields.

Soil surface conditions (Leys et al., 2007) and soil surface microtopography are among key factors in the generation of surface runoff (e.g. Jester and Klik, 2005; Prosdocimi et al., 2017) The microtopography greatly influences runoff generation, since it affects whether and when the water from a local microrelief depression starts to contribute to runoff (Antoine et al., 2009). Due to the microtopography, the overland flow may become channeled, and may therefore gain higher velocity and initiate soil erosion (Chen et al., 2013; Gómez and Nearing, 2005). Infiltration is also affected by microtopography. Soil sealing in a microrelief depression may reduce infiltration, while higher soil water content may increase infiltration (Thompson et al., 2010).

Surface roughness is often used to characterize the conditions of the soil surface (Taconet and Ciarletti, 2007; Croft et al., 2013; Moreno et al., 2008; Luo et al., 2018). Surface roughness has been investigated to estimate surface depression storage (Onstad, 1984), to partition rainfall water into infiltration and surface runoff (Zhao et al., 2018), and to estimate runoff and sediment flow rates (Luo et al., 2018). The initial roughness affects the runoff and the development of rill flow (Gómez and Nearing, 2005). In addition, temporal changes in surface roughness have been observed due to the impact of raindrops (Zobeck and Onstad, 1987; Bauer et al., 2015), surface runoff (Zobeck and Onstad, 1987), or during infiltration (Onstad et al., 1984). Random roughness (RR) decreases in wheel tracks, but this effect is diminished when no-till management systems are used (Lindstrom et al., 1981).

The principle of hydrological connectivity is often used to explore the linkages of various water pools within the landscape (Pringle, 2003; Bracken et al., 2013). Hydrological connectivity can be divided into concepts of structural (topography-based) connectivity and functional (process-based) connectivity (Bracken et al., 2013), which have been utilized in several studies (Antoine et al., 2009; Angermann et al., 2017; Jackisch et al., 2017; Rinderer et al., 2018).

Structural connectivity was developed from DEM-based topographic indices. Some of the most popular indices are the topography-wetness index (Beven and Kirkby, 1979) and modifications to it (Stieglitz et al., 2003, Hjerdt et al., 2004). A combination of indices can also be used to identify the spill and fill runoff behavior on hillslopes (Hopp and McDonnell, 2009). Furthermore, the index of connectivity (IC) was developed to assess the connectivity of water flow and sediment within a landscape (Borselli et al., 2008). Although IC was initially created with a focus on steep Alpine valleys and alluvial fans, it has been successfully used to identify sediment source areas at submeter scales with a Digital Elevation Model (DEM) of 1 cm resolution (e.g. Prosdocimi et al., 2017).

Small-scale functional connectivity is often studied through observations of the temporal changes in the inter-(dis)connection between soil surface depressions (Darboux et al., 2002a,b; Antoine et al., 2009) or roughness organization (Smith, 2014). Antoine et al. (2009) introduced the relative surface connection function (RSCf), which was a metric of surface depression connectivity. RSCf was then used in other studies to observe surface runoff connectivity (Antoine et al., 2011; Yang and Chu, 2013; Peñuela et al., 2016; Appels et al., 2011; Appels et al., 2016). RSCf expresses how much runoff is generated for a given fullness of the surface depressions storage (SDS), and therefore how well the surface depressions are hydraulically connected at each moment. In practical terms, the connectivity is assessed with a curve function relating the surface runoff and the actual filled surface depression storage. The gradient of the curve expresses how quickly the surface depressions are

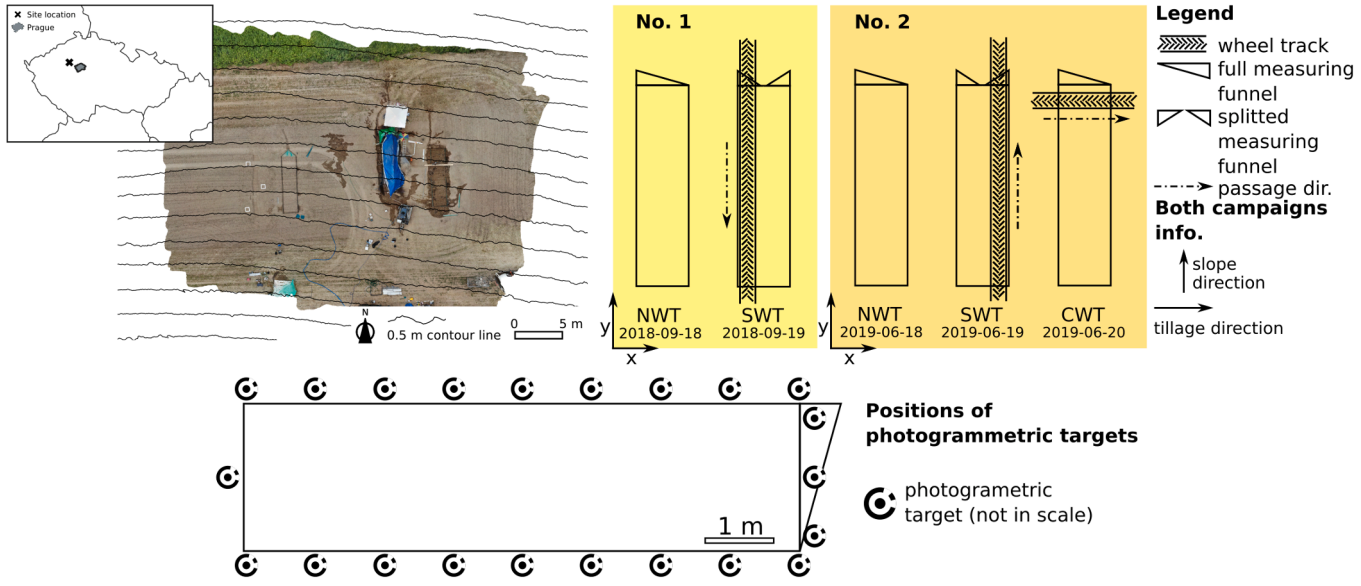

Fig. 1. Location and an orthophoto of the experimental site on the top left. Experimental plot setting of campaign No. 1 and campaign No. 2 on the right. The schema of the photogrammetric measurement at the bottom.

being connected and surface runoff is being generated. A large gradient indicates threshold behavior – the abrupt connection of a major surface storage to the outlet. A low gradient indicates a more complex surface, where e.g. multiple surface depressions need to be filled and connected with each other to produce runoff. A horizontal shift of the curve indicates an increase (or a decrease) in the surface depression storage during the experiment. According to Peñuela et al. (2016), the soil surface changes during a rainfall event and the subsequent response of the surface runoff are well explained by RSCf. Moreover, RSCf can be used to improve the simple stepwise surface retention parameter of large-scale hydrological models, as the runoff is usually observed before all depressions get filled (Antoine et al., 2009; Antoine et al., 2011; Peñuela et al., 2016).

As has been shown above, a vast amount of research has been done on analyzing the microrelief in terms of roughness or connectivity. However, there is a lack of studies on combinations of macro-features and micro-features, e.g. wheel tracks and the soil surface microrelief. In this study, we present a microrelief analysis of soil surfaces with the presence of wheel tracks, and we relate the analysis to direct measurements of the surface runoff and the sediment transport during a rainfall simulation. The goal is to better understand the dynamics of the initiation of surface runoff, soil erosion and rainfall-runoff-induced surface changes on a bare tilled soil. The Structure from Motion (SfM) photogrammetric method was used to capture the soil surface changes caused by rainfall and by surface runoff (Westoby et al., 2012), and to calculate the connectivity indices (Prosdocimi et al., 2017; Wolstenholme et al., 2020).

The specific objectives of our investigation are (1) to assess the changes in microtopography caused by a wheel track, and by rainfall and surface runoff, utilizing high-resolution microrelief DEMs and several indicators (surface roughness, structural and functional connectivity), and (2) to confront the observed changes in microrelief with the measured surface runoff and sediment transport on the plot scale.

2. Materials and methods

A series of artificial rainfall experiments were performed to study the effect of the presence and the orientation of wheel tracks on surface runoff and sediment transport. In general, we utilized two approaches: direct monitoring of surface runoff and sediment transport, and microrelief analysis utilizing random roughness and two connectivity indicators. In total, five experiments were performed in two independent experimental campaigns. The first experimental campaign was undertaken in September 2018 (referred to as campaign No. 1), and the second was undertaken in June 2019 (referred to as campaign No. 2). Two wheel-track orientations were examined: slope-wise direction (SWT) and contour-line direction (CWT). The experimental setup was complemented by reference experiments on plots with no wheel tracks (NWT), as shown in Fig. 1.

2.1. Location

The experiments were carried out on experimental plots located on an agricultural site ca 30 km to the north-west of Prague, Czech Republic, at coordinates 50°13′2.0″N, 14°1′2.2″E (Fig. 1). The site is at an elevation of 310–315 m a.s.l. The annual mean temperature is 8 °C, and the mean annual precipitation is 500 mm. The climate is characterized as humid continental. The site is located at the edge of larger fields, on which winter wheat and rapeseed were planted in both experimental years. The topsoil is classified as loam with 18.3% of clay, 33.8% of silt and 47.9% of sand. The soils are developed on sedimentary rocks consisting of claystone, sandstone and arkose, and are classified as Cambisols according to the World Reference Base for Soil Resources. The content of organic matter is in the range of 1.2–1.5% in the topsoil.

2.2. Experimental plots

All experimental plots had an inclination of approximately 10%, and were 8 m long and 2 m wide. The size of the plot was adopted from Kavka et al. (2018); the length of the plot is long enough to study the erosion process while preserving uniform rainfall distribution along the plot. The Each experimental plot was delineated by metal plates inserted ca 5 cm into the soil. The seedbed was prepared and the wheel tracks were created several days before the experiments. For both campaigns, no precipitation was recorded between the preparation of the topsoil and the experiments.

2.2.1. Campaign No. 1

Campaign No. 1 was conducted on September 18th and 19th, 2018. The soil was stubble tilled to a depth of 12–15 cm using a stubble cultivator one day before the experiment (September 17th). The wheel tracks were created directly after cultivation by four passages of a New Holland T7.185 tractor and a trailed cultivator (in non-operational state; with two axles) driving in the uphill direction in the case of the SWT plot (Fig. 1). Four passages were chosen in order to produce a representative wheel rut, without making an unrealistic number of passages. It has been shown that most compaction changes occur within the first 4 – 5 passages (Botta et al., 2009). The pressure in the tires of the tractor was 1.4 bar (front wheels) and 2.0 bar (rear wheels). The tire pressure of the stubble cultivator was 3.5 bar. The total weight of the machinery was 8.5 t (6 t for the tractor and 2.5 t for the stubble cultivator). The axle loads of the tractor were 2.8 t on the front axle and 3.2 t on the rear axle. The axle load of the stubble cultivator was 1.25 t. The maximum static ground pressure of a single tire was estimated using the soilphysics R package (de Lima et al., 2021) to be 201 kPa for the front axle of the tractor and 272 kPa for the rear axle, and 439 kPa for the stubble cultivator. The initial topsoil water conditions were very dry, with a volumetric water content of 0.10 ± 0.01 cm^3 cm^{-3}. The topsoil bulk density was 1.31 ± 0.09 g cm^{-3}. The topsoil bulk density of the soil in the wheel track was 1.40 ± 0.1 g cm^{-3}. The mean wheel rut depth was 3.9 ± 0.9 cm. During campaign No. 1 only the slope-wise WT was set.

2.2.2. Campaign No. 2

Experimental campaign No. 2 was conducted between July 18th and 20th, 2019. The vegetation cover (mainly Atriplex, *Galium Aparine* and common grasses) that had grown on the experimental plot location during the vegetation season was mulched on June 14th, 2019. Dry vegetation residues were manually removed from the soil surface. One day before the experiment, the topsoil was stubble tilled to a depth of 12–15 cm. The wheel tracks were prepared after stubble tillage with a New Holland T8040 tractor and a full 12 m^3 water tank trailer (with 4 wheels) driving 4 times in downhill direction (Fig. 1). The tire pressure of the tractor was 1.4 bar (front wheels) and 1.6 bar (rear wheels). The pressure of each water tanker tire was 3.5 bar. The total weight of the machinery was about 22 t (8 t for New Holland T8040, 2 t for the water tank, and 12 t for the water). The axle load of the tractor was 3.8 t for the front axle and 4.2 t for the rear axle. The axle load of the water tank was approximately 7 t. The maximum static single tire ground pressure was estimated to be 206 kPa for the front wheels of the tractor, 236 kPa for the rear wheels of the tractor, and 455 kPa for the wheels of the water tank (also using the soil physics R package (de Lima et al., 2021)). The initial soil water conditions were very dry, with a volumetric water content around 0.13 ± 0.02 cm^3 cm^{-3}. The topsoil bulk density was 1.19 ± 0.37 g cm^{-3}. The topsoil bulk density of the soil in the wheel track was 1.35 ± 0.03 g cm^{-3}. The mean wheel rut depth at the SWT plot was 3.5 ± 1.9 cm. Both slope direction and contour-line direction wheel tracks were set up for campaign No. 2.

2.3. Surface microtopography observation

The soil surface morphology was monitored by means of the

Structure from Motion close-range photogrammetry method. Images for photogrammetry were taken before and after each experiment, using a Sony A6000 mirrorless camera with an APS-C size sensor with resolution of 24 Mpx and equipped with a standard Sony 16–50 mm zoom lens fixed on 16 mm. Each measurement consisted of approximately 40–60 images taken in two rows from a distance of 1.5 m.

Photogrammetry reference targets were installed on the perimeter of each plot at a mutual distance of 1 to 2 m. The targets were inserted into the soil with 15 cm long screws, which held the targets in a steady position during the experiment. A small number of targets were also attached to the collection flume. The GPS positions of all targets were measured with vertical and horizontal accuracy of 15 mm. Images with geo-referenced targets were processed in Agisoft Photoscan Professional 1.4.2 build 6205 (Agisoft LLC). The output was an orthophoto and a digital elevation model (DEM) of the surface with a 1 mm ground sampling distance. 10 mm spatial resolution in × and y direction was used for all analyses. This resolution was optimized in order to maintain high detail in the analysis while providing reasonably low noise in the data and reasonable time for computation.

The DEMs were rotated to reorient the plots into the north direction in order to simplify further image processing (the coordinates are shown in Fig. 1). The installed sensors, which partially covered the soil surface, were clipped off the images and the missing areas were linearly interpolated in the south-north direction. The raster cells on the sides of the plots were raised by 0.2 m to form a boundary for the drainage area, which was in reality maintained by metal sheets during the experiment. The raster was further resampled to 10 mm spatial resolution in order to reduce the noise of the initial point clouds and to decrease the size of the data for further processing and computation.

2.4. Rainfall simulation

Artificial rainfall with intensity of 27.4 ± 7.8 mm h^{-1} (measured with multiple totalizators throughout the simulation) and mean rainfall kinetic energy of 127 J m^{-2} h^{-1} (measured on site with a disdrometer) was set for all experiments. The target value of the rainfall was 30 mm h^{-1}, which is the 5-year return period rainfall at the location (Kašpar et al., 2021). The duration of the experiments varied between 290 min and 433 min. Funnels were installed at the bottom of each experimental plot to collect the surface runoff and sediment. For a detailed description of the simulator, see Kavka et al. (2018). On the SWT plots, two flumes were installed in order to separate the water flowing through the wheel track and the water flowing from the adjacent tilled soil surface (Fig. 1). The runoff sampling interval was prolonged during the experiment, starting at 2.5 min and reaching 20 min when the runoff was approaching a steady state.

2.5. Microrelief analysis

2.5.1. Roughness

The random roughness RR was calculated from the before- and after-rainfall DEMs for each plot. In addition, the wheel tracks and the adjacent tilled soil surface were analyzed separately for the SWT and CWT plots. The RR calculation was adopted according to Taconet and Ciarletti (2007). The DEMs were leveled in order to exclude the plot slope from the RR calculation. Subsequently, RR was calculated as the standard deviation of the leveled pixel elevations:

$$RR = \sqrt{\frac{1}{(n-1)(m-1)}\sum_{i}^{n}\sum_{j}^{m}(Z_{i,j}-\overline{Z})^2} \quad (1)$$

where Z stands for detrended surface elevation and $\overline{Z}$ stands for the mean of the detrended surface elevation, n and m stand for the number of rows and columns in the rotated raster.

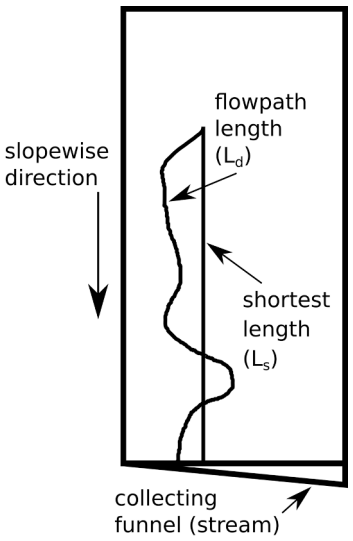

Fig. 2. An explanatory diagram of the normalized downslope distance NDD. NDD is the ratio between the flowpath length calculated using a downslope distance algorithm – the flowpath length from a given raster cell to the bottom of the plot (to the collection funnel) and the shortest geometrical distance between the raster cell and the collection funnel.

2.5.2. Structural connectivity analysis

The normalized downslope distance (NDD) was used to assess the structural connectivity. Our approach was inspired by the index of connectivity (Borselli et al., 2008), where the downslope distance is a part of the algorithm. The downslope distance algorithm provided by the TauDEM terrain analysis tool (Tarboton, 2015) was used to perform the analysis. As a result of the algorithm, a raster was created in which each cell contains a flow path length L_d to the bottom of the plot. At this stage, the downslope distance is dependent on the organization of the surface topography and the position of a given cell along the slope. To compensate the cell position along the plot, we normalized the pathway length L_d by the shortest length to the bottom of the plot L_s, as is shown in Fig. 2. NDD is therefore calculated as

$$NDD = \frac{L_d}{L_s}$$

The NDD expresses the bulk complexity of the surface topography from the perspective of the moving particle the trajectory of which is being tracked.

2.5.3. Functional connectivity analysis

Functional connectivity refers to a concept presented by Darboux et al. (2002b) and by Antoine et al. (2009), where a surface runoff model is used to assess the connectivity. For this task, we utilized the SMODERP2D[1] physically-based episodic distributed hydrological model (Dostál et al., 2000; Kavka et al., 2022; Landa et al., 2019). The results of the model were interpreted as the relationship between the runoff coefficient and the soil surface depressions storage. The interpretation of this relationship is shown in Fig. 3.

The initial surface depression storage is calculated by subtracting sink-less[2] DEM from the original DEM. Sink-less DEM is calculated with the Fill tool of the spatial analysis extension of ESRI ArcMap 10.7

[1] The model is provided in the public repository at the github online platform (github.com/storm-fsv-cvut/smoderp2d or on the web of the Department of Landscape Water Conservation, Faculty of Civil Engineering, CTU Prague (storm.fsv.cvut.cz/…/smoderp).

[2] Sinks in DEM are cells surrounded by cells with higher elevation. The sink-less DEM is a raster where such cells are artificially removed.

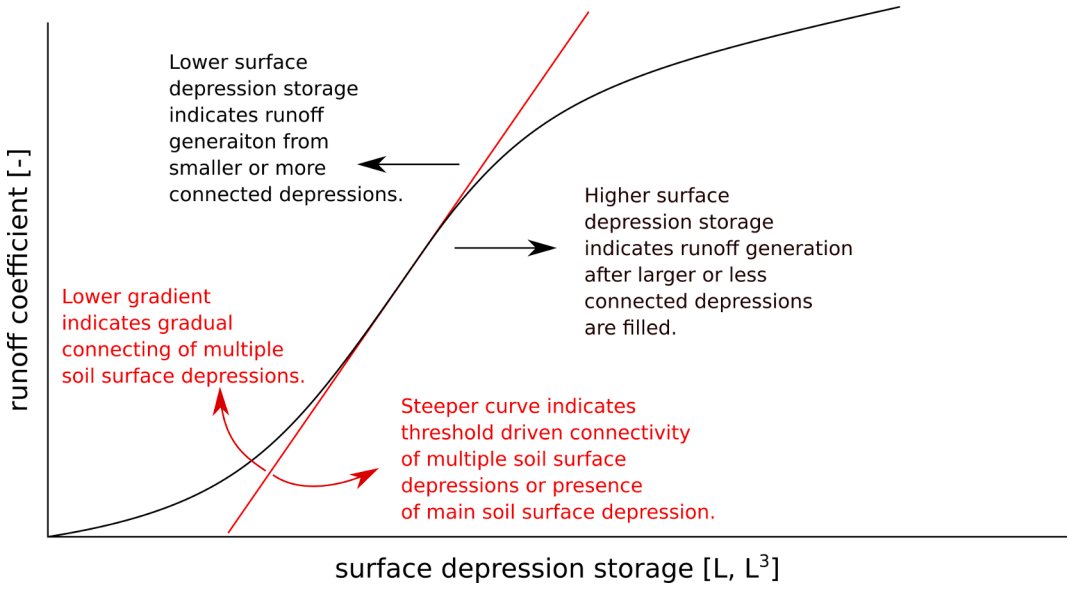

Fig. 3. An example of the runoff coefficient to soil surface storage relationship – functional connectivity. Black arrows and text explain the horizontal shift of the curve. The red line indicates the gradient of the example curve. Red arrows and text explain the meaning of the gradient shift. (For interpretation of the references to color in this figure legend, the reader is referred to the web version of this article.)

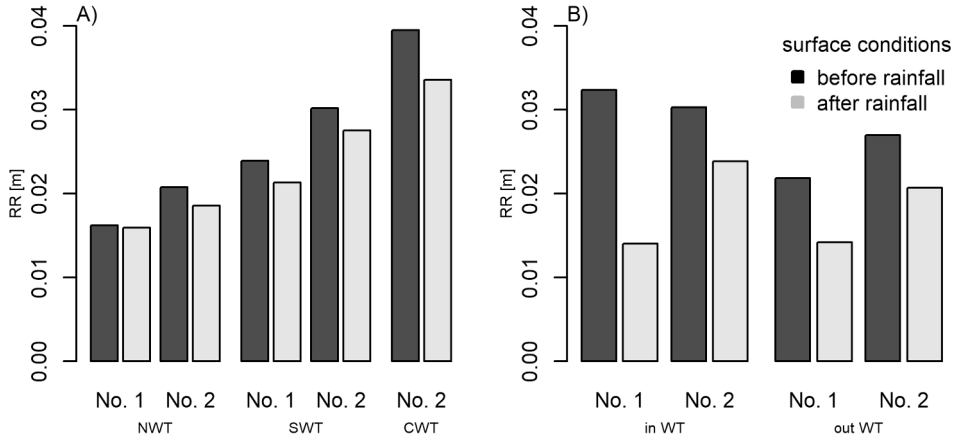

Fig. 4. A) Bar plots of the random roughness for slope-wise and counter slope-wise wheel track orientation, and the no wheel track plot for before-rainfall and after-rainfall soil surface conditions. B) Bar plots of the random roughness of the wheel track (in WT) and the surrounding soil surface (outside WT) on the SWT plots of both campaigns.

software. It was assumed that the plots have uniform soil hydraulic properties over the plot, which does not change in time. All plots were modeled with uniform rainfall intensity, which corresponded to the rainfall intensity used during the rainfall experiments. A more detailed description of the model and its infiltration and flow routing parameters is provided in Appendix Table 1

2.6. Laboratory analysis

The undisturbed soil samples were gravimetrically analyzed to obtain the initial soil water content and the bulk density. The sediment concentration in the runoff was obtained by filtering the sampled water. The paper filters with the trapped soil were oven-dried at 105 °C to obtain the mass of the eroded soil.

2.7. Statistical analysis

The significance of the wheel-track effect on surface runoff and sediment transport was analyzed using the Student *t*-test. In particular, the non-zero difference among the plots was tested. The test was performed with R software (R core team, 2018).

3. Results

3.1. Random roughness

Random roughness (RR) is shown in Fig. 4A for all experimental plots for before- and after-rainfall soil surface conditions. The RR of all the plots varies between 0.015 m and 0.045 m. The RR was larger in campaign No. 2 than in campaign No. 1 for all plots. A decline in roughness after rainfall was observed for all experiments, although the decrease in RR at the NWT plot in campaign No. 1 was only minor. The most pronounced drop in RR was observed for the NWT plot in campaign No. 1. The CWT plot exhibited the largest RR.

Fig. 4B shows the random roughness RR in the wheel track (in-WT) and of the surrounding soil (out-WT) for the SWT plot. Similarly, in Fig. 4A, the roughness decreased in all cases after the rainfall. The RR in Fig. 4B shows a more pronounced decrease in campaign No. 1, especially

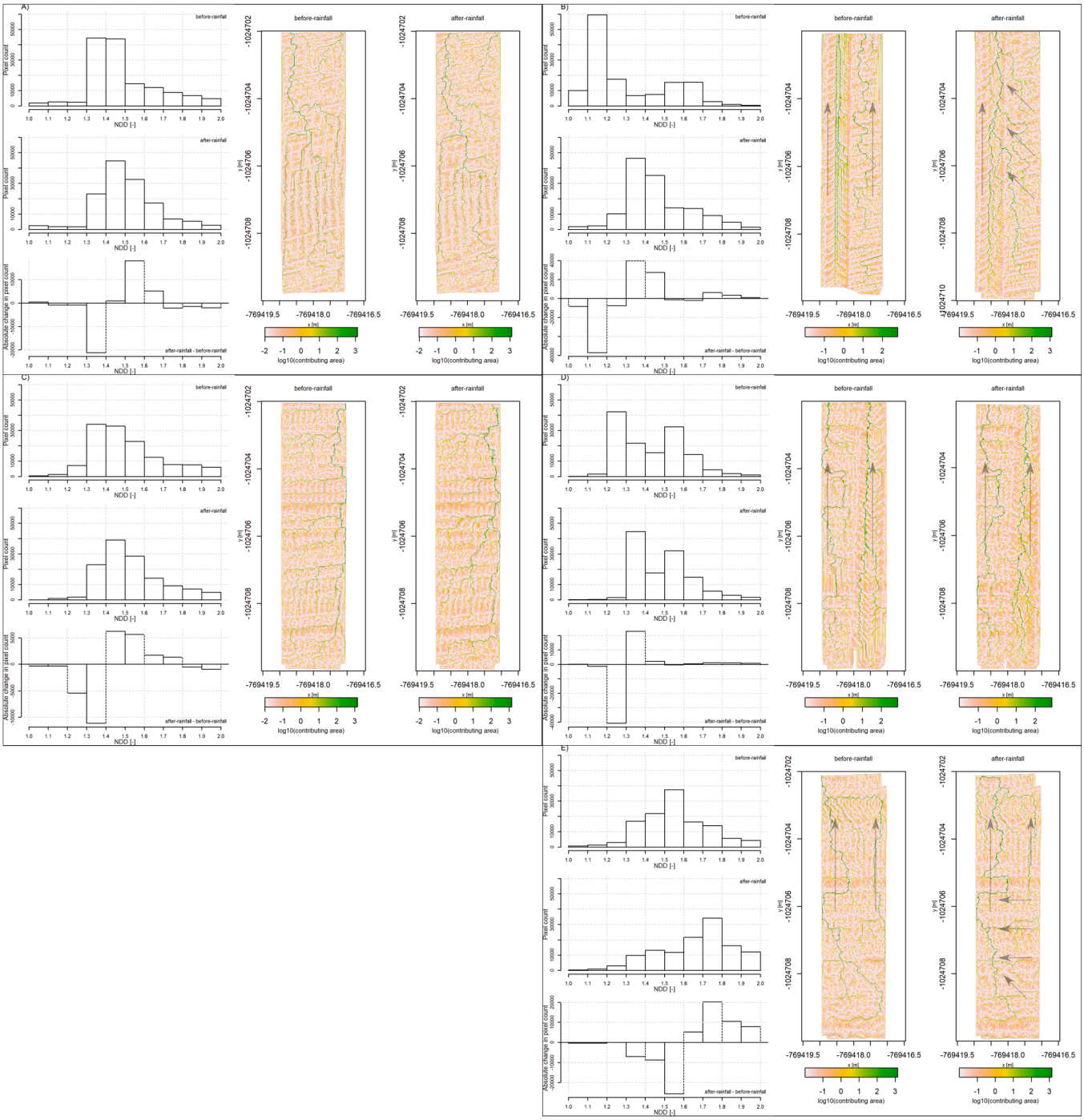

Fig. 5. The histogram of NDD and the corresponding contribution area raster of the before-rainfall and after-rainfall surface conditions of: A) NWT No. 1 plot, B) SWT No. 1 plot, C) NWT No. 2 plot, D) NWT No. 2 plot, and E) CWT No. 2 plot. The difference between the before-rainfall histogram and the after-rainfall histogram is shown below the corresponding histograms to indicate the increase/decrease in the normalized downslope distance in each interval of the histogram. The arrows in some of the flow accumulation rasters indicate the main flow direction and are described in the manuscript text.

in WT. Although a larger decrease was recorded, the overall roughness was lower in campaign No. 2. The decrease in RR was more pronounced between the campaigns than between the in-WT and the out-WT.

3.2. Structural connectivity

Histograms of the normalized downslope distance NDD with the before-rainfall and after-rainfall soil surface conditions, and the flow accumulation raster, are shown in Fig. 5. NDD was used to assess the tortuosity of the downslope pathway, which serves as a measure of the structural connectivity. The flow accumulation rasters are displayed in order to diagnose the shifts in the NDD histograms.

The before-rainfall soil surface conditions of the CWT exhibited the highest NDD pixel count in the interval of 1.5–1.6. On the NTW plots, the highest NDD pixel count was observed in the interval 1.3–1.5 (Fig. 5AC) plot during both campaigns. The SWT plots exhibited bimodal NDD distribution before the rainfall (Fig. 5BD). The first peak in the pixel count of the histogram lay in the NDD interval of 1.1–1.2 for the first campaign and in the interval of 1.2–1.3 for the second campaign. The second peak was observed in the NDD intervals of 1.5–1.7 and 1.5–1.6

Table 1
Summary of experiments. Single values are presented. SWT – slope wise wheel track; CWT – contour line wheel track; NWT – no wheel track. At the SWT plot, the runoff was collected from a wheel track and from the surrounding soil, separately (shown in gray).

campaign	No. 1	No. 1	No. 1	No. 2	No. 2	No. 2	No. 2
plot setting	NWT	SWT	SWT	NWT	SWT	SWT	CWT
collected below WT	no	no	yes	no	no	yes	yes
date	9/18/2018	9/19/2018	9/19/2018	6/18/2019	6/19/2019	6/19/2019	6/20/2019
rainfall duration [min]	290	249	249	316	433	433	319
rainfall depth [mm]	145	124.5	124.5	158	216.5	216.5	159.5
runoff time lag [min]	76	no runoff	15	51	102	22	32.5
max. runoff [mm/hour]	22.7	no runoff	25.4	25	2.8	21.6	14.4
cumulative runoff [mm]	31	no runoff	54.7	73.5	8.5	88.5	26.1
runoff coefficient [%]	21.3	no runoff	45	46.5	3.9	40.9	16.4
total soil loss [g m^{-2}]	204	no runoff	550	175	38	1360	48

during the first and second campaigns.

The NDD pixel count increased in the interval 1.4–2 while it decreased in intervals 1–1.4 at the CWT plot after rainfall. After rainfall, the NWT plots exhibited an increase in the NDD pixel count, especially in intervals 1.5 – 1.6 and 1.4 – 1.6 for campaigns No. 1 and No. 2, respectively. The NDD pixel count showed a different change at the SWT plots during each campaign (Fig. 5BD). The after-rainfall two-peak histogram became a single peak histogram due to the higher NDD values in intervals 1.3–1.5 and 1.7–2.0 during campaign No. 1. However, two peaks in the NDD histogram were preserved after the rainfall during campaign No. 2 – although the first peak shifted into the NDD interval 1.3–1.4.

The flow accumulation showed the main pathways and their complexity (Fig. 5). Two peaks of the before-rainfall NDD histogram at the SWT No. 2 plot clearly correspond to two main flow pathways identified in the flow accumulation raster; one in wheel tracks and one in the surrounding soil surface (Fig. 5B). The same situation applied for the SWT plot for the before-rainfall conditions, as shown in Fig. 5D. The flow accumulation in campaign No. 1 showed that the flow paths were diverted from the tilled surface into the wheel track, which corresponds to a shift from unimodal to bimodal distribution in the NDD histograms. Two main flow paths were preserved in the after-rainfall conditions in campaign No. 2, which again corresponded to bimodal NDD after-rainfall distribution. The NDD changes in the NWT plot could not be explained by a visual inspection of the flow accumulation raster. On the CWT plot (Fig. 5E), a change in the flow path can be observed in the lower right corner, which was disconnected from the upper right corner of the plot after the rainfall and was shifted to the left part of the plot.

3.3. Functional connectivity

The functional connectivity for before-rainfall and after-rainfall surface conditions is shown in Fig. 4. CWT plot No. 2 exhibited the largest storage capacity for the before-rainfall conditions (Fig. 4A), and SWT exhibited the lowest storage capacity during both campaigns (Fig. 4AB). NWT exhibited almost identical curves for the before-rainfall conditions during both campaigns (Fig. 4A), however the curves deviated from each other for the after-rainfall conditions. The depression storage capacity was smaller for the after-rainfall conditions than for the before-rainfall conditions, with the exception of reference plot NWT in campaign No. 1, where the storage capacities remained very similar.

For the before-rainfall conditions, the SWT plots of both campaigns and NWT plot No. 2 exhibited a sharp increase in the runoff coefficient when a certain threshold was reached (Fig. 4A). For NWT plot No. 1 and NWT plot No. 2, this increase occurred later, when more of the surface depression storage (SDS) was filled. This effect was most pronounced for the CWT plot, where the runoff coefficient increased more gradually while the SDS was being filled.

Threshold behavior was observed to some extent in all the experiments. Only a small portion of SDS had to be filled before runoff was initiated on the SWT plots in both before- and after-rainfall surface conditions. Up to 0.2 mm of SDS had to be filled at the NWT plots before the rainfall soil surface conditions initiated runoff. Interestingly, the CWT plot started to contribute to runoff for smaller filled SDS than the NWT plots for before-rainfall soil surface conditions (Fig. 4A), but the increase in runoff was more gradual on the CWT plot, as described above.

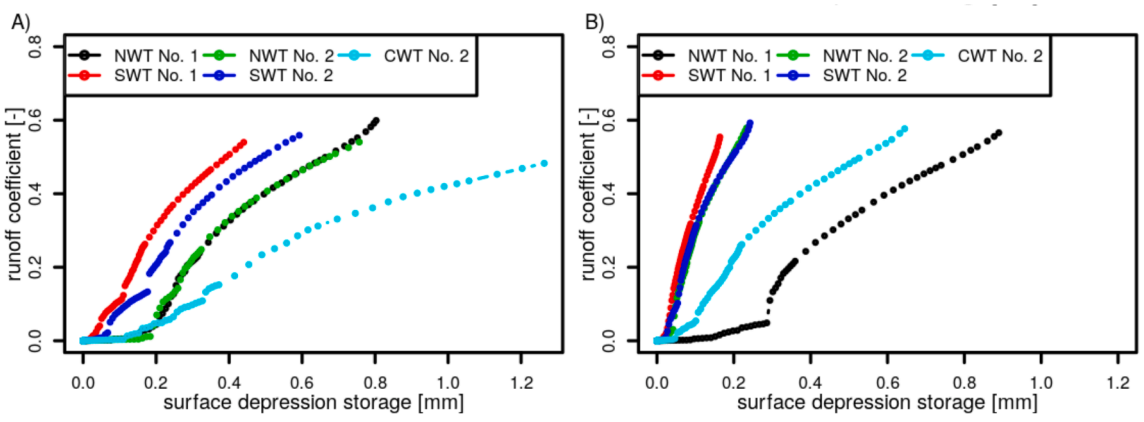

Fig. 6. Functional connectivity as the relation between the runoff coefficient and the filled soil surface storage of A) the before-rainfall situation, and B) the after-rainfall situation of all plots.

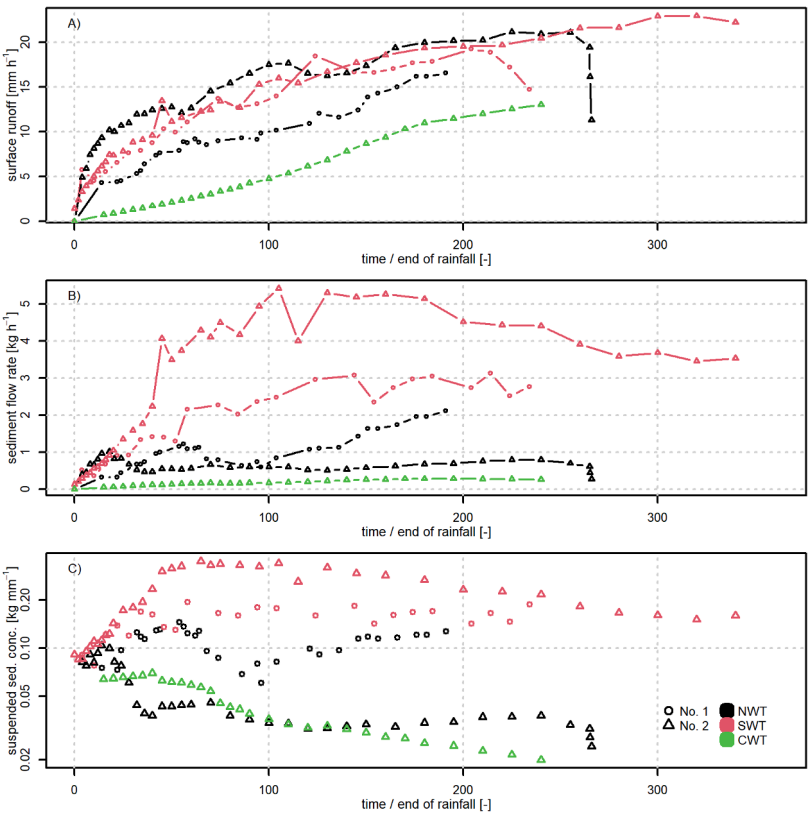

Fig. 7. Development of: A) the surface runoff, B) the sediment flow rate and C) the concentration of the suspended solids in time. The runoff time lag is excluded from the graphs; therefore, all graphs start at a common zero time on the vertical axes.

Table 2
The difference of: A) the surface runoff from the plots since the beginning of runoff; B) the sediment flow rate at the plots since the beginning of runoff. The Student *t* test was used, to test if the difference between the two plots is greater than 0. Red color indicates that the plot in the column exhibited significantly higher ($\alpha = 0.05$) values than the plot in the row. Green color indicates a non-significant difference.

A)

		No. 1		No. 2		
		NWT	SWT	NWT	SWT	CWT
No. 1	NWT	NA				
	SWT		NA			
No. 2	NWT			NA		
	SWT				NA	
	CWT					NA

B)

		No. 1		No. 2		
		NWT	SWT	NWT	SWT	CWT
No. 1	NWT	NA				
	SWT		NA			
No. 2	NWT			NA		
	SWT				NA	
	CWT					NA

3.4. Runoff and sediment transport

A summary of the direct measurements of surface runoff and sediment transport is shown in Table 1. The duration of the experiments differed, and therefore the total rainfall depth and the total rainfall kinetic also differed. The largest rainfall amount was received by SWT plot No. 2, and the smallest rainfall amount was received by SWT plot No. 1. During campaign No. 1, surface runoff from the SWT plot occurred only in the wheel track, while the surrounding tilled soil exhibited no runoff at the bottom of the plot. The surface runoff from the SWT plot during campaign No. 2 was drained through both parts of the plot – the wheel track and the surrounding tilled surface. However, the runoff from the surrounding tilled surface exhibited a much longer time lag (102 min), an almost 7.5 times lower cumulative runoff, and a 31.3 times lower total soil loss compared to the wheel track (see Table 1). No evidence of rill erosion was observed.

The runoff and the sediment flow development differed among the wheel track variants, as shown in Fig. 7 and Table 2A. Neither the surface runoff nor the sediment flow rate reached steady rates during the experiments. Similar values were reached on the SWT plots and on the NWT plot of the second campaign; however, the time lag was different (Fig. 7A). The NWT plots during campaign No. 2 exhibited significantly higher surface runoff when the lag time was excluded from the analysis (Table 2). NWT plot No. 1 exhibited similar behavior as the CWT plot in campaign No. 2, apart from the runoff time lag.

The sediment flow rate (Fig. 7B) varied during the experiments. The SWT plots exhibited significantly greater sediment flow rates than the other plots, with the peak at about one third of the duration of the

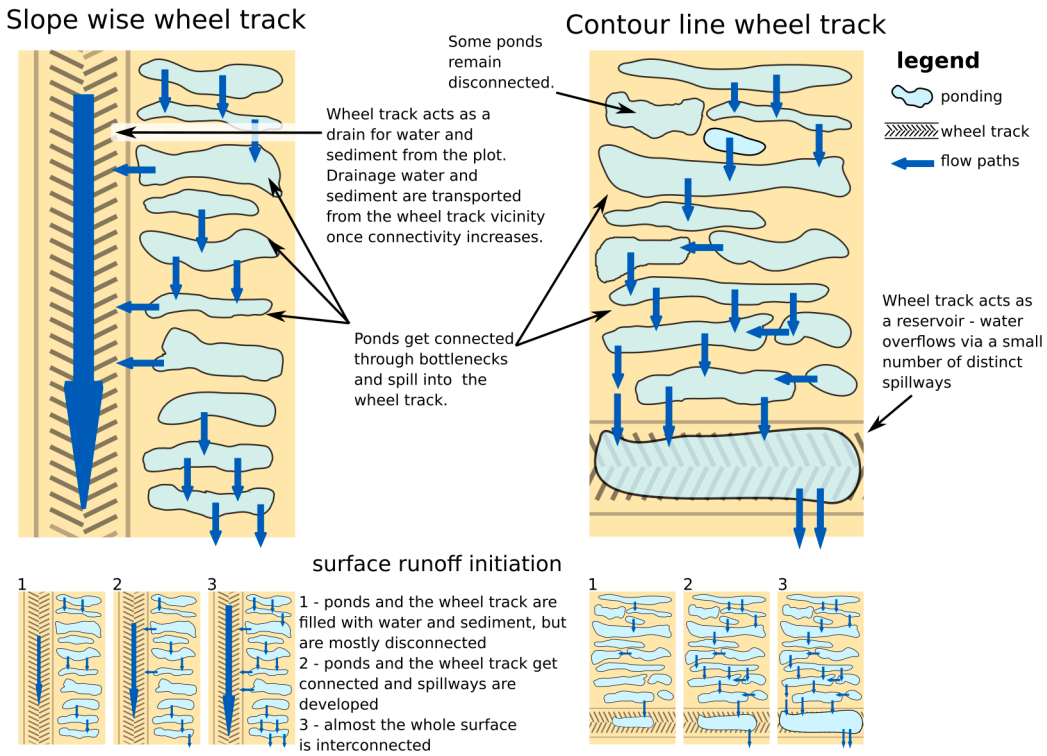

Fig. 8. Runoff development visually observed during the rainfall simulation at the SWT and CWT experimental plot. The lower bar plots show the development of the connectivity of the soil surface depressions.

experiment (Table 2B). The rising limb of the sediment mass plot increased more gradually during campaign No. 1 than during campaign No. 2. The sediment flow rate on the NWT plots exhibited similar behavior during both campaigns, with the exception of the time lag. The sediment flow rate was significantly higher during campaign No. 1 (Table 2B). The curves of the sediment flow rate on both NWT plots were generally flat, which contrasts with the surface runoff, where the rate increased throughout the experiment. The CWT plot showed the smallest surface runoff (Table 2A) and the slowest increase in surface runoff (Fig. 7A). The surface runoff increased throughout the experiment, while the sediment flow stabilized at a constant value (Fig. 7B). All experiments where the sediment flow reached a quasi-steady value exhibited a decrease in the concentration of the suspended sediment, see Fig. 7C.

4. Discussion

4.1. Effect of the wheel track on connectivity

The presence of a wheel track can be recognized by the structural connectivity. The greatest structural connectivity was observed on both SWT plots, while the lowest structural connectivity was observed on the CWT plot. The reference NWT plot exhibited medium values of structural connectivity. These findings indicate more prolonged paths of water and sediment on the CWT plot than on the NWT and SWT plots. As a consequence, water moves more slowly along the plot. This results in a decreased erosion rate. The two peaks of NDD in the SWT plots indicate that the higher connectivity is caused solely by the wheel track.

While structural connectivity expresses the connectivity among individual surface micro-depressions, functional connectivity indicates the connectivity between the soil surface and the outlet. As expected, functional connectivity showed that the SWT plots exhibited the highest connectivity, while the CWT plots exhibited the lowest connectivity. According to Antoine et al. (2009) the functional connectivity distinguished well between the microrelief composed of isolated craters and the microrelief composed of well-connected "valleys". This suggests that the CWT surface contains more distinct depressions than the NWT and SWT plots. The SWT plot, on the other hand, consists of better-connected pathways. Ultimately, the soil flattened by the wheel tracks (the tire patterns are smaller than the roughness of the surrounding soil) creates well-connected pathways and therefore increases the connectivity.

In all cases in our study, the tillage was in the direction of the contour lines. In the case of the SWT plot, this created an unusual situation of contour tillage and slope wheel tracks, which however can occur with conventional soil tillage technology or on headlands (Kroulík et al., 2011). The number of passages affects the depth of the wheel rut. It has been shown that the first few passages have the most significant effect, and that the wheel rut depth becomes less reduced after 5 passages (Botta et al., 2009). Also, the soil moisture conditions play a significant role. However, due to the low soil water content at the beginning of both campaigns we would not expect substantial deepening of the wheel track if more passages were performed. The shape and the pattern of the surface depressions would also vary for different tillage types (Tarolli et al., 2019). The length of the plot also affects connectivity; a longer plot decreases the runoff due to infiltration, and increases sediment transport due to increased velocity of the flow (Jourgholami and Labelle, 2020). A longer plot may have a higher effect on SWT than other wheel track configurations due to its connectivity and low infiltration capacity.

4.2. Impact of rainfall and runoff on connectivity

The surface runoff evolution mechanism is shown in Fig. 8. The surface runoff was formed by consecutive filling and spilling of water from the surface depressions. Once water reaches the wheel track it cannot return to the surrounding soil, and is preferentially transported downwards on the SWT plot. This contrasts with the CWT orientation, which acts as a large surface depression that releases runoff only when full. During runoff, the soil surface depressions gradually become filled with the mobilized sediment. This was observed during the experiment,

and is also indicated by the decrease in RR and by the changes in soil surface storage after rainfall. This kind of behavior has been reported in the literature (Zobeck and Onstad, 1987; Withers et al., 2006; Peñuela et al., 2016).

When a surface depression is overtopped, a small neck is eroded at the boundary of the depression, accelerating both the runoff and the sediment transport. In the experiment, no rill flow developed (similarly to (Helming et al., 1998)). Small necks acted as short bypasses connecting the depressions with each other and with the wheel track. Although this effect was clear during the experiment, it could only be observed qualitatively in the flow accumulation raster on the CWT plots, where several flow paths from the wheel tracks emerged after rainfall (Fig. 5).

The random roughness decreased due to the mechanical impact of the rain drops and the subsequent consolidation of the surface, which flattened the ridges formed by the tillage (Bauer et al., 2015; Zobeck and Onstad, 1987; Laburda et al., 2021). It has been shown in the literature that the surface roughness decreases exponentially with increasing rainfall amount or with rainfall kinetic energy (Zobeck and Onstad, 1987). This exponential relationship was shown to be consistent among multiple tillage systems (Guzha, 2004). However, simulated rainfall usually has an unnatural raindrop distribution, and the relation between random roughness and kinetic energy may therefore be altered. In this study, the same rainfall intensity and the same rainfall simulator – and therefore the same drop size distribution – was used. Only the rainfall depth (and the kinetic energy) differed among individual experiments. However, the extent to which the RR decreased did not coincide with the total rainfall depth.

The surface runoff also detached soil particles from ridges, and some of the particles later settled into the surface depressions. This led to decreasing surface roughness (Fig. 4) and to decreasing depression storage capacity (Fig. 6). Smoothing of the surface is clearly visible during all experiments, irrespective of the presence or the orientation of the wheel track. The roughness also decreased in the wheel track (Fig. 4), which confirms that there are both soil erosion and soil deposition in the compacted wheel tracks, as has also been reported by (Basher and Ross, 2001). This suggests that the wheel tracks also contribute to the overall changes in connectivity. Soil swelling may also affect the surface changes. However, it is hard to distinguish between soil swelling and consolidation, even if high temporal resolution microrelief data are available (Eltner et al., 2017).

After the rainfall, the structural connectivity decreased at all plots. This non-intuitive surface development was most pronounced on the CWT plot (Fig. 5E). The before-rainfall soil surface structures created only by tillage and by the passage of the tractor exhibited clear flow paths oriented downslope (arrows in Fig. 5E). The impact of rainfall and runoff may create new flow paths via soil erosion, causing the water pathways to increase in length. The structural connectivity provides valuable information when observing surface changes within the plot. This was most visible on the SWT plots, where the flux between wheel track and surrounding soil was identified. Even when the wheel track is initially disconnected from the surrounding soil, the rainfall and runoff may form a connection. In this study, this happened in one of the SWT scenarios. This contrasting behavior may have been caused by the different tire tread for campaigns 1 and 2, since the passage of the tractor was in opposite directions and was followed by the trailed cultivator. The rainfall depth was higher during campaign No. 2 (when the two flow paths remained unchanged), and the wheel rut was slightly shallower during the second campaign. Two reasons can be put forward for the different outcome possibly affecting the NDD: (i) the different tire tread pattern, and (ii) the different lowering of the wheel track below the surrounding soil surface. Both of these effects potentially made the runoff more prone to create flow paths towards the wheel tracks (as seen in Fig. 5B). These flow paths influenced the reorganization of the soil surrounding the wheel tracks.

An increase in connectivity and a decrease in soil surface storage capacity was observed in the functional connectivity for all plots. The surface storage capacity was observed to decrease after successive rainfall events, as has also been shown by Darboux et al. (2002a). However, the decrease in surface storage capacity cannot alone explain the increase in connectivity. A crucial factor is the spatial organization and the connectivity of the depressions. Similar trends were also observed by Peñuela et al. (2016) under natural rainfall. The storage depression capacity decreased rapidly after rainfall started, whereas the shift in the connectivity threshold first rose and then in some cases decreased (Peñuela et al., 2016).

The role of a wheel track in increased functional connectivity (unlike in the case of structural connectivity) is not shown explicitly. SWT plot No. 1 exhibited higher functional connectivity than SWT plot No. 2 in both before-rainfall and after-rainfall soil surface conditions. However, a connection between the wheel track and the surrounding soil may not always be created, even after a substantial rainfall.

4.3. Comparison between connectivity indices and direct measurements

The direct measurements of runoff and sediment flow were in agreement with both functional connectivity and structural connectivity. Both the runoff amount and the sediment transport followed the order SWT > NWT > CWT. Differences between the plots were more pronounced when comparing the sediment fluxes than when comparing the runoff. This is most likely caused by the flow velocity in the wheel track, which increased the carrying capacity of the water. Wheel-track compaction in the direction of the slope increased the runoff coefficient and the sediment transport across all studied tillage systems, Ryken et al. (2018). The direction of a passing tractor (upslope or downslope) and of course the initial moisture conditions alter the surface runoff and the transport of sediments (Withers et al., 2006). An accumulation of eroded soil was observed in wider wheel tracks, while narrower wheel tracks exhibited greater transport capacity due to the acceleration of the surface runoff (Eltner et al., 2017). This indicates the importance of the flow velocity.

The same behavior (SWT > NWT > CWT order in surface runoff and sediment transport) was observed with structural and functional surface connectivity for the before-rainfall soil surface conditions.

The structural connectivity agreed in terms of the connection of the wheel track and the surrounding soil, as shown on the SWT plot (Fig. 5BD). The bi-modal to uni-modal shift of the NDD distribution corresponded to the SWT measurement, where runoff and sediment transport only occurred in the wheel track (Table 1). The NDD distribution during campaign No. 2 remained bimodal for before-rainfall and after-rainfall soil surface conditions. This corresponded to the direct measurements, where the runoff was active on both halves of the plot. No effect of different tire treads could be observed in the functional connectivity analysis.

The SWC and NWT plots exhibited similar maximum runoff in direct monitoring, and also similar functional connectivity during campaign No. 2 (Figs. 6 and 7). The NWT in campaign No. 2 even exhibited significantly higher runoff compared to all other plots if the lag time was not taken into consideration in the analysis (Table 2). This was caused by the rapid increase in runoff after it started – after some time, the runoff reached values similar to those on both SWT plots (Fig. 7). This increase may have been caused by the sudden connection of a few larger puddles to the outlet. The effect of the prolonged time lag in the NWT plot was not shown by functional connectivity. However, the largest

time lag observed in the NWT plot during campaign No. 1 was well reproduced for the after-rainfall situation, in agreement with functional connectivity. The largest sediment flow rate occurred during campaign No. 2, but it was not reproduced by functional connectivity. However, functional connectivity was based on the model where erosion was not implemented, and correspondence with the sediment transport was therefore not to be expected.

4.4. Comparison of structural and functional connectivity metrics

Structural connectivity allows the soil surface to be observed in greater detail. This index was able to identify multiple major flow paths which reached the bottom of the plot (via identification of uni-modal or bimodal distribution). Structural connectivity in combination with the flow accumulation algorithm was able to assess which part of the plot was connected to /disconnected from the drainage flow paths – i.e. the inter-plot connectivity. In contrast to the functional connectivity, the structural connectivity did not incorporate soil surface depressions in the analysis, since sink-less REM was used to generate the data. Functional connectivity takes the dynamics of the processes into consideration. The changes in surface depression storage can therefore be incorporated. Although the functional connectivity used in this study does not require physically-based derivation of the parameters or any calibration or validation procedure, additional information about soil properties and rainfall data are needed in order to derive the functional connectivity. In addition, it is much more time demanding to run an overland flow model in 10 mm raster resolution than to compute the structural connectivity.

5. Conclusion

Surface runoff, sediment transport and hydrological connectivity have been analyzed on freshly-tilled topsoil with wheel tracks by means of microrelief DEM indices. Two wheel-track orientations were studied: slope-wise direction (SWT) and contour lines-wise direction (CWT). The experimental setup was supplemented by a reference plot with no wheel track (NWT). The experimental plots were subjected to artificial rainfall, and DEMs were obtained using the Structure from Motion method -before rainfall and after rainfall. The surface microrelief was assessed with random roughness, and two measures of connectivity were compared with direct runoff monitoring of surface runoff and sediment transport.

The slope-wise wheel tracks (SWT) increased the sediment and the hydraulic connectivity of the surface. The wheel track itself exhibited high structural connectivity and low roughness when oriented slope-wise. This led to an increase in runoff and sediment transport. The soil surface adjacent to SWT is connected to the wheel track only to some extent, as shown by the direct measurements. The plot with a contour line wheel track (CWT) exhibited even higher roughness and lower connectivity than the plot without wheel tracks. A temporal decrease in random roughness and in soil surface storage was observed on all plots as the effect of the kinetic energy of the rainfall and runoff. The surface became more connected during the rainfall, as shown via the functional connectivity metric.

The microtopography affects the water and sediment routing on the soil surface. The wheel tracks, depending on orientation, increase or decrease the water and sediment fluxes during runoff events. The effect of SWT after a rainfall-runoff event is pronounced, since it becomes more connected to the surrounding soil. On the other hand, the effect of CWT decreases in time, as it becomes filled with deposited sediment. The emergent connection of SWT to the surrounding soil needs to be further studied – however, our study has shown that microrelief analysis may be used to identify this process. The conditions under which the CWT effect is diminished also need to be further studied. Sudden connection of parts of fields previously disconnected by CWT increases the runoff and the risk of erosion. Since the rainfall and runoff process increases the functional connectivity regardless of the wheel track presence or orientation the importance of soil surface treatments is stressed.

The outcomes of this study may be used for large-scale modeling of arable lands, where a single computation cell of the large-scale model can be represented by the experimental plot in this study. The direct link to such models can be found in random roughness (RR) and functional connectivity. Different RR can be assigned to cells based on the orientation of the wheel tracks in the cells. However, this usage of RR may be misleading, since the wheel track is a physical feature in the model cell rather than the roughness of the soil surface. Functional connectivity can be used to represent the surface retention of the cell, as suggested by (Antoine et al., 2009; Antoine et al., 2011; Peñuela et al., 2016). In this case, different functional connectivity will represent the cells in the model with or without wheel tracks, as well as the orientation of the wheel tracks. This application has the potential to improve runoff generation modeling studies. However, further study is required to determine usability.

CRediT authorship contribution statement

Jakub Jeřábek: Conceptualization, Methodology, Investigation, Writing – original draft. **David Zumr:** Conceptualization, Investigation, Methodology, Project administration. **Tomáš Laburda:** Formal analysis, Investigation, Data curation. **Josef Krása:** Formal analysis, Investigation, Data curation, Writing – review & editing, Project administration, Funding acquisition. **Tomáš Dostál:** Investigation, Writing – review & editing, Supervision, Project administration, Funding acquisition.

Declaration of Competing Interest

The authors declare that they have no known competing financial interests or personal relationships that could have appeared to influence the work reported in this paper.

Data availability

Data will be made available on request.

Acknowledgments

We would like to give our thanks to Tomas Brunner and Anna Zeiser from BAW Petzenkirchen and to Nasrin Haacke from TU Berlin, to students of CTU in Prague Julie Winterová, Tomáš Najman, Jan-František Kubát, and to our colleagues Barbora Jáchymová, Adam Tejkl, Jakub Stašek, Nina Noreika, Tailin Li, Petr Koudelka, Petr Kavka, Vaclav David and others for their help with preparing the experimental plots and for their hard field work during the experiments. We would also like to thank Hanka Donátová for conducting the lab analyses and Michal Sněhota and Martin Šanda for providing the necessary equipment. We thank Robin Healey for correcting the language.

Funding sources

This research was supported by Horizon 2020 research and innovation program project no 773903 under the title "Shui – Soil Hydrology research platform underpinning innovation to manage water scarcity in European and Chinese cropping systems", by Ministry of Education, Youth and Sports of the Czech Republic project no. LTAUSA19019 "Connectivity of sediment transport within intensively-used rural catchments", and by Ministry of Agriculture of the Czech Republic project no. QK1920224" Ways of soil erosion protection on the farm level after glyphosate ban". Additional support from Grant Agency of the Czech Technical University in Prague project no. SGS20/156/OHK1/3T/11 "Monitoring, experiments, and mathematical modelling of rainfall runoff and soil erosion processes" is also gratefully acknowledged.

Appendix

.

Table A1
The soil hydraulic parameters of Loam soil used to calculate the functional connectivity with the SMODERP2D model.

parameter name	parameter value
saturated hydraulic conductivity Ks [m s^{-1}]	1.67E-06
sorptivity S [m s^{1/2}]	1.39E-04
shallow water flow eq. parameter b [-]	1.73
shallow water flow eq. parameter X [-]	10.08
shallow water flow eq. parameter Y [-]	0.56

References

Angermann, L., Jackisch, C., Allroggen, N., Sprenger, M., Zehe, E., Tronicke, J., Weiler, M., Blume, T., 2017. Form and function in hillslope hydrology: Characterization of subsurface flow based on response observations. Hydrol. Earth Syst. Sci. 21, 3727–3748. https://doi.org/10.5194/hess-21-3727-2017.

Ankeny, M.D., Kaspar, T.C., Horton, R., 1990. Characterization of tillage and traffic effects on unconfined infiltration measurements. Soil Sci. Soc. Am. J. 54 (3), 837–840. https://doi.org/10.2136/sssaj1990.03615995005400030037x.

Antoine, M., Javaux, M., Bielders, C., 2009. What indicators can capture runoff-relevant connectivity properties of the micro-topography at the plot scale? Adv. Water Resour. 32 (8), 1297–1310. https://doi.org/10.1016/j.advwatres.2009.05.006.

Antoine, M., Javaux, M., Bielders, C.L., 2011. Integrating subgrid connectivity properties of the micro-topography in distributed runoff models, at the interrill scale. J. Hydrol. 403, 213–223. https://doi.org/10.1016/j.jhydrol.2011.03.027.

Appels, W.M., Bogaart, P.W., van der Zee, S.E.A.T.M., 2011. Influence of spatial variations of microtopography and infiltration on surface runoff and field scale hydrological connectivity. Adv. Water Resour. 34, 303–313. https://doi.org/10.1016/j.advwatres.2010.12.003.

Appels, W.M., Bogaart, P.W., van der Zee, S.E.A.T.M., 2016. Surface runoff in flat terrain: How field topography and runoff generating processes control hydrological connectivity. J. Hydrol. 534, 493–504. https://doi.org/10.1016/j.jhydrol.2016.01.021.

Augustin, K., Kuhwald, M., Brunotte, J., Duttmann, R., 2020. Wheel load and wheel pass frequency as indicators for soil compaction risk: A four-year analysis of traffic intensity at field scale. Geosci. 10, 1–15. https://doi.org/10.3390/geosciences10080292.

Basher, L.R., Ross, C.W., 2001. Role of wheel tracks in runoff generation and erosion under vegetable production on a clay loam soil at Pukekohe, New Zealand. Soil Tillage Res. 62 (3–4), 117–130. https://doi.org/10.1016/S0167-1987(01)00220-3.

Bauer, T., Strauss, P., Grims, M., Kamptner, E., Mansberger, R., Spiegel, H., 2015. Long-term agricultural management effects on surface roughness and consolidation of soils. Soil Tillage Res. 151, 28–38. https://doi.org/10.1016/j.still.2015.01.017.

Beven, K., Kirkby, M.J., 1979. A physically based, variable contributing area model of basin hydrology/un modèle à base physique de zone d'appel variable de l'hydrologie du bassin versant. Hydrol. Sci. J. 24 (1), 43–69.

Boardman, J., Poesen, J., 2006. Soil Erosion in Europe, Soil Erosion in Europe: Major Processes, Causes and Consequences. John Wiley & Sons, Ltd, Chichester, UK. https://doi.org/10.1002/0470859202.

Boardman, J., Vandaele, K., Evans, R., Foster, I.D.L., Aitkenhead, M., 2019. Off-site impacts of soil erosion and runoff: Why connectivity is more important than erosion rates. Soil Use Manag. 35 (2), 245–256.

Borselli, L., Cassi, P., Torri, D., 2008. Prolegomena to sediment and flow connectivity in the landscape: A GIS and field numerical assessment. Catena 75 (3), 268–277. https://doi.org/10.1016/j.catena.2008.07.006.

Botta, G.F., Becerra, A.T., Tourn, F.B., 2009. Effect of the number of tractor passes on soil rut depth and compaction in two tillage regimes. Soil Tillage Res. 103, 381–386. https://doi.org/10.1016/j.still.2008.12.002.

Bracken, L.J., Wainwright, J., Ali, G.A., Tetzlaff, D., Smith, M.W., Reaney, S.M., Roy, A. G., 2013. Concepts of hydrological connectivity: research approaches, pathways and future agendas. Earth Sci. Rev. 119, 17–34. https://doi.org/10.1016/j.earscirev.2013.02.001.

Carpenter, S.R., Caraco, N.F., Correll, D.L., Howarth, R.W., Sharpley, A.N., Smith, V.H., 1998. Nonpoint pollution of surface waters with phosphorus and nitrogen. Ecol. Appl. 8, 559–568. https://doi.org/10.1890/1051-0761(1998)008[0559:NPOSWW]2.0.CO;2.

Chen, L., Sela, S., Svoray, T., Assouline, S., 2013. The role of soil-surface sealing, microtopography, and vegetation patches in rainfall-runoff processes in semiarid areas. Water Resour. Res. 49, 5585–5599. https://doi.org/10.1002/wrcr.20360.

European Commission, 2021. Communication from the commission to the European parliament, the council, the European economic and social committee and the committee of the regions EU Soil Strategy for 2030 Reaping the benefits of healthy soils for people, food, nature and climate, COM(2021) 699 final, CELEX number: 52021DC0699.

Couturier, A., Daroussin, J., Darboux, F., Souchère, V., Le Bissonnais, Y., Cerdan, O., King, D., 2013. Improvement of surface flow network prediction for the modeling of erosion processes in agricultural landscapes. Geomorphology 183, 120–129. https://doi.org/10.1016/j.geomorph.2012.07.025.

Croft, H., Anderson, K., Brazier, R.E., Kuhn, N.J., 2013. Modeling fine-scale soil surface structure using geostatistics. Water Resour. Res. 49, 1858–1870. https://doi.org/10.1002/wrcr.20172.

Daraghmeh, O.A., Jensen, J.R., Petersen, C.T., 2008. Near-saturated hydraulic properties in the surface layer of a sandy loam soil under conventional and reduced tillage. Soil Sci. Soc. Am. J. 72 (6), 1728–1737.

Darboux, F., Davy, P., Gascuel-Odoux, C., Huang, C., 2002a. Evolution of soil surface roughness and flowpath connectivity in overland flow experiments. Catena 46 (2–3), 125–139. https://doi.org/10.1016/S0341-8162(01)00162-X.

Darboux, F., Davy, P., Gascuel-Odoux, C., 2002b. Effect of depression storage capacity on overland-flow generation for rough horizontal surfaces: Water transfer distance and scaling. Earth Surf. Proc. Land. 27 (2), 177–191. https://doi.org/10.1002/esp.312.

de Lima, R.P., da Silva, A.R., da Silva, Á.P., 2021. soilphysics: An R package for simulation of soil compaction induced by agricultural field traffic. Soil Tillage Res. 206, 104824 https://doi.org/10.1016/j.still.2020.104824.

Deasy, C., Brazier, R.E., Heathwaite, A.L., Hodgkinson, R., 2009. Pathways of runoff and sediment transfer in small agricultural catchments. Hydrol. Process. 23, 1349–1358. https://doi.org/10.1002/hyp.7257.

Dostál, T., Váška, J., Vrána, K., 2000. SMODERP — A Simulation Model of Overland Flow and Erosion Processes. Soil Eros. 135–161 https://doi.org/10.1007/978-3-662-04295-3_8.

Eltner, A., Kaiser, A., Abellan, A., Schindewolf, M., 2017. Time lapse structure-from-motion photogrammetry for continuous geomorphic monitoring. Earth Surf. Process. Landforms 42, 2240–2253. https://doi.org/10.1002/esp.4178.

Gómez, J.A., Nearing, M.A., 2005. Runoff and sediment losses from rough and smooth soil surfaces in a laboratory experiment. Catena 59, 253–266. https://doi.org/10.1016/j.catena.2004.09.008.

Guzha, A.C., 2004. Effects of tillage on soil microrelief, surface depression storage and soil water storage. Soil Tillage Res. 76, 105–114. https://doi.org/10.1016/j.still.2003.09.002.

Heathwaite, A.L., Quinn, P.F., Hewett, C.J.M., 2005. Modelling and managing critical source areas of diffuse pollution from agricultural land using flow connectivity simulation. J. Hydrol. 304 (1–4), 446–461. https://doi.org/10.1016/j.jhydrol.2004.07.043.

Helming, K., Römkens, M.J.M., Prasad, S.N., 1998. Surface Roughness Related Processes of Runoff and Soil Loss: A Flume Study. Soil Science Society of America Journal 62 (1), 243–250. https://doi.org/10.2136/sssaj1998.03615995006200010031x.

Hjerdt, K.N., McDonnell, J.J., Seibert, J., Rodhe, A., 2004. A new topographic index to quantify downslope controls on local drainage. Water Resour. Res. 40 (5), 1–6. https://doi.org/10.1029/2004WR003130.

Hopp, L., McDonnell, J.J., 2009. Connectivity at the hillslope scale: Identifying interactions between storm size, bedrock permeability, slope angle and soil depth. J. Hydrol. 376 (3–4), 378–391. https://doi.org/10.1016/j.jhydrol.2009.07.047.

Jackisch, C., Angermann, L., Allroggen, N., Sprenger, M., Blume, T., Tronicke, J., Zehe, E., 2017. Form and function in hillslope hydrology: In situ imaging and characterization of flow-relevant structures. Hydrol. Earth Syst. Sci. 21, 3749–3775. https://doi.org/10.5194/hess-21-3749-2017.

Jester, W., Klik, A., 2005. Soil surface roughness measurement – Methods, applicability, and surface representation. Catena 64, 174–192. https://doi.org/10.1016/j.catena.2005.08.005.

Jourgholami, M., Labelle, E.R., 2020. Effects of plot length and soil texture on runoff and sediment yield occurring on machine-trafficked soils in a mixed deciduous forest. Ann. For. Sci. 77, 1–11. https://doi.org/10.1007/s13595-020-00938-0.

Kašpar, M., Bližňák, V., Hulec, F., Müller, M., 2021. High-resolution spatial analysis of the variability in the subdaily rainfall time structure. Atmos. Res. 248, 105202.

Kavka, P., Strouhal, L., Jáchymová, B., Krása, J., Báčová, M., Laburda, T., Dostál, T., Devátý, J., Bauer, M., 2018. Double Size Fulljet Field Rainfall Simulator for Complex Interrill and Rill Erosion Studies. Stavební Obz. - Civ. Eng. J. 27, 183–194. https://doi.org/10.14311/cej.2018.02.0015.

Kavka, P., Jeřábek, J., Landa, M., 2022. SMODERP2D—Sheet and Rill Runoff Routine Validation at Three Scale Levels. Water 14 (3). https://doi.org/10.3390/w14030327.

Kim, H., Anderson, S.H., Motavalli, P.P., Gantzer, C.J., 2010. Compaction effects on soil macropore geometry and related parameters for an arable fiel. Geoderma 160 (2), 244–251. https://doi.org/10.1016/j.geoderma.2010.09.030.

Krása, J., Dostal, T., Van Rompaey, A., Vaska, J., Vrana, K., 2005. Reservoirs' siltation measurements and sediment transport assessment in the Czech Republic, the Vrchlice catchment study. Catena 64, 348–362. https://doi.org/10.1016/j.catena.2005.08.015.

Kroulík, M., Kvíz, Z., Kumhála, F., Hůla, J., Loch, T., 2011. Procedures of soil farming allowing reduction of compaction. Precis. Agric. 12, 317–333. https://doi.org/10.1007/s11119-010-9206-1.

Laburda, T., Krása, J., Zumr, D., Devátý, J., Vrána, M., Zambon, N., Johannsen, L.L., Klik, A., Strauss, P., Dostál, T., 2021. SfM-MVS Photogrammetry for Splash Erosion Monitoring under Natural Rainfall. Earth Surf. Proc. Land. 46 (5), 1067–1082. https://doi.org/10.1002/esp.5087.

Lal, R., 1999. Long-term tillage and wheel traffic effects on soil quality for two central Ohio soils. J. Sustain. Agric. 14 (4), 67–84. https://doi.org/10.1300/J064v14n04_07.

Landa, M., Jeřábek, J., Pešek, O., Kavka, P., 2019. SMODERP2D soil erosion model entering an open source era with gpu-based parallelization. Int. Arch. Photogramm. Remote Sens Spat. Inf. Sci. - ISPRS Arch. 42, 143–149. https://doi.org/10.5194/isprs-archives-XLII-4-W14-143-2019.

Leys, A., Govers, G., Gillijns, K. and Poesen, J.: Conservation tillage on loamy soils: Explaining the variability in interrill runoff and erosion reduction, Eur. J. Soil Sci., 58(6), 1425–1436, 2007.
Lindstrom, M.J., Voorhees, W.B., Randall, G.W., 1981. Long-Term Tillage Effects on Interrow Runoff and Infiltration. Soil Sci. Soc. Am. J. 45 (5), 945–948. https://doi.org/10.2136/sssaj1981.03615995004500050025x.
Luo, J., Zheng, Z., Li, T., He, S., 2018. Assessing the impacts of microtopography on soil erosion under simulated rainfall, using a multifractal approach. Hydrol. Process. 32, 2543–2556. https://doi.org/10.1002/hyp.13170.
Moreno, R.G., Álvarez, M.C.D., Alonso, A.T., Barrington, S., Requejo, A.S., 2008. Tillage and soil type effects on soil surface roughness at semiarid climatic conditions. Soil Tillage Res. 98, 35–44. https://doi.org/10.1016/j.still.2007.10.006.
Onstad, C.A., 1984. Depressional storage on tilled soil surfaces. Trans. - Am. Soc. Agric. Eng. https://doi.org/10.13031/2013.32861.
Onstad, C.A., Wolfe, M.L., Larson, C.L., Slack, D.C., 1984. Tilled soil subsidence during repeated wetting. Trans. - Am. Soc. Agric. Eng. https://doi.org/10.13031/2013.32862.
Outram, F.N., Cooper, R.J., Sünnenberg, G., Hiscock, K.M., Lovett, A.A., 2016. Antecedent conditions, hydrological connectivity and anthropogenic inputs: Factors affecting nitrate and phosphorus transfers to agricultural headwater streams. Sci. Total Environ. 545–546, 184–199. https://doi.org/10.1016/j.scitotenv.2015.12.025.
Pagliai, M., Marsili, A., Servadio, P., Vignozzi, N., Pellegrini, S., 2003. Changes in some physical properties of a clay soil in Central Italy following the passage of rubber tracked and wheeled tractors of medium power. Soil Tillage Res. 73, 119–129. https://doi.org/10.1016/S0167-1987(03)00105-3.
Pagliai, M., Vignozzi, N., Pellegrini, S., 2004. Soil structure and the effect of management practices. Soil and Tillage Research 79 (2), 131–143. https://doi.org/10.1016/j.still.2004.07.002.
Peñuela, A., Darboux, F., Javaux, M., Bielders, C.L., 2016. Evolution of overland flow connectivity in bare agricultural plots. Earth Surf. Process. Landforms 41, 1595–1613. https://doi.org/10.1002/esp.3938.
Pringle, C., 2003. What is hydrologic connectivity and why is it ecologically important? Hydrol. Process. 17, 2685–2689. https://doi.org/10.1002/hyp.5145.
Probst, J.L., 1985. Nitrogen and phosphorus exportation in the Garonne Basin (France). J. Hydrol. 76 (3–4), 281–305. https://doi.org/10.1016/0022-1694(85)90138-6.
Prosdocimi, M., Burguet, M., Di Prima, S., Sofia, G., Terol, E., Rodrigo Comino, J., Cerdà, A., Tarolli, P., 2017. Rainfall simulation and Structure-from-Motion photogrammetry for the analysis of soil water erosion in Mediterranean vineyards. Sci. Total Environ. 574, 204–215. https://doi.org/10.1016/j.scitotenv.2016.09.036.
R Core Team. (2018). R: A Language and Environment for Statistical Computing.
Rinderer, M., Ali, G., Larsen, L.G., 2018. Assessing structural, functional and effective hydrologic connectivity with brain neuroscience methods: State-of-the-art and research directions. Earth-Science Rev. 178, 29–47. https://doi.org/10.1016/j.earscirev.2018.01.009.
Ryken, N., Vanden Nest, T., Al-Barri, B., Blake, W., Taylor, A., Bodé, S., Ruysschaert, G., Boeckx, P., Verdoodt, A., 2018. Soil erosion rates under different tillage practices in central Belgium: New perspectives from a combined approach of rainfall simulations and 7 Be measurements. Soil Tillage Res. 179 (January), 29–37. https://doi.org/10.1016/j.still.2018.01.010.
Seehusen, T., Riggert, R., Fleige, H., Horn, R., Riley, H., 2019. Soil compaction and stress propagation after different wheeling intensities on a silt soil in South-East Norway, Acta Agric. Scand. Sect. B Soil Plant Sci., 69(4), 343–355, https://doi:10.1080/09064710.2019.1576762.
Silgram, M., Jackson, D.R., Bailey, A., Quinton, J., Stevens, C., 2010. Hillslope scale surface runoff, sediment and nutrient losses associated with tramline wheelings. Earth Surf. Proc. Land. 35 (6), 699–706. https://doi.org/10.1002/esp.1894.
Smith, M.W., 2014. Roughness in the Earth Sciences. Earth-Science Rev. 136, 202–225. https://doi.org/10.1016/j.earscirev.2014.05.016.
Souchere, V., King, D., Daroussin, J., Papy, F., Capillon, A., 1998. Effects of tillage on runoff directions: Consequences on runoff contributing area within agricultural catchments. J. Hydrol. 206 (3–4), 256–267. https://doi.org/10.1016/S0022-1694(98)00103-6.
Stieglitz, M., Shaman, J., McNamara, J., Engel, V., Shanley, J., Kling, G. W., 2003. An approach to understanding hydrologic connectivity on the hillslope and the implications for nutrient transport. Global Biogeochemical Cycles, 17(4), n/a-n/a. https://doi.org/10.1029/2003gb002041.
Taconet, O., Ciarletti, V., 2007. Estimating soil roughness indices on a ridge-and-furrow surface using stereo photogrammetry. Soil Tillage Res. 93 (1), 64–76. https://doi.org/10.1016/j.still.2006.03.018.
Takken, I., Govers, G., Steegen, A., Nachtergaele, J., Guérif, J., 2001. The prediction of runoff flow directions on tilled fields. J. Hydrol. 248 (1–4), 1–13. https://doi.org/10.1016/S0022-1694(01)00360-2.
Tarboton, D.G., 2015. Taudem 5, Terrain Analysis Using Digital Elevation Models [Online]. Available from http://hydrology.usu.edu/taudem/taudem5/.
Tarolli, P., Cavalli, M., & Masin, R. (2019). High-resolution morphologic characterization of conservation agriculture. Catena, 172(July 2018), 846–856. https://doi.org/10.1016/j.catena.2018.08.026.
Thompson, S.E., Katul, G.G., Porporato, A., 2010. Role of microtopography in rainfall-runoff partitioning: An analysis using idealized geometry. Water Resour. Res. 46, 1–11. https://doi.org/10.1029/2009wr008835.
Westoby, M.J., Brasington, J., Glasser, N.F., Hambrey, M.J., Reynolds, J.M., 2012. "Structure-from-Motion" photogrammetry: A low-cost, effective tool for geoscience applications. Geomorphology 179, 300–314. https://doi.org/10.1016/j.geomorph.2012.08.021.
Withers, P.J.A., Hodgkinson, R.A., Bates, A., Withers, C.M., 2006. Some effects of tramlines on surface runoff, sediment and phosphorus mobilization on an erosion-prone soil. Soil Use Manag. 22 (3), 245–255. https://doi.org/10.1111/j.1475-2743.2006.00034.x.
Wolstenholme, J.M., Smith, M.W., Baird, A.J., Sim, T.G., 2020. A new approach for measuring surface hydrological connectivity. Hydrol. Process. 34, 538–552. https://doi.org/10.1002/hyp.13602.
Yang, J., Chu, X., 2013. Quantification of the spatio-temporal variations in hydrologic connectivity of small-scale topographic surfaces under various rainfall conditions. J. Hydrol. 505, 65–77. https://doi.org/10.1016/j.jhydrol.2013.09.013.
Zhao, L., Hou, R., Wu, F., Keesstra, S., 2018. Effect of soil surface roughness on infiltration water, ponding and runoff on tilled soils under rainfall simulation experiments. Soil Tillage Res., 179(June 2017), 47–53. https://doi.org/10.1016/j.still.2018.01.009.
Zobeck, T.M., Onstad, C.A., 1987. Tillage and rainfall effects on random roughness: A review. Soil Tillage Res. 9, 1–20. https://doi.org/10.1016/0167-1987(87)90047-X.

2. HYDROLOGICAL PROCESSES ON A CATCHMENT SCALE

Attached research articles:

- ***Zumr, D.**, Dostál, T., & Devátý, J. (2015). Identification of prevailing storm runoff generation mechanisms in an intensively cultivated catchment. Journal of Hydrology and Hydromechanics, 63(3). https://doi.org/10.1515/johh-2015-0022*

  First study presenting the Nučice experimental catchment. We analyzed rainfall-runoff events and based on the shapes of the hyetograph, the hydrograph recorded at the gauge station, and the eroded sediment flux to distinguish between different runoff generation processes. Shallow subsurface runoff and tile drains were identified as the most common mechanisms of fast runoff. Surface runoff occurs rarely only during extreme rainfall events or happens only in distinct areas within the catchment. Based on the relationship between runoff and sediment concentration in the runoff water, we were able to distinguish the origin of the sediment. Hysteretic behavior indicated sediment resuspension of the streambed sediment or soil erosion from the attached fields.

- *Jeřábek, J., **Zumr D.**, & Dostál, T. (2017). Identifying the plough pan position on cultivated soils by measurements of electrical resistivity and penetration resistance. Soil & Tillage Research, 174. https://doi.org/10.1016/j.still.2017.07.008*

  As shown by Zumr et al. (2015), compacted plough pan significantly influences soil water regime and runoff dynamics. In this study we successfully implemented the electrical resistivity tomography technique to map the shallow subsurface and identify the depth and uniformity of the plough pan.

- *Li, T., Jeřábek, J., Noreika, N., Dostál, T., & **Zumr, D.** (2021). An overview of hydrometeorological datasets from a small agricultural catchment (Nučice) in the Czech Republic. Hydrological Processes, 35(2), e14042. https://doi.org/10.1002/hyp.14042*

  This manuscript presents general activities that have been studied in the Nucice experimental catchment and lists the instrumentation of the catchment. Spatial and temporal variability of soil moisture within the catchment, which is one of the dominant factors for runoff generation (Zumr et

al., 2015), is elaborated in more detail. The manuscript also introduces a publicly available database (WALNUD) of the aggregated daily data that have been measured.

Additional relevant publications:

- *Li, T., Jeřábek, J., **Zumr, D.**, Noreika N., & Dostál, T. (2021). Assessing spatial soil moisture patterns at a small agricultural catchment. 2021 IEEE International Workshop on Metrology for Agriculture and Forestry, 175226. https://doi.org/10.1109/MetroAgriFor52389.2021.9628588*

  Analysis of spatiotemporal topsoil moisture distribution on the Nucice catchment. The monitoring was done repeatedly, handheld TDR soil moisture probe was used to measure soil water content in upper 10 cm of the soil profile in a dense grid over the catchment. It was shown that soil moisture exhibits higher spatial variability when the catchment has medium moisture conditions. Dry or saturated catchment has more uniform topsoil water content distribution.

- *Noreika, N., Li, T., **Zumr, D.**, Krasa, J., Dostal, T., & Srinivasan, R. (2020). Farm-Scale Biofuel Crop Adoption and Its Effects on In-Basin Water Balance. Sustainability 2020, Vol. 12, Page 10596, 12(24), 10596. https://doi.org/10.3390/SU122410596*

  Large scale simulation of the effect of rape seed crops on the overall water balance of the Nucice catchment. SWAT model was built and parametrized based on the measured data. The results indicate that especially due to different schedule of the rape seed seeding and harvesting, compared to eg. wheat, the crops require more soil water and more likely experience water stress during the vegetation season.

- *Jeřábek, J., & **Zumr, D.** (2021). Geophysical survey as a tool to reveal subsurface stratification at a small agricultural headwater catchment: a case study. Civil Engineering Journal, 30(3), 766–778. https://doi.org/10.14311/CEJ.2021.03.0059*

  Application of the electrical resistivity tomography on a scale of the whole catchment. The ERT was used to identify the 3D position of the bedrock, which is an important boundary condition in the numerical models.

- *Tenreiro, T. R., Jeřábek, J., Gómez, J. A., **Zumr, D.**, Martínez, G., García-Vila, M., & Fereres, E. (2022). Simulating water lateral inflow and its contribution to spatial variations of rainfed wheat yields. European Journal of Agronomy, 137, 126515. https://doi.org/10.1016/J.EJA.2022.126515*

  As was shown by Zumr et al. (2015) and Jeřábek et al. (2017), shallow subsurface lateral flow (interflow) is often responsible for soil water concentration in the converging parts of the catchments. This study presents a way of coupling Richards equation-based model HYDRUS 1D with crops growth model AquaCrop. The routine is based on an artificial network algorithm. The model was trained on data from a small catchment in southern Spain; the concept was proved to be valid.

J. Hydrol. Hydromech., 63, 2015, 3, 246–254
DOI: 10.1515/johh-2015-0022

Identification of prevailing storm runoff generation mechanisms in an intensively cultivated catchment

David Zumr*, Tomáš Dostál, Jan Devátý

Department of Irrigation, Drainage and Landscape Engineering, Faculty of Civil Engineering, Czech Technical University in Prague, Thákurova 7, 16629, Prague 6, Czech Republic.
* Corresponding author. Tel.: +420 224354745. E-mail: david.zumr@fsv.cvut.cz

Abstract: The fact that flash floods initiated in arable catchments are often accompanied by massive sediment and nutrient loads often leads to the assumption that surface runoff is the principle pathway by which runoff reaches watercourses. On the basis of an evaluation of several rainfall-runoff events in a representative agricultural catchment, we show that runoff from cultivated land may be generated in a way similar to that seen on forested slopes, where shallow subsurface runoff is the predominant pathway by which runoff makes its way to watercourses in most runoff events. To identify the predominant runoff pathway, we employed a combination of turbidity measurements and stream discharge data. Suspended sediment flux, a newly introduced index representing the ratio between precipitation duration and total sediment yield, and direction of the discharge-turbidity hysteresis loops were proposed as reflective indicators of the frequency of runoff via different pathways.

In our study, most of the events initiated by rainstorms of various intensities and durations resulted in rapid increases in stream discharge. Although we observed temporal variability of topsoil properties attributable to seasonal weather changes and agricultural activities, e.g. bulk density and porosity, runoff generation was mainly driven by precipitation characteristics and the initial catchment saturation.

Keywords: Shallow subsurface runoff; Surface runoff; Rainfall-runoff; Soil erosion; Suspended solids transport; Agriculture watershed.

INTRODUCTION

The IPCC has cited more frequent occurrences of intensive storm events as evidence of climate change in Central Europe (Kovats et al., 2014). Recent hydrological research has therefore focused on studies of rainfall-runoff processes, though far fewer studies have investigated cultivated agricultural catchments than forested catchments. Rainfall-runoff processes in cultivated catchments are of great importance, as many fields are situated on slopes, and because arable land is one of the main non-point sources of solid particles, nutrients, fertilizers and herbicides in rivers and lakes (Dorioz and Ferhi, 1994).

The runoff response of a catchment is determined by climate, size, topography, land use and soil parameters. Infiltration regime and runoff routing depend on many factors at various spatial and temporal scales. Runoff can make its way to watercourses via several pathways including overland flow, subsurface stormflow, pipeflow or groundwater flow (Jones, 1997). The hydrology of cultivated catchments has specific features. The temporary, variable properties of periodically cultivated soils are a crucial factor that must be taken into account in order to understand flow processes in agriculture catchments (Pare et al., 2011). Bachmair et al. (2012) and Birkel et al. (2011) have suggested that there is also seasonal variability of the catchment water storage and runoff generation on grasslands and forested hillslopes. Soil structure is a property that is often considered to be static rather than dynamic. This could be a reasonable assumption for extensively compacted land or subsoil, but not for regularly tilled topsoil layers. Anthropogenic effects, e.g. overuse of heavy machinery, tillage, ploughing and harvesting, and also natural processes such as rapid vegetation and root growth, edaphon activity, the kinetic energy of raindrops, freezing, thawing, etc., cause recurrent cycles of topsoil loosening, compaction and surface sealing (Alaoui et al., 2011). The gradual deformation of the soil structure within a growing season causes a reduction in the volume and the connectivity of inter-aggregate voids. Eroded fine particles clog the macropores and preferential pathways, and infiltration capacity and soil water storage decrease. Originally, connected large pores normally serve as a quick bypass for infiltrating water. Therefore, based on the state of the topsoil structure and subsoil permeability, one can expect different water runoff mechanisms; ranging from deep percolation and shallow subsurface lateral flow to surface runoff to play a greater or lesser role in runoff generation. This phenomenon does not necessarily have a significant effect on the soil water regime in soils where the subsoil contains a developed macropore network due to soil fauna and roots (Roulier et al., 2002; Steenhuis et al., 1988).

Stormflow generation at the hillslope scale has been widely studied since the 1960s (Whipkey, 1965), mainly on steep forested slopes, where subsurface runoff contributes greatly to the total runoff due to root channels, old root holes, and bio-pores. Various methods based on detailed hillslope inspection and dye tracer experiments, (e.g. Noguchi et al., 1999), indirect observations using natural isotopes and numerical modelling (e.g. Dušek et al., 2012; Holko et al., 2011; McDonnell et al., 1991; McGuire and McDonnell, 2010; Šanda et al., 2014; Schneider et al., 2014), and multiple regression analysis of selected rainfall-runoff events (Hrnčíř et al., 2010) have suggested that the dominant factors are shallow subsurface runoff, pipeflow of saturation excess overland flow, and rapid stream flow response to rainfall, often caused by pre-event water in the runoff in humid temperate catchments (Klaus et al., 2013).

Cultivated soils also exhibit similar runoff regimes. Cox et al. (2006) showed that the agricultural catchment described in their paper was much more likely to generate runoff than the forested catchment, due to rapid saturation of the tilled soil above the hardpan. Studies by Coquet et al. (2005), van Asch et

al. (2001) and Verbist et al. (2007) confirmed the importance of compacted subsoil and the presence of lateral subsurface water flow in cultivated soils. They observed the low-permeable pan beneath wheel tracks, which caused local saturation in the seed bed where lateral flow was initiated during rainstorms. Similar runoff formation on a plot scale was observed by Bertolino et al. (2010). Despite evidence of subsurface flow processes, models based on the infiltration excess (overland flow) mechanism, e.g. the Soil Conservation Service (SCS) Curve Number method (CN) (USDA, 1983), are mainly employed when modelling the initiation of surface runoff and related processes, e.g. transport of soil particles and nutrients from cultivated soils.

Classical modelling approaches are often based on parameterization of a single conceptual model. Temporary variable runoff mechanisms within an individual catchment are rarely taken into consideration. This issue is well known, and has been identified by several authors, e.g. Beven (2001), Grayson et al. (1992), Schmocker-Fackel et al. (2007). The problem is to identify the prevailing mechanism for each rainfall-runoff event or annual period, especially when only limited data are available.

The aim of our paper is to examine the runoff dynamics of a small arable catchment, and to identify the prevailing runoff generation mechanisms. On the basis of observations, we test a hypothesis which assumes two dominant runoff mechanisms that prevail based on the state of the actual topsoil structure, vegetation cover and rainfall intensity and amount:

(a) freshly tilled soil contains stable macro-aggregates with hydraulically conductive inter-aggregate voids (preferential pathways). Water percolates through the preferential pathways towards a compacted and less conductive subsoil layer, where interflow is formed. In this case, subsurface runoff is the most common form of catchment drainage and results in an instant increase in discharge into the stream channel, with only limited sediment transport. The solid particles originate only from remobilisation of the deposited sediment in the stream channel. No infiltration excess surface runoff occurs under these conditions;

(b) during summer, when the topsoil may be compacted, the surface is often sealed and the number of preferential pathways is reduced. The bulk soil infiltration capacity is reduced and surface runoff may appear. The same process and effect can theoretically also be observed for loosened topsoil when there is an extreme and sufficiently long rainfall event, when its intensity exceeds the saturated hydraulic conductivity.

Our study investigates the following questions: (i) Do the temporary variable hydraulic properties of topsoil play a significant role in runoff generation? (ii) Where do suspended solid particles monitored in the discharge come from (from the field – taken by surface runoff, or from the stream channel – resuspended particles from previous events) and can we use turbidity data as additional information for estimating the water pathways and the dominant runoff mechanism?

STUDY AREA AND METHODS

Study site

The Nucice experimental catchment, which was established in 2011, is located in central Bohemia (Czech Republic), 30 km east of Prague, in a moderately hilly area at elevations of 382 m to 417 m. The average elevation is 401 m. The position of the basin closing profile is 49°57'49.230"N, 14°52'13.242"E. The catchment has an area of 0.531 km^2 (Fig. 1). The inclination of the hillslopes ranges from 1% to 12% with a mean slope of 3.9% (Fig. 2). The climate is humid continental, with average annual precipitation of 630 mm, evapotranspiration of 500–550 mm, and mean annual air temperature 6°C. The maximum mean

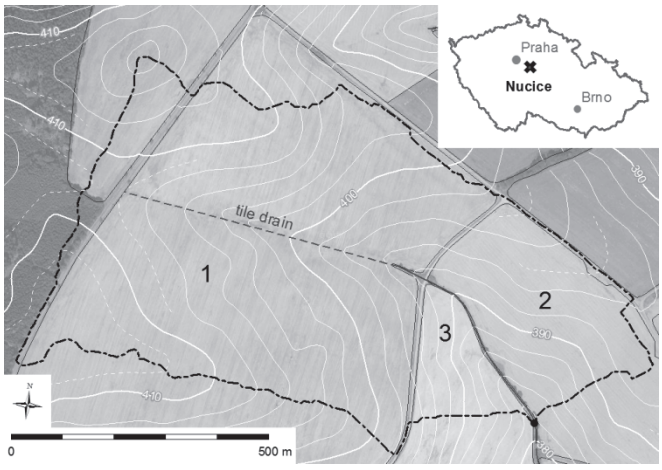

Fig. 1. Nucice catchment. Numbers denote the fields with different crops and tillage practices.

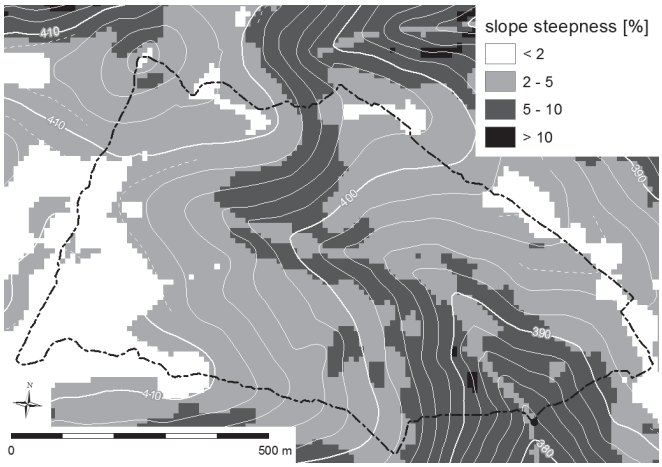

Fig. 2. Slope map of the Nucice catchment.

monthly rainfall occurs in July, and is delivered mostly by frontal and convective storms. The catchment was chosen for its uniform land use. 95.3% of the area is under active cultivation. The remaining area includes watercourse, sparse grasslands, riparian trees, shrubs and local roads. There is no urbanization or resident population.

The catchment is underlain by conglomerates, sandstone and siltstone. The soils are classified as Luvisols and Cambisols with a loamy Ap horizon (0.1–0.2 m deep) underlain by a silty and silty-clay B horizon. The content of clay particles in the topsoil is around 8%. The soil has low inner aggregate (soil matrix) hydraulic conductivity, with measured values of approximately 10^{-8} m s^{-1} – 2.3. 10^{-7} m s^{-1}. The bulk topsoil saturated hydraulic conductivity (K_s) ranges between 10^{-5} m s^{-1} and 10^{-4} m s^{-1}, depending on the season. The K_s is spatially variable, the higher values related to well developed and connected inter-aggregate voids. The divide between the topsoil and the subsoil is clearly observable via soil probing or penetration tests. The division between the uniform layers in Fields 1 and 2 was found at a depth of 0.14 ± 0.02 m. The subsoil in Field 3, which was conventionally tilled until 2013, was observed to be approximately 0.3 m in depth (Zumr et al., 2014). The subsoil is poor in structure, has a higher clay content and bulk density than the topsoil, and does not contain an extensive macropore network. The macropores that are present are formed by decayed roots and wormholes. They are mostly vertical, and are disconnected from each other.

The catchment is divided into three fields cultivated by two farmers. Field 1 (0.38 km^2) and Field 2 (0.09 km^2) (Fig. 1) have been tilled conservatively since 2000, with a combination of a compact disk harrow and a cultivator. The maximum depth of soil disturbance caused by tillage is 0.18 m. A GPS guidance system with preserved parallel traffic lanes of 8 m span is implemented. The standard crop rotation includes mainly winter wheat, summer oats, winter rape and mustard. As conservatively tilled soils cover most of the catchment, the main focus in following text will be on these fields. The remaining western part of the basin (Field 3, 0.03 km^2) was tilled conventionally until 2012, with ploughing depth up to 0.3 m, and in 2013 conservation tillage was introduced.

The catchment area is drained by a trained rural channel, which starts in the upper part of the catchment as a single tile drain. The total stream length is 1106 m, from which 566 m is an open channel with a regular trapezoid cross section, stabilized by concrete tiles. The channel is approximately 1.2 m in depth and 0.6 m in width at the stream bed. The mean slope of the drainage line is 3%. There are two culverts in the channel, each 0.8 m in diameter and about 8 m in length, but they do not have a significant effect on the water and sediment flow. The concrete lining is disturbed in some parts, and the stream bed is covered by sediment on the most of its length, which allows further sedimentation of solid particles and in-stream vegetation growth. The fields are cultivated right up to the stream banks with no buffer zones.

Catchment instrumentation

The experimental catchment is equipped with a standard meteorological station, where precipitation intensity, air temperature, humidity, wind speed and net solar radiation are monitored. The stream discharge is measured in an H flume with capacity up to 400 l s^{-1}, using a calibrated rating curve and duplicate water level recording with a pressure probe (LMP 307, BD Sensors, Czech Republic) and an ultrasonic sensor (U-GAGE T30UX, Banner, USA). A total suspended solids sensor (ViSolid 700 IQ, WTW, Germany) and a water sampling tube (3700 Full-size Portable Sampler, Teledyne ISCO, USA) are installed directly below the stream gauge in a small stilling basin. The recorded suspended sediment concentration is calibrated on the basis of the measured concentration of sediment in collected water samples, which are obtained during runoff events. The sediment yield is obtained through simultaneous measurement of the discharge and the suspended solids concentration. The groundwater level in the vicinity of the gauging station is monitored by means of two piezometers. The soil water regime is monitored by four multi-parameter water content reflectometers CS650 (Campbell Sci., UK), which are installed 20 m from the gauging station in Field no. 2 at a depth of 0.07 m, 0.12 m, 0.25 m and 0.4 m. The probes record water content, bulk electrical conductivity and soil temperature. All measured data are collected and recorded automatically every five minutes during the growing season and every ten minutes during the rest of the year by a CR1000 control and measurement datalogger (Campbell Sci., UK).

Since 2011, when the catchment was established, undisturbed 100 cm^3 soil samples have been regularly taken to evaluate seasonal changes in the physical macroscopic properties of the topsoil, such as bulk density, actual moisture content and porosity. The highest sampling frequency is in the period from May until October, when rapid macrostructural changes are expected due to crop growth and agrotechnical operations. During each sampling campaign, approximately twenty soil cores from selected sites are taken and analysed.

Complementary experiments related to runoff generation and sediment transport

For a clear interpretation of the monitored rainfall-runoff events, we used the outcomes of previously conducted experiments: (a) plot scale rainfall simulations to investigate stormflow routing under various rainfall and field conditions (Strouhal et al., 2014); and (b) artificial flood wave experiments to estimate volume and resuspension of streambed sediment (Dostál et al., 2013).

Strouhal et al. (2014) presented a plot scale experiment aimed at observing and quantifying the components of runoff from cultivated soil during high-intensity rainfall. They used a mobile rainfall simulator equipped with four solenoid-controlled nozzles (40WSQ FullJet, Spraying Systems Co) positioned 2.6 m above the soil. An inclined experimental plot (8 x 2 m) was successively exposed to uniform simulated rainfall with intensity ranging from 23 to 64 mm h^{-1} and duration ranging from 1 h to 2.5 h. These simulated rainfall parameters were selected to represent intensive rainfall events observed in the study locality, to generate surface runoff and to initiate soil erosion. Similar rainfall characteristics have been used is soil erosion studies elsewhere in Europe (e.g. Montenegro et al., 2013, Ries et al., 2013). The dynamics of surface and shallow subsurface runoff and the soil water regime at three soil depths were monitored. Various initial soil moisture conditions and vegetation stages; from cultivated fallow to stubble, delimited the simulations. Variable proportions of both monitored runoff components were observed in relation to rainfall intensity and duration, ranging from zero surface runoff to a distinct dominance of surface runoff. Both components reacted very dynamically to the precipitation: shallow subsurface runoff was formed first under all tested conditions on the given soil profile (a tilled loamy topsoil, compacted subsoil at a depth of 0.15 m). In two simulations out of seven, both runoff components reached quasi steady-state conditions, and the subsurface discharge ranged from 30% to 40% of the direct runoff intensity. Even with the highest tested precipitation intensities, surface runoff always formed due to saturation excess of the topsoil, irrespective of the topsoil properties and crops.

The results of Strouhal et al. (2014) prove that lateral runoff through the shallow topsoil can easily cause a very quick increase of stream discharge. This runoff mechanism is not accompanied by significant soil erosion, but the increased stream flow causes a resuspension of streambed sediment and increased water turbidity.

It is difficult to distinguish the origin of the solid particles that are monitored at the gauging station. Therefore, Dostál et al. (2013) conducted six artificial flood experiments in the stream on the catchment to estimate the volume of resuspended stream bed sediments. The artificial waves (uniform discharge of 40 l s^{-1}, volume of 16 m^3) were introduced into the channel 450 m upstream of the gauging station. The aim was to monitor the flood wave transformation and the sediment transport within the channel in a way similar to Eder et al. (2014). On the basis of the results, it was concluded that the channel does contain sediment from previous erosion events that can be mobilized by even a slight increase of discharge. The peak discharge at the catchment outlet reached approximately 20 l s^{-1} to 30 l s^{-1} (such values have been reached or exceeded five times in the last four years of natural runoff events observation) and duration of about 30 to 60 minutes, were able to carry the solid particles

only a short distance. The hysteresis loop between discharge and sediment concentration was always clockwise, which implies that the sediment originates from the stream bed in the vicinity of the gauging station (Eder et al. 2010, Seeger et al. 2004). The highest suspended solids concentration was observed at the very beginning of the flood wave, when the maximum measured value reached almost 8 g l^{-1} (corresponding to most of the natural flood events). The suspended solids flux reached as high as 900 kg h^{-1} at its peak, which is also comparable with recorded natural runoff events when no surface runoff was observed.

Separation of the dominant runoff mechanisms

In the Nucice catchment, three relevant runoff mechanisms are considered: (a) surface runoff due to infiltration excess, (b) shallow subsurface runoff in combination with pre-event water flow, (c) surface runoff due to saturation excess. Runoff due to deep water percolation causing a rise in the groundwater table is omitted, because the groundwater table is deep for most of the year, and its recharge is very slow due to the low hydraulic conductivity of the subsoil.

We aimed to identify the dominant runoff mechanism on the basis of rainfall, discharge, suspended solids and soil water regime data. To confirm the presence of surface runoff, we inspected the catchment after each event, when evidence of surface runoff was easy to document. The evidence of surface runoff is usually very clear; the most pronounced indicators are flattened riparian vegetation, flushed and wet man made shallow ditches, soil erosion resulting in suspension of particles and the development of rills. We quite often found small amounts of ponded or flowing water in wheel tracks. This runoff was neglected, because the area of wheel tracks was small and the tracks were not directly connected to the stream channel.

Each runoff mechanism produces greater or less runoff depending on actual catchment and rainfall conditions. Infiltration excess overland flow can be caused by very intensive rainfall, usually when the topsoil infiltration capacity is limited. This occurs when the topsoil is compacted or when the soil surface is sealed. A compacted topsoil has a low proportion of intra-aggregate voids and macropores, which results in low porosity and high bulk density. We estimate that infiltration excess overland flow may take place when the mean topsoil saturated hydraulic conductivity is below about 10^{-5} m s^{-1}. No values as low as this were measured at the studied location. A soil crust may appear in summer under sparse vegetation cover conditions and after a long dry period. Extensive surface sealing has not been observed in the catchment since 2011. The results from monitoring of the temporary variable physical properties of the topsoil in Nucice catchment show that the month in which infiltration excess overland flow is most likely to occur is August.

Interflow on an inclined subsoil layer may be initiated when the topsoil structure is well developed, with a high ratio of hydraulically conductive intra-aggregate pores and voids and when the subsoil has a significantly lower infiltration capacity. The rainfall intensity must exceed the infiltration capacity of the soil aggregates and the subsoil (soil matrix). Once interflow is initiated, the response of the stream discharge to changing precipitation patterns is very dynamic. Runoff via this mechanism causes the transport of few suspended solids (almost exclusively streambed particles are mobilized) and low runoff coefficients.

Saturation excess overland flow begins when precipitation is intense and long. Interflow causes water to accumulate in convergent parts of hillslopes. The water that does not fit into the topsoil pore space, begins to pond on the soil surface, thus forming return flow. Return flow is concentrated only in a part of the catchment, where soil erosion is initiated. These events are accompanied by high stream water turbidity and by a large quantity of soil particles transported from the fields. The state of the vegetation has to be taken into consideration.

We employed the monitored sediment fluxes at the catchment outlet as a measure of the dominant runoff mechanism and water flow pathways. Sediment concentration itself cannot serve as an unambiguous indicator. The sediment yield at the catchment outlet is only part of the total eroded soil particles, as a considerable quantity of the particles redeposit before reaching the stream. The soil erosion regime and sediment transport is very site specific. Verstraeten and Poesen (2001) identified catchment size as the most sensitive factor.

RESULTS AND DISCUSSION

From July 2011 to September 2014, approximately 40 rainfall-runoff events were recorded in the experimental catchment. Sixteen of these events with single and distinguishable peak hydrographs, with peak discharge greater than 4 l s^{-1} and with reliably recorded precipitation, runoff and turbidity were selected for an analysis of the runoff formation. The threshold of 4 l s^{-1} is twice the spring baseflow. A lower discharge usually mobilizes an amount of suspended solids too small to be estimated using the current setup. The difference between the peak discharge and the initial discharge had to be at least 2 l s^{-1}, and the suspended solids concentration had to reach a minimum of 1 g l^{-1}. Table 1 presents precipitation and runoff characteristics, and the runoff coefficient. The baseflow component was separated according to constant slope method. Characteristics of suspended solids are summarized in Table 2.

May to June is the part of the year when rainfall-runoff events were recorded most frequently (six events). This does not correspond to the temporal distribution of storm events that is assumed by soil erosion prediction methods (USLE – Wischmeier, 1976), modified for conditions in the Czech Republic (Janeček et al., 2012), where the most frequent occurrence of storm events is expected in June–July. During the period of May–July are the soil properties most susceptible to surface runoff, because the bulk density is high and the topsoil porosity is low (Fig. 3). Both the infiltration capacity and the water retention capacity are therefore at their annual minimum. The distribution of rain events during the rest of the growing season is uniform, with a mean rate of about one episode per month.

Surface runoff domination

In 2013, two extreme events were recorded within a single month. The peak discharge on 2.6.2013 exceeded the maximum capacity of the flume, so the discharge and total flood volume were estimated from evidence of the maximum water depth in the channel above the flume. The peak discharge was calculated according to Chezy formula, the limbs of the storm hydrograph were extrapolated from the measured discharge which was recorded for values below 400 l s^{-1}. The runoff was generated by a rainfall of 83.8 mm over a period ten hours. The soil had been almost saturated due to antecedent long precipitation of low intensity (three days of recurrent rainfall events with a maximum intensity of 4 mm h^{-1} resulting in 90% saturation of the soil profile to the monitored depth of 0.5 m). The total specific runoff of 79 mm, the runoff coefficient of 94% and the total suspended solids of 166 tons by far surpass all the other recorded events in our observations. Surface runoff, caused by

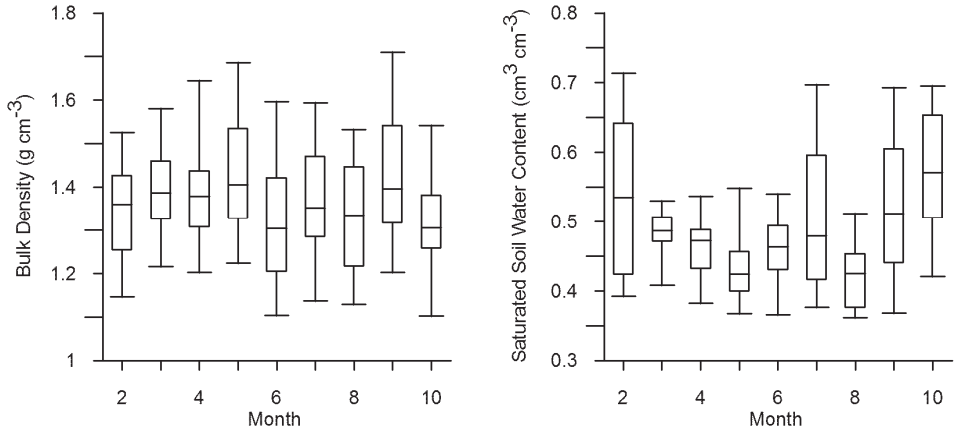

Fig. 3. Evaluation of the mean monthly soil bulk density (left) and saturated water content (right) of the cultivated topsoil as derived by regular soil sampling at the Nucice catchment from February until November between 2001 and 2014 (approx. 350 samples were analysed). Box and whisker plots depict minimum, maximum, median, first and third quartiles. There is a slight trend in increase in spring and decrease in late summer of the bulk density with its maximum in May to July. Saturated water content (which may be related to porosity) decreases in Spring and increases in Autumn with its minimum in May till August. High variability of soil physical parameters within the months are caused by spatial heterogeneity, crops growth, temporary variable soil organic matter content and agrotechnical operations.

Table 1. Rainfall and runoff characteristics of selected rainfall/runoff events recorded between 2011 and 2014 at the Nucice experimental catchment.

Event no.	Date D.M.Y	Rainfall			Runoff			Runoff coefficient (%)
		total (mm)	max. 10 min intensity (mm h^{-1})	duration (h)	total (m^3)	peak (l s^{-1})	specific (mm)	
1	11.7.2011	22.4	27	2.5	151	9.2	0.3	1.3
2	5.9.2011	23.4	25	5	170	7.6	0.3	1.5
3	3.8.2012	25	34	3	153	8.8	0.3	1.2
4	26.8.2012	15	20	1.5	23	4.1	0.1	0.3
5	9.5.2013	11.2	33.6	0.7	344	132	0.7	6.3
6	26.5.2013	7.4	14.4	2	23	6.4	0.1	0.7
7	27.5.2013	8.2	8.4	2	266	23.5	0.5	6.7
8	2.6.2013	83.8	46	10	39500[a]	900[a]	79[a]	94[a]
9	25.6.2013	81.4	8.4	8	5100	117	10.2	13
10	4.8.2013	15.1	36	2.5	34	6.3	0.1	0.5
11	5.2.2014	20.4	49	4	200	10.6	0.4	2.0
12	24.5.2014	18.7	30	4	177	15.5	0.2	1.9
13	27.5.2014	8.2	40	0.75	65	7.3	0.1	1.6
14	29.5.2014	19	17.4	6	55	29.5	0.1	0.6
15	21.7.2014	40.2	66.6	2.5	251	64	0.5	1.2
16	14.9.2014	12.2	30	5	380	15.7	0.8	6.2

[a] The capacity of the H-flume was exceeded, the values are estimated according to observed aftermath of the flooding (flattened vegetation) in the channel.

Table 2. Summary of suspended sediment data as recorded at the gauging station.

Event no.	Date D.M.Y	Total suspended solids (kg)	Max. suspended solids concentration (g l^{-1})	Max. suspended solids flux (kg h^{-1})	Runoff indication index[b] (kg h^{-1})
1	11.7.2011	51	2.1	31	20
2	5.9.2011	54	0.6	15	11
3	3.8.2012	120	2.7	83	40
4	26.8.2012	13	2	81	8
5	9.5.2013	4600[a]	> 26[a]	12500[a]	6600
6	26.5.2013	28	2	40	14
7	27.5.2013	400	2.4	194	199
8	2.6.2013	166000[a]	> 26[a]	52000[a]	16600
9	25.6.2013	6300	3	522	783
10	4.8.2013	34	1.6	31	14
11	5.2.2014	340	4.3	132	85
12	24.5.2014	100	5	72	25
13	27.5.2014	190	7.4	171	257
14	29.5.2014	990	4.3	282	165
15	21.7.2014	2500[a]	> 26[a]	200[a]	1000
16	14.9.2014	530	2.9	125	106

[a] records when the measurable turbidity range was exceeded, the total suspended solids and fluxes are estimated values
[b] runoff indication coefficient is a ratio between total suspended solids and precipitation duration (Equation 1).

the saturation excess of the soil profile, through the thalweg above the open stream channel and within wheel tracks throughout the whole catchment, was observed during a site inspection. The peakflow return period was estimated to be approximately 50 years from data available from the Czech Hydrometeorological Institute.

Examples of hydrographs and sedigraphs with the dominant surface runoff mechanism are shown in Fig. 4. The event from 9.5.2013 (event 5) was the result of a short rainfall with high intensity. The sediment flux of solid particles leaving the catchment reached over ten tons per hour at its peak, which must include a contributing soil eroded from the adjacent fields.

The discharge recorded on 25.6.2013 (event 9) with a peak discharge of 117 l s^{-1} was also partly caused by saturated excess overland flow. Surface runoff was initiated only in the convergent areas close to the stream and the thalweg due to topsoil saturation excess, and in compacted wheel tracks. The precipitation intensity was below the topsoil saturated hydraulic conductivity, but parts of the catchment were still saturated from the previous rainfall. The event came after the extreme event (8), followed by minor recurrent rainfall, and was initiated by a long period of low-intensity precipitation. The fine-grained stream bed sediment close to the gauge was immediately mobilized by the first raindrops. The maximum suspended solids flux only reached 500 kg h^{-1}. Due to the well established crops (wheat on Fields 1 and 2, mustard on Field 3) and the low precipitation intensity, no significant soil erosion began. The outflowing suspended solids are attributed to resuspended sediments from the stream bed deposited during the previous event.

Subsurface runoff domination

In twelve of the sixteen recorded events, no surface runoff was observed. Nevertheless, the reaction of the stream flow to the precipitation events was very rapid (Fig. 5). Subsurface runoff always initiated very quickly and reacted to small variations in rainfall intensity. Similar runoff regime on cultivated soils with fragipan layer was also observer by e.g. Dahlke et al. (2011), Klaus et al. (2013) or Steenhuis et al. (1988).

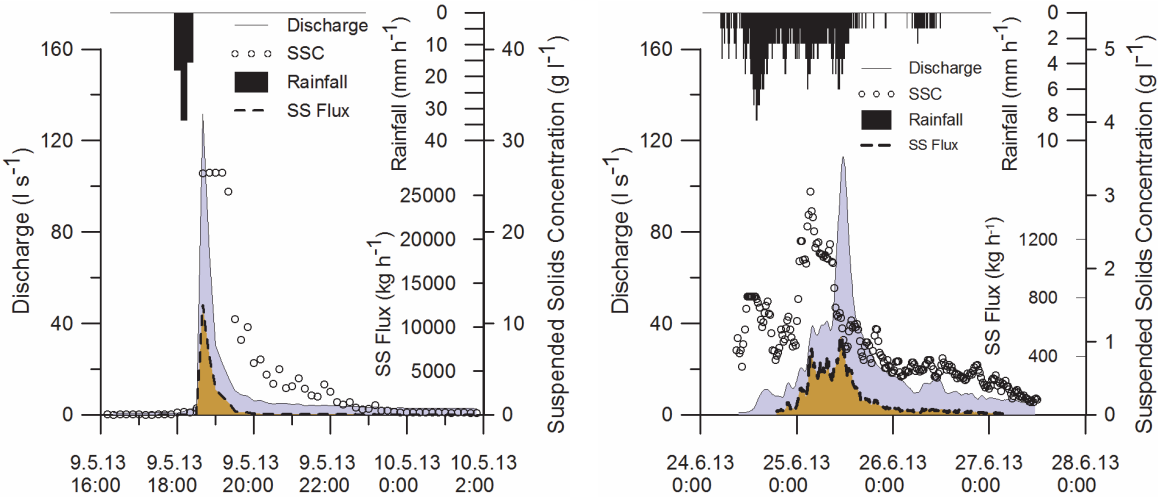

Fig. 4. Examples of hydrographs and sedigraphs of the events when overland flow contributed to the catchment outflow. The values of SS (suspended sediments) flux and discharge are higher by orders of magnitude than in case of no overland flow contribution (see Fig. 5); SSC is the suspended sediment concentration.

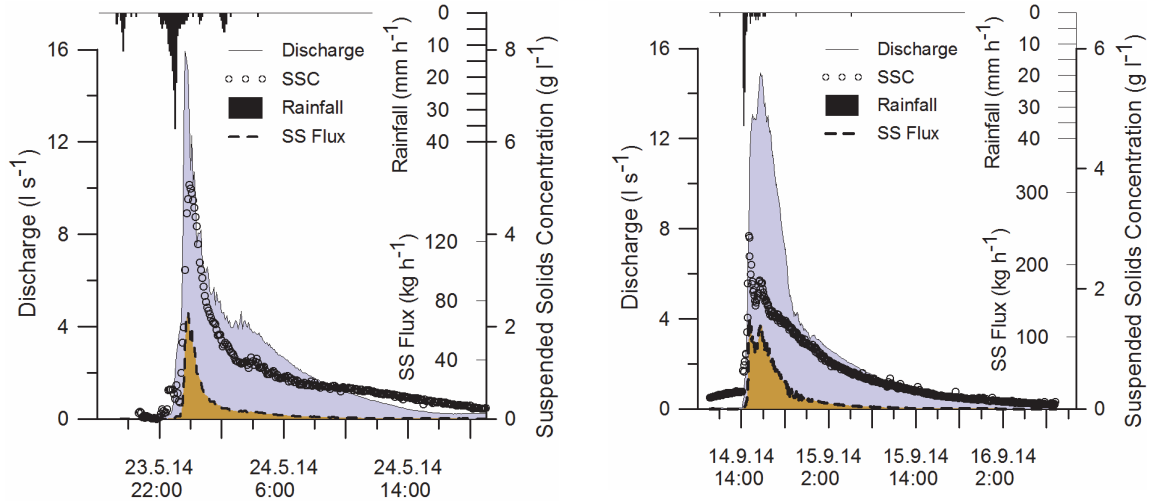

Fig. 5. Examples of rainfall outflow episodes when shallow subsurface runoff was the principle pathway of runoff to the stream.

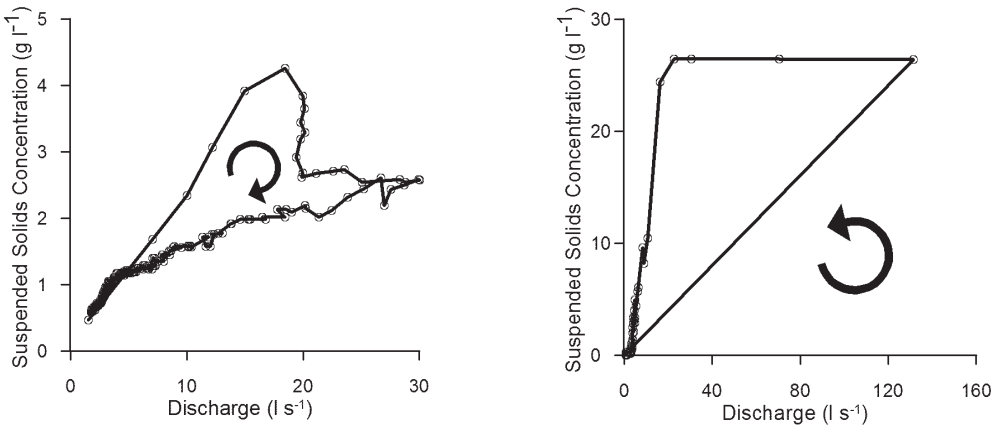

Fig. 6. Hysteretic loops indicating where the sediment originates. Example of domination of bed load sediment transport is on the left (event 14) and eroded particles from the arable fields on the right (event 5).

The maximum discharge initiated by subsurface runoff of almost 30 l s^{-1} (note the value similar to the peak flows during the artificial flood experiments) was recorded on 29.5.2014. In the course of the remaining events, the maximum suspended sediment concentrations did not exceed 8 g l^{-1} (as in the case of the artificial flood experiments).

The sediment concentration rose instanteously with the approaching flood wave, and the maximum turbidity was recorded approximately at the same time as the peak discharge, or a little before. In the event of a long peak discharge or double peaking, sediment concentration usually reached the maximum value within the first peak (Fig. 5 – 23.5.2014, 14.9.2014). As the baseflow was very low in all cases, the flood wave velocity and the celerity were almost equal. Most of the recorded hysteresis loops of discharge versus suspended solids concentration showed a clockwise direction (Fig. 6). This suggests that the main source of the sediment yield deposited on the stream bed close to the gauging station (Lefrançois et al., 2007). Very fine-grained deposited sediment also came from the tile drain above the open channel. As the stream channel is fortified with concrete tiles, we do not suppose that the stream bank or stream bed failures contributed significantly to the total quantity of transported solid particles. On a recession limb of a hydrograph, the sediment concentration decreases. The reason is that mobile fine-grained particles are quickly flushed from the stream bed, and the flowing water does not have sufficient kinetic energy to carry heavier particles over a long distance (Dostál et al., 2013; Eder et al. 2014).

Analysis of the suspended solids regime

The events show reasonable range in the total delivered suspended solids and in the maximum concentrations. During most of the rainfall episodes, irrespective of precipitation intensity, storm duration or hydrograph characteristics, the maximum suspended solids concentration did not reach values higher than 3 g l^{-1}.

We found no clear correlation between the runoff mechanism and the discharge or suspended solids regime. High turbidity and high peak discharge were also recorded during events when surface runoff was not observed. A better indicator than discharge, turbidity or total sediment yield is the maximum suspended solids flux averaged by ten-minute intervals. The values during events 5 and 8 (Table 2) were higher by orders of magnitude than during other episodes, or than the values measured during artificial flooding experiments (Dostál et al., 2013). These fluxes cannot be reached without influx of eroded particles from the cultivated fields, unless the high turbidity is caused by massive stream bank or stream bed failures (which were not observed here).

Another tested indicator of the prevailing runoff mechanism was the newly-introduced runoff indication index R (kg h^{-1}), which is the ratio between the total sediment yield SS_{tot} (kg) and the duration of the precipitation that caused the increase in discharge T_{prec} (h):

$$R = \frac{SS_{tot}}{T_{prec}} \quad (1)$$

This index characterizes not just the short-term peak sediment fluxes but the net response of the catchment to the rainfall. The calculated runoff indication indexes range from 8 kg h^{-1} (event 4) to 16600 kg h^{-1} (event 8). Episodes 5 and 8 have significantly higher R than the other events. Events 9 and 15, with R around 1000 kg h^{-1}, are the events when surface runoff most likely also occurred. Lower values are partly caused by dense vegetation (wheat) resulting in decreased soil erosion. During the events where lower R was calculated, subsurface runoff was prevalent. The runoff indication index does not depend directly on the peak discharge, turbidity or runoff coefficient, as is shown in Fig. 7, where the size of the circles represents the maximum turbidity and the peak discharge.

The hysteresis loops of the suspended solids concentration and discharge corresponded in most cases to the dominant runoff mechanism. In the case of subsurface runoff, when the sediment fluxes were smaller, the loops had a clockwise direction. The surface runoff causes significantly higher sediment loads, so the initial solids flux, which is caused by the stream bed sediments, is lower than the flux when the particles from the adjacent fields arrive. The direction of the loop is anti-clockwise. Examples of both scenarios are shown in Fig. 6.

CONCLUSIONS

Sixteen rainfall-runoff events that were recorded in a small agricultural catchment were evaluated in order to identify the major runoff mechanisms and their implication for soil erosion and sediment transport from the catchment. Most of the events that were initiated by precipitation of various intensities and durations resulted in a rapid increase of stream discharge with no surface runoff in the catchment (as documented by field survey).

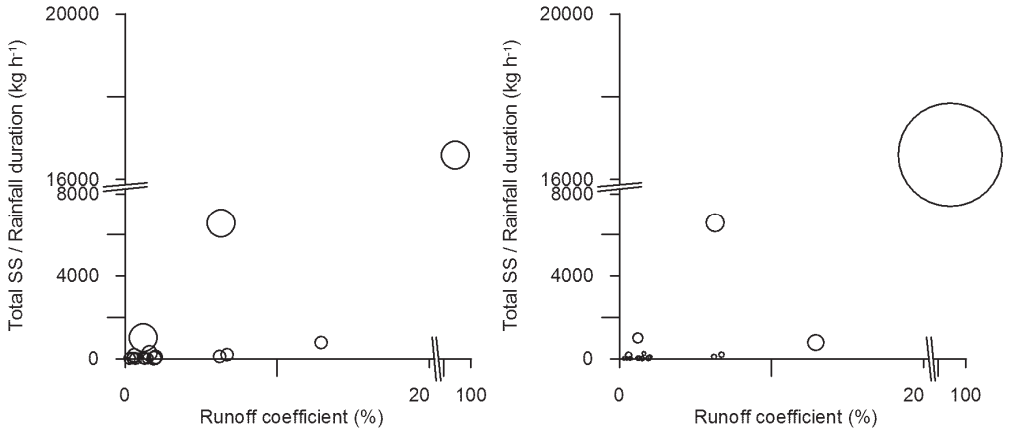

Fig. 7. Surface runoff indicator expressed as an index - ratio between total sediment yield and duration of rainfall. Circle sizes denote maximum suspended solids concentration (left) and peak stream discharge (right).

The shallow subsurface runoff taking place within the topsoil layer is the most common mechanism.

Monitoring of the topsoil physical properties shows seasonal variability, but we have not identified a clear relationship between actual soil conditions and dominant runoff formation mechanism in the studied catchment. The surface runoff, mostly saturated excess driven, occurs only seldom and was caused by heavy rainfall in combination with high antecedent catchment saturation. The topsoil was never compacted to such a level that infiltration excess overland flow could dominate. In the period of four years for which the catchment has been monitored, two extreme events have been observed, in which surface runoff caused by topsoil saturation excess overland flow was clearly dominant.

We identified the prevailing runoff mechanism (subsurface or surface runoff) indirectly based on the monitoring of the suspended solids regime at the catchment outlet. We employed analysis of the suspended sediment flux, the newly-introduced runoff indication index (the ratio between the rainfall duration and the total sediment yield), and direction of the discharge-turbidity hysteresis loops. We recognize these values to be reflective indicators of the runoff mechanism, even though the thresholds are very site specific, depend on actual state of the vegetation cover, and cannot be generalized. During most runoff events the recorded sediment loads came from the fine sediment deposited on the stream bed which indicates the predominance of subsurface runoff.

Acknowledgement. We thank our colleagues Josef Krása, Václav David, Petr Koudelka, Luděk Strouhal for their great help at the catchment. Robin Healey and Philip Moravcik are acknowledged for the English proofreading. This paper was prepared in the framework of Czech Science Foundation post-doctoral project GP13-20388P and Ministry of Agriculture project NAZV QJ1230056.

REFERENCES

Alaoui, A., Lipiec, J., Gerke, H.H., 2011. A review of the changes in the soil pore system due to soil deformation: a hydrodynamic perspective. Soil Till. Res., 115, 1–15.

Bachmair, S., Weiler, M., Troch, P.A., 2012. Intercomparing hillslope hydrological dynamics: spatio-temporal variability and vegetation cover effects. Water Resour. Res., 48, W05537. doi: 10.1029/2011wr011196.

Bertolino, A.V.F.A., Fernandes, N.F., Miranda, J.P.L., Souza, A.P., Lopes, M.R.S., Palmieri, F., 2010. Effects of plough pan development on surface hydrology and on soil physical properties in Southeastern Brazilian Plateau. J. Hydrol., 393, 1–2, 94–104.

Beven, K., 2001. How far can we go in distributed hydrological modelling? Hydrol. Earth Syst. Sci, 5, 1–12.

Birkel, C., Soulsby, C., Tetzlaff, D., 2011. Modelling catchment-scale water storage dynamics: reconciling dynamic storage with tracer-inferred passive storage. Hydrol. Process., 25, 25, 3924–3936.

Coquet, Y., Simunek J., Coutadeur, C., van Genuchten, M.Th., Pot, V., Roger-Estrade, J. 2005. Water and solute transport in a cultivated silt loam soil: 1. Field observations. Vadose Zone J., 4, 3573–3586.

Cox, C.A., Sarangi, A., Madramootoo, C.A., 2006. Effect of land management on runoff and soil losses from two small watersheds in St Lucia. Land Degrad. Dev., 17, 1, 55–72.

Dahlke, H.E., Easton, Z.M., Lyon, W.L., Walter, M.T., Destouni, G., Steenhuis, T.S., 2011. Dissecting the variable source area concept – subsurface flow pathways and water mixing processes in a hillslope. J. Hydrol., 420–421, 125–141.

Dorioz, J.M., Ferhi, A., 1994. Nonpoint pollution and management of agricultural areas - phosphorus and nitrogen transfer in an agricultural watershed. Water Res., 28, 2, 395–410.

Dostál, T., Zumr, D., Rosendorf, P., Strauss, P., Říha, V., 2013. Experimental assessment of transformation rate of flood wave in trained stream channel of small water course. Vodní hospodářství, 11, 373–378. (In Czech.)

Dušek, J., Vogel, T., Šanda, M., 2012. Hillslope hydrograph analysis using synthetic and natural oxygen-18 signatures. J. Hydrol., 475, 415–427.

Eder, A., Strauss, P., Krueger, T., Quinton, J.N., 2010. Comparative calculation of suspended sediment loads with respect to hysteresis effects (in the Petzenkirchen catchment, Austria). J. Hydrol., 389, 1–2, 168–176.

Eder, A., Exner-Kittridge, M., Strauss, P., Bloeschl, G., 2014. Re-suspension of bed sediment in a small stream - results from two flushing experiments. Hydrol. Earth Syst. Sci., 18, 3, 1043–1052.

Grayson, R.B., Moore, I.D., McMahon, T.A., 1992. Physically based hydrologic modeling. 1. A terrain-based model for investigative purposes. Water Resour. Res., 28, 10, 2639–2658.

Holko, L., Kostka, Z., Šanda, M., 2011. Assessment of frequency and areal extent of overland flow generation in a forested mountain catchment. Soil Water Res., 6, 1, 43–53.

Hrnčíř, M., Šanda, M., Kulasová, A., Císlerová, M., 2010. Runoff formation in a small catchment at hillslope and catchment scales. Hydrol. Process., 24, 16, 2248–2256.

Janeček M., Květoň V., Kubátová E., Kobzová D., 2012. Differentiation and regionalization of rainfall erosivity factor values in the Czech Republic. Soil Water Res., 7, 1–9.

Jones, J., 1997. Pipeflow contributing areas and runoff response. Hydrol. Process., 11, 1, 35–41.

Klaus, J., Zehe, E., Elsner, M., Kulls, C., McDonnell, J.J., 2013. Macropore flow of old water revisited: experimental insights from a tile-drained hillslope. Hydrol. Earth Syst. Sci., 17, 103–117.

Kovats, R.S., Valentini, R., Bouwer, L.M., Georgopoulou, E., Jacob, D., Martin, E., Rounsevell, M., Soussana, J.F., 2014. Europe. In: Barros, V.R., Field, C.B., Dokken, D.J., Mastrandrea, M.D., Mach, K.J., Bilir, T.E., Chatterjee, M., Ebi, K.L., Estrada, Y.O., Genova, R.C., Girma, B., Kissel, E.S., Levy, A.N., MacCracken, S., Mastrandrea, P.R., White, L.L. (Eds.): Climate Change 2014: Impacts, Adaptation, and Vulnerability. Part B: Regional Aspects. Contribution of Working Group II to the Fifth Assessment Report of the Intergovernmental Panel on Climate Change. Cambridge University Press, Cambridge, United Kingdom and New York, NY, USA, pp. 1267–1326.

Lefrançois, J., Grimaldi, C., Gascuel-ODoux, C., Gilliet, N., 2007. Suspended sediment and discharge relationships to identify bank degradation as a main source on small agricultural catchments. Hydrol. Process., 21, 2923–2933.

McDonnell, J.J., Stewart, M.K., Owens, I.F., 1991. Effect of catchment-scale subsurface mixing on stream isotopic response. Water Resour. Res., 27, 12, 3065–3073.

McGuire, K.J., McDonnell, J.J., 2010. Hydrological connectivity of hillslopes and streams: characteristic time scales and nonlinearities. Water Resour. Res., 46, W10543. doi: 10.1029/2010wr009341.

Montenegro, A.A.A., Abrantes, J.R.C.B., de Lima, J.L.M.P, Singh, V.P., Santos, T.E.M., 2013. Impact of mulching on soil and water dynamics under intermittent simulated rainfall. CATENA, 109, 139–149.

Noguchi, S., Tsuboyama, Y., Sidle, R.C., Hosoda, I., 1999. Morphological characteristics of macropores and the distribution of preferential flow pathways in a forested slope segment. Soil Sci. Soc. Am. J., 63, 5, 1413–1423.

Pare, N., Andrieuxa, P., Loucharta, X., Biarnesb, A., Voltza M., 2011. Predicting the spatio-temporal dynamic of soil surface characteristics after tillage. Soil Till. Res., 114, 2, 135–145.

Ries, J.B., Iserloh, T., Seeger, M., Gabriels, D., 2013. Rainfall simulations - constraints, needs and challenges for a future use in soil erosion research. Zeitschrift für Geomorphologie, 57, 1, 1–10.

Roulier, S., Angulo-Jaramillo, R., Bresson, L.M., Auzet, A.V., Gaudet, J.P., Bariac, T., 2002. Water transfer and mobile water content measurement in a cultivated crusted soil. Soil Sci., 167, 3, 201–210.

Šanda, M., Vitvar, T., Kulasová, A., Jankovec, J., Císlerová, M., 2014. Run-off formation in a humid, temperate headwater catchment using a combined hydrological, hydrochemical and isotopic approach (Jizera Mountains, Czech Republic). Hydrol. Process., 28, 8, 3217–3229.

Schmocker-Fackel, P., Naef, F., Scherrer, S., 2007. Identifying runoff processes on the plot and catchment scale. Hydrol. Earth Syst. Sci., 11, 2, 891–906.

Schneider, P., Pool, S., Strouhal, L., Seibert, J., 2014. True colors – experimental identification of hydrological processes at a hillslope prone to slide. Hydrol. Earth Syst. Sci., 18, 875–892.

Seeger, M., Errea, M.P., Beguería, S., Arnáez, J., Martí, C., García-Ruíz, J.M., 2004. Catchment soil moisture and rainfall characteristics as determinant factors for discharge/suspended sediment hysteretic loops in a small headwater catchment in the Spanish Pyrenees. J. Hydrol., 288, 299–311.

Steenhuis, T.S., Richard, T.J., Parlange, M.B., Aburime, S.O., Geohring, L.D., Parlange, J.Y., 1988. Preferential flow influences on drainage of shallow sloping soils. Agr. Water Manage., 14, 1–4, 137–151.

Strouhal, L., Zumr, D., David, V., Kavka, P., 2014. Experimental identification and numerical modelling of subsurface runoff on the compacted subsoil. In: Brych, K., Tesař, M. (Eds.): Hydrology of a Small Catchment 2014. Institute of Hydrodynamics AS CR, Prague, pp. 441–448. (In Czech.)

USDA, Soil Conservation Service, 1983. Computer Programs for Project Formulation – Hydrology, Technical Release 20, Washington, DC.

Van Asch, T., Van Dijck, S., Hendriks, M.R., 2001. The role of overland flow and subsurface flow on the spatial distribution of soil moisture in the topsoil. Hydrol. Process., 15, 12, 2325–2340.

Verbist, K., Cornelis, W.M., Schiettecatte, W., Oltenfreiter, G., Van Meirvenne, M., Gabriels, D., 2007. The influence of a compacted plow sole on saturation excess runoff. Soil Till. Res., 96, 1–2, 292–302.

Verstraeten, G., Poesen, J., 2001. Factors controlling sediment yield from small intensively cultivated catchments in a temperate humid climate. Geomorphology, 40, 1–2, 123–144.

Whipkey, R.Z., 1965. Subsurface stormflow from forested slopes. Bull. Int. Assoc. Sci. Hydrol., 10, 2, 74–85.

Wischmeier, W.H., 1976. Use and misuse of universal soil loss equation. J. Soil Water Conserv., 31, 1, 5–9.

Zumr, D., Devátý, J., Klípa, V., Kavka, P., Dušek, J., Dostál, T., 2014. Runoff and soil erosion formation on small arable catchment. In: de Lima, M.I.P., de Lima, J.L.M.P. (Eds.): Book of Abstracts of the 15th Biennial Conference of Euromediterranean Network of Experimental and Representative Basins. Department of Civil Engineering of the University of Coimbra, Coimbra, Portugal, p. 41.

Received 8 November 2014
Accepted 23 February 2015

Note: Colour version of Figures can be found in the web version of this article.

Soil & Tillage Research 174 (2017) 231–240

Contents lists available at ScienceDirect

Soil & Tillage Research

journal homepage: www.elsevier.com/locate/still

Identifying the plough pan position on cultivated soils by measurements of electrical resistivity and penetration resistance

Jakub Jeřábek*, David Zumr, Tomáš Dostál

Department of Irrigation, Drainage and Landscape Engineering, Faculty of Civil Engineering, Czech Technical University in Prague, Thákurova 7, 16629 Prague 6, Czech Republic

ARTICLE INFO

Keywords:
Electrical resistivity tomography (ERT)
Penetration resistance
Subsoil compaction

ABSTRACT

Long term tillage has led to soil profile degradation in many cultivated fields. The topsoil is disturbed by plowing. The movement of fine particles from the topsoil to the subsoil and direct pressure from agricultural machinery create an abrupt delineation in the form of a plough pan with very low permeability. The plough pan prevents water infiltrating deeper into the soil profile and reduces the water supply to the lower layers. The plough pan also has a negative effect on the root growth of the crop, leading to a reduced yield. In this paper we discuss the feasibility of using electrical resistivity tomography and penetrometry to identify the presence and the position of plough pans, and also their spatial uniformity, on two fields with different tillage depths. Electrical resistivity measurements were subjected to a comparison with soil physical characteristics, such as soil water content, porosity and bulk density. Standard statistical and geostatistical methods were used. Electrical resistivity tomography seems to be an attractive method that offers a faster and more efficient method than standard invasive soil sampling for obtaining continuous information about the plough pan. It has been shown that the position of a compacted layer within the soil profile can be identified reasonably well by combining electrical resistivity data and penetration resistance data. The semivariogram showed higher variation by orders of magnitude in the topsoil than in the subsoil. This suggests macroscopic homogeneity of the compacted layer formatted in the subsoil in two differently tilled fields. We conclude that a short span between the electrodes should be used (app 10 cm) in order to observe the shallow positioned plough pan clearly.

1. Introduction

Soil compaction, which may lead to the formation of a plough pan, is a well-recognized phenomenon in agricultural lands. Crop root degradation is one of the most dangerous effects of soil compaction. Roots are of reduced length (Lipiec et al., 2012) and there is reduced biomass (Colombi et al., 2016) in the compacted layer. Various effects can influence the degree of compaction in a field. Climatic or weather conditions, tillage system (Pagliai et al., 2004), the condition of the soil during harvesting (Boizard et al., 2002) and the machinery that is used (Pagliai et al., 2003) can lead to an increase or reduction in soil compaction. As a consequence, the hydraulic properties of the soil are affected. Ahuja et al. (1998), for example, showed how the water retention capacity of a field changes according to the tillage conditions. Dörner and Horn (2009) investigated of the isotropy/anisotropy of hydraulic conductivity in conventionally and conservationally tilled fields. Unlike conservationally tilled fields, conventionally tilled fields exhibited anisotropic conditions in the seedbed and in the plough pan.

A number of studies have investigated changes in the properties of porous media due to compaction. Bertolino et al. (2010) concluded that, in comparison with soils treated by minimum tillage, smaller and less connected pores occurred in the plough pan of conventionally tilled soil. Direct compaction due to the passage of traffic causes large differences in porosity (n) and differences in bulk density (ρ_{bd}) which leads to changes in the saturated hydraulic conductivity (Kim et al., 2010). However, the lower hydraulic conductivity of the plough pan is not necessarily the only reason. A significant decrease in hydraulic conductivity in combination with flow irregularity may also occur due the role of trapped air in the upper layer during infiltration (Císlerová et al., 1990; Sněhota et al., 2008). In contrast, Roulier et al. (2002) presented evidence of undisturbed bio-macropores in the plough pan, formed after soil cultivation or not yet disturbed e.g. by shrinkage, which allows water to flow through preferential pathways and to bypass the compacted plough pan. This consequently increased the overall hydraulic conductivity.

Changes of soil properties due to compaction lead to changes in the electrical properties of the soil. The changes in soil water content (θ), in the salinity of the water, in the clay fraction or in the bulk density lead

* Corresponding author.
E-mail address: jakub.jerabek@fsv.cvut.cz (J. Jeřábek).

http://dx.doi.org/10.1016/j.still.2017.07.008
Received 23 May 2016; Received in revised form 12 June 2017; Accepted 14 July 2017

to changes in the electrical resistivity (ρ) of the soil (e.g. Besson et al., 2004); Loke et al., 2013). The specific surface area of soil particles affects the resistivity because of an adsorbed water film on the soil particles (Revil et al., 2012), whereas the soil particles themselves (irrespective of size) and the soil air are often considered as an insulating material (e.g. Fukue et al., 1999). Macropores, cracks or voids and organic residues usually increase the electrical resistivity of the soil (Besson et al., 2013). Since the specific surface area of soil particles alters the electrical resistivity of the soil ρ, and it is affected by of soil compaction causing changes in the bulk density and in the structure of the soil, we assume that measurements of changes in ρ can provide information about the plough pan depth and homogeneity.

We used the electrical resistivity tomography (ERT) technique to obtain the position and the spatial uniformity of the plough pan. The study covered a series of 10 specific ERT transects. In general, this approach faces a few ambiguities. The electrical properties of soils, e.g. their electrical resistivity, are affected by several factors. It is problematic to recognize which factor is of major influence. Kowalczyk et al. (2014) conducted experiments with a sandy material in which it was shown that changes in electrical resistivity are caused by changes in bulk density, water content and total porosity. Similar results in field soils were observed by Besson et al. (2013), where the ERT data was influenced by the degree of water saturation. The bulk density was therefore tricky to determine. Organic carbon can also affect resistivity measurements, especially in the uppermost layer of the soil in agricultural land (Hadzick et al., 2011). When all quantities except the bulk densities are excluded, i.e. their effect is set as constant over a measured sample, the influence of bulk density is clearly present (Besson et al., 2004). In a study performed by Besson et al. (2004), 2D ERT measurements were compared with a visual inspection of the uncovered soil profile transect on an experimental plot. Although the resistivity was significantly lower in the plough pan, its exact position could not be determined. ERT did not detect the position of all clods in the topsoil. However, a clear negative relationship was found between electrical resistivity and bulk density for field soil samples. When the topsoil was less heterogeneous, it was less problematic to indicate the position of the plough pan.

Séger et al. (2009) presented a comparison of identifying topsoil features using 2D and 3D ERT. The 2D method was influenced by the hemisphere integration effect (Séger et al., 2009). The electrical current introduced to the ground by electrodes along a line introduces to the ground an electrical field that is hemispherical in shape. The records are therefore affected by lateral features to the side of the 2D line. Séger et al. (2009) showed that 3D measurements diminish the hemisphere integration effect, and enhance the sensitivity of the method to the structure of the topsoil. In qualitative terms, large clods, which occupied the whole depth of the topsoil (ca 30 cm), had the lowest resistivity; loose material had slightly higher resistivity, but smaller clods (∅ ca 5–10 cm) embedded in loose material had markedly higher resistivity. However, the position of the plough pan appeared only in the form of smoother changes in the horizontal 2D cross-sections of the 3D measurements. ERT and a penetration test were used by Basso et al. (2010). To assess the variations in soil resistivity in several differently tilled plots. They concluded that ERT can assist in identifying a compacted layer in the soil profile.

After a rain event, the infiltration capacity of the plough pan can be exceeded due to its low permeability. This causes the formation of lateral flow, (Coquet et al., 2005). Higher saturation above the plough pan affects data acquisition and makes the results more difficult to interpret. A detailed laboratory analysis of changes in the resistivity of different clays under variably saturated conditions was undertaken by Fukue et al. (1999). They measured abrupt changes in electrical resistivity at a certain saturation, at which the water film on the surface of a clay particle becomes connected, or ceases to be connected. The soil structure appeared to have a limited effect on the electrical resistivity (or conductivity) (Nadler, 1991). In many studies, the relationship between bulk density and electrical resistivity is assumed to be negative. However, some other studies have reached the opposite conclusion (e.g. Naderi-Boldaji et al., 2014). Electrical resistivity measurements of soil are also used in hydraulic conductivity assessments, (Mazáč et al., 1988), in soil classification based on resistivity distinctions between soil layers (Buvat et al., 2014) and in tracking distinct pedological volumes in a single soil layer (Séger et al., 2014).

The objective of our study is to assess the feasibility of using the ERT technique to determine the position of the plough pan, and its spatial uniformity and continuity. It is not our ambition to obtain the concrete physical properties of the soil layers. We utilize the sharp contrast in electrical properties between the topsoil and the subsoil caused by a combination of attributes such as organic matter content, clay particles, bulk density or current saturation to identify the divide. Data collection took place at two sites exposed to different tillage. From the agricultural, pedological, geological and climatological point of view, the two sites are representative of their region. The penetration resistance tests and the measurements of soil physical properties were collected in order to compile a data set for a comparative analysis. The results of the measurements are analyzed by means of standard statistical and geostatistical methods.

2. Material and methods

Our study consists of ERT measurements, penetration tests and measurements of the physical properties of soil core samples. We conducted four measurement campaigns. In each campaign, several ERT transects were measured. In selected ERT transects, three to five penetration tests were performed and soil core samples were collected at different depths. The penetration tests were performed to a depth of ca 65 cm. The soil core samples were taken at three to six depths, down to a depth of ca 50 cm. At least one set of core samples was taken from the top soil, and at least one was taken from the compacted layer if a plough pan was present. The penetration tests provided evidence of the presence and the position of a plough pan. The physical properties of the soil, namely soil bulk density, total porosity and water content, were evaluated to clarify the interpretation of the ERT data. The setup for typical ERT transect measurements, together with penetration tests and the collection of soil core samples is shown in Fig. 1. Each measurement campaign has its unique identifier (character A–D). The distribution of the measured transects (*T*) within the experimental catchment is depicted in Fig. 2. A summary of all measurements is shown in Table 1.

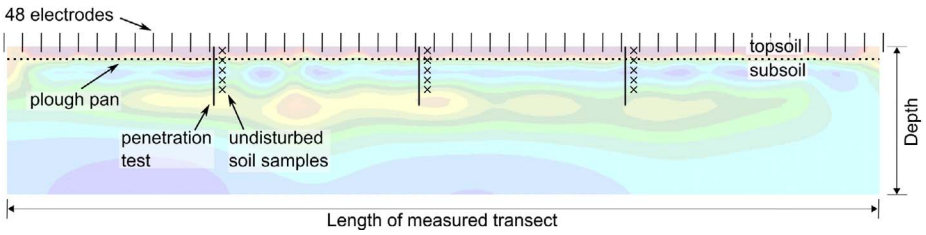

Fig. 1. Set up of ERT, penetration test and undisturbed soil sample sites at one ERT transect.

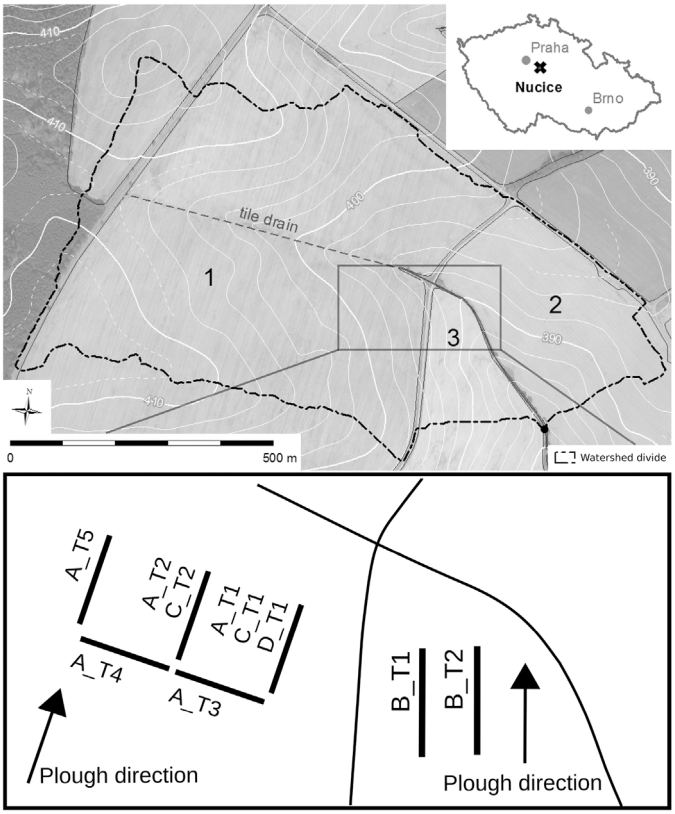

Fig. 2. The study site and the location of the experiment profiles; A–D denote the order in which the campaign was organized. The last digit denotes the order of the measurements undertaken in a transect identifier.

2.1. Study area

The study was performed in a small catchment located in the central part of the Czech Republic, 30 km south-east of Prague. The catchment, with a total area of 0.5 km^2, consists of three fields cultivated by two farmers.

The two largest fields (field 1 and 2 in Fig. 2) are exposed to conservation tillage. The crop in field 1 was white mustard (*Sinapis alba*) in season 2013 and winter wheat (*Triticum aestivum*) in seasons 2013–2014 and 2014–2015. After harvesting, a Horsch Joker 12 cultivator was used for stubble cultivation and a Horsch Tiger compact disk harrow was used for seedbed preparation. The farmer uses John Deere 9630T rubber tracked tractors. Cultivation is done to a depth of 10–12 cm, and seedbed preparation is done to a depth of 18 cm. After harvesting in October 2015, chisel plowing was done to a depth of 25–28 cm.

The smallest field (field 3 in Fig. 2) was treated by conventional tillage until 2012, after which conservation tillage was introduced. Deep plowing is done after harvesting in order to disturb the wheel tracks and the plough pan in field 3. In 2015, stubble cultivation was done to a depth of 8 cm using a Vaderstad Carrier CR 925-1225 cultivator. Deep plowing to a depth of 45 cm and seedbed preparation were done using a Vaderstad Topdown TD 300-900 cultivator. The farmer uses Vicon wheeled tractors with 1.2 bar wheel pressure. The crop in field 3 was winter wheat (*T. aestivum*) in the 2014–2015 season. The most important cultivation activities before each measurement are briefly presented in Table 1 .

Agricultural land covers 96.4% of the catchment area, with a mean slope of 3.9%. The soil is classified as Cambisols and Luvisols, with an Ap horizon between 0.1 and 0.2 m in depth and a B horizon beneath it. Both the topsoil and the subsoil were classified as a loamy soil, but there was a slightly higher clay content in the subsoil. The bedrock consists of conglomerates, sandstone and siltstone. The organic matter content is assumed to be homogeneous within the catchment. The mean annual precipitation is 630 mm, and the mean evapotranspiration is 500–550 mm. The mean annual temperature is 6 °C. Detailed information about the hydrology of the experimental site can be found in Zumr et al. (2015).

2.2. Electrical resistivity tomography

Electrical resistivity tomography (ERT) was used to determine the electrical resistivity (ρ) of the soil profile. The research was conducted using the ARES device, manufactured by GF Instruments (Czech Republic). Date of the 10 measurements are presented in Table 1 . After each measurement, the water content was determined (last column in Table 1). The measurements were made after the harvest, when the fields were bare. A dipole–dipole array with 48 electrodes was used for each transect. The electrodes were inserted to a depth of 2–4 cm, which coincided with the surface roughness. The spacing of the electrodes was 0.2 m for transects A and B, and 0.1 m for transects C and D. In transects A and B, the array parameter a was within an interval of a = 0.2–1.8. For transects C and D, array parameter a was within an interval of a = 0.1–0.9. For all transects, parameter n was between 1 and 4. A single measurement consisted of 1035 datum points and 45 depth levels.

The dipole–dipole array is weaker in capturing deep structures, but it is more sensitive in the shallowest part of the measured profile (Furman et al., 2003; Dahlin and Loke, 1997). It has higher horizontal sensitivity than other electrode arrays (Samouëlian et al., 2005), which we found convenient for capturing the heterogeneity of the plough pan. However, the dipole - dipole array has low sensitivity in deeper structures, which was taken into account during the inversion procedure.

To obtain the electrical resistivities, the datum points need to be inverted. In situ measurements offer the so-called apparent electrical resistivity. The apparent electrical resistivity represents the surficial effect of the introduced electrical field. A model of the apparent electrical resistivities based on an array geometry is fitted to the apparent electrical resistivities obtained in the field during the inversion procedure. The spatial distribution of the electrical resistivities serves as a set of model parameters (Loke, 2004).

Before inversion, data points which had, compared to adjacent data points, abnormal resistivity were filtered out to reduce the noisiness. Based on previous experiences, the abnormal resistivity is caused by weak connection between an electrode and a soil rather than on

Table 1
Overview of measurements and cultivation activities.

Date (D.M.Y.)	Transect	Penetrometry	Undisturbed core samples	Previous activity	Soil water cont.
2.10.2014	A_T1, A_T2, A_T3, A_T4, A_T5	Yes	Top soil only	12.8. cultivation depth 10–12 cm; 28.9. seeding preparation depth 18 cm	Wet θ_{top} = 0.29
27.10.2015	B_T1, B_T2	Yes	Yes	25.8. plowing 20 depth cm; 1.9. clover seeding	Wet θ_{top} = 0.34
20.11.2015	C_T1[a], C_T2[a]	At C_T1	Yes	28.10. chisel plowing 25–28 cm	Very wet θ_{top} = 0.39
30.3.2016	D_T1[a]	Yes	Yes	After winter with no agricultural activity	Wet θ_{top} = 0.29

[a] Electrode spacing = 0.1 m; θ_{top} topsoil volumetric water content [cm^3/cm^3].

properties of a soil material. The threshold error of the reciprocal measurements was set to 5%. The ratio of the removed noisy points varied between 0 and 4%. Due to the increased noisiness of the dipole–dipole array with depth (Furman et al., 2003; Dahlin and Loke, 1997), the number of layers was reduced to 10 for transects A and B and to 20 for transects C and D. The total number of computation blocks was reduced to 940 for transects A and B and to 1880 for transects C and D.

Typically 3–6 iterations were needed to bring the relative change in the subsequent RMS error below 1%. The maximum number of iterations was set to 7. In all cases, the desired results were reached before the 7th iteration. In most cases, the number of iterations was 3 or 4. A finite-elements mesh with triangular elements and one half of the space of the electrodes span was used. The smoothness constraint on the model resistivity values was used for transects B_T1 and B_T2. For field 3, a smoother transition between the topsoil and the subsoil was expected, as was also suggested by the profiles of the apparent electrical resistivities (as was discussed in Section 3.1). The robust inversion option was used for other transects measured in field 1 (transects A, C and D), where a sharper transition was expected between the soil and subsoil. The standard Gauss–Newton method was employed for the optimization.

2.3. Penetration resistance

We measured the penetration resistance (p_{pr}) in the subset of ERT profiles with spacing from 1 to 2 m along the profile. Eijkelkamp penetrologger agrisearch equipment (art. no. 06.15.01) was used. At each location, 5 consecutive penetration tests were performed to a depth of approximately 65 cm. The probing cone had a 30° top angle and a base area of 1.3 cm^2. The resolution of data points were 1 cm. The resulting p_{pr} profile at each location was obtained as the average of 5 depth measurements.

2.4. Soil core samples

At each p_{pr} measurement location, undisturbed soil samples were taken in metallic cylinders at various depths. One sample was always taken in the topsoil (the upper 20 cm of the profile). The number of samples in the subsoil depended on the time available during each campaign. The number varied between 2 and 5 in the subsoil. The volume of each cylinder was 137.4 cm^3. Gravimetric methods were used to obtain the bulk density ρ_{bd}, the total porosity n, and the volumetric water content θ. We used a displacement method to estimate porosity based on difference of fully saturated and dry masses of undisturbed samples with a known volume.

2.5. Statistics and geo-statistics

Semivariograms were used for the geostatistical analysis. The general semivariogram can be written as follows,

$$E[Y(s+\mathbf{h}) - Y(s)]^2 = \mathrm{Var}(Y(s+\mathbf{h}) - Y(s)) = 2\gamma(\mathbf{h})$$

where $Y(s)$ is an observed variable at position s and $\mathbf{h}$ is the vector denoting the spatial shift of variable Y from position s. $2\gamma(\mathbf{h})$ is the variogram and $\gamma(\mathbf{h})$ is the semivariogram, and both are dependent only on $\mathbf{h}$, which is the relative distance between variable Y at positions s and $s + \mathbf{h}$ (Banerjee et al., 2014). Here, we want to point out the ambiguity of the last statement in relation to the use of semivariograms to analyze ERT data. The reason is that ρ obtained by ERT is position dependent. However, we assume that for shallow depths this fact can be neglected.

In our paper we use a binned empirical semivariogram. A binned empirical semivariogram is defined as

$$\gamma_{ij} = \frac{1}{2N_{B_{ik}}} \sum_{(k,j):(s_k - s_l)\in B_{ij}} (Y(s_k) - Y(s_l))^2$$

where B_{ik} is a so-called bin which contains pairs of points with a certain relative distance, and $N_{B_{ik}}$ is the number of pairs in a bin.

The inverted electrical resistivity data was linearly interpolated before the semivariance analysis. The linear interpolation was based on triangles of adjacent datum points, which corresponds to the finite-element modeling used in the inversion procedure.

The simple linear regression Student's t-test was used to evaluate whether or not the penetration resistance p_{pr} measurement can serve as an explanatory variable for electrical conductivity σ (inverse electrical resistivity). We tested the hypotheses of zero slope a and zero intercept b in the linear formula $\sigma = ap_{pr} + b$.

3. Results

3.1. ERT transects

Some trends can be evaluated from the ERT transects (Figs. A8–A.10, for convenience displayed in Appendix A) together with information about the water content in the topsoil during the measurements (last column in Table 1).

The apparent electrical resistivity (ρ_{ap}) of the transects is displayed in the topmost panel in Figs. A8– A.10. For transects A_T5 and C_T1 (Figs. A8– A.10) ρ_{ap} is higher (> 80 Ωm) in the upper 20 cm of the soil profile. The ρ_{ap} is generally lower below the first 20 cm of the profile for transects A_T5 and C_T1. Some areas of higher resistivities are scattered evenly over the profile below a depth of 20 cm ($\rho_{ap} \in \langle 40 - 50 \rangle$ Ωm) in these transects. This suggests a sharper transition between the topsoil and the subsoil. In transects A_T5 and C_T1 we therefore used the robust inversion model option, which better captures sharp resistivity transitions. Apparent electrical resistivity ρ_{ap} exhibits different patterns for transect B_T1 (Fig. A.9). The highest ρ_{ap} values are found in the topsoil but, in comparison with transects A_T5 and C_T1, the decrease of ρ_{ap} with depth is more gradual. For this reason, we used the standard smoothness-constrained inversion model.

The inverted electrical resistivity ρ (second panel in Figs. A8– A.10) has the highest value in the shallowest part of all profiles, and it shows the greatest variation (variability is not shown in Figs. A8– A.10 due to the colour scale). Deeper in the profile, ρ is lower than 60 Ωm in transects A_T5 and C_T1.

The third and fourth panels in Figs. A8– A.10 show the sensitivity and the uncertainty of the model. In the case of transects A_T5 and C_T1 (Figs. A8– A.10), the sensitivity of the model is greatest in the upper 30–40 cm of the profile, where the transition between topsoil and subsoil is located. In transect B_T1, higher sensitivity values are propagated deeper in the profile to a depth of ca 50 cm. The higher ρ patterns located at a depth of 60–70 cm in the central area of all transects exhibit lower sensitivity of the model. Therefore it is not possible to identify the central areas as a more conductive area or as an inversion artefact. In transect B_T1, the uncertainty of the model increases rapidly with depth. The uncertainty values are the highest in the position of the high ρ object located in the central part of transect B_T1 at a depth of 60–90 cm. The uncertainty of the model is difficult to interpret for transects A_T5 and C_T1 because a robust inversion model underestimates the uncertainty value (Loke, 2004). Scattered areas of higher uncertainty are located below the possible topsoil/subsoil transition (ca 30 cm) for transect A_T5 and for the upper 20–30 cm in transect C_T1.

The ERT measurements were also conducted under very dry conditions (the topsoil water content was 0.09 cm^3/cm^3). These data are not presented here, but the electrical resistivity results exhibited large errors due to these conditions, especially due to weak contact between the electrodes and the soil. The penetration test also performed poorly in this measurement. Although these results are not shown here, it

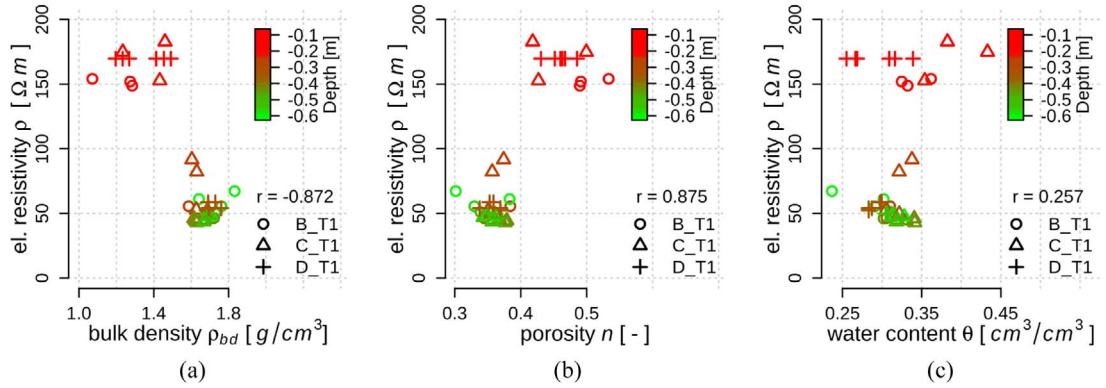

Fig. 3. Correlation between electrical resistivity (ρ) and the physical properties of soil samples ((a) bulk density (ρ_{bd}); (b) porosity (n); (c) volumetric water content (θ)); r stands for Pearson's correlation coefficient.

should be pointed out that moderate to high water content has to be reached in order to obtain reliable measurements of this type.

3.2. ERT and soil physical properties (ρ_{bd}, n, θ)

Fig. 3 shows the relationship between the electrical resistivity ρ and the physical properties of the soil. The relations between ρ and bulk density ρ_{bd} are displayed in Fig. 3a; porosity n is displayed in Fig. 3b and water content θ in Fig. 3c. The negative correlation between ρ and ρ_{bd} corresponds to findings published in the literature (Besson et al., 2004; Basso et al., 2010; Kowalczyk et al., 2014). The correlation between ρ and n is positive and it is also as expected. The correlation between ρ and θ depends on the antecedent weather conditions. Data from transect A_T are not shown due to missing physical properties data from the subsoil. The data points for all graphs in Fig. 3 form two clusters, one cluster of higher ρ (around 150 Ωm) and the second cluster of lower ρ (around 50 Ωm). Data points belonging to the higher ρ cluster are located in the topsoil. Data points belonging to the lower ρ cluster are located in the subsoil and in the plough pan. Two data clusters can be distinguished for ρ values and also for ρ_{bd} values (Fig. 3a). The same behavior applies for the ρ and n values in Fig. 3b. Two clusters can be distinguished only for ρ values in Fig. 3c.

3.3. ERT and the penetration resistance

In Fig. 4, we show the electrical resistivity ρ and penetration resistance p_{pr} results for four transects. The selected transects represent typical $\rho \propto p_{pr}$ behavior.

The ρ values were extracted from the 60 cm wide strip of ten measured transects, and correspond to the location of the p_{pr} measurements. The location of the p_{pr} measurement along each ERT transect is depicted in the legend of Fig. 4. Penetrometry allows the p_{pr} to be captured at a greater number of depths (obtaining finer observation resolution) than ERT. In Fig. 4, the p_{pr} are linearly approximated from the two closest ρ measurements. Since the recorded depths are rather dense in the penetrometry measurement, and because p_{pr} is already averaged over 5 consecutive measurements, the linear approximation seems to be justifiable.

Fig. 4 shows that p_{pr} and ρ are almost inversely symmetric. An increase in p_{pr} corresponds to a decrease in ρ. An abrupt increase in p_{pr} at a certain depth indicates the surface of a plough pan. When the cone of the penetrologger penetrates through the plough pan, p_{pr} remains constant or decreases slightly. According to the p_{pr} profiles in Fig. 4a, c and d, the plough pan emerges at a depth of 20 cm. In transect B_T2 (measured on field 3 where there is a different tillage regime) in Fig. 4b, a more compacted layer emerges at a depth of 30 cm. We assume that there is also decreased electrical resistivity in the plough pan for transects B_T2, C_T1 and D_T1. The lowest values of ρ were deeper than the corresponding high p_{pr} for transect A_T5. The other measurements indicated in Table 1 have a similar trend to transects B_T1, C_T1 or D_T1 (transect B_T2) similar to transect A_T5 (transects A_T1, A_T2, A_T3, A_T4).

When 10 cm electrode spacing was used (Fig. 4c, d), better symmetry between electrical resistivity ρ and penetration resistance p_{pr} was identified (field 1 in Fig. 2). Sufficient symmetry between ρ and p_{pr} was shown for electrode spacing of 20 cm in field 3 in Fig. 4b.

The correlation between normalized penetration resistance p_{pr} and electrical conductivity $\sigma(=1/\rho)$ for all penetrometry data are shown in Fig. 5. The scattering of the points increases with increasing p_{pr}. However, if a single transect is under consideration, the relationship appears to be almost linear, with a certain deflection above or below the 1:1 line. A Student's t-test of the simple linear regression analysis of slope a and intercept b of the fitted line $\sigma = ap_{pr} + b$ for each transect is displayed in Table 2 . In terms of the slope, the null hypothesis (the hypothesis that the slope is equal to zero) is not rejected only for transect A_T5. In terms of intercepts, the null hypothesis (the hypothesis that the intercept is zero) is rejected, with the exception of profiles A_T5 and D_T1.

3.4. Semivariograms of ERT results

The spatial soil heterogeneity of a particular layer can be assessed with the use of a semivariogram. Fig. 7a–d shows the semivariance of transects A_T5, B_T1, C_T1 and D_T1. The semivariance is shown only to half the depth of the measured ERT transects to zoom the topmost part of each transect. The semivariogram exhibits a rapid increase in semivariance in dependence on the increase in distance in the uppermost layer for all profiles. The increase in semivariance becomes more gradual below a depth of 20 cm in transects A_T5, C_T1 and D_T1. A one order of magnitude decrease in semivariance occurs up to the points at a distance of 2 m for C_T1 and D_T1. In the case of transect A_T5, the semivariance below a depth of 20 cm is lowered by 2 orders of magnitude in comparison with the layers above.

Similar behavior is observed for transect B_T1 in Fig. 7b. However, the semivariance increases more gradually even in the first 20 cm of the transect.

4. Discussion

ERT was used to measure the electrical resistivity ρ on agricultural soils. In general, these soils are submitted to intense cultivation of the topsoil. This causes a distinct nature of the soil structure, and as a result a distinct ρ is measured in the first tens of centimeters of the soil profile.

The correlation between ρ and the soil physical properties (in Fig. 3) exhibited two clusters. Higher bulk density ρ_{bd} and low porosity n data points correspond to lower electrical resistivity measurements ρ. These

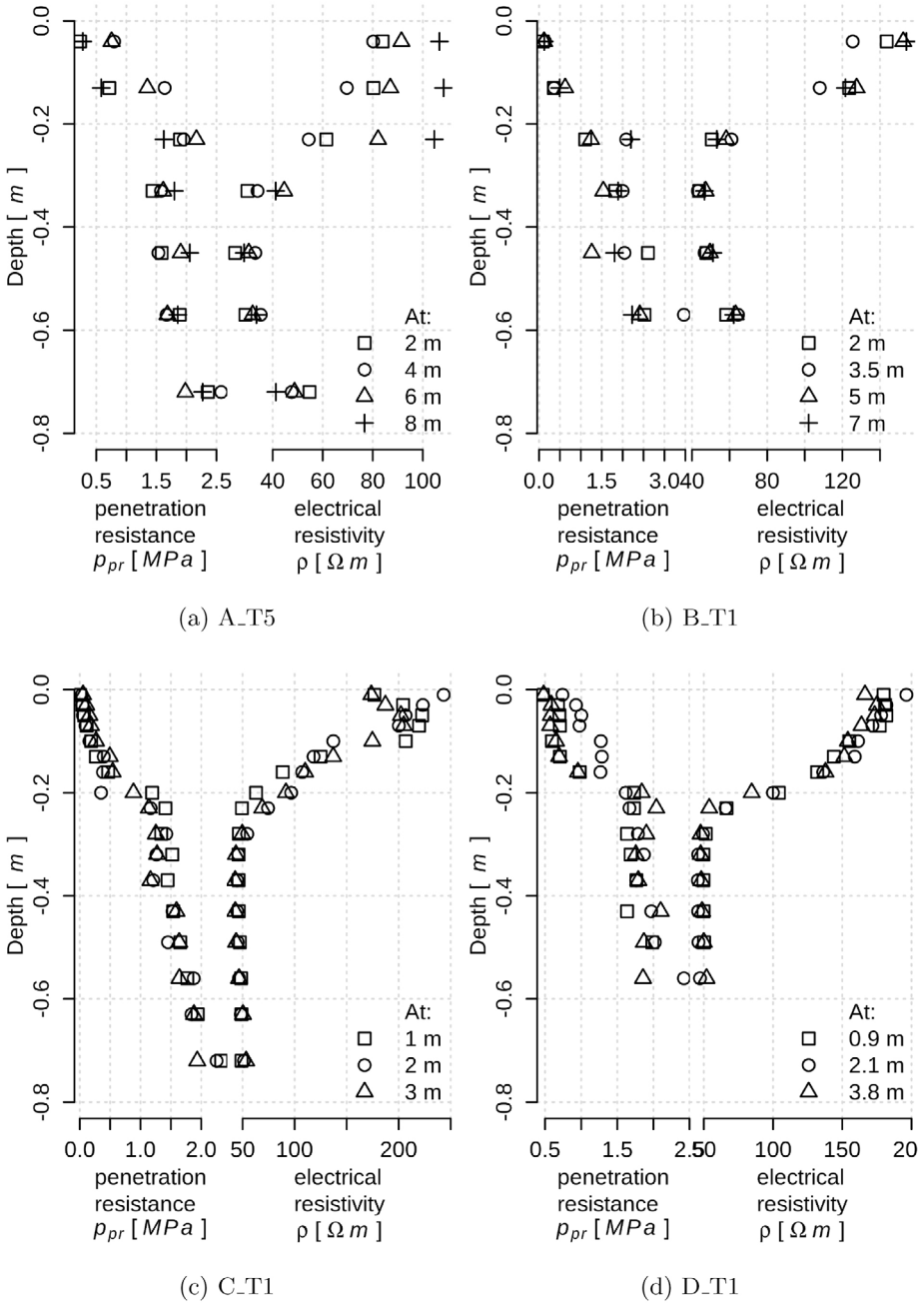

Fig. 4. A comparison between the penetration resistance measurements (p_{pr}) and the electrical resistivity (ρ) measurements within the selected transects.

data were collected from the subsoil where the plough pan is formed. Lower ρ_{bd} and higher n data points correspond to higher ρ and all these data were collected in the topsoil.

Besson et al. (2004) conducted a study where the soil samples were taken from a known (compacted or non-compacted) location within the topsoil and the corresponding ρ were compared. In their study, the decreasing relation between electrical resistivity and bulk density was less pronounced than in our results. Measurements taken from loose material exhibited high electrical resistivity ρ and low bulk density ρ_{bd} (Besson et al., 2004). Low ρ and high ρ_{bd} were measured in the samples taken from the compacted clods in Besson et al. (2004). This $\rho \propto \rho_{bd}$ relation corresponds to subsoil measurements in our research. This leads to the conclusion that the two distinct clusters of points in the $\rho \propto \rho_{bd}$ ($\sim n$) plot in Fig. 3a and b indicate the topsoil and the compacted plough pan, and that the data obtained by ERT reflect the changes in the physical properties of the soil.

The results for a comparison between electrical resistivity ρ and penetration resistance p_{pr} (Section 3.3) indicate an agreement between the quantities and the depth. We assume that p_{pr} reveals the real position of the plough pan. A comparison between electrical resistivity and penetration resistance for transects C_T1 and D_T1 indicated that the plough pan was at a depth of ca 20 cm, and the shapes of the two measured curves are inversely symmetric.

The ERT data was measured with shorter electrode spacing (10 cm, transects C_T1 and D_T1), which led to higher resolution of the electrical resistivity data. The measurements for profile B_T1 indicate that the plough pan is deeper in the soil profile due to deeper plowing. The peaks of the p_{pr} and ρ measurements are at a similar depth. Although the p_{pr} and ρ profiles are not perfectly inversely symmetric in all cases (A_T5; Fig. 4a), the depth of the lowest ρ values is very similar along the transects. In other words, the absolute depth of the plough pan is not clear in terms of ERT, but the relative change in the depth of the plough pan along the profile is reasonable in transect A_T5.

The correlations between penetration resistance p_{pr} and electrical

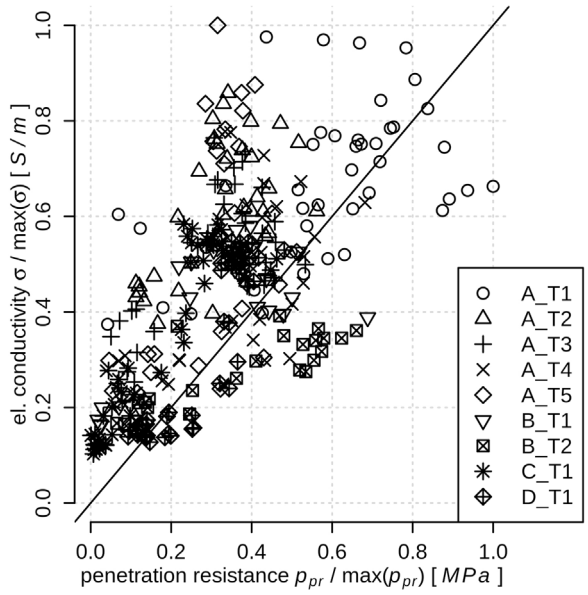

Fig. 5. Correlation between normalized penetration resistance (p_{pr}) and electrical conductivity (σ).

Table 2
Results of Student's *t*-test of the linear regression analysis; $\sigma = ap_{pr} + b$.

Transect	*b*	*a*	*P*-value *b*	*P*-value *a*
A_T1	0.471	0.371	< 0.001	< 0.001
A_T2	0.459	0.464	< 0.001	< 0.001
A_T3	0.409	0.445	< 0.001	< 0.001
A_T4	0.291	0.567	< 0.001	< 0.001
A_T5	0.256	0.469	0.032	0.012
B_T1	0.38	0.682	< 0.001	< 0.001
B_T2	0.429	0.501	< 0.001	< 0.001
C_T1	0.222	0.939	< 0.001	< 0.001
D_T1	−0.083	1.196	0.15	< 0.001

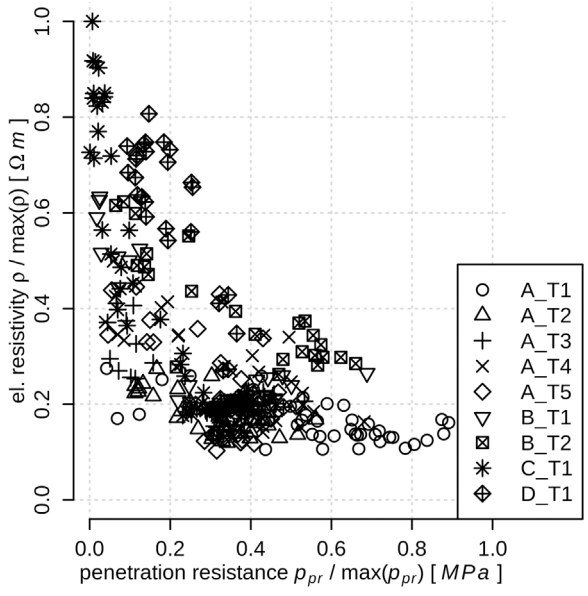

Fig. 6. Correlation between normalized penetration resistance (p_{pr}) and electrical resistivity (ρ).

conductivity σ and between penetration resistance p_{pr} and electrical resistivity ρ shown in Figs. 5 and 6 exhibit visible trends. The Student's *t*-test of the linear regression slope and the intercept indicates that σ can

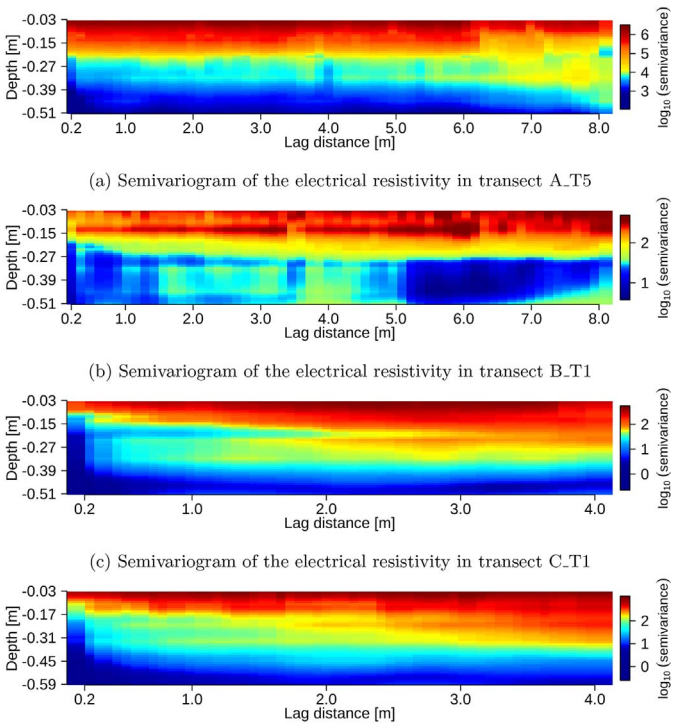

(a) Semivariogram of the electrical resistivity in transect A_T5

(b) Semivariogram of the electrical resistivity in transect B_T1

(c) Semivariogram of the electrical resistivity in transect C_T1

(d) Semivariogram of the electrical resistivity in transect D_T1

Fig. 7. Semivariograms of the electrical resistivity in transects A_T5, B_T1, C_T1 and D_T1. Figure represents the series of semivariograms in various depths (*Y*-axis). Each semivariogram was calculated separately for ca 1–2 cm thick slice of soil. The value of semivariance for every soil layer and the lag distance (*X*-axis) is represented by the colour scale. The lag distance is the spatial distance between pairs of datum points along each transect. The semivariance is shown in a logarithmic scale.

serve as an explanatory variable for p_{pr} (and implicitly as a degree of compaction identifier). However, the intercept of the regression line differed from zero with a high level of significance. It may be in conflict with the physical meaning of this relationship. A zero p_{pr} is assumed to lead to zero σ when the porosity is equal to one. The inverse relation (Fig. 6) fulfills this assumption much better, since the asymptotic approach of ρ towards infinity at zero p_{pr} is observed. The relationship between p_{pr} and ρ is much stronger than has been suggested in the literature. In Basso et al. (2010), the correlation between p_{pr} and ρ was less significant; in Sudha et al. (2009) no correlation was shown; and in Naderi-Boldaji et al. (2014) the correlation was opposite to our findings and assumptions. However, different methods were used in the cited articles to assess the penetration resistance.

Electrical resistivity semivariograms provide evidence about the conformity or non-conformity of the soil layers. A decrease in semivariance in depth and distance indicates spatial uniformity of the subsoil. In Fig. 7a, c and d, a more gradual rise in semivariance along the distance emerges below the identified plough pan. This leads to the conclusion that the soil structure changes below a certain depth and becomes more homogeneous. Transect B_T1 in Fig. 7b, which was measured in a field that is more deeply plowed, exhibits a decrease in semivariance along the distance above the plough pan. Deeper plowing disturbed the compacted soil but keeps the soil relatively homogeneous. The decrease in the variability of the electrical resistivity was observed by Séger et al. (2009) with the use of 3D ERT, where the hemisphere effect is lower than for 2D measurements.

5. Conclusions

Measurements of electrical resistivity, mechanical penetration resistance and the physical properties of undisturbed soil samples were

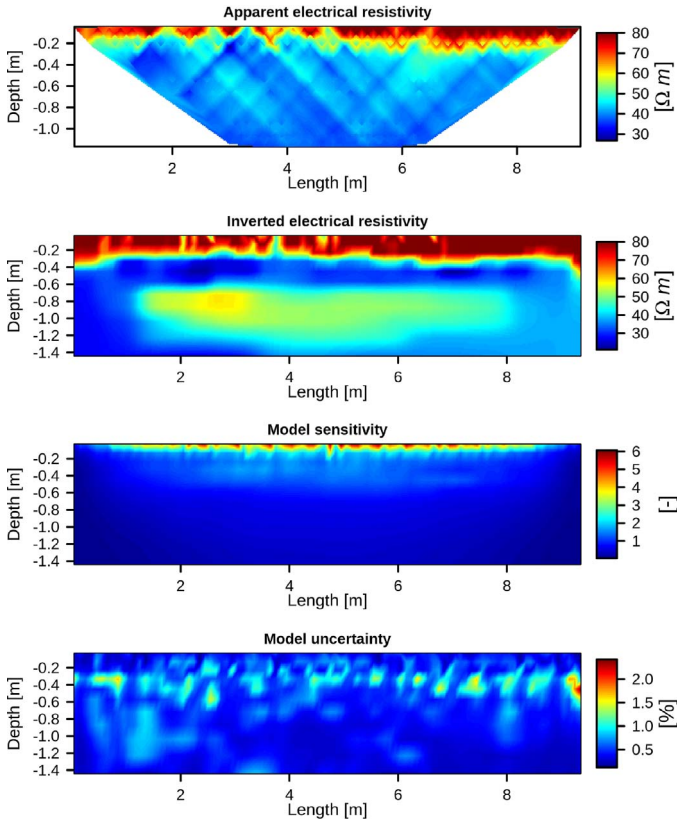

Fig. A.8. The results of the ERT transect A_T5; at the topmost panel are measured apparent electrical resistivities, at the second panel are depicted inverted electrical resistivities, at the third panel is the model sensitivity and at the bottommost panel is depicted the uncertainty of the model.

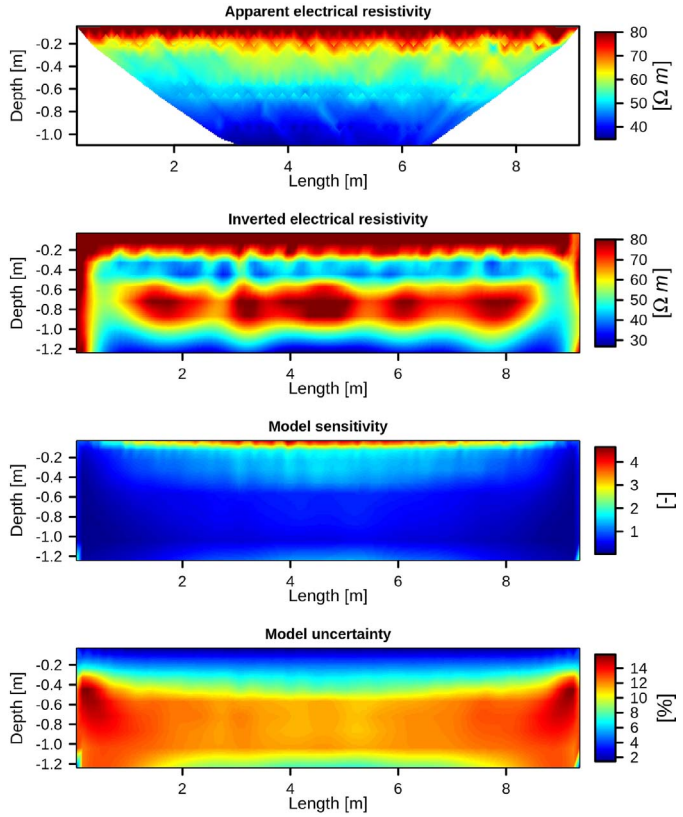

Fig. A.9. The results of the ERT transect B_T1; at the topmost panel are measured apparent electrical resistivities, at the second panel are depicted inverted electrical resistivities, at the third panel is the model sensitivity and at the bottommost panel is depicted the uncertainty of the model.

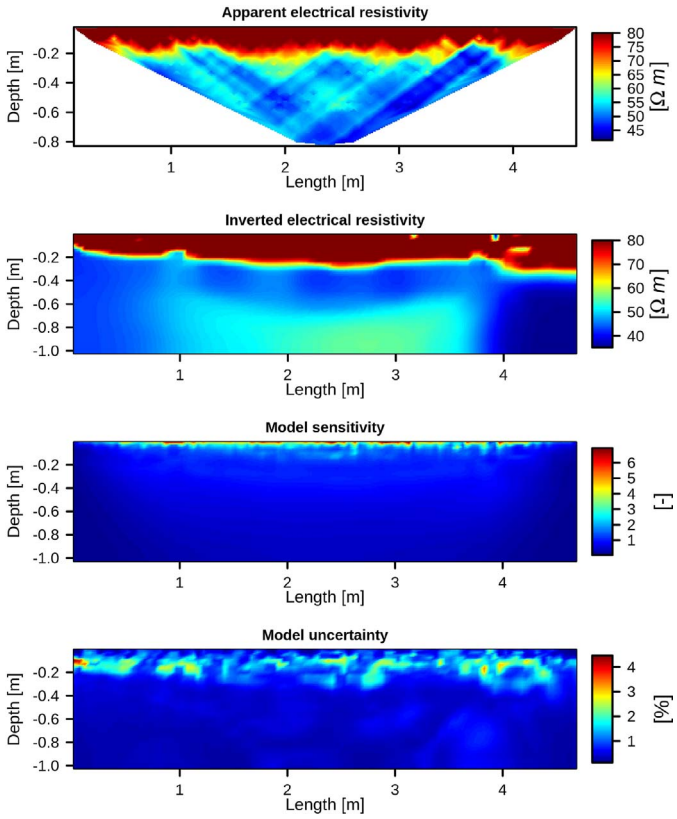

Fig. A.10. The results of the ERT transect C_T1; At the topmost panel are measured apparent electrical resistivities, at the second panel are depicted inverted electrical resistivities, at the third panel is the model sensitivity and at the bottommost panel is depicted the uncertainty of the model.

performed in order to assess the presence and the spatial uniformity of the plough pan along 10 transects in a small agricultural catchment in the central part of the Czech Republic. The measurements showed clearly that the plough pan is present in the soil profiles of the catchment in two distinctly tilled fields. According to the semivariance calculated from the electrical resistivity data, the plough pan exhibits a certain spatial variability, but the spatial variability of the topsoil is higher by one or two orders of magnitude. This leads to the conclusion that the plough pan is macroscopically uniform along the 2D transects.

We have demonstrated that the ERT technique is a useful tool for making a qualitative assessment of the spatial characteristics of the plough pan in cultivated fields. However, the success of this approach is dependent on the current saturation state of the soil, and on suitable electrode spacing according to the depth of the topsoil. Based on our findings, the water saturation should not be lower than field capacity. The electrode spacing is recommended to be approximately half of the expected depth of the plough pan. This is inhered from used ERT array.

Acknowledgements

The research presented here was performed within the framework of Czech Science Foundation postdoctoral project GP13-20388P, with support from a project supported by Czech Ministry of Agriculture grant no. QJ1230056, and with support from CTU internal project no. GS16/143/OHK1/2T/11.

Appendix A. ERT profiles

References

Ahuja, L., Fiedler, F., Dunn, G., Benjamin, J., Garrison, A., 1998. Changes in soil water retention curves due to tillage and natural reconsolidation. Soil Sci. Soc. Am. J. 62, 1228–1233.

Banerjee, S., Carlin, B.P., Gelfand, A.E., 2014. Hierarchical Modeling and Analysis for Spatial Data. CRC Press.

Basso, B., Amato, M., Bitella, G., Rossi, R., Kravchenko, A., Sartori, L., Carvahlo, L.M., Gomes, J., 2010. Two-dimensional spatial and temporal variation of soil physical properties in tillage systems using electrical resistivity tomography. Agron. J. 102, 440–449.

Bertolino, A.V., Fernandes, N.F., Miranda, J.P., Souza, A.P., Lopes, M.R., Palmieri, F., 2010. Effects of plough pan development on surface hydrology and on soil physical properties in southeastern Brazilian plateau. J. Hydrol. 393, 94–104.

Besson, A., Cousin, I., Samouëlian, A., Boizard, H., Richard, G., 2004. Structural heterogeneity of the soil tilled layer as characterized by 2d electrical resistivity surveying. Soil Tillage Res. 79, 239–249.

Besson, A., Sger, M., Giot, G., Cousin, I., 2013. Identifying the characteristic scales of soil structural recovery after compaction from three in-field methods of monitoring. Geoderma 204205, 130–139.

Boizard, H., Richard, G., Roger-Estrade, J., Dürr, C., Boiffin, J., 2002. Cumulative effects of cropping systems on the structure of the tilled layer in northern France. Soil Tillage Res. 64, 149–164.

Buvat, S., Thiesson, J., Michelin, J., Nicoullaud, B., Bourennane, H., Coquet, Y., Tabbagh, A., 2014. Multi-depth electrical resistivity survey for mapping soil units within two 3 ha plots. Geoderma 232234, 317–327.

Císlerová, M., Vogel, T., Simunek, J., 1990. Field-scale water and solute flux in soils. Birkhäuser Basel, Basel. The Infiltration-Outflow Experiment Used to Detect Flow Deviations. pp. 109–117.

Colombi, T., Braun, S., Keller, T., Walter, A., 2016. Artificial macropores attract crop roots and enhance plant productivity on compacted soils. Sci. Total Environ.

Coquet, Y., Coutadeur, C., Labat, C., Vachier, P., van Genuchten, M.T., Roger-Estrade, J., Šimůnek, J., 2005. Water and solute transport in a cultivated silt loam soil 1. Field observations. Vadose Zone J. 4, 573–586.

Dahlin, T., Loke, M., 1997. Quasi-3d resistivity imaging–mapping of three dimensional

structures using two dimensional dc resistivity techniques. 3rd EEGS Meeting.
Dörner, J., Horn, R., 2009. Direction-dependent behaviour of hydraulic and mechanical properties in structured soils under conventional and conservation tillage. Soil Tillage Res. 102, 225–232.
Fukue, M., Minato, T., Horibe, H., Taya, N., 1999. The micro-structures of clay given by resistivity measurements. Eng. Geol. 54, 43–53.
Furman, A., Ferré, T., Warrick, A., 2003. A sensitivity analysis of electrical resistivity tomography array types using analytical element modeling. Vadose Zone J. 2, 416–423.
Hadzick, Z., Guber, A., Pachepsky, Y., Hill, R., 2011. Pedotransfer functions in soil electrical resistivity estimation. Geoderma 164, 195–202.
Kim, H., Anderson, S., Motavalli, P., Gantzer, C., 2010. Compaction effects on soil macropore geometry and related parameters for an arable field. Geoderma 160, 244–251.
Kowalczyk, S., Maślakowski, M., Tucholka, P., 2014. Determination of the correlation between the electrical resistivity of non-cohesive soils and the degree of compaction. J. Appl. Geophys. 110, 43–50.
Lipiec, J., Horn, R., Pietrusiewicz, J., Siczek, A., 2012. Effects of soil compaction on root elongation and anatomy of different cereal plant species. Soil Tillage Res. 121, 74–81.
Loke, M., Chambers, J., Rucker, D., Kuras, O., Wilkinson, P., 2013. Recent developments in the direct-current geoelectrical imaging method. J. Appl. Geophys. 95, 135–156.
Loke, M.H., 2004. Tutorial: 2-D and 3-D Electrical Imaging Surveys.
Mazáč, O., Císlerová, M., Vogel, T., 1988. Application of geophysical methods in describing spatial variability of saturated hydraulic conductivity in the zone of aeration. J. Hydrol. 103, 117–126.
Naderi-Boldaji, M., Sharifi, A., Hemmat, A., Alimardani, R., Keller, T., 2014. Feasibility study on the potential of electrical conductivity sensor veris 3100 for field mapping of topsoil strength. Biosyst. Eng. 126, 1–11.
Nadler, A., 1991. Effect of soil structure on bulk soil electrical conductivity (ECa) using the TDR and 4P techniques. Soil Sci. 152, 199–203.
Pagliai, M., Marsili, A., Servadio, P., Vignozzi, N., Pellegrini, S., 2003. Changes in some physical properties of a clay soil in central Italy following the passage of rubber tracked and wheeled tractors of medium power. Soil Tillage Res. 73, 119–129.
Pagliai, M., Vignozzi, N., Pellegrini, S., 2004. Soil structure and the effect of management practices. Soil Tillage Res. 79, 131–143.
Revil, A., Karaoulis, M., Johnson, T., Kemna, A., 2012. Review: some low-frequency electrical methods for subsurface characterization and monitoring in hydrogeology. Hydrogeol. J. 20, 617–658.
Roulier, S., Angulo-Jaramillo, R., Bresson, L.M., Auzet, A.V., Gaudet, J.P., Bariac, T., 2002. Water transfer and mobile water content measurement in a cultivated crusted soil. Soil Sci. 167, 201–210.
Samouëlian, A., Cousin, I., Tabbagh, A., Bruand, A., Richard, G., 2005. Electrical resistivity survey in soil science: a review. Soil Tillage Res. 83, 173–193.
Séger, M., Cousin, I., Frison, A., Boizard, H., Richard, G., 2009. Characterisation of the structural heterogeneity of the soil tilled layer by using in situ 2D and 3D electrical resistivity measurements. Soil Tillage Res. 103, 387–398.
Séger, M., Guérin, R., Frison, A., Bourennane, H., Richard, G., Cousin, I., 2014. A 3d electrical resistivity tomography survey to characterise the structure of an albeluvic tonguing horizon composed of distinct elementary pedological volumes. Geoderma 219, 168–176.
Sněhota, M., Sobotková, M., Císlerová, M., 2008. Impact of the entrapped air on water flow and solute transport in heterogeneous soil: experimental set-up. J. Hydrol. Hydromech. 56, 247–256.
Sudha, K., Israil, M., Mittal, S., Rai, J., 2009. Soil characterization using electrical resistivity tomography and geotechnical investigations. J. Appl. Geophys. 67, 74–79.
Zumr, D., Dostál, T., Devaty, J., 2015. Identification of prevailing storm runoff generation mechanisms in an intensively cultivated catchment. J. Hydrol. Hydromech. 63, 246–254.

Received: 28 September 2020 | Revised: 30 December 2020 | Accepted: 5 January 2021

DOI: 10.1002/hyp.14042

RESEARCH AND OBSERVATORY CATCHMENTS: THE LEGACY AND THE FUTURE

WILEY

An overview of hydrometeorological datasets from a small agricultural catchment (Nučice) in the Czech Republic

Tailin Li | Jakub Jeřábek | Nina Noreika | Tomáš Dostál | David Zumr

Faculty of Civil Engineering, Czech Technical University in Prague, Prague, Czech Republic

Correspondence
Tailin Li, Faculty of Civil Engineering, Czech Technical University in Prague, Thákurova 7, 16629 Praha 6, Prague, Czech Republic.
Email: tailin.li@fsv.cvut.cz

Funding information
České Vysoké Učení Technické v Praze, Grant/Award Number: SGS20/156/OHK1/3T/11; European Commission, Grant/Award Number: 773903

Abstract

We introduce the freely available web-based Water in an Agricultural Landscape—NUčice Database (WALNUD) dataset that includes both hydrological and meteorological records at the Nučice experimental catchment (0.53 km^2), which is representative of an intensively farmed landscape in the Czech Republic. The Nučice experimental catchment was established in 2011 for the observation of rainfall–runoff processes, soil erosion processes, and water balance of a cultivated landscape. The average altitude is 401 m a.s.l., the mean land slope is 3.9%, and the climate is humid continental (mean annual temperature 7.9°C, annual precipitation 630 mm). The catchment is drained by an artificially straightened stream and consists of three fields covering over 95% of the area which are managed by two different farmers. The typical crops are winter wheat, rapeseed, and alfalfa. The installed equipment includes a standard meteorological station, several rain gauges distributed across the basin, and a flume with an H-type facing that is used to monitor stream discharge, water turbidity, and basic water quality indicators. Additionally, the groundwater level and soil water content at various depths near the stream are recorded. Recently, large-scale soil moisture monitoring efforts have been introduced with the installation of two cosmic-ray neutron sensors for soil moisture monitoring. The datasets consist of observed variables (e.g. measured precipitation, air temperature, stream discharge, and soil moisture) and are available online for public use. The cross-seasonal, open access datasets at this small-scale agricultural catchment will benefit not only hydrologists but also local farmers.

KEYWORDS
agricultural catchment, hydrological modelling, hydrology, soil moisture

1 | DATA SET NAME

Water in an Agricultural Landscape—Nučice Database (WULNUD).

2 | SITE DESCRIPTION

The Nučice experimental catchment was established in 2011 with the main aim to study the water balance of cultivated fields and associated rainfall–runoff and soil erosion processes. The catchment is 0.531 km^2 and located 30 km east of Prague in an agricultural landscape in the Central Bohemian Region, Czech Republic (catchment outlet location: 49°57′49.230″N, 14°52′13.242″E) (Figure 1). The morphology, climatic conditions, and agricultural management are representative of farmlands of the Czech Republic. The area belongs to the moderately hilly Bohemian Massif, the catchment has an average altitude of 401 m a.s.l. and slopes ranging from 1 to 12%. The climate is humid continental with average annual precipitation of 630 mm

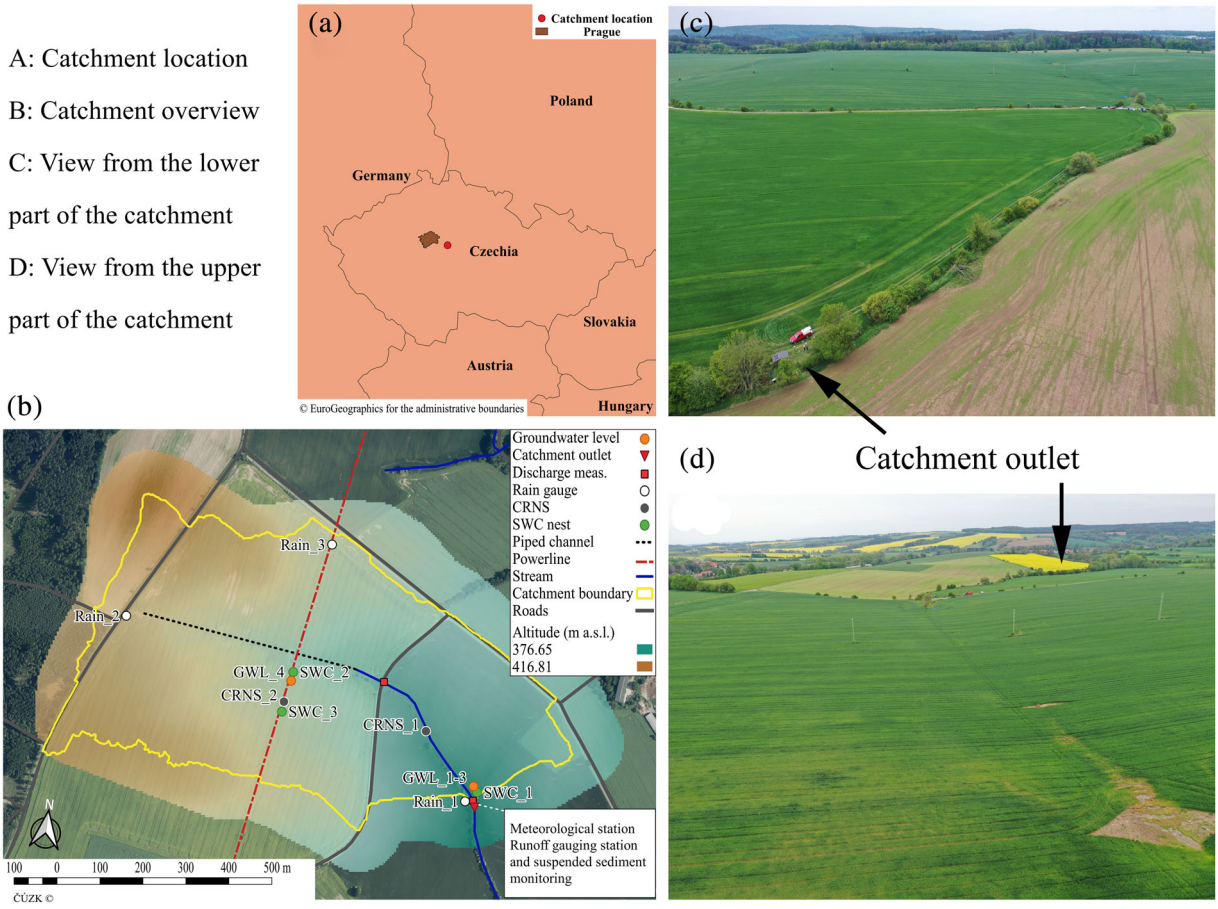

FIGURE 1 Overview of the Nučice catchment: (a) catchment location, (b) catchment overview, (c) view from the lower part of the catchment, and (d) view from the upper part of the catchment

from 1975 to 2015, mean annual potential evapotranspiration between 500 and 550 mm, and mean annual air temperature of 7.9°C (Hanel et al., 2013). The catchment is drained by a 950 m long, narrow stream which begins as a subsurface drainage pipe in the uppermost field. The channel has a trapezoidal cross-section that is 0.6 m wide at the stream bed with an average depth of 1.5 m (Zumr et al., 2017).

The area of the catchment is almost exclusively covered by arable land. Less than 5% of the area consists of the stream, paved roads, and shrublands. The fields are tilled to the edge of the stream banks; grass strips are not present. Therefore, the surface runoff and eroded soil may enter the stream without significant transformation in a riparian zone. The catchment is divided into three parcels which have existed since 2000 (Noreika et al., 2020). The standard crop rotation is dominated by winter wheat (*Triticum aestivum* L.), rapeseed (*Brassica napus*), summer oats (*Avena sativa*), and alfalfa (*Medicago sativa*).

The soils are developed on Palaeozoic conglomerate and are classified as Haplic Luvisols and Cambisols. The soil texture is considered sandy loam (9% clay, 58% silt, and 33% sand, on average; Zumr et al., 2019). Several geophysical surveys using electrical resistivity tomography (ERT) have been conducted to capture the degree of homogeneity/heterogeneity present in the plough pan and to determine the depth of the bedrock (Jeřábek et al., 2017). Based on geophysical monitoring and a geological borehole survey conducted at a close by location, the bedrock ranges in depth from 6 to 20 m. The soil is tilled to approximately 12 cm and below the tilled topsoil there is a compacted plough pan with low hydraulic conductivity that ranges between 10^{-8} m/s and 2.3. 10^{-7} m/s (Zumr et al., 2015).

The catchment often exhibits dry conditions during the summer and the baseflow recorded at the catchment outlet declines to 0–0.2 L/s, while in winter and early spring the baseflow is around 4 L/s. The average annual runoff coefficient is 1%. The runoff coefficient is low since the ground water level is usually below the water level in the stream, some water leaves the catchment as unmonitored groundwater flow (Noreika et al., 2020; Zumr et al., 2015). Runoff exhibits a threshold response to rainfall. Based on the measured rainfall–runoff data, we have identified a rather scattered rainfall–runoff relationship with a strong dependence of the runoff on the actual topsoil saturation. Different runoff pathways and runoff mechanisms have been observed. Once the soil moisture conditions are below a certain threshold value, the magnitude of the stormflow is not correlated to rainfall total (Zumr et al., 2015). Therefore, the shallow topsoil and its water holding capacity play a significant role in runoff generation. As the topsoil becomes saturated over a large part of the catchment, water is quickly routed via surface (especially through the compacted wheel tracks in the slope wise direction) and shallow subsurface runoff processes towards the drainage channel. Even though the channel

is straight and short, it has a high retention capacity and the flood wave peaks during runoff events are attenuated. The channel serves as a trap for eroded sediment during the summer months due to dense instream vegetation (Zumr et al., 2017).

3 | WATER IN AN AGRICULTURAL LANDSCAPE—NUČICE DATABASE

The catchment is equipped with instrumentation for basic meteorological, hydrological, and hydropedological monitoring. Most of the variables are recorded at 5-min intervals. As the experimental catchment does not belong to the World Meteorological Organization (WMO) nor the Czech Meteorological Institute monitoring networks, the monitoring scheme does not strictly follow WMO standards. A detailed description of the equipment, including sensor accuracies and calibration frequencies, is listed in Appendix (Table A1).

Discharge is monitored at two locations in the stream. Firstly, in the culvert below the upper field; a pressure probe is installed for water depth monitoring and the discharge is calculated based on the circular culvert free-flow discharge relationships, which has been recalibrated during flood wave experiments in 2013, 2014, and 2020 (Zumr et al., 2017) when known discharge (ranging between 2 and 40 L/s) was flowing through the culvert. Secondly, at the catchment outlet there is a flume with an H-type facing with a capacity of 400 L/s that is serially connected to a triangular overflow Thomson weir (90° V-notch) installed approximately 5 m further downstream with a capacity of 5 L/s. The water level is measured in both the flume with the H-type facing and the V-notch weir independently. This setup allows us to measure both high discharge (with the flume with H-type facing) and low discharge (with the Thomson weir), since each

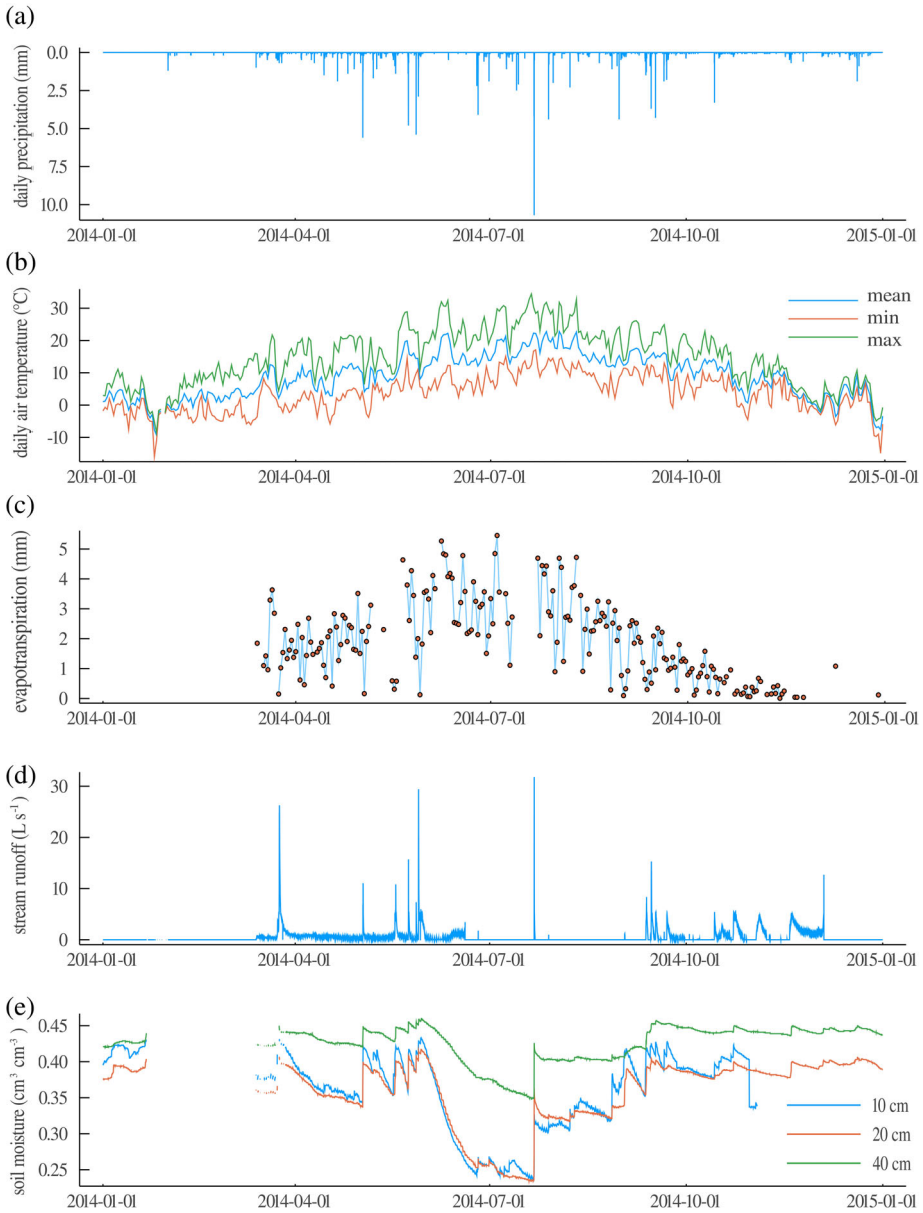

FIGURE 2 Time series plots for observation data in 2014: (a) precipitation at Rain_1, (b) air temperature at Rain_1, (c) evapotranspiration at Rain_1, (d) stream runoff at the outlet, and (e) soil moisture dynamic at SWC_1

has the best accuracy at their respective discharge ranges. The water level is measured by pressure transducers (LMP307, BD Sensors, Czech Republic, accuracy = ±0.1%) and a sonic distance sensor (SR50A, Campbell Sci., UK, accuracy = ±10 mm) in the flume with H-type facing. Stream water temperature, electrical conductivity (CS547A, Campbell Sci., accuracy = ±5%), and turbidity (VisoTurb 700 IQ, WTW, Germany, accuracy = ±0.1 mg/L) are also recorded. The meteorological station records air temperature, relative humidity (CS215, Campbell Sci., UK, accuracy = ±0.4°C, RH ±2%), wind speed and direction (03002, R. M. Young, accuracy = ±0.5 m/s, ±5°), and net radiation (NR Lite 2, Kipp & Zonen, accuracy = ±10 μV W^{-1} m^{-2}). The groundwater level is monitored hourly via three 5 m deep piezometers (water level monitored with pressure transducers LMP307, BD Sensors, accuracy = ±2 mm for GWL_1, ±2.5 mm for GWL_2 and GWL_3). The soil water regime is monitored at two points by water content reflectometers (CS650, Campbell Sci., accuracy = ±1%) at depths between 10 and 60 cm. Two cosmic-rays neutron sensors (Cosmic-Ray Neutron Detector System, StyX Neutronica, accuracy = ±6%; Bogena et al., 2013) are installed in the catchment for larger scale topsoil water content estimation (Figure 1).

Three rain gauges (Rain_1–Rain_3; tipping buckets with 0.1 mm resolution) are distributed across the catchment (Figure 1). Rainfall observations near the catchment outlet (Rain_1) have been measured with an MR3-01s tipping bucket rain gauge (Meteoservis, Czech Republic) and recorded with a CR1000 datalogger (Campbel Sci., UK) at a 5-min resolution since 2013 while the rain gauge (RAIN-OMATIC PRO, Pronamic ApS, Denmark) in the upper field (Rain_2) began recording data at the end of 2019. The Rain_3 gauge was installed during autumn 2020 (during the datanote preparation) and its data will be regularly (every 6 months) added to the database with the rest of the data. All of the precipitation records in the dataset have been post-processed for quality control assurance (to exclude extreme values caused by measurement errors). The air temperature has been recorded every 10 min simultaneously at the same locations as precipitation intensity: near the outlet (Rain_1) since 2013 and at the Rain_2 station from 2019. The dataset contains temperature data including daily minimums, averages, and maximums at both stations. Daily net radiation, mean daily wind speed, maximal/minimal daily temperatures, and relative air humidity are also measured at Rain_1. Additionally, daily reference evapotranspiration (ET_o) is calculated based on the data recorded at location Rain_1. ET_o is calculated according to the FAO methodology (Allan et al., 1998), where ET_o is expressed in terms of the Penman–Monteith ET equation calculated for grass as a reference crop.

For the hydrological data, the stream discharge in the dataset includes the measured discharge at the catchment outlet since the end of 2013. Quality control of the runoff data (removal of extreme values caused by measurement errors) was implemented, and the runoff was saved at a 10-min time resolution. Based on the runoff observations, one or two peak flows usually happen in the summer after intensive summer storms. In addition, the measurement errors of runoff have often occurred during the winter due to the sensor failure caused by ice cover in the flume (Figure 2). Moreover, the dataset contains temporal soil moisture records from two points:

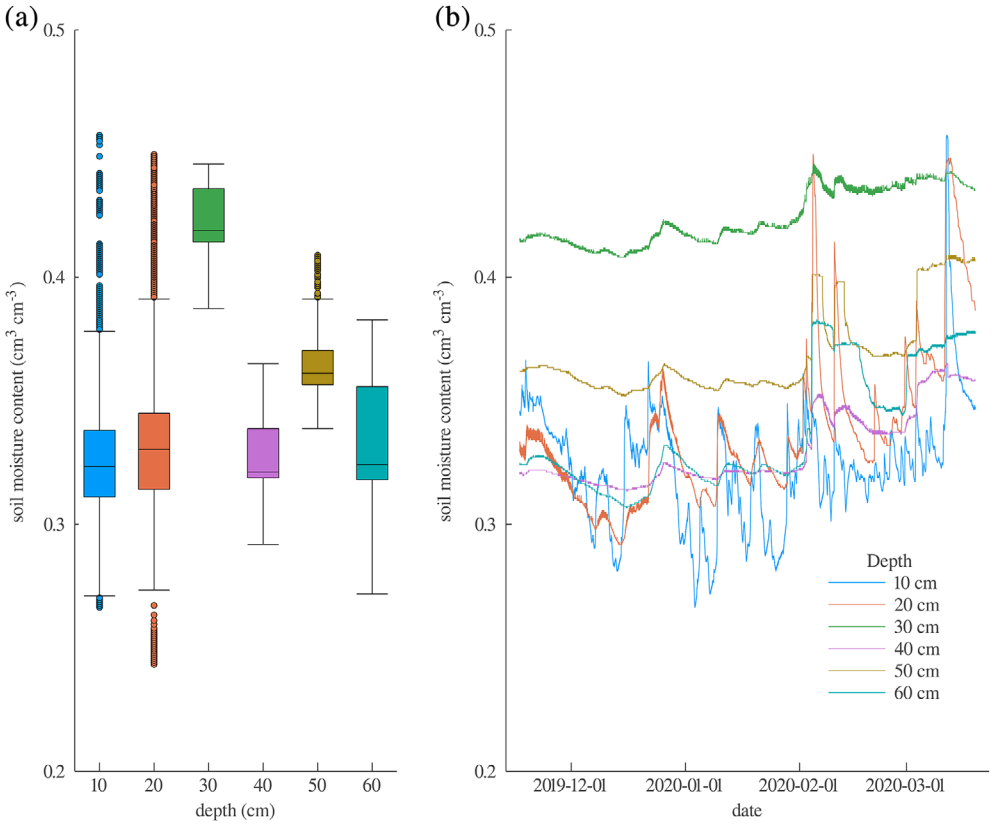

FIGURE 3 Soil moisture dynamics during winter at SWC_2: (a) boxplot of the soil moisture content at six depths, (b) time series of soil moisture dynamics

one is located near the outlet (SWC_1; at three depths from 10 to 40 cm) since the end of 2013, the other is close to the powerline (SWC_2; at six depths from 10 to 60 cm) since the end of 2019 (Figure 1). In general, the soil moisture dynamics (especially the topsoil) are behaviorally similar to the runoff variation (Figure 2). The soil moisture in the uppermost layer has a higher degree of fluctuation when compared to the deeper layers (Figure 3). To summarize the data and provide a more comprehensive perspective of the observations for each year, we have included metadata and annual reports in the dataset. However, since more devices have been deployed at the catchment recently, the dataset will be updated every 6 months with the observed data also from the newly deployed devices.

4 | APPLICATION

4.1 | Application of the data

The hydrometeorological dataset in Nučice has been primarily used for the investigation of hydrological responses under the impacts of agricultural activities. Zumr et al. (2015) shows that based on the rainfall–runoff event analysis, the subsurface runoff dominated the storm runoff generation. The topsoil physical properties (bulk density, porosity) exhibited expected changes with topsoil consolidation during a growing season. However, the unsaturated hydraulic conductivity showed inconsistent trends in subsequent growing seasons (Zumr et al., 2019). The data have also been used to calibrate and validate a hydrological model in the Soil and Water Assessment Tool (SWAT) to conduct scenario analysis to determine the effects of crop changes on in-basin water balance (Gómez et al., 2020; Noreika et al., 2020).

5 | CONTRIBUTORS AND DATA OWNERSHIP

Several people, including Master of Science and PhD students, have been involved in the sensor installations, maintenance, fieldwork, and experiments. Tomáš Dostál initiated the establishment of the experimental catchment. The environmental data have been collected primarily by David Zumr (2012–2020), Jakub Jeřábek (2015–2020), and Tailin Li (2019–2020). Nina Noreika analysed and proofread data for the annual reports and the data note. The research at the Nučice experimental catchment would not be possible without the support of the local farmers Mr Kopecký and Mr Morávek. Czech Technical University in Prague has full ownership of the dataset.

ACKNOWLEDGEMENTS

The establishment and the further maintenance of the Nučice catchment have been possible thanks to numerous research projects funded by the Czech Science Foundation, the Ministry of Education, Youth and Sport, the Ministry of Agriculture of the Czech Republic, and European Social Fund. This work has been supported by the Grant Agency of the Czech Technical University in Prague, Grant No. SGS20/156/OHK1/3T/11 and the Project SHui which is co-funded by the European Union Project: 773903 and the Chinese Ministry of Science and Technology.

DATA AVAILABILITY STATEMENT

The main aim of the WALNUD dataset is to provide long term data of runoff dynamics and water fluxes within the soil–plant–atmosphere system in an intensively cultivated landscape of the Czech Republic. The WALNUD dataset is available at http://storm.fsv.cvut.cz/o-nas/vybaveni/povodi/nucice. We have also provided guidance to the available data at http://storm.fsv.cvut.cz/data/files/readme.txt. Additional data from field campaigns and ad hoc monitoring can be made available upon request to Tailin Li (tailin.li@fsv.cvut.cz) or David Zumr (david.zumr@fsv.cvut.cz). All the data in the dataset are shared under a Creative Commons attribution license (CC BY) and must be appropriately cited.

ORCID

Tailin Li https://orcid.org/0000-0002-9648-3347

REFERENCES

Allan, R., Pereira, L., & Smith, M. (1998). *Crop evapotranspiration – Guidelines for computing crop water requirements – FAO irrigation and drainage paper 56* (Vol. 56), Rome: Food and Agriculture Organization of the United Nations. http://www.fao.org/3/x0490e/x0490e00.htm.

Bogena, H. R., Huisman, J. A., Baatz, R., Hendricks Franssen, H.-J., & Vereecken, H. (2013). Accuracy of the cosmic-ray soil water content probe in humid forest ecosystems: The worst case scenario. *Water Resources Research*, *49*(9), 5778–5791. https://doi.org/10.1002/wrcr.20463

Gómez, J. A., Ben-Gal, A., Alarcón, J. J., de Lannoy, G., de Roos, S., Dostál, T., Fereres, E., Intrigliolo, D. S., Krása, J., Klik, A., Liebhard, G., Nolz, R., Peeters, A., Plaas, E., Quinton, J. N., Miao, R., Strauss, P., Xu, W., Zhang, Z., … Dodd, I. C. (2020). SHui, an EU-Chinese cooperative project to optimize soil and water management in agricultural areas in the XXI century. *International Soil and Water Conservation Research*, *8*(1), 1–14. https://doi.org/10.1016/j.iswcr.2020.01.001

Hanel, M., Mrkvičková, M., Máca, P., Vizina, A., & Pech, P. (2013). Evaluation of simple statistical downscaling methods for monthly regional climate model simulations with respect to the estimated changes in runoff in the Czech Republic. *Water Resources Management: An International Journal, Published for the European Water Resources Association (EWRA)*, *27*(15), 5261–5279.

Jeřábek, J., Zumr, D., & Dostál, T. (2017). Identifying the plough pan position on cultivated soils by measurements of electrical resistivity and penetration resistance. *Soil and Tillage Research*, *174*, 231–240. https://doi.org/10.1016/j.still.2017.07.008

Noreika, N., Li, T., Zumr, D., Krasa, J., Dostal, T., & Srinivasan, R. (2020). Farm-scale biofuel crop adoption and its effects on in-basin water balance. *Sustainability*, *12*(24), 10596. https://doi.org/10.3390/su122410596

Zumr, D., Dostál, T., & Devátý, J. (2015). Identification of prevailing storm runoff generation mechanisms in an intensively cultivated catchment. *Journal of Hydrology and Hydromechanics*, *63*(3), 246–254. https://doi.org/10.1515/johh-2015-0022

Zumr, D., Dostál, T., Devátý, J., Valenta, P., Rosendorf, P., Eder, A., & Strauss, P. (2017). Experimental determination of the flood wave transformation and the sediment resuspension in a small regulated stream in an agricultural catchment. *Hydrology and Earth System Sciences*, *21*(11), 5681–5691. https://doi.org/10.5194/hess-21-5681-2017

Zumr, D., Jeřábek, J., Klípa, V., Dohnal, M., & Sněhota, M. (2019). Estimates of tillage and rainfall effects on unsaturated hydraulic conductivity in a small central european agricultural catchment. *Water*, *11*(4), 740. https://doi.org/10.3390/w11040740

How to cite this article: Li T, Jeřábek J, Noreika N, Dostál T, Zumr D. An overview of hydrometeorological datasets from a small agricultural catchment (Nučice) in the Czech Republic. *Hydrological Processes*. 2021;35:e14042. https://doi.org/10.1002/hyp.14042

APPENDIX A

TABLE A1 List of sensors in the Nučice catchment

Station ID	Measured variable	Sensor	Manufacturer	Accuracy	Active monitoring period	Datalogger	Temporal resolution (min)	Calibration
Meteo	Air temperature	PT100-XM	Fiedler AMS, České Budějovice, Czech Republic	0.15°C	2011–2016	LEC-3000, Libor Daneš, Roztoky, Czech Republic	10	
	Relative humidity	HS005	J. Tlusťák, Praha, Czech Republic	6% RH	2011–2016		10	
	Air temperature and relative humidity	HST		0.15°C, 6% RH	2016–2020		10	
	Air temperature and relative humidity	CS215	Campbell Sci., Logan, UK	0.4°C, 2% RH	2019–	CR300, Campbell Sci., Logan, UK	5	
	Wind speed	W1	C. T. M. Praha, Czech Republic	0.1 m/s	2011–2019	LEC-3000	10	
	Wind speed and direction	03002 Wind Sentry	R. M. YOUNG, Traverse City, MI	0.5 m/s, 5°	2019–	CR300	5	
Rain_1	Precipitation intensity	SR1	J. Tlusťák	<9%	2011–2020	LEC-3000	10	Once a year
	Precipitation intensity	MR3-01s	METEOSERVIS, Vodňany, Czech Republic	<5%	2014–	CR1000, Campbell Sci., Logan, UK	5	Once a year
	Net radiation	NR Lite	Kipp & Zonen, Delft, Netherlands	10 μV W^{-1} m^{-2}	2014–		5	In 2017
Rain_2	Precipitation intensity	RAIN-O-MATIC PRO	Pronamic ApS, Ringkoebing, Denmark	2%	2018–	Minikin ERi, EMS, Brno, Czech Republic	1	Once a year
	Air temperature	Pt 1000 A-class	EMS, Brno, Czech Republic	0.2°C	2019–		1	
Rain_3	Precipitation intensity	MR3-01s	METEOSERVIS	<5%	2020–		5	Once a year
GWL_1	Ground water level	LMP307i-451 pressure transducer	BD Sensors Buchlovice, Czech Republic	2 mm	2017–	H40, Fiedler AMS, České Budějovice, Czech Republic	60	Once a year
GWL_2	Ground water level	LMP307-451 pressure transducer		2.5 mm	2017–	MINILOG, Fiedler AMS, České Budějovice, Czech Republic	60	Once a year
GWL_3	Ground water level	LMP307-451 pressure transducer		2.5 mm	2017–		60	Once a year
GWL_4	Ground water level	LMP307-451 pressure transducer		2.5 mm	2017–		60	Once a year

(Continues)

TABLE A1 (Continued)

Station ID	Measured variable	Sensor	Manufacturer	Accuracy	Active monitoring period	Datalogger	Temporal resolution (min)	Calibration
Catchment outlet	*Large discharge (H-flume)*	H-flume, capacity up to 400 L/s	Based on HOAL, Petzenkirchen, Austria	2–5%	2011–			Rating curve calibrated in hydraulic lab of TU Vienna, Austria; recalibrated during flood experiments in 2012, 2013, and 2020
	H-Flume water level	LMP307-451 pressure transducer	BD sensors	2.5 mm	2011–2014	LEC-3000	10	Four times a year
	H-Flume water level	LMP307i pressure transducer		1 mm	2014–	CR1000	5	Four times a year
	H-Flume water level	U-GAGE T30 ultrasonic sensor	Banner Engineering Corp., Mpls, MN	2 mm	2012–2016	LEC-3000	10	Four times a year
	H-Flume water level	SR50A ultrasonic sensor	Campbell Sci.	10 mm	2017–	CR1000	5	Four times a year
	Air temperature (SR50A temp correction)	107 thermistor probe		0.4°C	2018–		5	
	Small discharge	V-notch, 90°, capacity up to 4.5 L/s		2%	2016–			Rating curve during flood experiments in 2012, 2013, and 2020
	V-notch water level	LMP307-151 pressure transducer	BD sensors	1 mm	2016–2018	MINILOG	60	Four times a year
	V-notch water level	TSH22 pressure transducer and termistor	Fiedler AMS	0.1%, 0.3°C	2018–	H7 Hydro controller, Fiedler AMS, České Budějovice, Czech Republic	10	Four times a year
	Turbidity	ViSolid 700 IQ + DIQ/S 181	WTW, Xylem Analytics, Germany	0.1 mg/L	2013–2019	CR1000	10	Four times a year
	Turbidity	S461	Chemitec, Firenze, Italy	5%	2019–	H7 Hydro controller	10	Four times a year

TABLE A1 (Continued)

Station ID	Measured variable	Sensor	Manufacturer	Accuracy	Active monitoring period	Datalogger	Temporal resolution (min)	Calibration
	Electrical conductivity and water temperature	CS547A	Campbell Sci.	Cond 5%, temp 0.2°C	2016–2019	CR1000	10	
	Electrical conductivity and water temperature	CS547A		Cond 5%, temp 0.2°C	2019–		10	
	Water sampling (turbidity calibration, stable isotopes)	3700 Full-size portable sampler	Teledyne ISCO, Lincoln, NE		2013–		Event based	
Culvert	Water level and water temperature	TSH22 pressure transducer and termistor	Fiedler AMS	0.1%, 0.3°C	2014–	STELA	10	Rating curve during flood experiments in 2012, 2013, and 2020
SWC_1	Soil moisture, temp, el. cond.—water content reflectometer	4 × CS650 in three depths	Campbell Sci.	1%	2015–	CR1000	10	
SWC_2	Soil moisture, temp, el. cond.—water content reflectometer	6 × CS655 in three depths		1%	2019–	Microlog, EMS, Brno, Czech Republic	10	
CRNS 1 and 2	Thermal neutron counts, air temperature, relative humidity, and pressure	2 × STYX neutronica detectors	STYX Neutronica, Heidelberg, Germany	Water content 6% (Bogena et al., 2013)	2020–	STYX Neutronica, Heidelberg Germany	60	

3. INTERACTION OF WATER WITH EARTH STRUCTURES

Attached research articles:

- ***Zumr, D.**, Dostál, T., Devátý, J., Valenta, P., Rosendorf, P., Eder A., & Strauss, P. (2017). Experimental determination of the flood wave transformation and the sediment resuspension in a small regulated stream in an agricultural catchment. Hydrology and Earth System Sciences, 21(11). https://doi.org/10.5194/hess-21-5681-2017*

  Once runoff water enters the drainage channels, it causes a flood wave which has enough kinetic energy to carry a bedload of sediment. As Zumr et al. (2015) showed, during some rainfall runoff events, only the bedload material was mobilized and nearly no eroded particles entered the stream from the adjected fields. The research question was therefore to estimate the quantity and distance that stream sediment can travel during floods. The translocation regime of the bedload sediment was experimentally evaluated based on in total six artificially generated waves. The experiments were carried out under different conditions of stream vegetation. It was shown that even small waves mobilize the sediment, though the travel distance is quite short. Instream vegetation significantly influences the sediment runoff regime.

- ***Zumr, D.**, & Císlerová, M. (2010). Soil moisture dynamics in levees during flood events variably saturated approach. Journal of Hydrology and Hydromechanics, 58(1). https://doi.org/10.2478/v10098-010-0007-z*

  The soil water regime within the earth made water retaining bodies, such as dams or embankments, is of great importance when evaluating water seepage, internal soil erosion or piping due to rapidly percolating water, or slope stability. The soil water regime of the dam is traditionally evaluated using the Darcy law, which serves to estimate the depression cone of the saturated zone. In this study, we used more complex two-dimensional Richards equation to simulate the regime during filling and emptying of a levee. Therefore, we were able to simulate the saturated-unsaturated character of soil water dynamics within earth-filled dams.

- ***Zumr, D.**, David, V., Jeřábek, J., Noreika, N., & Krása, J. (2020). Monitoring of the soil moisture regime of an earth-filled dam by means of electrical resistance tomography, close range photogrammetry, and thermal imaging. Environmental Earth Sciences, 79(12). https://doi.org/10.1007/s12665-020-09052-w*

  Synergic approach of implementation of several techniques to noninvasively estimate water seepage pathways through an earth dam. Combination of remote sensing (unmanned aerial vehicle (UAV) thermal imaging), close range photogrammetry, and electrical resistivity tomography allowed to identify potential water seepage. The UAV monitoring system provided reliable data for a surface temperature distribution map that corresponded well to the topsoil water content and electrical resistivity.

Hydrol. Earth Syst. Sci., 21, 5681–5691, 2017
https://doi.org/10.5194/hess-21-5681-2017

Hydrology and Earth System Sciences
Open Access
EGU

Experimental determination of the flood wave transformation and the sediment resuspension in a small regulated stream in an agricultural catchment

David Zumr[1], Tomáš Dostál[1], Jan Devátý[1], Petr Valenta[1], Pavel Rosendorf[2], Alexander Eder[3], and Peter Strauss[3]

[1]Faculty of Civil Engineering, Czech Technical University in Prague, Prague, 16629, Czech Republic
[2]T. G. Masaryk Water Research Institute, Prague, 16000, Czech Republic
[3]Institute for Land & Water Management Research, Federal Agency for Water Management, 3252 Petzenkirchen, Austria

Correspondence to: David Zumr (david.zumr@fsv.cvut.cz)

Received: 5 May 2017 – Discussion started: 6 June 2017
Revised: 5 September 2017 – Accepted: 25 September 2017 – Published: 16 November 2017

Abstract. This paper presents the methodology used for artificial flood experiments conducted in a small artificial, trained (regulated) channel on the Nučice experimental agricultural catchment (0.5 km^2), central Czech Republic, and the results of the experiments. The aim was to monitor the transformation of the flood wave and the sediment transport within the channel. Two series of experiments were carried out in contrasting initial conditions: (a) in September, when the stream banks were dry, the baseflow was negligible, and the channel was fully overgrown with vegetation; and (b) in March, when the stream banks were almost water saturated, the baseflow was above the annual average, and there was no vegetation present. Within each campaign, three successive flood waves, each with an approximate volume of 17 m^3 and peak flow of ca. 40 L s^{-1}, were pumped into the upper part of the catchment drainage channel. The transformation of the flood wave and the sediment transport regime within an approximately 400 m long channel section were monitored by measuring the discharge, the turbidity, and the electrical conductivity in three profiles along the stream. On the basis of the results, it was concluded that there is a considerable amount of deposited sediment, even in the well-trained and straight channel that can be re-mobilized by small floods. Part of the recorded sediment therefore originates from the particles deposited during previous soil erosion events. The flood waves initiated in dissimilar instream conditions progressed differently – we show that the saturation of the channel banks, the stream vegetation and the actual baseflow had a strong influence on the flood transformation and the sediment regime in the channel. The sediment moves quickly in winter and early spring, but in the later part of the year the channel serves as a sediment trap and the resuspension is slower, if dense vegetation is present.

1 Introduction

Excessive soil erosion from upland areas resulting in the transport of soil particles with bound organic matter, nutrients, microbes, or pollutants into the rivers and reservoirs is considered as a major environmental problem (Drummond et al., 2014; Lal et al., 2007; Pimentel et al., 1995; Stoate et al., 2001). The processes of soil particle mobilization and transportation within agriculturally used fields, including the transfer into streams and rivers, have been extensively studied (Báčová and Krása, 2016; Boardman, 2003; Lal, 1998; Neal and Anders, 2015).

The headwater streams and drainage channels in sediment source areas, typically small rural catchments with intensively cultivated soils, have considerable retention capacities for sediment and nutrients (Hession et al., 2003). The streams are narrow with a small flow profile, the baseflow is usually low, the stream bed contains fine-grained particles with a high concentration of nutrients, and extensive vegetation can therefore often be found there. Soil particles that enter the channel during an erosion event can easily get embedded in the channel bed alluvium and be remobilized during subsequent runoff events, and the nutrients tend to be retained (Withers and Jarvie, 2008). The source of the sediment and

the processes related to the suspended sediment dynamics in the closing profiles are therefore of fundamental importance for an assessment of the sediment budget and the transport of dissolved or absorbed substances in the catchment (Walling, 2005). However, even physically based mathematical models of soil erosion assume that the sediment transported through water courses originates from a recent (or current) rainfall–runoff event. Similarly, traditional experiments and soil erosion monitoring usually rely on measurements of the sediment yield at the catchment outlet, assuming that the measured sediment yield originates on the hillslopes. If any retention in the channel is expected, no resuspension is then assumed, and this affects the total sediment budget. Minella et al. (2008) point out that the transport capacity of the channel may increase, and that the stream bed sediment is easily mobilized during runoff events with no eroded sediment from the catchment. Zumr et al. (2015) and also Musolff et al. (2015) show that a quick runoff response with no soil erosion on the fields is very commonly observed on cultivated catchments where subsurface runoff or tile drains are the dominant controls. The resuspension regime of the stream bed sediment and the connected nutrient transport depend on the characteristics of the stream, the hydrograph of the flood wave and the actual conditions of the channel (Peterson and Benning, 2013).

The sources of the suspended sediments recorded at the catchment outlet also vary due to seasonally varying vegetation (Hearne et al., 1994). The development of aquatic macrophytes limits the discharge capacity of the channels. Keesstra et al. (2012) evaluated the effect of temporary variable vegetation cover within the natural and semi-natural headwater channels and the stream riparian zone on water and sediment transport. On the basis of numerical modelling, they concluded that vegetation affects resuspension especially during high-flow conditions in streams that are not sediment supply limited. Similarly, Huisman et al. (2013) showed that the previously suspended sediment is mobilized during the later parts of the year. In spring the recently eroded sediment is quickly flushed downstream. Shore et al. (2015) showed that in the case of well-trained channels there is greater potential for fast sediment transportation downstream. However, this is not necessarily the rule in sparsely maintained and over-vegetated channels, where the sediment retention capacity is not negligible.

The key questions that we will address in this paper are as follows.

- Can well-trained and well-regulated stream channels act as a temporal sediment trap and sediment source due to the resuspension of sediments deposited from previous erosion events?
- How does the flood wave transformation regime and the suspended solids remobilization regime change within one season as a consequence of various instream vegetation and baseflow conditions?
- How does the resuspended sediment concentration and the mass movement change in the event of repeated short flood waves?

To answer these questions, we initiated two sets of three small artificial floods into a typical drainage channel in the rural landscape of central Bohemia, Czech Republic. The experiments were performed recurrently in September and in March, when the channel vegetation, the baseflow, and the channel saturation differ most.

2 Methods

2.1 Site description

The experiments were performed in the stream which drains the Nučice rural experimental catchment, Czech Republic (Fig. 1). The Nučice catchment (49°57′49.230″ N, 14°52′13.242″ E) was established in 2011 with the main purpose to monitor and study the rainfall–runoff and soil erosion processes by water originating from intensive rainfall over cultivated fields (Zumr et al., 2015).

The catchment (0.531 km^2) is located at elevations ranging from 382 to 417 m a.s.l. The inclination of the slopes varies between 1 and 12 %, the average slope being 3.9 %. The annual average precipitation is 630 mm, and the annual evapotranspiration is 500 mm. The mean air temperature is 6 °C, and the climate is considered as humid continental. The catchment is unique with its very uniform land use. More than 95 % of the area is arable land, while the remaining parts are the watercourse, riparian trees and shrubs, and paved roads. There are no forests, grassland, or urbanized areas. The arable land is cultivated down to the stream banks, and conservation tillage is practised. The usual crops are winter wheat (*Triticum aestivum* L.), mustard (*Sinapis alba* L.), and rapeseed (*Brassica napus*). The soil types are classified as Cambisols and Luvisols. The topsoil has loamy texture with content of 13 % clay, 42 % silt, and 45 % sand. The average annual topsoil saturated hydraulic conductivity is 4.8×10^{-7} m s^{-1}, and the mean organic carbon content is 1.9 %.

The Nučice catchment is drained by an artificially trained narrow stream, which has been piped in the uppermost part. The channel was modified into its current form in the 1950s, with the aim to decrease the groundwater level and to prevent inundation of the fields. The piped section is 530 m in length, and the open channel down to the outlet profile of the experimental catchment extends to 424 m. The straight, deep channel is in direct contact with the surrounding fields. The riparian vegetation is only sparse.

The channel has a trapezoid profile which is 0.6 m in width at the stream bed, and the slope of the banks is 1 : 2. The stream bed and footslopes up to 0.3 m are stabilized with concrete tiles. There are two culverts on the stream. One is 56 m from the start of the open channel, and it is 0.8 m in inner

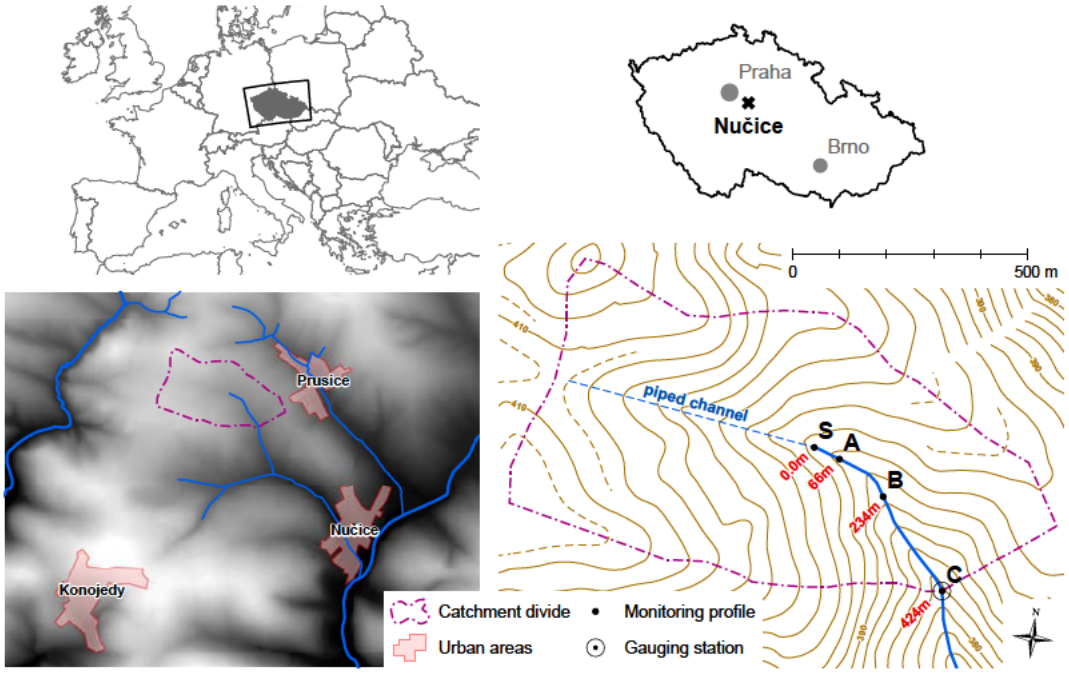

Figure 1. Map of the Nučice catchment with the measurement sites.

diameter and 10.2 m in length. The second culvert is 337 m from the start, and is 0.6 m in diameter and 7.8 m in length. The average depth of the channel is 1.5 m. The current situation of the channel represents very well the situation in most small regulated drainage channels in the country: there has been very little maintenance during the last ca. 30 years. Locally, therefore, the stabilization is defective and the channel profile has been covered by extensive weed vegetation with a predominance of stinging nettles (*Urtica dioica*), orchard grass (*Dactylis glomerata*), pigweed (*Chenopodium album*), and hogweed (*Heracleum sphondylium*).

The typical flow conditions at the gauging station, as observed during the period of monitoring (2011–2016), are as low as 0.1–0.2 L s^{-1} during the summer months and around 4 L s^{-1} towards the end of winter. Summer storm–runoff events accompanied by an increase in the concentration of suspended solids in the runoff are characteristic events. The storms cause a short, steep wave with a concentration time of 50 to 240 min (Zumr et al., 2015).

2.2 Experimental set-up

The experiments were performed in the open section of the channel (Fig. 1). The total monitored length was 424 m, which is the distance between the injection profile (profile S) and the basin closing profile (profile C). The point where we injected water is considered as the start (0 m), and the basin outlet is considered as the end (424 m). The release profile was placed directly at the beginning of open channel section. Water was pumped into the stream over a period of 7 min simultaneously from a filled water reservoir and from the onboard supply of a fire truck, using four fire hoses. We used drinking water from a nearby reservoir. The total pumped water volume for each wave was approximately 17 m^3. The very first wave (W1) was initiated with ca. 15 m^3 of water, because the pump could not draft the remaining 2 m^3 from the bottom of the water reservoir. The discharge fluctuated around 40 L s^{-1}, and no significant peaks were produced during injection. The water was pumped first into a small stilling basin to prevent excessive disturbance to the streambed, and to be able to make precise measurements of the discharge produced by the pump. The discharge was measured with a mobile H flume, where the water level was recorded automatically with a pressure transducer.

We established three monitoring stations along the watercourse (Figs. 1 and 2) to monitor the discharge and the electrical conductivity, and to collect samples for measuring the concentration of the suspended solids. After taking the initial water sample for an evaluation of the baseflow water properties, we started the water sampling in each experimental profile immediately after the flood wave arrived. Samples approximately 1 L in volume were taken every minute during the rise, the peak, and shortly after the decrease of the discharge. After that, the sampling interval was reduced to 2 to 5 min intervals to obtain approximately 30 samples for each wave and observation profile. The samples were analysed in the laboratory. The concentration of suspended solids, phosphorus, and nitrogen were measured. Each station was equipped with a pre-programmed camera on a tri-

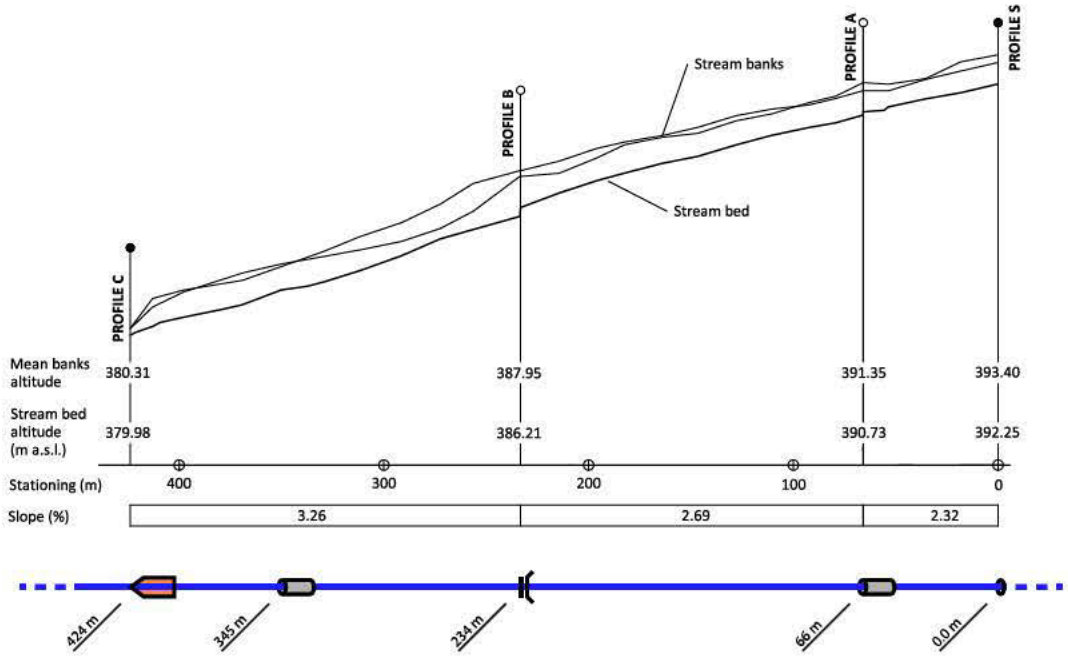

Figure 2. Stream longitudinal profile with monitoring sites and culverts on the Nučice experimental catchment.

pod to confirm the exact time of arrival of the wave and to document the progress of the wave and the sampling.

The first 66 m long section between pumping station S and profile A was meant to be used for wave dispersion and fluctuation stilling due to non-homogeneities in the pumping process. Station A was situated at the upper outlet of the culvert. The culvert ends with a free outflow, where the discharge was measured both volumetrically and hydrometrically. Monitoring profile B, in a distance of 224 m, was equipped with a rectangular weir, and the discharge was estimated on the basis of the measured depth of the water and the known rating curve. Profile C was located at the outlet of the experimental basin, positioned 424 m from the beginning of open channel section. The outlet is permanently equipped with an H flume with capacity of up to 400 $L\,s^{-1}$. The H flume's inlet is 1.3 m wide and 0.68 m high, the straight approach length is 2 m. The water depth was measured simultaneously with a pressure transducer and with an ultrasonic probe every 10 s. The sediment concentration was measured in the lab on samples taken from the outlet and with a turbidity probe (ViSolid 700IQ, WTW, Germany) installed in a stilling basin below the H flume. The onsite data were logged automatically with a CR1000 data logger (Campbell Sci., UK). The electrical conductivity of the water in profiles B and C in September 2012 and in profiles A, B, and C in March 2013 was measured with HQ40D portable multimeters (Hach Lange, Germany).

The experiments were conducted in September 2012 and in March 2013. Within each of the campaigns we carried out three wave experiments (W1 to W3 in September, W4 to W6 in March). Subsequent waves were always initiated after the discharge in the outlet profile (station C) had dropped close to the initial baseflow. The second waves in the series (W2 and W5) were enriched with NaCl as a tracer to compare the water velocity and the water celerity during wave propagation. The tracer was dissolved in the water reservoir to obtain a concentration of approximately 6 $g\,L^{-1}$. The first and third waves in each set contained no tracer.

Table 1. Initial conditions before the experiments.

Wave no.	W1, W2, W3	W4, W5, W6
General conditions	Dry	Wet
Date	4 September 2012	26 March 2013
Baseflow ($L\,s^{-1}$)	0.4	1.5
Soil moisture conditions	Dry, below field capacity	Nearly saturated
Vegetation in channel	Extensive	Negligible
Air temperature (°C)	12	−2
Baseflow water temperature (°C)	7	2

The general conditions within the catchment and the stream prior to the experiments differed in September 2012 and in March 2013 (Table 1). In September, the stream baseflow was at its annual minimum, the soil water content was below its field capacity, and the instream vegetation was densely overgrown. In March 2013, the baseflow was at its annual maximum because of saturated soil from the snow melting, the instream vegetation was sparse, and the

Figure 3. Stream vegetation conditions during the two experiments. Dense instream vegetation in September 2012 (**a**) and no erect vegetation in March 2013 (**b**).

remaining plants were flattened on the stream bed and banks (Fig. 3).

2.3 Numerical modelling of the propagation of the waves

For a quantitative evaluation of the impact of the vegetation on the transformation of the flood wave, we built a simple 1-D hydraulic model in HEC-RAS unsteady flow. The variable parameter between the September and March experiments was the stream roughness factor, which we attribute as a proxy of the actual character and density of the vegetation (Brookes, 1986). The approach is similar to the one of Nikora et al. (2008), who showed that the flow resistance is determined mainly by the general characteristics of the bulk instream vegetation, rather than by individual species. We assume that the vegetation resistance is mainly due to the stem blockage factor causing frictional energy losses, rather than by volume displacement effect, as the dense canopy occupies the cross section of the channel (Green, 2005).

The simulation of the hydraulic conditions in a channel system is based on a system of Saint Venant's equations. The evaluation of the energy gradient (friction slope) is based on Chézy's equation for velocity, where complex energy losses are represented by friction (Manning's formula). Unsteady flow is solved by the one-dimensional version of the finite difference method using the Preissman's implicit differential scheme.

The geometry of the channel was based on a set of 28 measured cross sections obtained by land surveying. To improve the precision of the simulations and to overcome numerical stability problems, intermediate profiles were added to the model by geometrical interpolation between the original cross sections. The average distance between cross sections in the final geometry set was 0.5 m. Moreover, each cross section was extended by a narrow Preismann bottom slot to deal with numerical stability issues in cases of very low discharges (propagation of the wave in an originally dry channel). The model was loaded on the upper end with the measured flow. The rating curve based on the Chezy equation for uniform flow was used as a downstream boundary condition.

The water exfiltration into the channel banks was simulated with the Richards equation; van Genuchten's model for soil water retention curve was used. The hydraulic characteristics and the saturated hydraulic conductivity of the stream banks were assumed to be the same as the measured subsoil matrix characteristics on the surrounding fields (residual water content $\theta_r = 0.095\,\mathrm{cm^3\,cm^{-3}}$, saturated water content $\theta_S = 0.44\,\mathrm{cm^3\,cm^{-3}}$, $\alpha = 0.019\,\mathrm{cm^{-1}}$, $n = 1.31$, $K_S = 2.3 \times 10^{-7}\,\mathrm{m\,s^{-1}}$). The modelling procedure was identical to the methodology described in Zumr and Císlerová (2010).

3 Results

The hydrographs and sedigraphs of all six waves are shown in Figs. 4–6. The shape characteristics of the waves and the transformation are summarized in Table 2. The water and sediment balance are presented in Table 3.

3.1 Water flow regime

The hydrographs of the subsequent experiments differed on all the monitoring profiles. The velocity of the waves and the maximum flow rates increased between the successive waves (Fig. 4). All the waves approached the A profile less than 5 min after the start of the experiments, and the subsequent waves reached the profile slightly earlier. The time difference between the approaches of waves W1 and W3 is 41 s. Waves W1 and W2 reached a similar peak discharge of approximately $30\,\mathrm{L\,s^{-1}}$, and wave W3 reached a peak discharge of $36.3\,\mathrm{L\,s^{-1}}$. The difference was mainly caused by the slightly fluctuating rate of water pumping and by transient filling of the depression storages on the channel bed during the first wave experiment. Water exfiltration into the hyporheic zone contributed only a little over such a short dis-

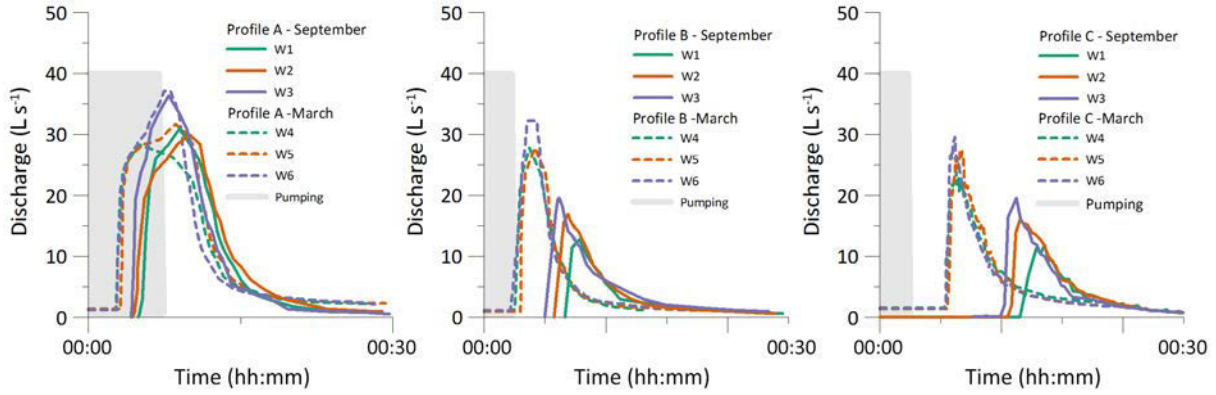

Figure 4. Hydrographs of flood propagation along the monitored stream in the Nučice catchment. The different dynamics in September (W1–W3) and March (W4–W6) are caused by the current state of the stream and the vegetation conditions.

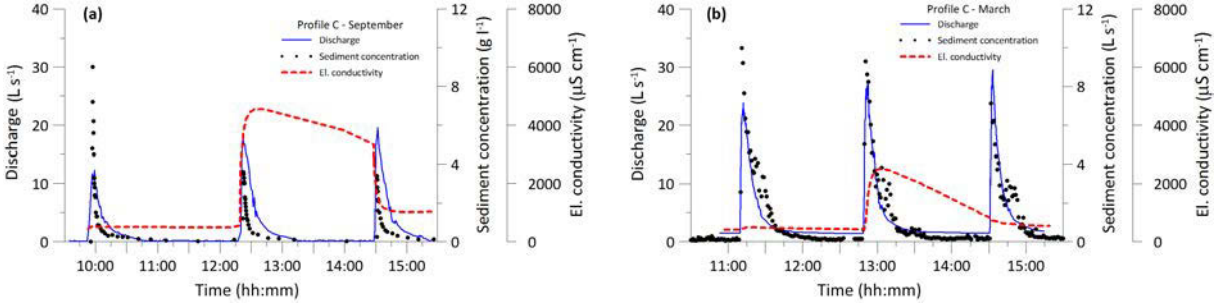

Figure 5. Measured outflow rates and the concentration of suspended solids in the Nučice catchment outlet during experiments conducted in September 2012 **(a)** and in March 2013 **(b)**. The sediment mobility in September was limited by the lower peak discharge rates due to high vegetation density and dry initial conditions.

tance and period of time, as was also observed by Exner-Kittridge et al. (2016).

The time lags in the B profile already differed. Wave W1 arrived after almost 20 min. Waves W2 and W3 were faster, and appeared 15 min after pumping began. The peak discharge also increased, with subsequent waves starting at 12.8 L s^{-1} for W1 and reaching 19.6 L s^{-1} for W3. The difference between the arrival times of W1 and W3 in the C profile was also 5 min, and the maximum flow rate increased from 12.3 L s^{-1} (W1) to 19.6 L s^{-1} (W3). The volume of water that reached the closing profile was 9.8 m^3 for W1, 13.7 m^3 for W2 and 14.8 m^3 for W3. Within W1, only 69 % of the pumped water was recovered in the C profile. For W2 and W3, the recovery rate was 90 %.

The wave celerity along the stream was calculated according to the wave arrival time, which we defined as the time of the first rise of the hydrograph (Table 2). The average wave celerity for W1 was 0.20 m s^{-1}, for W2 it was 0.23 m s^{-1}, and for W3 the celerity was 0.24 m s^{-1}. The water flow velocity was calculated on the basis of the time of arrival of the tracer. The tracer was always detected later than the rise in the hydrograph (Fig. 5). The mean water flow velocity was 0.15 m s^{-1}.

The hydrographs of waves W3–W6 are very similar to each other, and the time lags differ by less than 1 min. The waves approached profile A after 3 min, profile B after 9 min, and profile C after 16 min. The peak discharge values observed in the individual profiles were also similar, but the last wave, W6, reached slightly higher values. The average peak discharge of W4 to W6 in profile A was 32.5 L s^{-1}, in profile B the peak discharge was 29.3 L s^{-1}, and in profile C the peak discharge was 26.5 L s^{-1}. The initial pumped water volume was 85 % recovered in the C profile in all the March experiments, which is similar to the results for waves W2 and W3 (in the September experiment). The waves propagated with average celerity of 0.44 m s^{-1}, which is twice the velocity of the September waves.

For each flood wave, the simulated flow hydrograph at the downstream end was compared with the measured discharge data (Fig. 6). The accuracy of the fit was evaluated by comparing two characteristic parameters – the time and the discharge at the wave peak. Manning's hydraulic roughness was used as the calibration parameter, separately for the September scenario and for the March scenario.

Table 2. Hydrograph characteristics. n/a: data not available.

Wave no.	Profile	Time of first	Peak		Duration of limb		Volume (m^3)	Wave celerity	Wave velocity
		arrival (mm:ss)	discharge ($L\,s^{-1}$)	time (mm:ss)	rising	falling		($m\,s^{-1}$)	($m\,s^{-1}$)
W1	A	04:53	30.9	09:00	04:07	26:10	14.2	0.23	n/a
	B	19:53	12.8	23:25	03:32	40:00	9.9	0.19	n/a
	C	34:35	12.3	40:35	06:00	40:00	9.8	0.22	n/a
W2	A	04:22	29.9	10:00	05:38	31:50	16.0	0.25	n/a
	B	17:13	16.9	20:40	03:27	45:00	12.9	0.22	0.13
	C	31:29	17.7	34:29	03:00	47:00	13.7	0.22	0.15
W3	A	04:12	36.3	07:55	06:43	28:45	16.4	0.26	n/a
	B	15:00	19.6	08:32	03:32	44:28	15.8	0.26	n/a
	C	29:40	19.6	33:40	04:00	44:00	14.8	0.22	n/a
W4	A	3:08	28.4	4:55	1:47	27:30	14.6	0.35	n/a
	B	8:36	27.9	11:14	2:38	35:30	14.5	0.45	n/a
	C	16:28	22.8	19:23	2:55	41:00	13.3	0.43	n/a
W5	A	3:15	31.8	5:24	2:09	27:00	16.3	0.34	0.09
	B	9:14	27.8	12:35	3:21	33:00	14.1	0.42	0.19
	C	16:45	27.2	20:20	3:35	44:00	14.5	0.42	0.14
W6	A	2:51	37.2	8:06	5:15	28:30	16.3	0.39	n/a
	B	8:54	32.2	13:00	4:06	32:30	16.2	0.44	n/a
	C	15:58	29.6	18:33	2:35	44:00	14.1	0.44	n/a

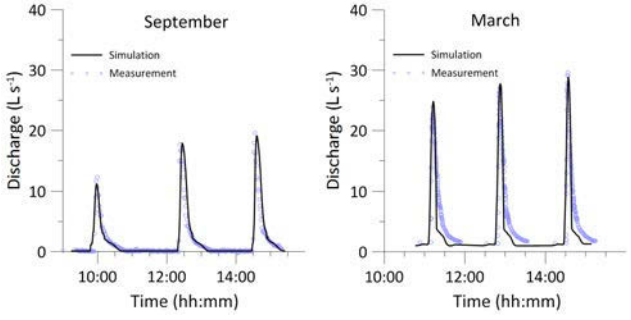

Figure 6. Comparison of the flood wave characteristics measured at the gauging profile and simulated by HEC-RAS.

Table 3. Water and sediment budget as measured at the gauging stations (profile C).

Wave no.	Inflow volume (m^3)	Outflow volume (m^3)	Cumulative sediment mass at the outlet (kg)
W1	14.2	9.8 (69 %)	18.2
W2	16.0	13.7 (86 %)	13.8
W3	16.4	14.8 (90 %)	9.6
W4	15.7	13.3 (85 %)	48.5
W5	17.2	14.5 (84 %)	45.3
W6	16.4	14.1 (86 %)	30.7

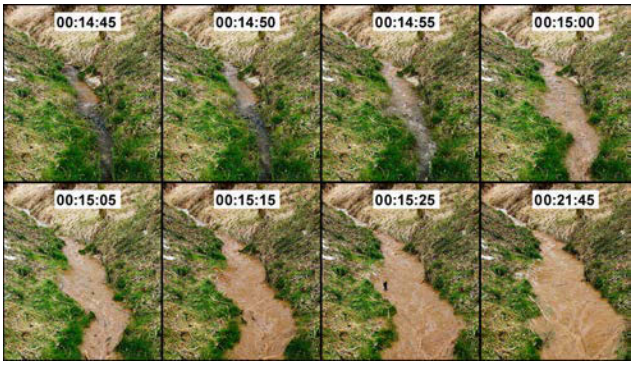

Figure 7. The approach of the W4 wave front at stationing of 400 m. The times (hh:mm:ss) stand for the duration from the start of the experiment.

3.2 Sediment regime

The total amount of sediment released during the September experimental campaign was 41.6 kg, and during the March experimental campaign the amount was 124.5 kg. Assuming regular initial distribution and uniform release of the sediment, this represents 0.10 $kg\,m^{-1}$ of the channel for the September campaign and 0.29 $kg\,m^{-1}$ of the channel for the March campaign.

The maximum suspended solids concentration in profile A, with a value of 9 $g\,L^{-1}$, was observed at the moment when W1 and W4 were approaching (Fig. 7). The minimum peak concentration of 1.7 $g\,L^{-1}$ was reached for wave W3. In

profile C, the peak sediment concentration reached 7.5 g L^{-1} and dropped to 3.9 g L^{-1} for waves W2 and 3.7 g L^{-1} for wave W3. The total sediment mass that passed the catchment outlet was 18.2 kg during the first wave, 13.8 kg during W2, and 9.6 kg during W3.

The amount of carried sediment measured at site C decreased from 48.5 to 30.7 kg between waves W4 and W6. The peak concentration of suspended solids in profile C reached close to 8 g L^{-1} for W5 and 5 g L^{-1} for W6.

4 Discussion

4.1 A comparison with the results from a natural catchment

The set-up of our experiment was based on a study made by Eder et al. (2014), who carried out two flushing experiments in a natural stream in the HOAL experimental catchment in Austria (Blöschl et al., 2016). The catchment is similar in size, climate, soils, and management to the Nučice catchment. The HOAL stream meanders through a forested belt. The monitored length is 590 m, with an average slope of 2.4 %. The stream cross section is irregular, and the channel width varies from 0.6 to 1.0 m. The longitudinal slope is relatively homogeneous over the whole monitored length, with the exception of the initial 90 m, which are significantly steeper. Our experimental section had a convex course, with the slope gradually increasing from 2.3 % in the first section of ca. 70 m to 3.3 % in the last section ca. 200 m in length (nearly half of the length of the total monitored course).

The HOAL experiments were carried out in August 2011 on 2 days separated from each other by a gap of approximately 1 week. The volume of pumped water was 17 m^3, and the wave propagation was monitored on three observation sites. The two recurrent waves had a very similar character. The average celerity was 0.22 m s^{-1}, which corresponds very well with the celerity measured in our experiment in summer conditions (waves W1–W3), and reached about 50 % celerity in comparison to our experiment in March (waves W4–W6). The amount of water recovered in the closing profile was 79 and 75 % of the pumped volume, which is comparable with Nučice experiments W1 to W3. However, the wave transformation in HOAL was extreme, and the peak discharges were reduced from 57 to 8.7 L s^{-1} and 7.9 L s^{-1} at the outlet profile. This is due to lowering of the longitudinal profile, and probably also due to higher surface roughness of the natural stream channel. In the HOAL experiments, only 7.0 and 7.7 kg of suspended solids were recorded, which is only about 50 % of the amounts of sediment for the Nučice catchment in September conditions, and 15 % of the amounts of sediment for the Nučice catchment in March. Both the HOAL experiment and the Nučice experiment resulted in major stream bed sediment mobilization during the rising limb of the hydrograph. A similar sediment regime in channels has also been observed during large flood events on other streams (Guan et al., 2015). A comparison of the measured hydrographs and the physical and geometrical characteristics of the stream channels shows that, for the HOAL experiment, there is an extremely high flood wave transformation, with relatively low retention. This is partly due to the decreasing longitudinal slope of the river bed, and partly due to the higher surface roughness of the natural stream channel. It shows that the transport capacity of the generated waves was exceeded and the amount of transported sediment decreases along the monitored course. In the Nučice experiment, the flood wave transformation was considerably lower. However, we observed relatively significant water retention in the first experiment in September (see the section in the Results referring to mathematical hydraulic modelling). We conclude that the transport capacity of the flood wave was exceeded during the HOAL experiment, and detached sediment from upper, steeper parts of the experimental course was redeposited downstream, as in most of the natural streams monitored by Naden et al. (2016). By contrast, during our experiment in Nučice, the transport capacity of the flood waves was not reached, either in September or March. The sediment concentrations and also the fluxes therefore increased continuously throughout the section.

4.2 Stream potential for sediment trapping

We have to keep in mind that the artificial flood waves used in this experiment were relatively small in volume and of short duration. Based on the monitoring of the natural runoff events, we estimate that the minimum time needed for complete bedload sediment removal with comparable discharge is in the range of 10–24 h (Zumr et al., 2015). Although the amount of sediment transported by the waves decreased within each set of experiments, there was still enough sediment left in the channel that could be released if there were to be a larger wave. The clockwise hysteresis of the sediment concentration–discharge relation suggests that the sediment originates from nearby. Similar results were observed, for example, by Molder et al. (2015) and Seeger et al. (2004). The amount of resuspended sediment was significantly lower in summer conditions. We relate this to the particular conditions in the channel with dense erect vegetation and dry conditions, which led to storage of a considerable proportion of the water.

Significant changes in surface roughness, which also affect this process, may be documented by mathematical modelling of the movement of the wave through the experimental section using a 1-D hydraulic model.

These processes, though with reverse trends exhibiting a decrease in the amount of resuspended sediment over sections downstream, due to very different stream channel characteristics, have also been confirmed by the similar HOAL experiment, performed by Eder et al. (2014). The results clearly show the potential of even well-trained channels with-

out visible signs of sediment accumulation to release sediment during flood events.

The experiments showed that a well-trained stream can act both as a trap and as a sediment source. However, the hydraulic characteristics of the flood wave and the physical and geometrical characteristics of the channel will be crucial for indicating whether deposition or remobilization will occur in a given section and during a given event.

4.3 Temporal variability of sediment resuspension

All the sedigraphs show similar behaviour (Fig. 5). The sediment concentration increases rapidly immediately after the arrival of the wave. The highest sediment concentration is always directly measured at the wave front, and does not necessarily correspond to the peak discharge. After culmination of the wave, the concentration of the sediment also decreases. The highest sediment concentration peak was observed when waves W1 and W4 were approaching, i.e. in the initial experiment of each campaign. We relate this to the fine-textured sediment that had been deposited in the stream during previous events. Our initial assumption was that most of the solid particles move only a short distance, because of low water velocity and short wave duration. Only the finest particles would be mobile enough to travel longer distances. However, our experiment showed that while the discharges decreased along experimental sections A to C, the sediment concentration increased (see Tables 2, 3 and Fig. 4). This suggests that the transport capacity of the stream had not been reached, even for lower discharges at the outlet point, and at least fine-textured soil particles were resuspended and transported over the whole observed section of the stream channel. To test this assumption, we estimated the maximum clear water transport capacity during the observed flow according to the simple transport capacity equation proposed by Govers (1990). The transport capacity of the peak flow was $990\,\mathrm{g\,L^{-1}}$, which greatly exceeds the measured values. The sediment concentration behaviour during waves W2 to W6 was similar (Fig. 5).

The remobilized sediment mass was two to three times higher in March than in September. We relate this to higher water velocity, as a result of which heavier particles contribute to the recorded amount, due to the higher transport capacity. It is not technically possible to measure the total initial mass of the sediment in the stream, and we can only make an estimate on the basis of previous runoff events that the conditions in September and March were similar, and were close to a quasi-steady state for the stream. In both cases, the last antecedent erosion event had taken place more than 2 months before the experiment, followed by at least one runoff event when no soil erosion was recorded and the discharge was above $5\,\mathrm{L\,s^{-1}}$.

The experiments confirmed our assumption that vegetation development is a crucial parameter that affects flood wave retention and propagation, as well as the sediment dynamics. Contrasting vegetation conditions are documented by Fig. 3 – fully erect well-developed dense vegetation in the September set of experiments (W1–W3) vs. no erect vegetation in the March set of experiments (W4–W6).

The general behaviour of the sediment transport during both sets of experiments (September conditions vs. March conditions) is the same, since the bedload sediment is available throughout the year. In both cases, it decreases event by event, but the sediment load increases along the sections. The general difference between the resuspension in fully-developed vegetation (September) vs. the March conditions is 2.7 times higher for the first event and 3.2 times higher for the second and third events, as regards total transported sediment. As regards sediment concentrations, the peak values were the same for the first events and ca. 50 % for the second and third events. Well-developed vegetation therefore significantly increased the trapping capacity of the stream channel (Keesstra et al., 2012).

The flood waves propagate differently in September and in March. While in September the successive waves speed up, in March the wave velocities are very similar for all experiments. When we compare the speed of flood propagation in a vegetated channel and in an empty channel, the March waves propagate twice as fast, and reach a 30 % higher peak discharge. The reason is twofold: (i) there is higher vegetation resistance in September, and (ii) there is higher baseflow and therefore a greater difference between the water velocity and the wave celerity in March. The volume of water recovered on site C is slightly larger during the March experiments. It should be noted that in reality the general summer and winter regime may vary because of variable rainfall patterns and catchment conditions (Buendia et al., 2016; Walling and Amos, 1999).

There is a significant water loss in the case of wave W1, which was released into an almost empty channel with dry stream banks (Table 1). Because of water exfiltration, interception on the vegetation, and filling of the streambed depressions along the 424 m long channel, the water loss reached 31 %. During all other experiments, including W4, the water loss was only 10–15 %.

A comparison of the simulated hydrographs and the measured hydrographs is presented in Fig. 6. It can be stated that the numerical simulations mimic the monitored hydrographs, and the effect of the vegetation seems to be a correct assumption. In the simulation of the September experiments, very high Manning roughness values ($n = 0.20$) were reached, while in March the optimized Manning n was equal to 0.12. The values fit well into the common ranges for sparsely vegetated and densely vegetated streams published, for example, by Luhar et al. (2008) and by Vereecken et al. (2006).

5 Conclusion

Our paper has presented the methodology for an artificial flood experiment conducted on an experimental agricultural catchment, and the results of the experiment. Three successive flood waves, each with an approximate volume of 17 m^3, were released into the upper part of the drainage channel. The aim was to monitor the transformation of the flood wave and the sediment transport within the channel.

On the basis of our results, we concluded that even well-trained and straight channels trap sediment, which can be mobilized by subsequent small floods.

The resuspension regime depends on the current conditions of the stream and the instream vegetation, and therefore changes significantly in the course of a year. The sediment moves quickly in winter and early spring, but in the later part of the year the channel serves as a sediment trap and the resuspension is slower, if dense vegetation is present.

The resuspension regime and the sediment loads within the succeeding small flood waves do not change considerably. The artificial waves that we initiated do not have sufficient magnitude to flush the bedload sediment out from the entire channel.

Data availability. All data is available upon request.

Author contributions. DZ managed the experiments, analysed data, and prepared the paper with contributions from all the other co-authors. TD and JD co-organized the experiments. PV did the HEC-RAS simulation. PR was responsible for all the laboratory analyses. PS and AE participated on the experiments and the data evaluation.

Competing interests. The authors declare that they have no conflict of interest.

Acknowledgements. We thank our colleagues Josef Krása, Václav David, Petr Koudelka, Luděk Strouhal, Vladimír Říha and Dan Fiala for their great help during the experiments. This research was prepared within the framework of Czech Science Foundation post-doctoral project GP13-20388P, Ministry of Agriculture projects NAZV QJ1230056 and QJ1530181, and ÖAD WTZ Mobility project no. CZ18/2016 – 7AMB16AT002.

Edited by: Patricia Saco
Reviewed by: two anonymous referees

References

Báčová, M. and Krása, J.: Application of Historical and Recent Aerial Imagery in Monitoring Water Erosion Occurrences in Czech Highlands, Soil Water Res., 11, 267–276, https://doi.org/10.17221/178/2015-SWR, 2016.

Blöschl, G., Blaschke, A. P., Broer, M., Bucher, C., Carr, G., Chen, X., Eder, A., Exner-Kittridge, M., Farnleitner, A., Flores-Orozco, A., Haas, P., Hogan, P., Kazemi Amiri, A., Oismüller, M., Parajka, J., Silasari, R., Stadler, P., Strauss, P., Vreugdenhil, M., Wagner, W., and Zessner, M.: The Hydrological Open Air Laboratory (HOAL) in Petzenkirchen: a hypothesis-driven observatory, Hydrol. Earth Syst. Sci., 20, 227–255, https://doi.org/10.5194/hess-20-227-2016, 2016.

Boardman, J.: Soil erosion and flooding on the eastern South Downs, southern England, 1976–2001, Trans. Inst. Br. Geogr., 28, 176–196, https://doi.org/10.1111/1475-5661.00086, 2003.

Brookes, A.: Response of aquatic vegetation to sedimentation downstream from river channelisation works in England and Wales, Biol. Conserv., 38, 351–367, https://doi.org/10.1016/0006-3207(86)90060-1, 1986.

Buendia, C., Vericat, D., Batalla, R. J., and Gibbins, C. N.: Temporal Dynamics of Sediment Transport and Transient In-channel Storage in a Highly Erodible Catchment, Land Degrad. Dev., 27, 1045–1063, https://doi.org/10.1002/ldr.2348, 2016.

Drummond, J. D., Davies-Colley, R. J., Stott, R., Sukias, J. P., Nagels, J. W., Sharp, A., and Packman, A. I.: Retention and remobilization dynamics of fine particles and microorganisms in pastoral streams, Water Res., 66, 459–472, https://doi.org/10.1016/j.watres.2014.08.025, 2014.

Eder, A., Exner-Kittridge, M., Strauss, P., and Blöschl, G.: Resuspension of bed sediment in a small stream – results from two flushing experiments, Hydrol. Earth Syst. Sci., 18, 1043–1052, https://doi.org/10.5194/hess-18-1043-2014, 2014.

Exner-Kittridge, M., Strauss, P., Blöschl, G., Eder, A., Saracevic, E., and Zessner, M.: The seasonal dynamics of the stream sources and input flow paths of water and nitrogen of an Austrian headwater agricultural catchment, Sci. Total Environ., 542, 935–945, https://doi.org/10.1016/j.scitotenv.2015.10.151, 2016.

Govers, G.: Empirical relationships for transport capacity of overland flow, IAHS Publ., 189, 45–63, 1990.

Green, J. C.: Modelling flow resistance in vegetated streams: review and development of new theory, Hydrol. Process., 19, 1245–1259, https://doi.org/10.1002/hyp.5564, 2005.

Guan, M., Wright, N. G., and Andrew Sleigh, P.: Multiple effects of sediment transport and geomorphic processes within flood events: Modelling and understanding, Int. J. Sediment Res., 30, 371–381, https://doi.org/10.1016/j.ijsrc.2014.12.001, 2015.

Hearne, J., Johnson, I., and Armitage, P.: Determination of ecologically acceptable flows in rivers with seasonal changes in the density of macrophyte, Regul. Rivers Res. Manag., 9, 177–184, https://doi.org/10.1002/rrr.3450090304, 1994.

Hession, W., Pizzuto, J., Johnson, T., and Horwitz, R.: Influence of bank vegetation on channel morphology in rural and urban watersheds, Geology, 31, 147–150, https://doi.org/10.1130/0091-7613(2003)0312.0.CO;2, 2003.

Huisman, N. L. H., Karthikeyan, K. G., Lamba, J., Thompson, A. M., and Peaslee, G.: Quantification of seasonal sediment and phosphorus transport dynamics in an agricultural watershed using radiometric fingerprinting techniques, J. Soils Sediments, 13, 1724–1734, https://doi.org/10.1007/s11368-013-0769-0, 2013.

Keesstra, S. D., Kondrlova, E., Czajka, A., Seeger, M., and Maroulis, J.: Assessing riparian zone impacts on water and sediment movement: a new approach, Neth. J. Geosci., 91, 245–255, https://doi.org/10.1017/S0016774600001633, 2012.

Lal, R.: Soil Erosion Impact on Agronomic Productivity and Environment Quality, Crit. Rev. Plant Sci., 17, 319–464, https://doi.org/10.1080/07352689891304249, 1998.

Lal, R., Follett, R. F., Stewart, B. A., and Kimble, J. M.: Soil carbon sequestration to mitigate climate change and advanced food security, Soil Sci., 172, 943–956, https://doi.org/10.1097/ss.0b013e31815cc498, 2007.

Luhar, M., Rominger, J., and Nepf, H.: Interaction between flow, transport and vegetation spatial structure, Environ. Fluid Mech., 8, 423–439, https://doi.org/10.1007/s10652-008-9080-9, 2008.

Minella, J. P. G., Walling, D. E., and Merten, G. H.: Combining sediment source tracing techniques with traditional monitoring to assess the impact of improved land management on catchment sediment yields, J. Hydrol., 348, 546–563, https://doi.org/10.1016/j.jhydrol.2007.10.026, 2008.

Molder, B., Cockburn, J., Berg, A., Lindsay, J., and Woodrow, K.: Sediment-assisted nutrient transfer from a small, no-till, tile drained watershed in Southwestern Ontario, Canada, Agr. Water Manage., 152, 31–40, https://doi.org/10.1016/j.agwat.2014.12.010, 2015.

Musolff, A., Schmidt, C., Selle, B., and Fleckenstein, J. H.: Catchment controls on solute export, Adv. Water Resour., 86, 133–146, https://doi.org/10.1016/j.advwatres.2015.09.026, 2015.

Naden, P. S., Murphy, J. F., Old, G. H., Newman, J., Scarlett, P., Harman, M., Duerdoth, C. P., Hawczak, A., Pretty, J. L., Arnold, A., Laizé, C., Hornby, D. D., Collins, A. L., Sear, D. A., and Jones, J. I.: Understanding the controls on deposited fine sediment in the streams of agricultural catchments, Sci. Total Environ., 547, 366–381, https://doi.org/10.1016/j.scitotenv.2015.12.079, 2016.

Neal, C. W. M. and Anders, A. M.: Suspended sediment supply dominated by bank erosion in a low-gradient agricultural watershed, Wildcat Slough, Fisher, Illinois, United States, J. Soil Water Conserv., 70, 145–155, https://doi.org/10.2489/jswc.70.3.145, 2015.

Nikora, V., Larned, S., Nikora, N., Debnath, K., Cooper, G., and Reid, M.: Hydraulic Resistance due to Aquatic Vegetation in Small Streams: Field Study, J. Hydraul. Eng., 134, 1326–1332, https://doi.org/10.1061/(ASCE)0733-9429(2008)134:9(1326), 2008.

Peterson, E. W. and Benning, C.: Factors influencing nitrate within a low-gradient agricultural stream, Environ. Earth Sci., 68, 1233–1245, https://doi.org/10.1007/s12665-012-1821-x, 2013.

Pimentel, D., Harvey, C., Resosudarmo, P., Sinclair, K., Kurz, D., McNair, M., Crist, S., Shpritz, L., Fitton, L., Saffouri, R., and Blair, R.: Environmental and economic costs of soil erosion and conservation benefits, Science, 267, 1117–1123, https://doi.org/10.1126/science.267.5201.1117, 1995.

Seeger, M., Errea, M.-P., Beguerìa, S., Arnáez, J., Martì, C., and Garcìa-Ruiz, J.: Catchment soil moisture and rainfall characteristics as determinant factors for discharge/suspended sediment hysteretic loops in a small headwater catchment in the Spanish pyrenees, J. Hydrol., 288, 299–311, https://doi.org/10.1016/j.jhydrol.2003.10.012, 2004.

Shore, M., Jordan, P., Mellander, P.-E., Kelly-Quinn, M., and Melland, A. R.: An agricultural drainage channel classification system for phosphorus management, Agr. Ecosyst. Environ., 199, 207–215, https://doi.org/10.1016/j.agee.2014.09.003, 2015.

Stoate, C., Boatman, N., Borralho, R., Carvalho, C. R., Snoo, G. R. D., and Eden, P.: Ecological impacts of arable intensification in Europe, J. Environ. Manage., 63, 337–365, https://doi.org/10.1006/jema.2001.0473, 2001.

Vereecken, H., Baetens, J., Viaene, P., Mostaert, F., and Meire, P.: Ecological management of aquatic plants: effects in lowland streams, Hydrobiologia, 570, 205–210, https://doi.org/10.1007/s10750-006-0181-5, 2006.

Walling, D. E.: Tracing suspended sediment sources in catchments and river systems, Sci. Total Environ., 344, 159–184, https://doi.org/10.1016/j.scitotenv.2005.02.011, 2005.

Walling, D. E. and Amos, C. M.: Source, storage and mobilisation of fine sediment in a chalk stream system, Hydrol. Process., 13, 323–340, https://doi.org/10.1002/(SICI)1099-1085(19990228)13:3<323::AID-HYP741>3.0.CO;2-K, 1999.

Withers, P. J. A. and Jarvie, H. P.: Delivery and cycling of phosphorus in rivers: a review., Sci. Total Environ., 400, 379–95, https://doi.org/10.1016/j.scitotenv.2008.08.002, 2008.

Zumr, D. and Císlerová, M.: Soil moisture dynamics in levees during flood events – variably saturated approach, J. Hydrol. Hydromech., 58, 64–72, https://doi.org/10.2478/v10098-010-0007-z, 2010.

Zumr, D., Dostál, T., and Devátý, J.: Identification of prevailing storm runoff generation mechanisms in an intensively cultivated catchment, J. Hydrol. Hydromech., 63, 246–254, https://doi.org/10.1515/johh-2015-0022, 2015.

DOI: 10.2478/v10098-010-0007-z

SOIL MOISTURE DYNAMICS IN LEVEES DURING FLOOD EVENTS – VARIABLY SATURATED APPROACH

DAVID ZUMR, MILENA CÍSLEROVÁ

Czech Technical University in Prague, Faculty of Civil Engineering, Dept. of Irrigation, Drainage and Landscape Engineering, Thákurova 7, 166 29 Prague 6, Czech Republic; Mailto: david.zumr@fsv.cvut.cz

Growing occurrence of extreme floods in the Czech Republic has attracted attention to the security of protective earthfill embankments along the rivers. A suddenly increased amount of water on the waterside slope of the embankment may have destroying or even catastrophic consequences. Predictions of seepage patterns through the earth body are usually done considering the saturated flow beneath the free water level only, neglecting the saturated-unsaturated character of the soil water dynamics within earthfill dams.

The importance of water dynamics within an earth dam is known and may be addressed using numerical simulation models. In this study the solution based on transient simulation of seepage through protection levee using saturated-unsaturated theory is presented. Simulations were carried out by a two-dimensional numerical model based on Richards' equation for water flow in porous medium.

It has been shown that proposed approach is, with certain limitations, suitable for large scale engineering applications.

KEY WORDS: Floods, River Embankment, Earth Dam, Unsaturated Soil, Vadose Zone, Seepage Modelling, Soil Water Dynamics, Richards' Equation.

David Zumr, Milena Císlerová: DYNAMIKA VODNÍHO REŽIMU V TĚLESE OCHRANNÉ HRÁZE BĚHEM POVODNĚ S UVÁŽENÍM NENASYCENÉHO PROUDĚNÍ. J. Hydrol. Hydromech., *58*, 2010, 1; 24 lit., 5 obr., 1 tab.

Vyšší pravděpodobnost výskytu extrémních klimatických jevů obrací pozornost k ochraně před následky, které tyto jevy způsobují. Zájem se soustředí na protipovodňové ochranné zemní hráze a jejich bezpečnost při povodních. Výpočet průsaku zemními hrázemi se často omezuje pouze na tu část hráze, která byla plně nasycená vodou, to znamená na plně nasycené proudění. Tento způsob modelování průsaku je dodnes považován za standardní, přestože je velmi limitující. Bez zahrnutí nenasycené části tělesa hráze je zanedbán vliv časově i prostorově proměnlivého pole vlhkostí (např. při infiltraci vody ze srážky) na polohu hladiny.

V naší studii je simulováno proudění v tělese hráze s použitím numerického modelu, který umožňuje řešit proudění vody v proměnlivě nasyceném heterogenním pórovitém prostředí, s obecnými okrajovými podmínkami.

Výsledky potvrdily, že přístup, který uvažuje proudění i v nenasycené části hráze, lze k řešení průsaků zemními tělesy úspěšně využít.

KLÍČOVÁ SLOVA: záplavy, protipovodňová hráz, sypaná zemní hráz, nenasycená půda, vadózní zóna, modelování průsaku, vodní režim půd, Richardsova rovnice.

Introduction

Extreme floods represent an increased risk for urban areas, infrastructure, industrial structures and agriculture. Since the river embankments, polders and dams are often the only flood control measure, the safety of protective structures has attracted increased attention.

Time to time, the protective barriers along the rivers are destroyed by a suddenly increased amount of water with destructive or even catastrophic consequences (*Rinaldi*, *Casagli*, 1999). The most frequent causes of failures are overtopping, internal erosion, erosion of the banks and settling of the structure. Heavy rainfalls and rapid rise of water also cause wetting of unsaturated region in the up-

per part of the structure which often ends up with slope failures.

Despite of today's advanced mathematical and computational capabilities, the predictions of seepage patterns are usually based merely on consideration of steady-state saturated zone beneath the phreatic surface. This assumption, even with introduction of finite element methods, is not accurate enough for fine grained soils. The key problem lies in determination of the position of phreatic surface in transient simulations, when water table level dramatically changes during extreme floods (*Chen*, *Zhang*, 2006). Generally, the seepage analysis belongs to the basic geotechnical problems which are related to seepage failures, contamination of ground water, slope stability issues, foundations and design of earthfill structures.

The first authors, who considered unsaturated hydraulic properties of soils for transient seepage analysis of earth dams, were *Freeze* (1971) and *Neuman* (1972). The inclusion of unsaturated zone in the modelling of seepage has practical consequences for engineering problems. Actual soil moisture conditions in vadose zone influence the position of water table, especially on fine grained soils (*Szilagyi*, 2004). This effect is significant for example in water regime of clay cores in earthfill dams or layered soil profiles (*Starnaud*, 1995). The flood events are commonly accompanied with heavy or long lasting rainfalls which may lead to saturation of the top soil at the surface of a dam body.

The permeability and shear strength of each soil vary with the degree of saturation. Thus saturated and nearly saturated conditions may cause reduction of stability of slopes, dams and earth dikes. *Schmertmann* (2006) provides a general engineering screening procedure to estimate the slope stability risk induced by atmospheric conditions such as rainfalls and droughts. Finite element hydromechanical numerical models are already being used in the river embankment stability studies (*Rinaldi*, *Casagli*, 1999; *Dapporto* et al., 2001; *Pham*, *Fredlund*, 2003), the earth dam seepage (*Freeze*, 1971; *Thieu*, 2000; *Chen*, *Zhang*, 2006) or the landslides simulations (*Wilkinson* et al., 2002; *Gerscovich* et al., 2006).

The aim of this study is to simulate the water dynamics in saturated and unsaturated zones of an arbitrary homogeneous earthfill dam during a flood event. A simple case was chosen. Any other more realistic dam structures (e.g. including clay core or material heterogeneities of any kind) may be simulated as well. The soil moisture propagation through a vertical cross section of the earth body during the flood event is simulated using the latest version of the numerical two-dimensional simulation model SWMS II (*Vogel*, 1987), the code S2D (*Vogel* et al., 2000).

Theory

The saturated-unsaturated soil water fluxes in a continuum of soil, air and water at the scale of representative elementary volume are being calculated according to Richards' flow equation. The equation is based on Darcy-Buckingham's law and continuity equation. Richard's equation for nearly laminar flow in variably saturated rigid porous media with incompressible water and continuous air phase with inclusion of root water uptake can be written as (*Šimůnek* et al., 2006):

$$\frac{\partial \theta}{\partial t} = C(h)\frac{\partial h}{\partial t} = \frac{\partial}{\partial x_i}[K(K_{ij}^A \frac{\partial h}{\partial x_j} + K_{iz}^A)] - S\,, \qquad (1)$$

where θ is the volumetric water content [$L^3\ L^{-3}$], h – the pressure head [L], C – the moisture capacity ($d\theta/dh$) [L^{-1}], t – the time [T], x_i (i = 1,2) – the spatial coordinates [L], K – the unsaturated hydraulic conductivity function [LT^{-1}], K_{ij}^A – components of a dimensionless anisotropy tensor $\mathbf{K}^A$ and S is a sink term for root water extraction [T^{-1}].

The assumption of the air phase continuity has not to be always fulfilled when the soils are nearly saturated (*Sněhota*, 2003; *Sněhota* et al., 2008). Nevertheless, already *Freeze* (1971) showed that for simulation of seepage, when one is more interested in water fluxes than in air movement, inclusion of no more than the water phase is adequate and Eq. (1) may be used.

To solve transient flow problems we need to introduce relations between soil water content and pressure head (retention curve) and pressure head and hydraulic conductivity (hydraulic conductivity function). Both functions, called soil hydraulic characteristics, are commonly described by a set of parametric equations (*van Genuchten* (1980) and *Mualem* (1976)). Eq. (1) is a parabolic partial differential equation with highly nonlinear physical relationship between water content, pressure head and hydraulic conductivity, therefore is impossible to be solved analytically.

In the applied simulation model S2D a modification of retention curve is implemented (*Vogel* et al., 2001):

$$\theta(h) = \begin{cases} \theta_r + (\theta_m - \theta_r)(1 + (-\alpha h)^n)^{-m} & h < h_s \\ \theta_s & h \geq h_s \end{cases} \quad (2)$$

and

$$K(h) = \begin{cases} K_s K_r(S_e(h)) & h < h_s \\ K_s & h \geq h_s \end{cases}, \quad (3)$$

where:

$$S_e(h) = \frac{\theta(h) - \theta_r}{\theta_s - \theta_r}, \quad (4)$$

$$K_r(S_e) = S_e^{1/2} \left(\frac{1 - F(S_e)}{1 - F(1)} \right)^2, \quad (5)$$

$$F(S_e) = \left(1 - \left(\frac{\theta_s - \theta_r}{\theta_m - \theta_r} S_e \right)^{\frac{1}{m}} \right)^m \quad (6)$$

in which S_e is the effective soil water content, θ_r and θ_s – the residual and the saturated water contents [L^3 L^{-3}], θ_m – the extrapolated fictitious parameter [L^3 L^{-3}] to allow non-zero air entry value h_s [L], α [L^{-1}], the retention curve parameter m is equal to $1 - 1/n$ where $n > 1$. K_s is the saturated hydraulic conductivity [L T^{-1}] and K_r – the relative hydraulic conductivity function.

The solution of Eq. (1) requires known initial distribution of the pressure head within the flow domain:

$$h(x,z,t) = h_0(x,z) \text{ for } t = 0. \quad (7)$$

Two types of conditions were used to describe system independent interactions at the flow boundaries along the flow region (*Vogel* et al., 2004). These conditions are specified pressure head (Dirichlet type) boundary conditions in form:

$$h(x,z,t) = \psi(x,z,t) \text{ for } (x,z) \in \Gamma_D \quad (8)$$

and specified the flux (Neumann type) boundary conditions given by:

$$-[K(K_{ij}^A \frac{\partial h}{\partial x_j} + K_{iz}^A)]n_i = \sigma_1(x,z,t) \text{ for } (x,z) \in \Gamma_N, \quad (9)$$

where Γ_D and Γ_N indicate Dirichlet and Neumann boundary segments, Ψ [L], σ_1 [L T^{-1}] are prescribed functions of x, z, and t, n_i – the components of the outward unit vector normal to boundary Γ_N.

S2D code numerically solves Richards' equation for saturated-unsaturated water flow. The numerical solution is based on Galerkin linear finite element method applied on a triangular elements mesh. The time derivatives are approximated by finite differences using a fully implicit approximation for both saturated and unsaturated conditions. The time step is adjusted automatically during the simulation to ensure stability and fulfilment of mass balance (*Vogel*, 1987). The solution of the Richards equation gives the information about macroscopic spatio-temporal distribution of water content, pore pressures and water fluxes within the flow domain.

Material and methods

To illustrate the suitability of the numerical code and the saturated-unsaturated approach, we ran a numerical study to show the effect of a flood wave on water dynamics of protection embankment and its underlying subsoil. The simulation was performed by numerical model S2D (*Vogel* et al., 2000; *Dušek* et al., 2008).

The subject of the study is a protective homogeneous levee made of loamy-clay soil. The structure is founded on loamy top soil, which covers a deep layer of permeable sandy soil (see Fig. 1). The top of the dam is 2 m above terrain and 2.7 m above normal river water level, the width of the dam at the base is 12 m. The waterside slope is 3 : 1, the landside slope is 2.5 : 1. There is a drain pipe beyond the toe of the dam. A draining ditch, which is often built up along the drain pipe, is not considered. The part behind the dam is enlarged to incorporate also the region where the possible upward flow caused by the flood event could take place. We consider no sealing layer at the contact with the river bed and the waterside slope.

The arrangement of soil horizons is typical for fluvial plains along lower parts of river basins. There the thick permeable alluvial layers are usually covered by the less permeable thin top soils. The top soil horizon serves as a natural anti-percolation barrier and so offers the convenient material for foundation of a dam (*Říha*, 2006). Unfortunately, especially in urban areas, the top layer is often spatially heterogeneous and may lead to preferential flow and preferential seepage below the dams. We do not consider preferential flow in this study.

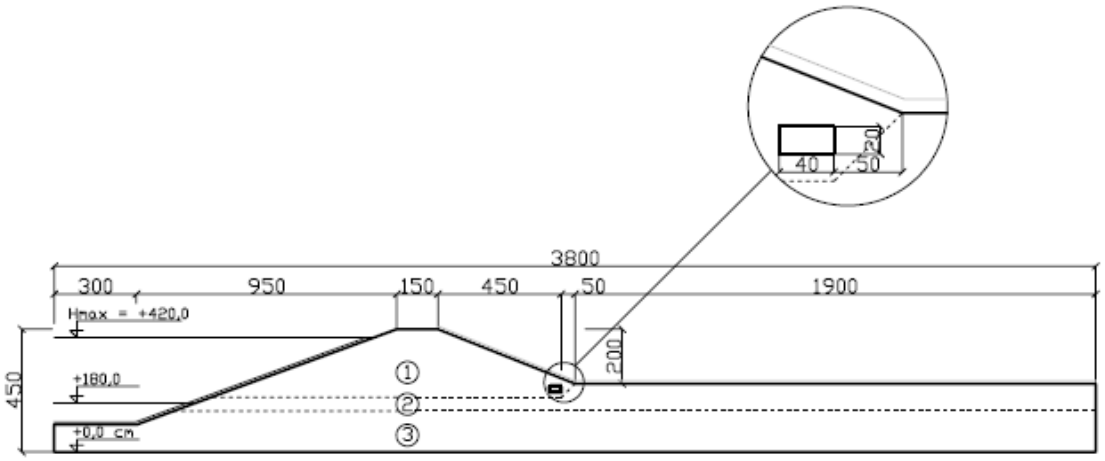

Fig. 1 Drawing of the simulated domain (in cm). Dashed lines stand for three homogeneous soil materials.
Obr. 1. Nákres modelované oblasti (v cm). Přerušované čáry vyznačují tři odlišné materiály.

T a b l e 1. Parameters of soil hydraulic characteristics.
T a b u l k a 1. Hydraulické charakteristiky.

	Texture	θ_r	θ_s	θ_m	α [cm^{-1}]	n	K_s [cm d^{-1}]
Earth dam body	loamy – clay	0.095	0.41	0.415	0.019	1.31	6.24
A horizon – loamy sediments	loamy	0.078	0.43	0.435	0.036	1.56	24.96
B horizon – permeable alluvial layer	sandy – loam	0.065	0.41	0.415	0.075	1.89	106.1

The finite-element mesh was created with ARGUS ONE mesh generator. The triangular element mesh is composed of 45225 nodes and 89095 elements. The finite element mesh is finer (order of centimetres) at the waterside slope, where steep wetting front develops. The appropriate soil hydraulic characteristics of particular soil materials were taken from UNSODA database, the parameters are given in Tab. 1. Values of θ_m were assumed slightly higher than saturated water contents to incorporate air entry value (*Vogel* et al., 2001).

The propagation of the flood wave was simulated as a time-dependent pressure head boundary condition (Dirichlet type) prescribed at the waterside slope of the dam. The boundary nodes below the water level had given pressure head corresponding to the actual water level (Eq. (8)). The boundary conditions above the actual water level were assumed as no flow boundary (Neumann type, Eq. (9)). In this scenario we do not consider any rainfall or evapotranspiration, the both can be easily implemented in future simulations. The river water level position during the uprising and dropping stages were simplified by stepwise pressure function (13 steps, see Fig. 2). The simulated flood event lasts eight days, the maximum water level upraise was 240 cm at the flood wave peak. The shape of the wave (together with simulated course of water amount in the dam body) is on Fig. 2. Although the increase of the water level at the waterside slope is stepwise, the water flow within the simulated domain is transient.

To the landside slope terrain behind the dam and to the drain the seepage boundary condition was assigned. This condition assumes zero flux when the nodes at the boundary are under unsaturated conditions and zero pressure head during periods of full saturation. Zero flux boundary condition is prescribed to the remaining boundaries. We assume that the right edge of the domain is in a sufficient distance not to influence flow in the area of interest.

Initial condition (at the moment of the flood start) is prescribed as the equilibrium pressure field corresponding to the river water level position at 80 cm.

Results

The results of the simulation are shown in Figs. 3, 4 and 5. It can be noticed that the groundwater

DOI: 10.2478/v10098-010-0007-z

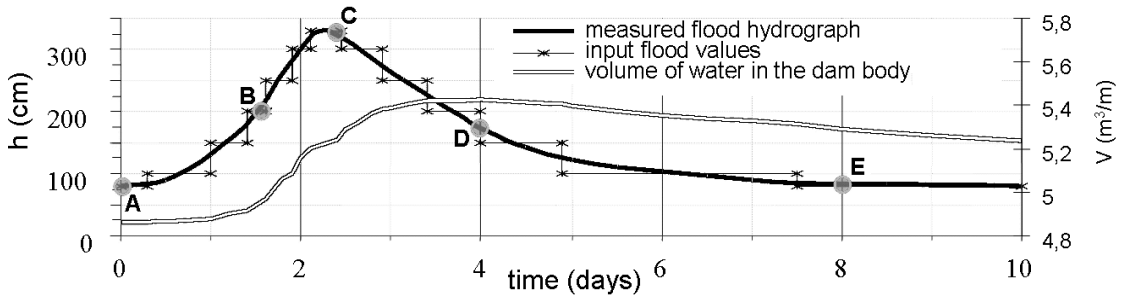

Fig. 2. Water level graph and the course of the volume of water in the levee. Asterix line shows the step approximation which was used as the input into the simulation model. Letters A to E correspond with marking in Figs. 3 and 4.
Obr. 2. Průběh hladiny na vodním líci ochranné hráze a objem vody v tělese hráze.

level (GWL) directly behind the toe of the dam increases by approximately 40 cm and continues to the drain pipe. For a given flood, GWL does not rise up to the surface behind the dam (this conclusion does not need to hold for longer lasting flooding).

During the flood event, which culminated on the third day at the water level of 320 cm (see Fig. 2), the 5.5 m^3 of water was infiltrated per one length meter of the dam body. The maximum volume of water in the levee was four days after the beginning of the flood, when the water level in the river was already falling down (see Fig. 2).

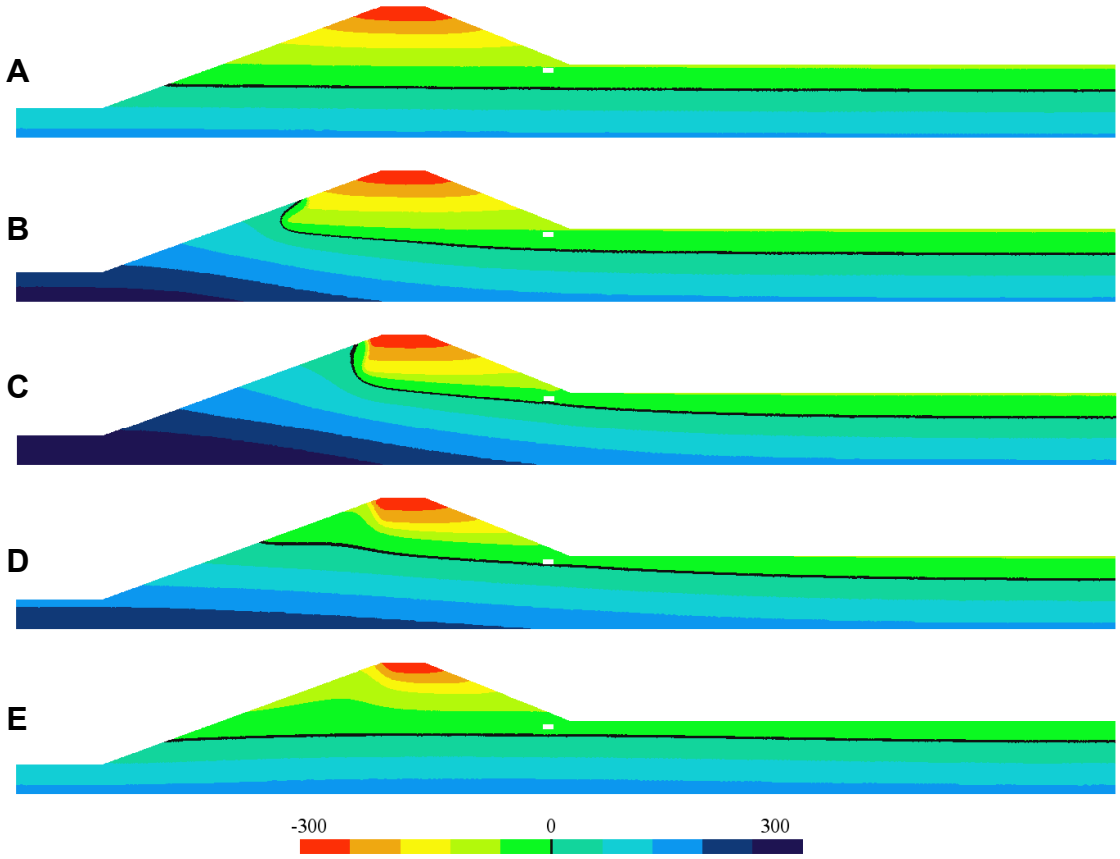

Fig. 3. Distributions of simulated pressure heads (cm) in particular times of the flood event A) 0; B) 1,6 days; C) 2,5 days; D) 4 days and E) 8 days after the beginning of the water level increase. The black solid line represents a phreatic surface.
Obr. 3. Rozložení modelovaných tlakových výšek (cm) v reakci na povodňovou vlnu. Černá čára vyznačuje hladinu podzemní vody.

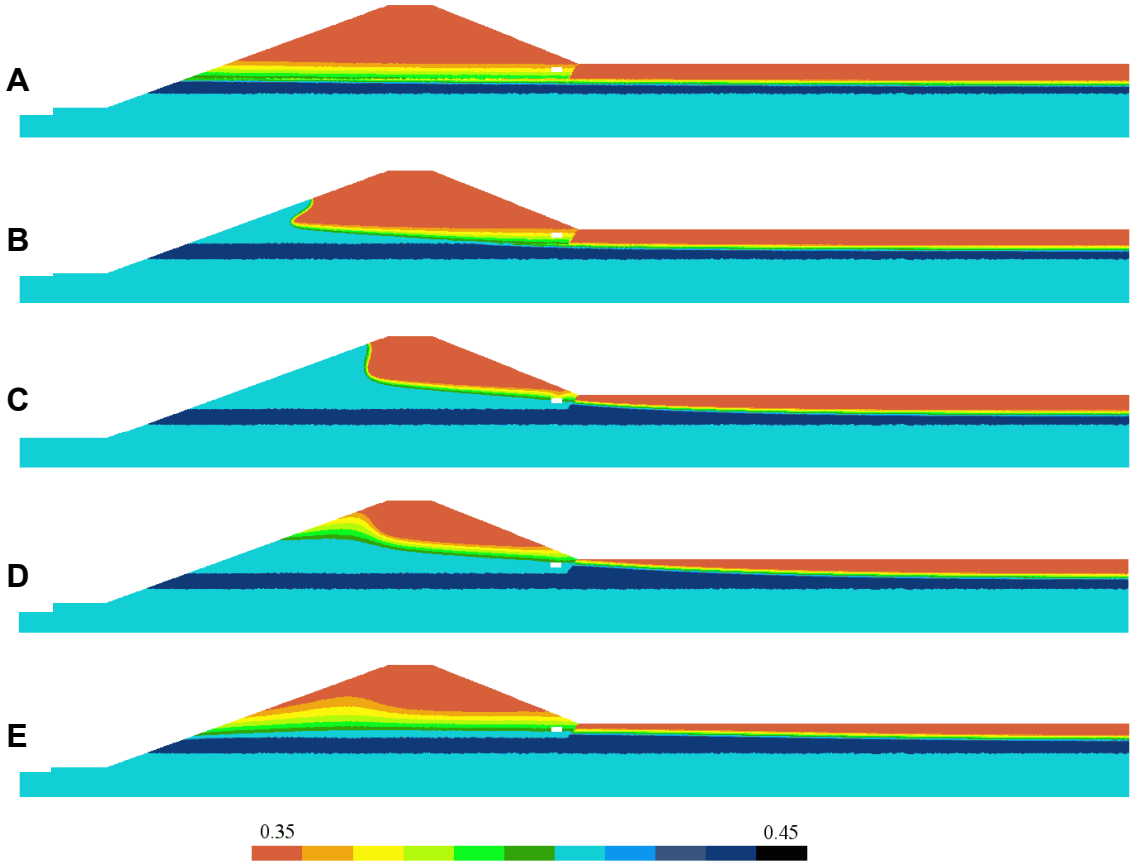

Fig. 4. Distributions of simulated soil water content in particular times of the flood event A) 0; B) 1.6 days; C) 2.5 days; D) 4 days and E) 8 days after the beginning of the water level increase.
Obr. 4. Rozložení modelovaných vlhkostí v reakci na povodňovou vlnu.

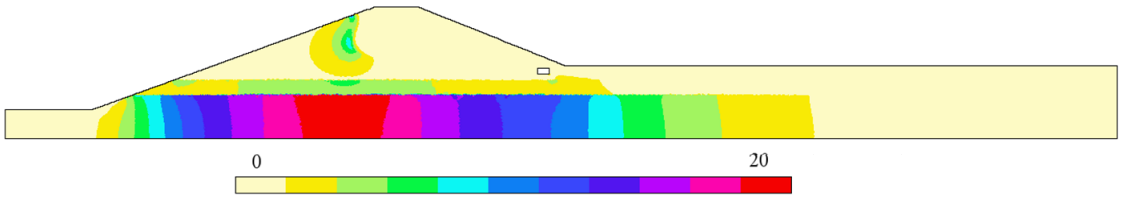

Fig. 5. Simulated field of horizontal velocities (in cm/d) at 2.5 days. The maximum velocities are reached in saturated permeable B horizon and at the wetting front.
Obr. 5. Modelované pole rychlostí proudění vody v horizontálním směru (cm/d).

In the Figs. 3 and 4 the simulated distribution of soil water pressure and water content in five selected stages of the flood event are presented. The *A* part of the figures corresponds to the initial state at the start of the flood, the *B* part shows the state during the flood rise, *C* stands for the flood peak, *D* for the maximum water volume in the dam structure when the level in the river is already decreasing, and *E* is the state when water in the river is back at the initial state. The steady state conditions (the same as at the beginning of the simulation) are reached after approximately 40 days (not shown here).

Fig. 5 shows horizontal water flow velocities when the river water level was at its peak. At this moment the highest values of flow rates occure. In the saturated permeable sandy loam horizon the velocities reached the values of 20 cm d^{-1}. The velocities at the water front are lower because of lower permeability of the particular soil considered

to form the dam body. Even these magnitudes might be still significant for the potential waterside bank erosion.

Conclusions

Two-dimensional transient infiltration and seepage through the vertical cross section of the model protection embankment was simulated using variably saturated flow theory. The evolution of wetting front was expressed by means of pore-water pressure contours in different times. It has been shown that the proposed approach is not only a theoretical exercise, but it is a suitable procedure to be used in engineering applications.

Nonlinearity of Richard's equation is demanding in terms of computing time, hardware and experience. Input data for hydraulic characteristics are in most cases difficult and time consuming to obtain. Stability of the numerical solution is strongly dependent on proper design of finite element mesh, minimum allowed time increments in time discretization and detailed description of the flood wave formation. In any case, the presented methodology has still a strong potential to increase accuracy of the results of simulations in many real world applications, especially in those where fine grained soils are involved.

The transient simulations do result in a different velocity fields than the steady-state simulations. The steady-state approach cannot take into account the dynamics of water at the shallow layer of the dam slopes and at the wetting front. With increasing permeability of soil material the flux rates at the water front might become crucial. In contrast, the extreme flux rates in the permeable alluvial horizon are of the same magnitude as if they were simulated with a steady state approach. The transient approach provides the information not only about spatial but also temporal distribution of the critical velocities.

The simulation can be used for the design of earthfill structures with respect to different types of hydraulic failures. In the case of levees the most probable failures result from internal erosion and piping. The safety analysis may be done by comparing the simulated pore pressures and hydraulic gradients with the estimated critical values (*Frank* et al., 2004). The hydraulic gradients are not the direct outputs of the S2D model, but can be easily calculated from the velocities matrix. Values of velocity vectors at any node are available.

The simulation model S2D is suitable for engineering applications related to the earth dams due to its ability to describe the saturated and unsaturated flow complexly. As *Freeze* (1971) states, the failure to exclude unsaturated zone in transient analyses can lead to the results that are in error. Identifying the proper critical scenarios, the results of simulations using the model S2D may also help in designing of safe flood control dams or in evaluating reasons of possible failures to prevent future disasters.

The study is a part of the broader research with the aim to find out a methodology to simulate hydrological and soil mechanical behaviour of small earth dams and river embankments during extreme events. We also plan to propose a scheme for heterogeneity assessment of earth bodies based on geophysical tools to be able to incorporate the heterogeneity and preferential pathways into numerical simulations.

Acknowledgement. The research has been supported by project SP/2e7/229/07 and the Research Program of the Ministry of Education of the Czech Republic project no. VZ 04 CEZ MSM 6840770005. We would like to thank to Michal Dohnal and to anonymous reviewer for their helpful comments.

REFERENCES

CHEN Q., ZHANG L.M., 2006: Three-dimensional analysis of water infiltration into the Gouhou rockfill dam using saturated-unsaturated seepage theory. Can. Geotech. J., *43*, 449––461.

DAPPORTO S., RINALDI M., CASAGLI N., 2001: Failure mechanisms and pore water pressure conditions: analysis of a riverbank along the Arno river (Central Italy). Engineering Geology, *61*, 221–242.

DUŠEK J., GERKE H.H., VOGEL T., 2008: Surface Boundary Conditions in Two-Dimensional Dual-Permeability Modeling of Tile Drain Bromide Leaching. Vadose Zone J., *7*, 4, 1287–1301.

FRANK R., BAUDUIN C., DRISCOLL R., KAWADAS M., KREBS OVESEN N., ORR T., SCHUPPENER B., 2004: Designers' guide to EN 1997-1 EUROCODE 7: Geotechnical design – general rules, Thomas Telford Ttd., London.

FREEZE R.A., 1971: Influence of the unsaturated flow domain on seepage through earth dams. Water Resources Research, *7*, 4, 929–941.

GERSCOVICH D. M. S., VARGAS E. A., DE CAMPOS T. M.P., 2006: On the evaluation of unsaturated flow in a natural slope in Rio de Janeiro, Brasil. Engineering Geology, *88*, 23–40.

MUALEM Y., 1976: A new model for predicting the hydraulic conductivity of unsaturated porous media. Water Resources Research, *12*, 513–522.

NEUMAN S.P., 1972: Saturated-unsaturated seepage by finite elements. Journal of the Hydraulics Division, *99*, 12, 2233––2250.
PHAM H.T.V., FREDLUND D.G., 2003: The application of dynamic programming to slope stability analysis. Canadian Geotechnical Journal, *40*, 4, 830–847.
RINALDI M., CASAGLI N., 1999: Stability of streambanks formed in partially saturated soils and effects of negative pore water pressures: the Sieve River (Italy). Geomorphology, *26*, 253–277.
ŘÍHA J., 2006: Flood protection – subterranean water problems. (In Czech.) Sborník z konference Vodní toky 2006, 38–43.
SCHMERTMANN J.H., 2006: Estimating slope stability reduction due to rain infiltration moulding. Journal of Geotechnical and Geoenvironmental Engineering, *132*, 9, 1219––1228.
ŠIMŮNEK J., VAN GEUNCHTEN M.TH., ŠEJNA J., 2006: The HYDRUS software package for simulating the two- and three-dimensional movement of water, heat, and multiple solutes in variably-saturated media, Technical manual, Version 1.0, PC Progress, Prague, Czech Republic.
SNĚHOTA M., 2003: Evaluation of infiltration-outflow experiment using MRI. [Doctoral Thesis.] Czech Technical University in Prague.
SNĚHOTA M., SOBOTKOVÁ M., CÍSLEROVÁ M., 2008: Impact of the entrapped air on water flow and solute transport in heterogeneous soil: Experimental set-up. J. Hydrol. Hydromech., *56*, 4, p. 247–256.
STARNAUD G., 1995: The high pore pressures within embankment dams – an unsaturated soil approach. Canadian Geotechnical Journal, *32*, 5, 892–898.
SZILAGYI, J., 2004: Vadose zone influences on aquifer parameter estimates on saturated-zone hydraulic theory. Journal of Hydrology, *286*, 78–86.
THIEU, N. T. M., FREDLUND, D. G., HUNG, V. Q., 2000: General partial differential equation solvers for saturated-unsaturated seepage. In: Rahardjo H., Toll D.G., Leong E.C. (Eds.), Unsaturated Soils for Asia, 201–206.
VAN GENUCHTEN M.TH., 1980: A closed-form equation for predicting the hydraulic conductivity of unsaturated soils. Soil Sci. Soc. Am. J., *44*, 892–898.
VOGEL T., 1987: SWMS II – Numerical model of two-dimensional flow in a variably saturated porous medium. Research Report No. 87*,* Dept. of Hydraulics and Catchment Hydrology, Agricultural Univ., Wageningen, The Netherlands.
VOGEL T., GERKE H.H., ZHANG R., VAN GENUCHTEN M.TH., 2000: Modeling flow and transport in a two-dimensional dual-permeability system with spatially variable hydraulic properties. Journal of Hydrology, *238*, 1-2, 78–89.
VOGEL T., VAN GENUCHTEN M.TH., CÍSLEROVÁ M., 2001: Effect of the shape of the soil hydraulic functions near saturation on variably-saturated flow predictions. Advances in Water Resources, *24*, 133–144.
VOGEL, T., DOHNAL, M., DUŠEK, J., 2004: Bench scale modeling approaches. Research Report C1.1, Eberhard Karls Universität Tübingen.
WILKINSON P.L., ANDERSON M. G., LLOYD D.M., 2003: An integrated hydrological model for rain-induced landslide prediction. Earth Surface Processes and Landforms, *27*, 12, 1285–1297.

Received 19 February 2009
Accepted 14 October 2009

DYNAMIKA VODNÍHO REŽIMU V TĚLESE OCHRANNÉ HRÁZE BĚHEM POVODNĚ S UVÁŽENÍM NENASYCENÉHO PROUDĚNÍ

David Zumr, Milena Císlerová

Vyšší pravděpodobnost výskytu extrémních klimatických jevů obrací pozornost k ochraně před následky, které tyto jevy způsobují. Zájem se soustředí na protipovodňové ochranné zemní hráze a jejich bezpečnost při povodních. Výpočet průsaku zemními hrázemi se často omezuje pouze na tu část hráze, která byla plně nasycená vodou, to znamená na plně nasycené proudění. Tento způsob modelování průsaku je dodnes považován za standardní, přestože je velmi limitující. Na význam nenasycené zóny na průběh průsaků hrází a na dynamiku tlakových poměrů uvnitř tělesa hráze upozornila celá řada autorů (např. *Freeze*, 1971; *Dapporto* et al., 2001). Zahrnutí nenasycené zóny je velmi důležité zejména u jemnozrnných, málo propustných zemin, ze kterých jsou často budována jádra zemních hrází. Bez zahrnutí nenasycené části tělesa hráze je zanedbán vliv časově i prostorově proměnlivého pole vlhkostí (např. při infiltraci vody ze srážky) na polohu hladiny.

V naší studii je simulováno proudění v tělese hráze s použitím numerického modelu, který umožňuje řešit proudění vody v proměnlivě nasyceném heterogenním pórovitém prostředí, s obecnými okrajovými podmínkami. Pro ilustraci použitelnosti přístupu byla zvolena geologická skladba vrstev podloží typická pro údolní nivy dolních tratí větších toků, tak jak ji popisuje například *Říha* (2006). Jedná se o mocné vrstvy velmi propustných sedimentů, které jsou překryty vrstvami málo propustných povodňových hlín (obr. 1).

Průběh povodňové vlny byl simulován pomocí proměnlivé okrajové podmínky na návodním líci hráze. Okrajová podmínka byla v zatopené části definována jako předepsaná tlaková výška (Dirichletova podmínka), která se skokově měnila podle aktuální výšky zatopení (obr. 2). Nezatopené části návodního líce byla přiřazena atmosférická okrajová podmínka (Neumanova). Na horním okraji hráze byla nastavena atmosférická okrajová podmínka, za hrází a v patě hráze výronová plocha. Tok dnem i horizontální tok podložím byly uvažovány jako nulové. Bylo simulováno celkem čtyřicet dní, během simulovaného období nebyly uvažovány žádné srážky ani výpar. Pro řešení byl použit simulační model S_2D_DUAL (*Vogel* et al., 2000), který využívá metody konečných elementů pro prostorovou diskretizaci a konečných diferencí pro diskretizaci času.

Výsledky simulace jsou na obr. 3, 4 a 5. Během povodně, která kulminovala ve třetím dni na stavu 320 cm, bylo do tělesa hráze infiltrováno přes 5,5 m^3 vody na metr šířky hráze. Nejvíce vody bylo v hrázi čtyři dny po

začátku povodně, kdy hladina v korytu řeky již klesala (obr. 2).

Dynamika infiltrace vody do tělesa hráze a do podloží je ilustrována na obr. 3 a 4. Obr. 3 vyjadřuje rozložení tlakových výšek ve vybraných časech, na obr. 4 jsou odpovídající aktuální vlhkosti. Případ (a) odpovídá počátečnímu ustálenému stavu, (b) stavu během vzestupu hladiny, (c) kulminaci povodňové vlny, (d) maximálnímu objemu zadržené vody v tělese hráze a (e) stavu po opadnutí vlny.

Výsledky potvrdily, že přístup, který uvažuje proudění i v nenasycené části hráze, lze k řešení průsaků zemními tělesy úspěšně využít při aplikacích, které vyžadují podrobnou znalost vodního režimu i v nenasycené zóně. Jedná se například o zjišťování tlaků vody v pórech během sycení a prázdnění zemních hrází pro posuzování stability těles, modelování vývoje vlhkosti jílových jader v nehomogenních hrázích při nízkých nebo nulových stavech v nádrži, kdy hrozí nebezpečí vzniku puklin vlivem vysušení. Model dovoluje testovat vliv různého počátečního nasysení ochranných hrází nebo hrází poldrů a vliv infiltrace dešťové vody.

Seznam symbolů

θ – objemová vlhkost [$L^3\ L^{-3}$],
h – tlaková výška [L],
C – vlhkostní kapacita [L^{-1}],
t – čas [T],
x_i (i = 1, 2) – prostorové souřadnice [L],
K – nenasycená hydraulická vodivost [$L\ T^{-1}$],
K_{ij}^A – složky tenzoru anisotropie,
S – propadový člen pro odběr vody kořenovou zónou [T^{-1}],
S_e – stupeň nasycení,
θ_r – residuální vlhkost [$L^3\ L^{-3}$],
θ_s – nasycená vlhkost [$L^3\ L^{-3}$],
θ_m – parametr modifikované retenční křivky [$L^3\ L^{-3}$],
h_s – vstupní hodnota vzduchu [L],
α – parametr retenční křivky podle van Genuchtena [L^{-1}],
m – parametr retenční křivky podle van Genuchtena,
n – parametr retenční křivky podle van Genuchtena,
K_s – nasycená hydraulická vodivost [$L\ T^{-1}$],
K_r – funkce relativní hydraulické vodivosti,
Γ_D – Dirichletova okrajová podmínka,
Γ_N – Neumannova okrajová podmínka,
Ψ, σ_1 – předepsané funkce [L], [$L\ T^{-1}$].

Environmental Earth Sciences (2020) 79:299
https://doi.org/10.1007/s12665-020-09052-w

ORIGINAL ARTICLE

Monitoring of the soil moisture regime of an earth-filled dam by means of electrical resistance tomography, close range photogrammetry, and thermal imaging

David Zumr[1] · Václav David[1] · Jakub Jeřábek[1] · Nina Noreika[1] · Josef Krása[1]

Received: 10 December 2019 / Accepted: 7 June 2020

Abstract
Small earthen dams usually lack a detailed monitoring system that would provide high-resolution data concerning changes in seepage flow. Geophysical methods and remote sensing are useful techniques for non-destructive and non-invasive investigation of subsurface processes. We have utilized a combination of electrical resistivity tomography (ERT), close range photogrammetry, and unmanned aerial vehicle (UAV) thermal imaging techniques to detect specific superficial and internal structures of a historical earth-filled dam. Longitudinal and transversal profiles of a typical fishpond dam in the Czech Republic were measured. The dam was constructed during the fifteenth century, but has since gone through some minor reconstruction. The aims of the applied geophysical methods are to detect and localize the boundary of the dam foundation, new earth material from reconstruction, the cone of water depression, the reservoir's outlet location, potential internal erosion, cavities, and heterogeneity in water content pattern and any other anomalies. The primary results show that ERT is suitable to detect dam stratification and large anomalies. The UAV monitoring system provided reliable data for a surface temperature distribution map which corresponded well to topsoil water content and electrical resistivity.

Keywords Earth-filled dam · Electrical resistance tomography · Geophysics · Unmanned aerial vehicle · Infrared spectra · Fishpond

Introduction

Throughout the Czech Republic, there is a network of earthen-dammed fishponds that provides both historic and touristic value, some of these structures date back 1000 years (Pokorná et al. 2014). The presence of these ponds and dams creates an interesting opportunity to apply various water and landscape conservation techniques, as they are typically protected by numerous cultural and environmental policies. Due to the protected status of these dams, it is imperative to preserve their integrity; first, to protect the local, historical tradition of fish farming that dates back to the 1100s AD and second, to avoid dam failure to protect the downstream area.

Many of the fishpond dams in the Czech Republic are historical, built in a time before current techniques were applied and regulations were enforced. When compared to modern dams, many of these historical dams are lacking in their material quality, overall design, and degree of soil compaction and consolidation making any engineering intervention rather complicated if a seepage or stability issue were to arise. The original outlets were typically constructed from wood and have since either degraded or become clogged, additionally, there is rarely any documentation concerning a dam's foundational design and material composition and many have been reinforced, repaired, or elevated over the years.

There are many threats to the soundness of old earth-filled dams—overtopping, uneven settling, tampering from rodents, etc. One of the common causes of failure is increased seepage due to internal erosion (Singh and Scarlatos 1988; Lawton et al. 1992; Panthulu et al. 2001; Richards and Reddy 2007; Zhang et al. 2009; Beneš et al. 2011; Morales-Nápoles et al. 2014). The internal erosion of poorly compacted soil can lead to "piping events" via fine sediment loss through the development of preferential pathways and can occur at any location of the dam's body. The severity

✉ David Zumr
david.zumr@fsv.cvut.cz

[1] Faculty of Civil Engineering, Czech Technical University in Prague, 16629 Prague, Czech Republic

Published online: 12 June 2020

of such piping events can be influenced by many factors including: dam material (homogeneity and composition), dam geometry, percolating water velocity, and erodibility of the soils used (Omofunmi et al. 2017) and these factors are amplified by rapid changes in reservoir water levels (Zumr and Císlerová 2010).

There are two main classifications of techniques to monitor the internal structure of a dam: invasive and non-invasive. Since the earthen dam in this study is historical and protected, the use of invasive techniques (e.g., boreholes, sensor installation, extensive sampling) is not feasible, so non-invasive monitoring techniques are necessary. A combination of different methods of modern geophysical surveying has become a popular option for this monitoring purpose as these surveys are relatively quick and inexpensive to conduct (Beneš et al. 2011; Perri et al. 2014). Current examples of these non-invasive surveying methods include: electrical resistivity tomography (ERT) (Cho et al. 2014; Lin et al. 2014; Arosio et al. 2017; Sentenac et al. 2017), ground penetrating radar (GPR) (Kim et al. 2007), electromagnetic methods (Sungkono et al. 2014), and seismic surveys (Karl et al. 2011). Although most of these techniques were originally developed for the survey of geological formations and deep soil horizons, GPR and ERT have been shown to be effective for shallow surveys as well (Zumr et al. 2012; Jeřábek et al. 2017; Guo et al. 2020).

Remote sensing and photogrammetry are very simple and useful non-invasive surface monitoring approaches. A precise surface model of the dam is necessary to map and display the internally monitored parameters. Close range photogrammetry and laser scanning provide very detailed digital surface models (DSM) with sub-millimeter accuracy that can aid in the monitoring of a soil's surface and the calculation of erosion rill volumes and surface roughness parameters (Peter Heng et al. 2010; Báčová and Krása 2016). The monitoring of such volumetric changes can help detect potential dam movements. A thermal imagery map of an area may be useful in dam monitoring efforts; significant variation in a dam's temperature (indicating variations in soil water content) can indicate possible failure areas (Chen et al. 2018). Unmanned aerial vehicles (UAVs or drones) are most commonly used to acquire data in these photogrammetry techniques.

Non-invasive monitoring techniques have been used in case studies of more recently constructed earthen dams (Al-Fares 2011; Hasani et al. 2013; Lin et al. 2013). No studies found have surveyed dams that are ~500 years old; the challenge with surveying such structures is the lack of data available for ground truthing results with pre-dammed geological data, so it is necessary to employ multiple techniques to cross-reference the survey findings.

Due to the various influences on the structural integrity of fishpond dams and in the face of climate change (with the expectation of more extreme weather events), it is important to assess the applicability of different non-invasive techniques available for active monitoring, in addition to regular visual inspections. The purposes of this study are threefold: (1) to detect faults, voids, and/or piping events within the structure of the dam, (2) to determine if any of the outlined techniques are able to distinguish between original and reconstructed portions of the dam along with the locations of any technical structures (like the reservoir outlet), and (3) to compare the outputs from close range photogrammetry and remote sensing with the electrical resistivity tomography surveys. The manuscript presents a comparison of the above-mentioned non-invasive monitoring techniques to determine if there is a synergistic solution to historical earthen dam surveying using a combination of these techniques. It also presents the various factors that must be considered when employing such techniques. It is considered that a non-invasive dam monitoring protocol would be valuable to watershed managers, engineers, and stakeholders to determine when dam maintenance is necessary.

Materials and methods

Study site

The surveys took place on a homogeneous earth-filled dam that creates the historical fishpond, Podviňák (constructed in the fifteenth century), located 30 km east of Prague in central Bohemia, Czech Republic (dam's crest GPS coordinates: 50.0604683 N, 14.8486778 E; 50.0599311 N, 14.8506947 E; altitude 217 m a.s.l.). The dam is 165 m long and the height at the reservoir's outlet is 3.7 m. Its trapezoidal cross-section is 7 m wide at the top, the upstream area is reinforced by a 1.8 m stone wall, and its downstream slope has an inclination of 1:5 (Fig. 1).

The Podviňák fishpond was selected for this study because of the historical age and the relative robustness of data available due to recent reconstruction. Prior to 2002, this fishpond was excessively silted and the owner, also being concerned about the dam's safety, initiated a reservoir de-siltation and dam reconstruction project using the sediment that had been deposited in the reservoir for dam enlargement. Prior to reconstruction, the crest's width was approximately 4 m and after reconstruction, the crest was widened to its current width of 7 m and the downstream slope was elongated.

Electrical resistance tomography

The geophysical survey was completed in November 2017 when the reservoir was empty. The antecedent monthly rainfall recorded by a nearby meteorological station was 45 mm

Fig. 1 Dam of Podviňák fishpond in **a** February 2017 and **b** November 2017

(slightly below the regional long-term average), there was no rainfall 7 days prior to the survey. The air temperature on the day of the measurement was greater than the long-term average and reached 14 °C.

The electrical resistivity tomography (ERT) surveys (in longitudinal and transversal directions) were conducted to obtain the electrical resistivity distribution of the dam's subsurface using an automated resistivity system (trade name ARES, produced by GF Instruments, Czech Republic). For all measurements, passive multi-electrode cables were used and the spacing between electrodes was limited to 1 m (Zumr et al. 2018). The narrow spacing of electrodes (up to 1 m) results in a high spatial resolution output of the shallow subsurface layers, as shown in previous earthen dam surveys (e.g. Al-Fares 2011; Hasani et al. 2013; Lin et al. 2013; Camarero et al. 2019).

The high soil water content allowed for an easy installation of the electrodes and established very good electrical contact between the device and the soil. To survey the subsurface, we utilized a Wenner–Schlumberger array, which is an appropriate method for the detection of shallow structures (Fazzito et al. 2009). The measured data points of the apparent electrical resistivity field were numerically inverted to obtain the electrical resistivity distribution using the standard Gauss–Newton optimization method (Loke et al. 2013) within RES2DInv software (Geotomo). Prior to inversion, the data with significantly different resistivity values (compared to the adjacent data points) were filtered out (less than 1% of datapoints were removed). The accepted inversion was consistently reached between 3 and 5 iterations, and the model residuals were below 2%.

To analyze the electrical resistivity transects, a binned empirical semivariogram was used (Banerjee et al. 2003; Jeřábek et al. 2017). A single semivariogram was calculated for all 20 depth levels in the longitudinal ERT transect to assess the spatial variability of electrical resistivity due to depth. A 5-m bin size was used for all depths. Due to the trapezoidal shape of the ERT transect, the maximum distance between analyzed points was restricted to 100 m, with this restriction, 20 semivariances were obtained for each depth level.

Two perpendicular ERT profiles were measured (Fig. 2):

(i) The longitudinal profile was located on the dam's crest, parallel to the dam's structure, toward its downstream edge (as the downstream side is of particular interest regarding seepage) and we omitted the center of the crest as it was not possible to properly insert electrodes into a gravel road. A passive multi-electrode cable with 96 electrodes at 1 m spacing

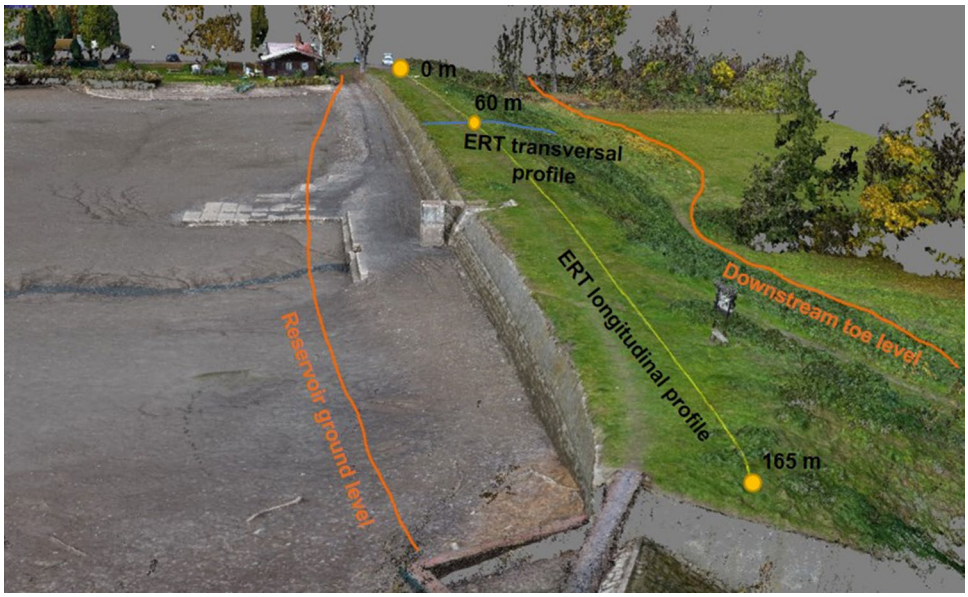

Fig. 2 ERT profile locations on the dam of the fishpond

was used. We surveyed the longitudinal profile in two steps as the multi-electrode cable was very short to survey the entire dam at once. Each profile was 95 m long, the second survey was shifted by 74 m (21 m overlapped between the first and second surveys). The length of the entire profile was 169 m. The measured apparent resistivity data from each section were merged into a single profile for the inverse analysis using Res2DInv (Loke et al. 213). The reliable output depth of the survey is approximately 20% of the length of each section (95 m) resulting in a maximal survey depth of ~19 m. For this analysis, a 10 m depth was selected, as deeper data have a coarser resolution, are affected by interpolation, and 10 m is well below the foundation of the dam anyway.

(ii) The transversal profile began on the upstream-most edge of the dam, adjacent to the stone wall and perpendicular to the dam's orientation. This ERT profile ran over the dam's crest to the foot of the downstream slope totaling 19 m in length, resulting in a reliable output depth down to ~4 m. This survey was conducted using the passive multi-electrode cable with an electrode spacing of 0.2 m.

Remote sensing

The Podviňák fishpond was first monitored by unmanned aerial vehicle (UAV) in February 2017 under full reservoir conditions and without vegetation cover. A second monitoring event was conducted over several days during the autumn of 2017 under moderately wet conditions when the reservoir was empty. Neither rainfall nor significant temperature changes were recorded across either set of surveying dates.

The dam was inspected by three optical systems. First, a DJI Phantom 4 equipped with the FC330 visible spectrum RGB camera (4000 × 3000 pix) served to build the orthophoto and 3D surface model of the entire dam. These data were collected both in February 2017 and in November 2017 (Fig. 1); at an elevation of 42 m a 16-mm ground sampling distance (GSD) was obtained. Then the DJI Phantom 4 was equipped with the Flir Tau2 13 mm radiometric IR camera (336 × 256 pix) at an elevation of 88 m, thermal imagery of the below-dam area was captured resulting in a 110 mm GSD. Finally, the entire dam area was monitored using a Tarot X hex-copter equipped with an Optris Micro-Epsilon TIM 450 infrared (IR) camera (382 × 288 pix) from a 23-m elevation resulting in a GSD of 90 mm. IR UAV surveys were completed across the same dates and times as the ERT monitoring (Krása and David 2018).

Agisoft PhotoScan Professional (v. 1.4.5) was used to process the UAV data by structure from motion photogrammetry. Twenty ground positioning targets were set in the area, the real-time kinematic global positioning system (RTK GPS) with a 15-mm standard deviation positioning error served as a reference set-up (Fig. 3).

The IR monitoring data for measuring temperatures can reach 10 mm GSD, but due to lower IR camera resolutions, it is impossible to cover areas of thousands of square meters with reasonable UAV flight times. Therefore, 100 mm GSD was selected as a reasonable compromise between data availability and output detail.

Soil water content and soil temperature monitoring

Topsoil volumetric soil water content was measured using an ML3 ThetaProbe (Delta-T Devices, UK) and a

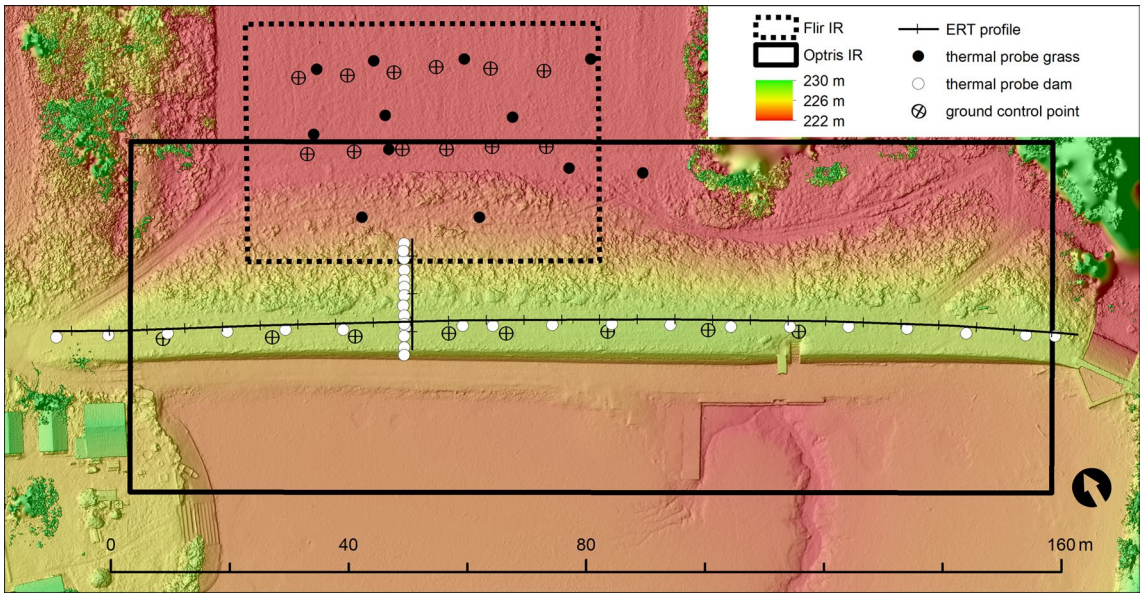

Fig. 3 Podviňák dam overview of temperature sampling points. Two separate IR models were evaluated: (i) Optris IR—covering the earth dam; (ii) Flir IR—below the dam

TRIME-PICO32 TDR sensors (IMKO Micromodultechnik, Germany). Both sensors have integrated soil temperature sensors. The ML3 Theta Probe measurements are representative of the top 6 cm of the soil profile and the TRIME-PICO32 is representative of the top 11 cm. The monitored soil volume is approximately 170 cm^3 for the ThetaProbe and 250 cm^3 for the TRIME-PICO32.

Soil water content and soil temperatures were measured in two profiles identical to the ERT profiles (on the transversal profile × 39 points on longitudinal profile). Additionally, 12 points were measured on the grassed area below the downstream slope. Five replicated measurements with both probes were completed in a square plot (0.5 m by 0.5 m) for each data point. All the data were imported into ArcGIS 10.5 (ESRI) to perform interpolations, spatial analyses, and data comparisons.

Results and discussion

Electrical resistance tomography

The results of the geophysical surveys were plotted as 2D transects representing the spatial distribution of the subsurface electrical resistivity (Fig. 4). Even though the reservoir was empty during the geophysical monitoring, the earthen dam was very wet and the observed electrical resistivity inside the dam was very low, ranging from 10 to 60 Ω m. Only close to the surface were distinct areas where the electrical conductivity reached up to 150 Ω m. The transversal ERT profile shows the resistivity distribution to a depth of 4 m below the surface of the dam's downstream slope. The rest of the dam's body was not monitored as we could not install the ERT electrodes into the stone wall on the waterside of the dam.

The transversal ERT profile (Fig. 4a) shows a rather isotropic distribution of electrical resistivity, with higher electrical resistivity in the middle of the dam's crest and the reasoning for this is twofold. First, the soil texture at the top of the dam is very different from the remaining material as there is a gravel pathway in the crest's center. This area is covered with a less conductive gravel that extends into the subsurface. The second reason is lower saturation as the pathway is neither protected by vegetation nor gravel so it drains more quickly; close to the dam's crest a trace of the historical dam's boundary can be detected (outlined with the dashed yellow line). The less resistive area in the central lower part of the ERT profile (violet color) is the same depth as the normal water level in the reservoir, the lower resistivity indicates the remnants of the seepage line. The topsoil in the middle of the downstream slope has a higher electrical resistivity, this area has low vegetation density compared to the surroundings. Via remote sensing methods and the point measurements, we observed higher surface temperature and lower soil moisture in this part of the slope as well. Even though it has been previously shown that the relationships between electrical resistivity and soil water content (or any other physical parameter) are generally uncertain (Kotikian et al. 2019), in this case, it seems that the high resistivity is associated with the distinct vegetation pattern and soil moisture [as was shown e.g. by Loke et al. (2013) and Dick et al. (2018)].

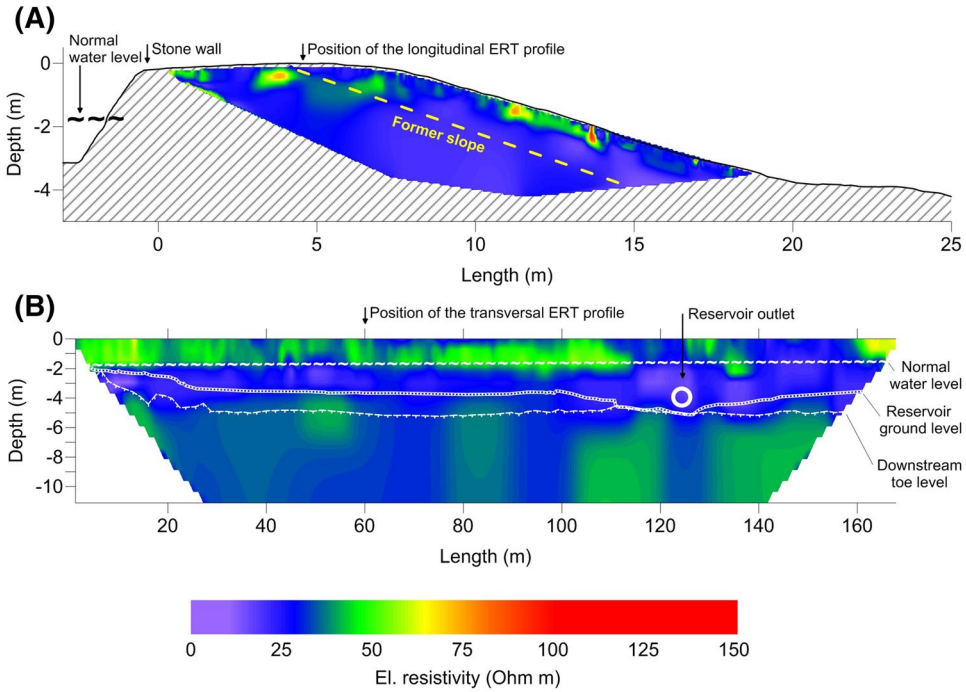

Fig. 4 **a** Transversal 2D ERT transect; **b** longitudinal 2D ERT transect. Blue represents nearly saturated regions, green to red areas close to the surface are drier with higher electrical resistivity

The longitudinal ERT profile, extending to a depth of 10 m below the dam's crest, does not show any significant anomalies or divisions between the dam's body and the bedrock (Fig. 4b). The position of the outlet corresponds to the area of lower electrical resistivity. Low resistivity below the outlet indicates the original position of the stream. Similar resistivity patterns in the vicinity of a dam's outlet have been previously observed (Yilmaz and Koksoy 2017).

Three distinct horizontal layers can be observed in the longitudinal profile. The top 2 m exhibits higher electrical resistivity with values of approximately 50 Ω m. The lower boundary of this uppermost zone corresponds to the normal water level. The subsurface layer, ranging from 2 to 4 m below the crest, has a very low electrical resistivity. The upper and lower boundaries of the second layer correspond to the reservoir's normal water level and the reservoir's ground level, respectively. Low resistivity can be explained by nearly saturated soil. Below the reservoir's ground level are alternate zones with higher and lower electrical resistivity, likely representing soils with different textures. Horizontal zonation of the electrical resistivity is also apparent from the semivariogram of the longitudinal ERT profile (Fig. 5). Electrical resistivity semivariograms have been previously used to determine the degree of heterogeneity in a particular soil layer (Jeřábek et al. 2017). In this study, the uppermost layer has much higher spatial variability (greater than one order of magnitude) for any lag distance than the subsurface layer. The semivariance increases more gradually with distance in the deeper soil layers, indicating that soil water properties change at large spatial scales. This electrical resistivity semivariance decrease in response to depth and distance from the crest

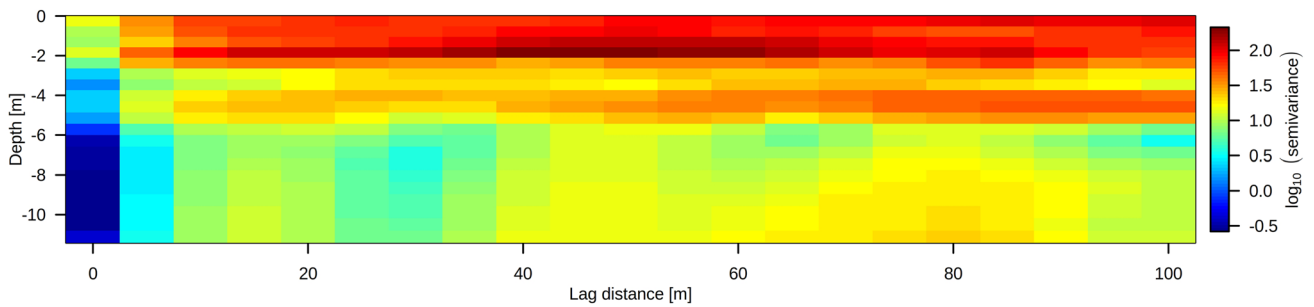

Fig. 5 Semivariogram of the longitudinal ERT transect. Each row in the grid represents a semivariogram for a single depth level. The semivariance is depicted by color on a logarithmic scale

of the dam indicates a spatial uniformity of the subsoil below the dam's toe level.

The surveyed dam was recently reconstructed, so one can hardly expect evidence of any current significant preferential seepage or piping, and the geophysical survey did not detect any. Recent studies suggest that recurrent monitoring of dams under varying soil moisture and water level conditions is necessary to detect potential failures (Song et al. 2005; Lin et al. 2014; Arosio et al. 2017; Sentenac et al. 2017) even though such an approach is more demanding.

Remote sensing outputs

The results of the remote sensing are:

- Accurate dam shape and 3D models from February to November 2017 with a precision of 16 mm GSD, illustrating differences due to water level and varying levels of vegetation cover. November imagery allowed the capture of vegetation cover influences and the bottom of the reservoir at the time of the ERT experiment. February imagery allowed for a better shape estimation of the dam's top (due to no vegetation cover) and detection of spatial variability in snowmelt at the dam's toe.
- High-resolution orthophotographs of the dam and reservoir area from both periods.
- IR orthophoto of the dam and the downstream area of the dam's slope (November 2017).

3D modeling and orthophotography are able to detect topographical changes and aid in analyzing potential shape changes over time. Detailed dam cross sections were derived from the model (Fig. 6) and difference raster surface models (Peter et al. 2014) were utilized to detect shape shift. 3D modeling and orthophotography serve also as supporting data for ERT and moisture monitoring, since the ERT modeling must be coordinated and the dam cross sections allow for the projection of ERT imagery to a realistic dam shape.

Finally, the orthophotography and 3D modeling accounts for differences in vegetation properties (both vegetation spatial distribution, height, and volume) which may explain differences in the soil water content of the dam's downstream slope (Fig. 6). The difference raster and cross sections indicate vegetation height (up to 1 m) and rather high spatial variability. The entire slope is not regularly cut.

Remote IR monitoring was examined alongside orthophotography and 3D modeling to identify areas of temperature hotspots of the dam (Fig. 7). The surface temperature is spatially variable, especially along the dam's downstream slope. The drainage channel of the empty reservoir was the coldest detected surface (8 °C). The saturated sediment of the reservoir and the rills in the vicinity of the channel tended to

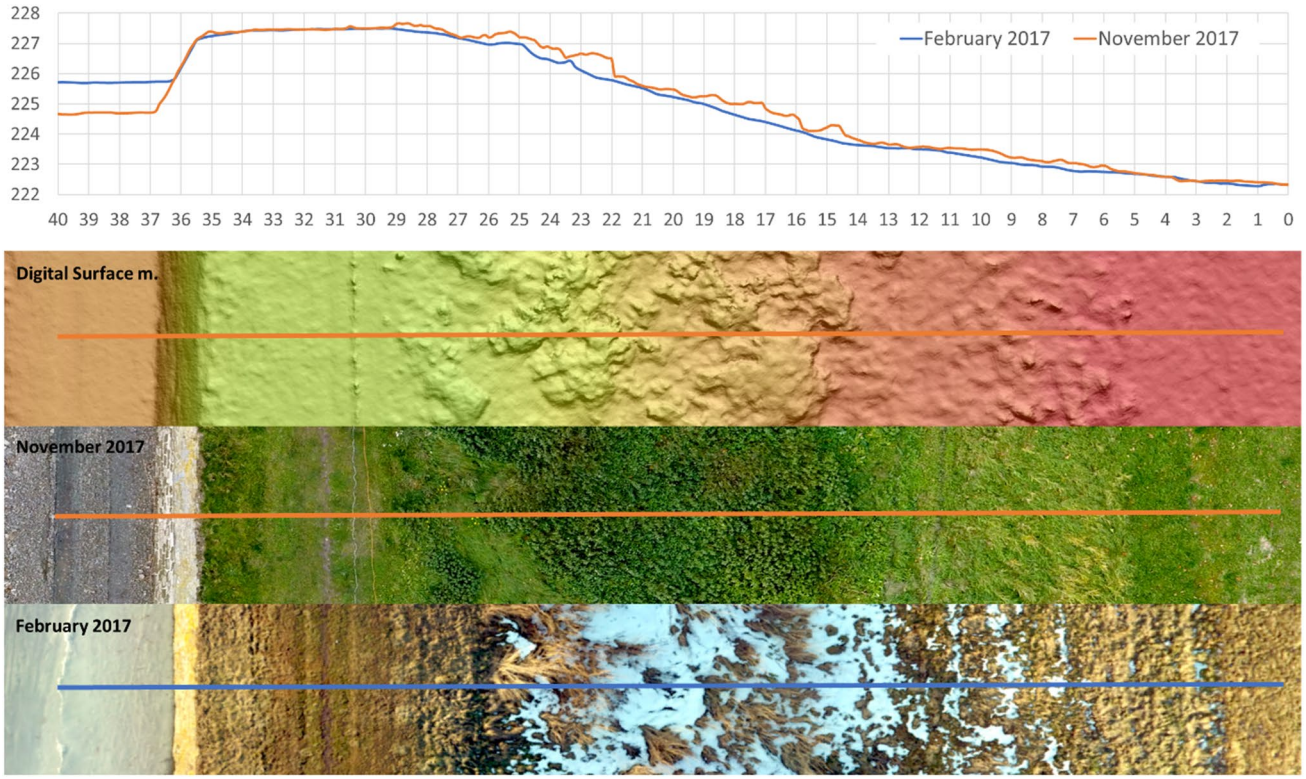

Fig. 6 Dam profiles by UAV monitoring showing the water level changes and vegetation growth in 2017

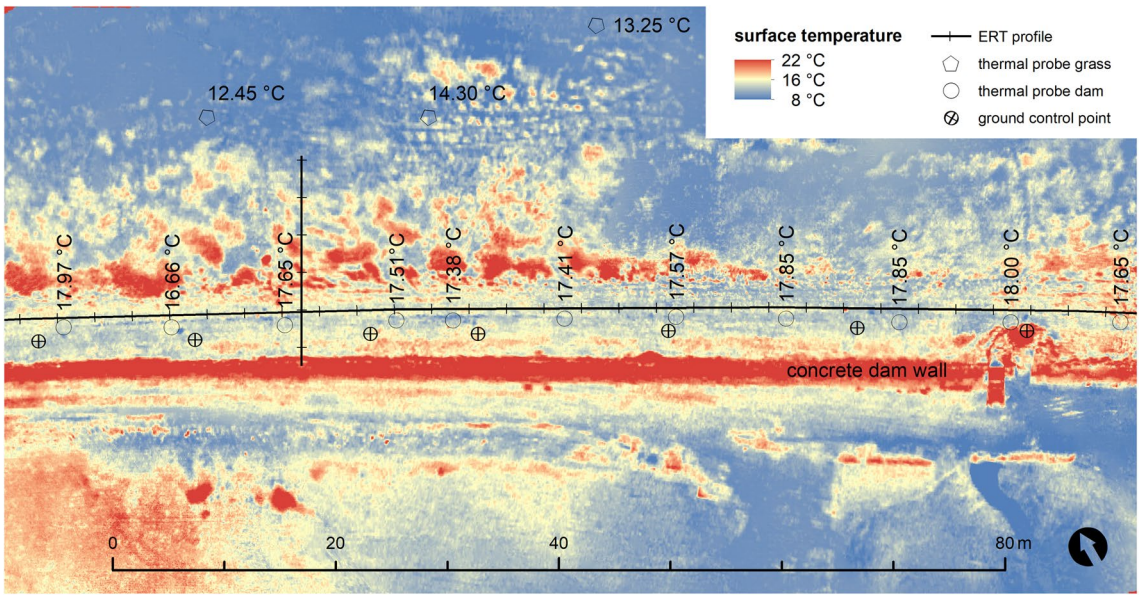

Fig. 7 IR orthophoto via Optris IR monitoring in November 2017

be cooler than the dry sediment in the left part of the figure, where the temperature reached 17 °C. The warmest surface detected was the wall (above 20 °C) and the sun-oriented parts of the areas with higher vegetation. This effect was caused by sunset time co-occurring with IR monitoring; the temperature of all surfaces significantly dropped, but the higher vegetated surfaces prevented cooling. The surface of the dam is on average 5 °C warmer than the grassland below the dam. The significant effect of vegetation was also observed during ERT data analysis, as previously mentioned.

Topsoil water content

Measured soil water content values were separated into three groups according to their position (Fig. 8); 320 measurements were taken on the dam's crest with an observed

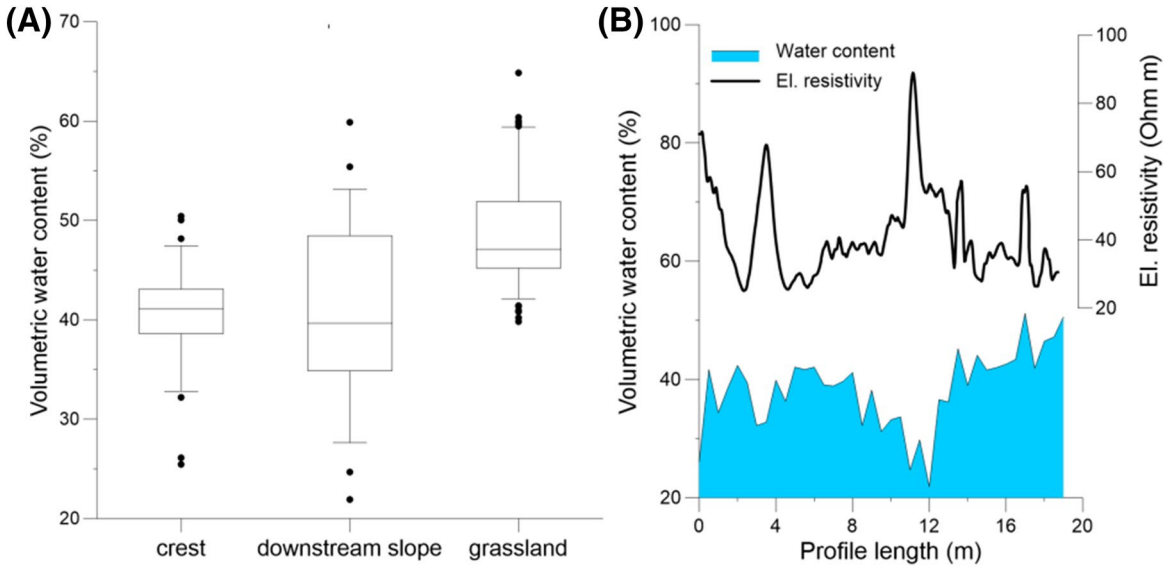

Fig. 8 Comparision of the volumetric water content measured on the dam's crest, its downstream slope, and the grassland below the dam. The upper and lower bounds of the boxes are the first and third quartiles inner band represents the water content median. The whiskers represent minimal and maximal values, outliers are represented by dots (left). Topsoil water content and electrical resistivity along the transversal ERT profile (right)

average water content of 41.5 ± 4.7%, 220 measurements were taken on the dam's downstream slope with an observed average water content of 40.7 ± 8.7%, and 625 points were taken in the grassland area below the dam with an observed average water content of 48.5 ± 5.2%. The mean values for the crest and the downstream slope are similar, but it should be noted that the position of the crest's datapoints is identical to those of the longitudinal ERT profile, which was located within a grassed area at the edge of the crest. The sloped area is the most variable in soil water content, which corresponds well with the vegetation density variability observed with the UAV. The grassland below the dam has the highest topsoil water content, which corresponds to the observed low surface temperature (as can be seen in Fig. 7). This direct association of the soil moisture with surface temperature infrared images on a maize field was observed by Hassan-Esfahani et al. (2015).

Figure 8b presents a comparison between the near surface soil electrical resistivity (10 cm below the surface) and the volumetric water content as measured along the transversal ERT profile (Fig. 4a). Generally, the decrease in the volumetric water content corresponds with increased electrical resistivity (visible on profile lengths 0, 3 and 11 m on Fig. 8b). This trend is expected, as electrical resistivity depends on, among other soil characteristics, actual water content (Michot et al. 2003; Samouëlian et al. 2005).

Conclusions

The purpose of this study was to evaluate the applicability of various non-invasive monitoring techniques of earthen fishpond dams in the Czech Republic. The implementation of non-invasive dam monitoring techniques is necessary to ensure their structural stability for safety, historical, and cultural reasons. The applied techniques were able to detect various heterogeneities within the dam. Electrical resistivity was able to indicate traces of the original stream location and was isotropically distributed across the dam without any glaring irregularities, suggesting that there were no large-scale structural issues within the dam, but this analysis would be more sensitive when the pond is at full capacity. The high level of variability found in surface temperatures and electrical resistivity measurements on the dam's downstream slope could indicate seepage problems and/or piping events but in this case, it is likely due to the variation in vegetative characteristics. Through the analysis of ERT, various layers of the dam (corresponding to annual variation in water levels) were identified along with the location of the reservoir's outlet. Neither DSM (constructed via close-range photogrammetry nor infrared imagery) indicated any major faults or structural issues.

The presented method of comparing UAV monitored and measured topsoil temperatures shows that UAV monitoring can give reliable data. UAV monitoring in the visible and infrared spectra serves to support non-invasive techniques by providing data on dam geometry and its changes over time. Assessing surface parameters (vegetation status, vegetation density and height, soil moisture, and surface temperature) by UAV techniques can explain the spatial distribution of soil profile conductivity. Commercial drones and cameras (Phantom 4) are precise enough to build models of entire dams with approximately a 15-mm ground sampling distance (GSD), provided that enough positioned targets are available for georeferencing.

For IR temperature monitoring, two optical systems were used and both systems produced similar data quality (GSD and spectral resolution) but they differ in feasibility and terrain applications. Orthophotography assembling over larger structures allows for easier data collection due to the wide angle of the Optris system.

To properly assess the temperature and soil water content relationship, one needs to consider vegetation influences. Since old fishpond dams rarely have bare soil or non-vegetated surfaces, climate conditions (no direct sunlight, stable air temperature) and vegetation status (ideally non-vegetative season) need to be carefully controlled. The study has shown drawbacks and potential uses of UAV IR imagery. Highly saturated surfaces such as the original streamline, are easily detectable and could be even automatically classified. Tall and dense vegetation on the dam's surface can hide many effects of water percolation, especially when temperature is quickly decreasing after a relatively warm day. Usually a combination of visible spectrum (RGB), digital surface model (DSM), and infrared data can help to identify individual effects from different factors and enhance the ability to reliably define the water saturated areas of a dam structure.

There is a potential in searching for a synergy using a combination of subsurface non-invasive surveying methods and surface imaging in various spectra. Each method has its drawbacks and uncertainties, but especially UAV imaging is developing quickly and we may expect improvements in resolution and reliability of IR imaging techniques. Still more research will be needed to connect the results from subsurface and surface surveys and to be able to quantitatively and precisely identify the locations and the degree of a dam's failures and to relate it to seepage that can be detected from superficial surveys. The next anticipated step will be the use of numerical models to predict seepage where geophysics surveys and the remote sensing can provide both input and validation data.

Acknowledgements This research was funded within project no. DG16P02M036 "Conservation, reparations and monitoring of

historical pond dams as our cultural heritage," granted by the Ministry of Culture of the Czech Republic.

Author contributions DZ, VD, and JK carried out the data collection and analysis, JJ performed the ERT analysis and prepared the figures, VD provided funding acquisition. DZ, NN, and JK prepared the manuscript with the contribution of all other authors. All authors contributed to the study conception and design. Material preparation, data collection, and analysis were performed by DZ, VD, JJ, NN, and JK. The first draft of the manuscript was written by DZ and all authors commented on previous versions of the manuscript. All authors read and approved the final manuscript.

Compliance with ethical standards

Conflict of interest The authors declare no conflict of interest. The funding sponsors had no role in the design of the study; in the collection, analyses, or interpretation of data; in the writing of the manuscript, and in the decision to publish the results.

References

Al-Fares W (2011) Contribution of the geophysical methods in characterizing the water leakage in Afamia B dam, Syria. J Appl Geophys 75:464–471

Arosio D, Munda S, Tresoldi G et al (2017) A customized resistivity system for monitoring saturation and seepage in earthen levees: installation and validation. Open Geosci 9:457–467. https://doi.org/10.1515/geo-2017-0035

Báčová M, Krása J (2016) Application of historical and recent aerial imagery in monitoring water erosion occurrences in Czech highlands. Soil Water Res 11:267–276. https://doi.org/10.17221/178/2015-SWR

Banerjee S, Carlin BP, Gelfand AE (2003) Hierarchical modeling and analysis for spatial data. Chapman and Hall/CRC, New York. https://doi.org/10.1201/9780203487808

Beneš V, Tesař M, Boukalová Z (2011) Repeated geophysical measurement—the basic principle of the GMS methodology used to inspect the condition of flood control dikes. River Basin Manag VI, Conf., pp 105–115

Camarero PL, Moreira CA, Pereira HG (2019) Analysis of the physical integrity of earth dams from electrical resistivity tomography (ERT) in Brazil. Pure Appl Geophys 176:5363–5375

Chen CY, Chen SC, Chen KH, Liu ZH (2018) Thermal monitoring and analysis of the large-scale field earth-dam breach process. Environ Monit Assess 190:483. https://doi.org/10.1007/s10661-018-6869-y

Cho IK, Ha IS, Kim KS et al (2014) 3D effects on 2D resistivity monitoring in earth-fill dams. Near Surf Geophys 12:73–81. https://doi.org/10.3997/1873-0604.2013065

Dick J, Tetzlaff D, Bradford J, Soulsby C (2018) Using repeat electrical resistivity surveys to assess heterogeneity in soil moisture dynamics under contrasting vegetation types. J Hydrol 559:684–697. https://doi.org/10.1016/j.jhydrol.2018.02.062

Fazzito SY, Rapalini AE, Cortés JM, Terrizzano CM (2009) Characterization of Quaternary faults by electric resistivity tomography in the Andean Precordillera of Western Argentina. J S Am Earth Sci 28:217–228. https://doi.org/10.1016/j.jsames.2009.06.001

Guo L, Mount GJ, Hudson S et al (2020) Pairing geophysical techniques improves understanding of the near-surface critical zone: visualization of preferential routing of stemflow along coarse roots. Geoderma 357:113953. https://doi.org/10.1016/j.geoderma.2019.113953

Hasani H, Mamizadeh J, Karimi H (2013) Stability of slope and seepage analysis in earth fills dams using numerical models (case study: Ilam DAM-Iran). World Appl Sci J 21:1398–1402

Hassan-Esfahani L, Torres-Rua A, Jensen A, McKee M (2015) Assessment of surface soil moisture using high-resolution multi-spectral imagery and artificial neural networks. Remote Sens 7:2627–2646. https://doi.org/10.3390/rs70302627

Jeřábek J, Zumr D, Dostál T (2017) Identifying the plough pan position on cultivated soils by measurements of electrical resistivity and penetration resistance. Soil Tillage Res 174:231–240. https://doi.org/10.1016/j.still.2017.07.008

Karl L, Fechner T, Schevenels M et al (2011) Geotechnical characterization of a river dyke by surface waves surface waves. Near Surf Geophys 9:515–527. https://doi.org/10.3997/1873-0604.2011030

Kim JH, Yi MJ, Song Y et al (2007) Application of geophysical methods to the safety analysis of an earth dam. J Environ Eng Geophys 12:221–235. https://doi.org/10.2113/JEEG12.2.221

Kotikian M, Parsekian AD, Paige G, Carey A (2019) Observing heterogeneous unsaturated flow at the hillslope scale using time-lapse electrical resistivity tomography. Vadose Zone J 18:1–16. https://doi.org/10.2136/vzj2018.07.0138

Krása J, David V (2018) Close range photogrammetry and thermal imagery in monitoring of soil moisture in dam structures of historical fishponds. Proceedings 2:623. https://doi.org/10.3390/proceedings2110623

Lawton EC, Fragaszy RJ, Hetherington MD (1992) Review of wetting-induced collapse in compacted soil. J Geotech Eng 118:1376–1394. https://doi.org/10.1061/(ASCE)0733-9410(1992)118:9(1376)

Lin CP, Hung YC, Yu ZH, Wu PL (2013) Investigation of abnormal seepages in an earth dam using resistivity tomography. J Geoeng 8:61–70

Lin CP, Hung YC, Wu PL, Yu ZH (2014) Performance of 2-D ERT in investigation of abnormal seepage: a case study at the Hsin-Shan earth dam in Taiwan. J Environ Eng Geophys 19:101–112. https://doi.org/10.2113/JEEG19.2.101

Loke MH, Chambers JE, Rucker DF et al (2013) Recent developments in the direct-current geoelectrical imaging method. J Appl Geophys 95:135–156. https://doi.org/10.1016/j.jappgeo.2013.02.017

Michot D, Benderitter Y, Dorigny A et al (2003) Spatial and temporal monitoring of soil water content with an irrigated corn crop cover using surface electrical resistivity tomography. Water Resour Res 39:1138. https://doi.org/10.1029/2002WR001581

Morales-Nápoles O, Delgado-Hernández DJ, De-León-Escobedo D, Arteaga-Arcos JC (2014) A continuous Bayesian network for earth dams' risk assessment: methodology and quantification. Struct Infrastruct Eng 10:589–603. https://doi.org/10.1080/15732479.2012.757789

Omofunmi OE, Kolo JG, Oladipo AS et al (2017) A Review on effects and control of seepage through earth-fill dam. Curr J Appl Sci Technol Br J Appl Sci Technol China 22:1–11. https://doi.org/10.9734/CJAST/2017/28538

Panthulu TV, Krishnaiah C, Shirke JM (2001) Detection of seepage paths in earth dams using self-potential and electrical resistivity methods. Eng Geol 59:281–295. https://doi.org/10.1016/S0013-7952(00)00082-X

Perri MT, Boaga J, Bersan S et al (2014) River embankment characterization: the joint use of geophysical and geotechnical techniques. J Appl Geophys 110:5–22. https://doi.org/10.1016/j.jappgeo.2014.08.012

Peter Heng BC, Chandler JH, Armstrong A (2010) Applying close range digital photogrammetry in soil erosion studies. Photogramm Rec 25:240–265. https://doi.org/10.1111/j.1477-9730.2010.00584.x

Peter KD, d'Oleire-Oltmanns S, Ries JB et al (2014) Soil erosion in gully catchments affected by land-levelling measures in the Souss

Basin, Morocco, analysed by rainfall simulation and UAV remote sensing data. CATENA 113:24–40. https://doi.org/10.1016/j.catena.2013.09.004

Pokorná A, Houfková P, Novák J et al (2014) The oldest Czech fishpond discovered? An interdisciplinary approach to reconstruction of local vegetation in mediaeval Prague suburbs. Hydrobiologia 730:191–213. https://doi.org/10.1007/s10750-014-1837-1

Richards KS, Reddy KR (2007) Critical appraisal of piping phenomena in earth dams. Bull Eng Geol Environ 66:381–402. https://doi.org/10.1007/s10064-007-0095-0

Samouëlian A, Cousin I, Tabbagh A et al (2005) Electrical resistivity survey in soil science: a review. Soil Tillage Res 83:173–193. https://doi.org/10.1016/j.still.2004.10.004

Sentenac P, Benes V, Budinsky V et al (2017) Post flooding damage assessment of earth dams and historical reservoirs using non-invasive geophysical techniques. J Appl Geophys 146:138–148. https://doi.org/10.1016/j.jappgeo.2017.09.006

Singh VP, Scarlatos PD (1988) Analysis of gradual earth-dam failure. J Hydraul Eng 114:21–42. https://doi.org/10.1061/(ASCE)0733-9429(1988)114:1(21)

Song S-H, Song Y, Kwon B-D (2005) Application of hydrogeological and geophysical methods to delineate leakage pathways in an earth fill dam. Explor Geophys 36:92. https://doi.org/10.1071/EG05092

Sungkono HA, Prasetyo H et al (2014) The VLF-EM imaging of potential collapse on the LUSI embankment. J Appl Geophys 109:218–232. https://doi.org/10.1016/j.jappgeo.2014.08.004

Yilmaz S, Koksoy M (2017) Electrical resistivity imaging and dye tracer test for the estimation of water leakage paths from reservoir of Akdeğirmen dam in Afyonkarahisar, Turkey. Environ Earth Sci 76:829. https://doi.org/10.1007/s12665-017-7174-8

Zhang LM, Xu Y, Jia JS (2009) Analysis of earth dam failures: a database approach. Georisk Assess Manag Risk Eng Syst Geohazards 3:184–189. https://doi.org/10.1080/17499510902831759

Zumr D, Císlerová M (2010) Soil moisture dynamics in levees during flood events—variably saturated approach. J Hydrol Hydromech 58:64–72. https://doi.org/10.2478/v10098-010-0007-z

Zumr D, David V, Krása J, Nedvěd J (2018) Geophysical evaluation of the inner structure of a historical earth-filled dam. Proceedings 2:664. https://doi.org/10.3390/proceedings2110664

Zumr D, Snehota M, Cislerova M (2012) Numerical simulation of tension infiltration experiment monitored by 3D ERT. In: 5th Asia-Pacific conference on unsaturated soils 2012